

Swansea University

The corrosion and mechanical performance
of industry relevant additively
manufactured steels and alloys

by

Iwan Salvu Grech

in the

College of Science and Engineering
Department of Engineering

April 2023

Copyright: The Author, Iwan S. Grech, 2023.

'Never confuse education with intelligence, you can have a PhD and still be an idiot.'

Richard P. Feynman

Declarations

This work has not previously been accepted in substance for any degree and is not being concurrently submitted in candidature for any degree.

Signed 

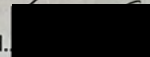
Date 4/9/22

This thesis is the result of my own investigations, except where otherwise stated. Other sources are acknowledged by footnotes giving explicit references. A bibliography is appended.

Signed 

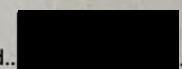
Date 4/9/22

I hereby give consent for my thesis, if accepted, to be available for photocopying and for inter-library loan, and for the title and summary to be made available to outside organisations.

Signed 

Date 4/9/22

The University's ethical procedures have been followed and, where appropriate, that ethical approval has been granted.

Signed 

Date 4/9/22

Abstract

Laser Powder Bed Fusion (LPBF) is a manufacturing technique that allows for the production of metallic components directly from CAD files. The technique allows for parts of increased strength to weight ratio to be produced in comparison to wrought parts. Complex geometries with internal lattices can be printed without the need for post manufacture machining. Parts manufactured by LPBF suffer from inherent build defects including porosity that can negatively impact both the mechanical and corrosion properties of these parts. Whilst the mechanical properties of the materials manufactured using this method have been investigated since the infancy of the technique the corrosion performance of these materials is still largely not understood. This PhD thesis aims to improve and expand upon the current knowledge of the corrosion properties of LPBF manufactured parts, specifically in chloride environments.

In order to accomplish this LPBF was used to produce components of various build parameters in Invar, 17-4PH and 316L. The corrosion properties of LPBF manufactured Invar was compared to its wrought counterpart through a range of techniques including time-lapse microscopy (TLM), scanning vibrating electrode technique (SVET), white light interferometry and electron back scatter diffraction (EBSD). It was determined that the inherent porosity of the LPBF manufactured Invar resulted in the material being susceptible to localised corrosion attack. This attack occurred predominantly at porosity defects with the majority of localised corrosion initiating at porosity defects located at the melt pool boundary region of the microstructures.

316L was also built using LPBF with the distribution of density across the build plate being investigated as well as the corrosion performance of the material. CT scanning was also implemented to evaluate the morphology and location of porosity within the material. To reduce the porosity within LPBF manufactured 316L post production processing via Hot Isostatic Pressing (HIP) was investigated. A total of 12 HIP treatment cycles were devised varying temperature, pressure and time with an additional treatment being further treated by a furnace treatment and water quenching. The mechanical and corrosion performance of the components post HIP was investigated using a range of techniques including potentiodynamic scanning, hardness, fatigue and tensile testing as well as microscopy and x-ray diffraction (XRD). It was found that Post-processing HIP cycles at mid (1125 °C) and high (1200 °C) temperatures remove the melt pools, melt pool boundaries and sub-grain cellular features that are present in the microstructure from the additive process. The post-process HIP cycle at the lowest of the temperatures (700 °C) was found to result in an increased yield strength and a reduced elongation to fracture compared to other treatments. Variations in pressure did not induce a significant difference in properties. HIP treatment 4 - HIP (T₇₀₀ P₁₃₇) was seen to have the highest

Nf at higher stress over 10 – As built, whilst being intermediate on ultimate tensile strength and recording the lowest average pitting potential. Samples subject to treatment 4 - HIP (T₇₀₀ P₁₃₇) retained their cellular substructures and grain boundaries have not become enlarged, whilst density has been increased by the HIP treatment. HIP treatments succeeded in reducing the spread of the pitting potentials by 52.5 % compared to as-built parts with the largest reduction in the spread of pitting potentials being achieved in low temperature cycles. However, there is still too large a variation in the corrosion performance of AM parts compared to wrought to instil confidence in their service in corrosive environments over wrought counterparts.

LPBF 17-4PH samples were manufactured and the density distribution across the build plate was investigated as well as the corrosion properties of the material. CT scanning was also used to evaluate the porosity of these manufactured samples which contained irregularly shaped lack of fusion defects.

Acknowledgements

I'm going to break all of the rules when writing academic/scientific documents in this section so chill out and hold on thankfully this is going to be a long one because I've met some absolute characters. Doing this PhD has been a challenge with a lot of obstacles along the way. Lots of things have gone wrong and lots of things have gone well. Going from a background in Physics it's been funny to see the differences between how physics and engineering people think and work. Engineering is the making of things that did not previously exist, whereas science is the discovering of things that have long existed. Whilst I prefer neither I wish that physics enthusiasts would work less and have more fun and I wish that engineering enthusiasts work more and have less fun! Ultimately, I'm fairly happy with the end product but things could always have been better (they also could've gone a hell of a lot worse!). Any modern day scientific work is truly credited to standing on the shoulders of giants. The sheer volume of work that is being published hourly is gargantuan but it all comes down to the original scientific pioneers who crawled to allow modern scientists to fly. It's truly flabbergasting how far we have come from Archimedes, Newtons laws, Gauss law and L'Hôpital's rule which undermine the fundamentals of the majority of science and engineering in my humble opinion.

Lots of people have come and gone throughout this "journey" some people I'm extremely saddened to have either lost or have drifted away for whatever reason. Despite this nonsense there are a lot of people I'm very thankful for helping me along the way and supporting me when I quite honestly was very fed up with everything. If you're reading this (which I don't imagine many people will) and you feel left out then I've either forgotten to include you by mistake or you genuinely were no help whatsoever! I'll leave it as an exercise for the reader to figure out where they belong.

The main thanks go to my parents for very obvious reasons including but not limited to always being there for me whenever and wherever I am and for always supporting me in every possible way well beyond the call of duty. Next comes the members of my family of whom I love and care for greatly who are too numerous to name. Next is my partner Lauren, who has supported me tremendously, especially whilst I've made the corrections to this thesis. This support includes the constant production and delivery of food and drink, never ending walks with Dewi our flat-coated retriever and trips to the peak district. Following this we're down to my closest friends Tom Chess, Luca Vella, the "Strade Skwl Bois", Jonny Cleverly, Alexis Pala, Isaac Mehraj, Eduardo Dork, ZhenXiong Ye - "Singapore Isaac", Rob Amner Evans and Jody Amner Evans. Without the support from you guys I never would've made it through this PhD and I am truly grateful to each and every one of you and am fortunate to have made your acquaintance.

Moving along a big thank you goes to my primary supervisor James Sullivan who has put the faith and trust in me to allowing me not only to carry out this PhD but to allow me to pursue this PhD with a large degree of freedom following the direction that I wanted to take the work. As well as this Jim is a great guy who's always been there when I needed someone to bounce ideas off and for support in anything I needed including photography. Another big thank you goes to my "secondary" supervisor Nick Lavery, who put the time, effort and interest in to effectively be a second primary supervisor. Nick is always available to help and support and gave me the freedom to take this PhD in whichever direction I wanted and I've always been extremely grateful for his contributions to the work and also his desire for continual improvement and development. Sometimes the extra push of a challenge and debate on my work is what's needed to get the best out of me. Additionally I have to thank Kevin O'Keeffe and Aled Isaac, the help and time that they gave me during my undergraduate degree when I was even more lost was extremely influential and without them I likely wouldn't have completed my undergraduate degree let alone my masters or PhD.

Next I'd like to thank some people who've helped me in carrying out a lot of this experimental work from teaching me how to use a 3D metal printer, to showing me the dial to rotate samples in the SEM after I'd spent hundreds of hours thinking that very same dial would have some catastrophic effect. Natalie Wint and Shahin Mehraban guided me from when I first stepped into the labs and their time and kindness is greatly appreciated. Tom Lewis, for being available seemingly 24/7 and for always going out of his way and doing his utmost to help you regardless of whether it was of any benefit to himself or not. Rhodri Rees, Jordan Rosser, Steve Millward, Adam Philo, Jon Cullen, Dan Butcher, Phil Ansell and many others for all the good times and chats in the lab.

Long story short I'm dedicating this to my parents, Tina and Joe.

Contents

Abstract	iii
List of Figures	xi
1 Literature review and theory	1
1.1 Additive Manufacturing (AM)	1
1.2 Introduction to additive manufacturing	2
1.3 Laser Powder Bed Fusion Build Parameters	3
1.3.1 Point Distance	3
1.3.2 Hatch Spacing	4
1.3.3 Exposure Time	4
1.3.4 Power	4
1.4 Volumetric Energy Density	5
1.5 Non-Build Parameters	6
1.6 Melt pool formation and spatter	7
1.7 General AM Microstructures	10
1.8 General AM Mechanical Properties	11
1.9 Post production treatments	14
1.9.1 Vacuum Heat Treating	14
1.9.2 Hot Isostatic Pressing (HIP)	14
1.10 Introduction to corrosion	14
1.10.1 Dissimilar metals corrosion and electrode potentials	15
1.10.2 Gibbs free energy and Nernst equation	16
1.10.3 Butler-Volmer equation	17
1.10.4 Tafel plot	19
1.10.5 Pourbaix diagrams	20
1.11 Pitting Corrosion	22
1.11.1 Stages of Pitting	26
1.11.1.1 Passive film breakdown	26
1.11.1.2 Metastable Pitting	30
1.11.1.3 Pit Growth and Stability	31
1.12 Scanning Electron Microscopy and Energy Dispersive X-Ray Spectroscopy (SEM)(EDX)	32
1.13 Corrosion Techniques	32
1.13.1 Polarisation Scanning	32

1.13.2	Cyclic Potentiodynamic Polarisation (CPP)	35
1.14	The corrosion performance of Invar	38
1.15	Additively Manufactured 316L	40
1.15.1	General	40
1.15.2	316L LPBF Inert Atmosphere	42
1.15.3	Corrosion Behaviour of AM 316L	42
1.16	The effects of HIP treating on Additively Manufactured 316L	46
1.16.1	HIP Process	46
1.16.2	Sensitisation of Stainless Steels	47
1.16.3	Tensile Performance of AM 316L	48
1.16.4	Fatigue Performance of AM 316L	48
1.17	Additively Manufactured 17-4PH	50
1.17.1	Introduction	50
1.17.2	Pitting performance of additively manufactured 17-4PH	51
1.18	Literature Review Summary	56
1.19	Aims and objectives of this work	57
2	The additive manufacturing process	59
2.1	Introduction	59
2.2	Printing material	59
2.2.1	Planning steps	59
2.2.1.1	Initial steps	59
2.2.1.2	Software steps	60
2.2.2	Feed stock material change over	60
2.2.3	Build preparation	61
2.2.4	Build completion and removal	61
3	Experimental methods	62
3.1	Introduction	62
3.2	The additive manufacturing process	62
3.2.1	Planning steps	63
3.2.1.1	Initial steps	63
3.2.1.2	Software steps	63
3.2.2	Feed stock material change over	63
3.2.3	Build preparation	64
3.2.4	Build completion and removal	65
3.3	Renishaw 400	65
3.4	L9 orthogonal arrays	65
3.5	Taguchi Analysis	66
3.6	Time lapse microscopy	67
3.7	Scanning Vibrating Electrode Technique (SVET)	67
3.8	Potentiostat experiments	71
3.8.1	OCP recording	71
3.8.2	Potentiodynamic scanning	71
3.8.3	Potentialapse	72
3.9	Etching	73
3.10	Density measurements	74

3.11	Porosity analysis	74
3.12	X-ray diffraction	75
3.13	CT Scanning	76
3.14	Hot Isostatic Pressing	76
3.15	Hardness testing	78
3.16	Tensile testing	79
3.17	Fatigue testing	80
4	The corrosion performance of additively manufactured Invar ®	81
4.1	The Invar build process and introduction	81
4.2	Material characterisation	82
4.2.1	Powder Analysis	82
4.2.2	Density measurements and porosity analysis	83
4.2.3	Microstructure	86
4.2.3.1	White light interferometry	89
4.2.4	XRD	91
4.3	Corrosion testing results	92
4.3.1	Scanning vibrating electrode technique	92
4.3.2	Time lapse microscopy	93
4.4	Discussion	95
4.5	Conclusions	98
5	The corrosion performance of additively manufactured 316 L	100
5.1	Powder Analysis	100
5.2	Mass and density variation across the build plate	101
5.3	Optical porosity measurements	107
5.4	CT scanning	109
5.5	Corrosion testing	112
5.6	Conclusions	116
6	The mechanical and corrosion properties of additively manufactured 316 L treated by HIP	117
6.1	Introduction	117
6.2	Methodology	117
6.3	Mass and density measurements	118
6.4	Microscopy	121
6.5	XRD Analysis	128
6.6	Hardness testing	131
6.7	Tensile testing	132
6.8	Fatigue testing	136
6.9	Corrosion testing	140
6.10	Overall ranking	146
6.11	Conclusions and further discussion	149
7	The corrosion performance of additively manufactured 17-4 PH	150
7.1	Introduction	150
7.2	Building methodology and approach for 17-4PH	151
7.3	Density Measurement Results	151

7.3.1	Density variation across the build plate	152
7.4	CT scanning	152
7.5	Corrosion experimentation	156
7.5.1	Potentiodynamic Scanning	156
7.5.2	Potentialmap	158
7.6	17-4PH summary and conclusions	162
8	Final Conclusions and Future Work	163
8.1	Final conclusions	163
8.2	Further Work	165
	 Bibliography	 166

List of Figures

1.1	"Family tree" of AM machines	3
1.2	Point Distance diagram showing successively increasing point distances and how this can affect the heat affected zone.	4
1.3	Diagram showing hatch spacing (a) and point distance (b)	5
1.4	Schematic showing the formation mechanisms of all spatter types. (a) Solid spatter (A). (b) Metallic jet spatter (B). (c) Powder agglomeration splatter (C1, liquid-solid agglomeration spatter, C2, liquid-liquid agglomeration spatter). (d) Entrainment melting powder spatter (D). (e) Defect induced spatter (E) reproduced with permission from Young et al. [14].	8
1.5	Schematic showing the formation mechanisms of solid spatter:(a) The transverse section of the laser scan direction and (b) longitudinal section used with permission from Ikeshoji et al. [16].	9
1.6	Schematic showing formation mechanisms of spatter in LPBF with defects highlighted. [17].	10
1.7	Summary of Ti-6Al-4V AM tensile properties. Abbreviations: DMD, direct metal deposition; DMLS, direct metal laser sintering (synonym of LPBF); EBM, electron beam melting; HT, heat treated; LENS, laser-engineered net shaping; UTS, ultimate tensile strength; YS, yield stress. Used with permission from Lewandowski et al. [24]	12
1.8	Plot of the Butler-Volmer curve showing anodic and cathodic branches $\alpha_a = \alpha_c = 0.5$	18
1.9	Plots of the Butler-Volmer curve showing anodic and cathodic branches for varying α_a and α_c values.	19
1.10	Example of a Tafel plot	20
1.11	Representative Pourbaix diagram of iron water system at room temperature [37]	21
1.12	Cross sections through a model pit grown at 190 mV, after (a) 0.5, (b) 1.0, (c) 1.5, and (d) 2.5 s. The contour lines indicate the concentration of dissolved metal ions. The axis units are micrometers. Used with permission. [42]	23
1.13	Variation of pit current with time in a potentiostatic measurement carried out on 304 at 650 mV (Ag/AgCl) in 0.005 M NaCl solution, together with radiographs showing the appearance of the pit at different times; the current increases as the pit grows and periodically drops due to perforation of the cover and local passivation.	24

1.14	A series of radiographs of a 2D pit growing at the edge of 20 μm foil of 304 stainless steel that was initiated in 0.1 M NaCl at +650 mV (Ag/AgCl) for 10 s then propagated galvanostatically at 10 μA . The time at which each radiograph is taken is shown (+650 mV (Ag/AgCl) was applied at $t = 0$). [43]	25
1.15	Penetration Mechanism diagram	27
1.16	Adsorption Mechanism steps from left to right	29
1.17	Film Breaking mechanism diagram	30
1.18	Example of elemental mapping used with permission [62]	33
1.19	Theoretical anodic polarisation scan [63]	34
1.20	Theoretical cathodic polarisation scan	35
1.21	Idealised CPP Curve [64]	36
1.22	Representative CPP curve [64]	37
1.23	Illustration of the sensitisation process taken from "Callister, Materials Textbook eighth edition" [72]	47
1.24	Fatigue S–N curves of L-PBF 316L reproduced with permission [120]	50
3.1	Internal diagram of Renishaw 400 (not completely to scale)	66
3.2	In-situ optical microscope [137]	68
3.3	Apparatus diagram for SVET measurements	69
3.4	Example of an SVET measurement on a corroding mild-steel sample [139]	70
3.5	3-d data produced from SVET measurements [140]	70
3.6	Three electrode aerated potentiodynamic setup	72
3.7	Three electrode deaerated potentiodynamic setup	73
3.8	Flow chart showing porosity analyses macro steps	75
3.9	Flow chart outlining CT scanning process	77
3.10	Images showing the CT image recreation process	77
3.11	Engineering drawing and final alumina sample holder for HIP treating, note 1:1 and 1:2 scale not accurate.	78
3.12	Tensile and fatigue specimen drawings	79
4.1	Left:Invar build layout. Right: One of the completed Invar builds	82
4.2	SEM micrograph showing virgin Invar powder with particle size measurements.	83
4.3	SEM micrograph showing low magnification virgin Invar powder.	84
4.4	Invar density against VED for every AM Invar sample.	85
4.5	Example image showing porosity in an Invar sample taken from cube 27.	86
4.6	Optical image showing AM Invar (cube 28) (a) and wrought Invar (b) with spherical porosity highlighted (blue dotted circles) and larger irregular porosity points (red circles).	87
4.7	SEM image on sample from cube 28 showing AM Invar with EDS measurement locations. Locations 1,3 and 4 are melt pool boundaries and points 2 and 5 are within melt pools.	87
4.8	EBSD image showing AM Invar (cube 28) (a) and wrought Invar (b).	88
4.9	Invar cube 28 images showing surface topography (left) and surface height (right).	89
4.10	Invar cube 28 3D reconstructed topography front view, note the horizontal length of the sample is 1.3 mm.	90

4.11	Invar cube 28 3D reconstructed topography flipped, note the horizontal and depth of the samples are 1.3 and 0.94 mm respectively.	90
4.12	Invar XRD scan for wrought and LPBF manufactured (cube 28) samples.	91
4.13	Enlarged XRD scans showing individual peaks on wrought and LPBF (cube 28) samples.	91
4.14	SVET derived false colour maps for AM and wrought Invar™ (cube 28) immersed in pH 5.5 0.17 mol.dm ⁻³ NaCl solution showing corrosion current density values. An optical image of the surface is shown in the second SVET map showing that the location of red rust was coincident with the localised anodic features observed by the SVET.	93
4.15	SVET localised corrosion intensity measurements as a function of distance at 0, 5, 10, 15, 20 ,25, 29 hours from cube 28.	93
4.16	Images a-f showing the progression of corrosion in AM Invar (cube 28) at 30 minute intervals between 115 and 250 minutes whilst immersed in pH 5.5 0.17M NaCl electrolyte.	95
4.17	: Microscopy images of AM Invar™ (cube 28) immersed in pH 5.5 0.17M NaCl electrolyte, corrosion is seen to initiate at irregularly shaped porosity located at melt pool boundaries.	96
5.1	SEM micrograph showing virgin 316L powder with particle size measurements.	101
5.2	SEM micrograph showing an overview of virgin 316L powder.	102
5.3	Build 3 with L9 arrays numbered, note sample 4 was produced using optimum parameters as supplied by Renishaw and sample 9 being the authors choice of parameters. Parameters are visible in table 5.3.	103
5.4	Mean density all LPBF 316L parts against VED and line speed fitted with a non-linear curve.	105
5.5	Density of build 3 316L parts by cube number.	106
5.6	Density of build 3 316L parts by bloc.k	106
5.7	Graph showing the density of all tested 316L parts with respect to V.E.D.	107
5.8	Line speed against relative density of all 316L parts produced by LPBF against line speed with a 95 % confidence band shown in pink.	108
5.9	SEM micrograph showing a lack of fusion porosity defect in LPBF 316L with partially and/or completely unmelted powder trapped in the defect.	110
5.10	3D reconstructed image of porosity within sample from top down view.	111
5.11	3D reconstructed image of porosity within sample from side on view.	112
5.12	3D reconstructed image of sample (bottom scan) using projection (left) and volume (right) reconstruction methods.	112
5.13	316L pitting (blue squares) and repassivation (red circles) potentials plotted against relative sample density, where wrought samples have 100 % density.	114
5.14	Potentiodynamic scan of LPBF sample 1 and wrought 316L sample.	115
5.15	OCP recordings taken on samples prior to potentiodynamic scanning Left: AM specimens, Right, Wrought specimens.	115
6.1	Comparison of density measurements made on post HIP treated samples using optical and Archimedes principle methods.	120

6.2	Microstructures of X-Y plane, parallel to the build plate for wrought, conditions 10 - As-built, 1 - HIP (T ₇₀₀ P ₂₀₀), 5 - HIP (T ₁₁₂₅ P ₁₃₇) and 9 - HIP (T ₁₂₀₀ P ₂₀₀).	123
6.3	Microstructures of X-Y plane, parallel to the build plate for conditions 11 - HIP (T ₁₁₂₅ P ₂₀₀ - long hold) and 12 - HIP (T ₇₀₀ P ₂₀₀ - quench).	124
6.4	Measured grain sizes of samples.	125
6.5	SEM micrograph and EDS data from sample 1 - HIP (T ₇₀₀ P ₂₀₀).	125
6.6	SEM micrograph and EDS data from sample 9 - HIP (T ₁₂₀₀ P ₂₀₀).	126
6.7	SEM micrograph and EDS data from sample 9 - HIP (T ₁₂₀₀ P ₂₀₀).	127
6.8	XRD peaks for sample 10 as-built, low, medium and high temperature treated HIP samples.	129
6.9	XRD peaks for sample 10 as-built, low, medium and high temperature treated HIP samples.	130
6.10	Representative tensile curves of the different samples from each treatment. The colours blue, green and red represent low, medium and high temperature setpoints respectively. Solid, dash and dotted lines represent low medium and high pressure setpoints respectively. The yellow lines represent samples 10, 11 and 12 with solid dash and dot lines to differentiate between them respectively. Groups labelled A and B represent samples with and without the presence of the intrinsic AM microstructural features	133
6.11	Hardness plotted against UTS. The colours green, yellow and red represent low, medium and high HIP temperature setpoints respectively. The colour blue represents treatments, 10, 11 and 12.	135
6.12	SEM fractographic images of a. Treatment 9 at low magnification, b. Treatment 9 at high magnification, c. Treatment 10 at low magnification and d. Treatment 10 at high magnification.	138
6.13	SEM fractograph showing striations tracking perpendicularly to cracks and dimples throughout the surface.	139
6.14	SEM high magnification fractograph showing a dimple characteristic of ductile material failure.	140
6.15	Cyclic potentiodynamic scans of all conditions compared to wrought 316L. Scans are separated into plots comparing samples treated at the same HIP temperature.	143
6.16	Cyclic potentiodynamic scans of wrought and 1 - HIP(T ₇₀₀ P ₂₀₀) Repeat 2.	144
6.17	Mean pitting potential values plotted against treatment number.	145
6.18	Micrographs showing a: Porosity feature in the HIP treated part and b: the same porosity feature after localised corrosion attack.	145
6.19	3D plot showing the relationship between ultimate tensile strength, fatigue cycles survived and pitting performance.	147
6.20	Graphs depicting the variation of experimental results with low, medium and high setpoints for temperature and pressure.	148
7.1	17-4PH measured relative density against V.E.D.	152
7.2	17-4PH build showing location of blocks on build plate.	153
7.3	Mean recorded density with error bars giving the standard deviation per block across repeat measurements.	154
7.4	CT reconstructed image showing the front view of non spherical lack of fusion and spherical porosity within a 17-4PH specimen.	155

7.5	CT reconstructed image showing Left: Side view and Right: Top down view of non spherical lack of fusion and spherical porosity within a 17-4PH specimen.	155
7.6	CT image showing the largest observed porosity observed.	156
7.7	Pitting and repassivation potentials on samples from cube 25 (left) and 79 (right) printed using the same build parameters but at different locations on the build plate at three different height slices per cube.	157
7.8	Pitting and repassivation potentials on AM 17-4PH samples against measured relative density in 1 % NaCl solution.	158
7.9	Potentialapase technique with samples surface in left column and corresponding potentiodynamic plot in right column.	160

1. Literature review and theory

1.1 Additive Manufacturing (AM)

Additive Manufacturing (AM) is a general term used to describe the additive process of producing parts or objects from 3D model data [1]. AM processes typically achieve this by repeatedly melting metallic powder layer by layer to build the component. The ability to computationally design a 3D part to precise dimensions allows AM to produce extremely intricate parts that would be extremely difficult, if not impossible, to produce using traditional production methods such as casting or forging. In the cases that such intricate components could be produced by casting and forging, post production machining and joining would almost certainly be required. These applications include producing tailor-made medical parts such as teeth or bone prosthesis [2] [3]. AM can also be used to design and reproduce existing parts with an optimised "strength-weight" ratio that meets the functional requirements of a part while minimising the material volume used [4].

Further applications exist in the use of AM in hard-to-reach places where ordering a replacement part and having it delivered promptly is not an option. Examples of this include military bases, remote scientific research facilities in the arctic or even the international space station[1].

AM is a relatively new manufacturing technique and understanding the characteristics of the produced material is still under significant investigation. Further to this, the technology is evolving rapidly and brand new equipment can become outdated in a matter of weeks. This can lead to confusion as the composition and characteristic microstructure of materials produced using this technique can vary from machine to machine as well as with input parameters.

The manufacturing process lends itself to a controlled supply chain, producing small batches of customised parts. This type of supply chain allows for a close relationship between the manufacturer and the customer that can promote long term trust and business which will be advantageous to both parties. This production method also reduces the risk of being required to hold on to unsold inventory, while also improving revenue

flow as goods are paid for prior to being manufactured. In order to reduce the production time of components AM manufacturers are creating AM machines with multiple lasers. For example the Renishaw AM 500Q is equipped with four high-power 500 W lasers with each laser "able to access the whole powder bed simultaneously." This allows "significantly higher build rates, vastly improving productivity and lowering the cost per part." [5].

Problems can also arise with regards to intellectual property. For example, AM machine manufacturers, who also produce the supporting software with their machine, can introduce complex legal documents that must be agreed by their customers which the manufacturer to monitor and observe what the machine is being used to print.

AM produced parts often require post production treatments before they can be used. These treatments can vary significantly and are specified to optimise specific properties within the component. These include relieving internal stresses, optimising the fatigue strength or reducing porosity, which historically has been an issue in AM techniques [6]. Post production treatments will be expanded upon within section 1.9 and 6.

1.2 Introduction to additive manufacturing

There are several different methods used to produce AM parts. These methods have varying build faults and build features, this makes comparing literature or test results completed from one type of machine to another a complex task. Generally, AM requires melting metallic powder using a heat source. Machines can therefore be categorised by the heat source they use, these include laser beams, electron beams or a plasma. Machines can be further classified by the type of material that is fed into the machine, be it powder or wire. A "family tree" classifying AM machines is displayed in figure 1.1. Note that the Renishaw 400 used to produce samples for this work is classified as a Laser Powder Bed Fusion (LPBF) machine, the term (LPBF) is interchangeable with the term Selective Layer Melted (SLM) and the term Direct Metal Laser Sintering (DMLS).

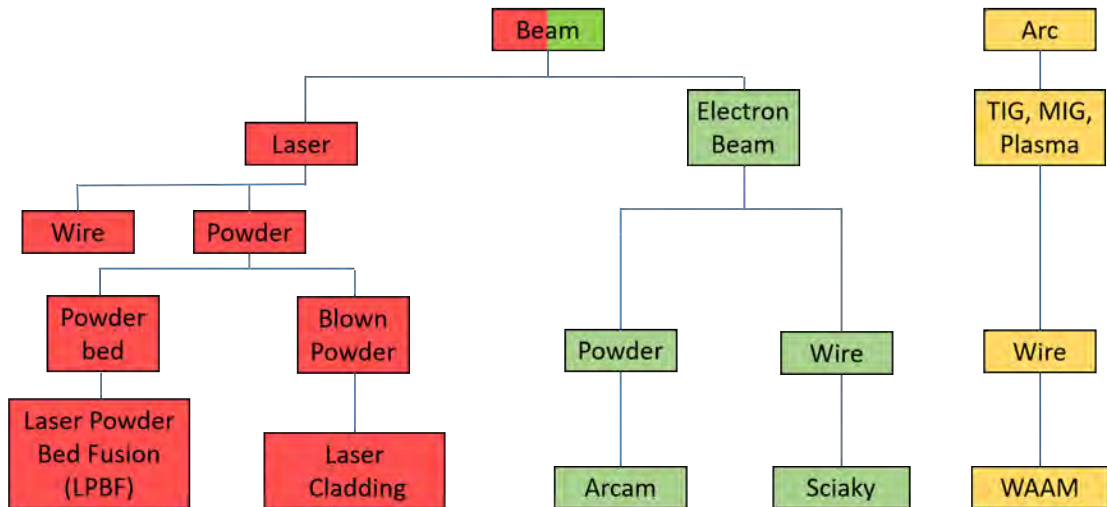


FIGURE 1.1: "Family tree" of AM machines

1.3 Laser Powder Bed Fusion Build Parameters

This section will discuss the numerous build parameters that can be modified within the STL document prior to beginning a build. There are other parameters that can be modified outside of the STL file, these parameters will be discussed in section 1.5. The majority of literature considers the effects of varying build parameters with the goal of optimising the build for a specific test. One of the historic issues with ALM parts has been porosity, where builds have suffered from low relative densities due to the nature of ALM. There is therefore significant literature on modifying build parameters to achieve the maximum relative density possible by varying build parameters [7][8][9]. An additional parameter to consider that is not necessarily easy to control is the time between layers being melted. For example, building shapes that are non uniform in the planes perpendicular to the build direction will result in varying the amount of time printing each layer takes. Additionally, the number of parts being built (or more specifically the total scan area required) results in the time taken per layer to change. This can result in some layers having more time to cool than other layers, these variations in cooling rate layer by layer could result in mechanical properties varying as a function of build height. This variation will depend on the geometry of the build as the amount of powder melted varies.

1.3.1 Point Distance

The point distance refers to the distance between the centre of consecutive laser spots as illustrated in figure 1.2. The figures represents progressive increases to the point distance ranging from diagram a where the melt pools overlap significantly to diagram c where

the melt pools are at the point where they are as close together as possible without overlapping.

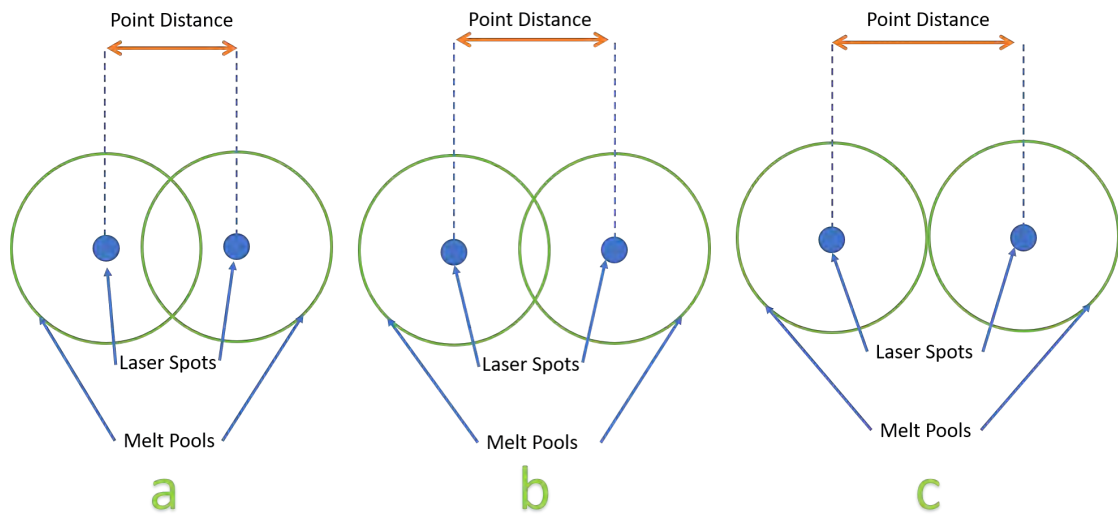


FIGURE 1.2: Point Distance diagram showing successively increasing point distances and how this can affect the heat affected zone.

1.3.2 Hatch Spacing

The hatch spacing is the distance between one melt line and another. Hatch spacing is illustrated in figure 1.3, where the point distance is also shown to provide differentiation between the two measurements. The diagram shows how the heat affected zone between melt lines can vary based on the hatch spacing selected.

1.3.3 Exposure Time

The exposure time is the period of time the laser is firing on each laser spot. A longer exposure time results in more energy being deposited within the build and increases the energy density of the build. Additionally a longer exposure time results in a larger melt pool as the thermal gradient produced by the laser impacts a larger region of the sample.

1.3.4 Power

The power of the laser, this can be adjusted up to a value of 400W for the Renishaw 400. Increasing the laser power results in more energy being deposited into the powder bed per unit volume.

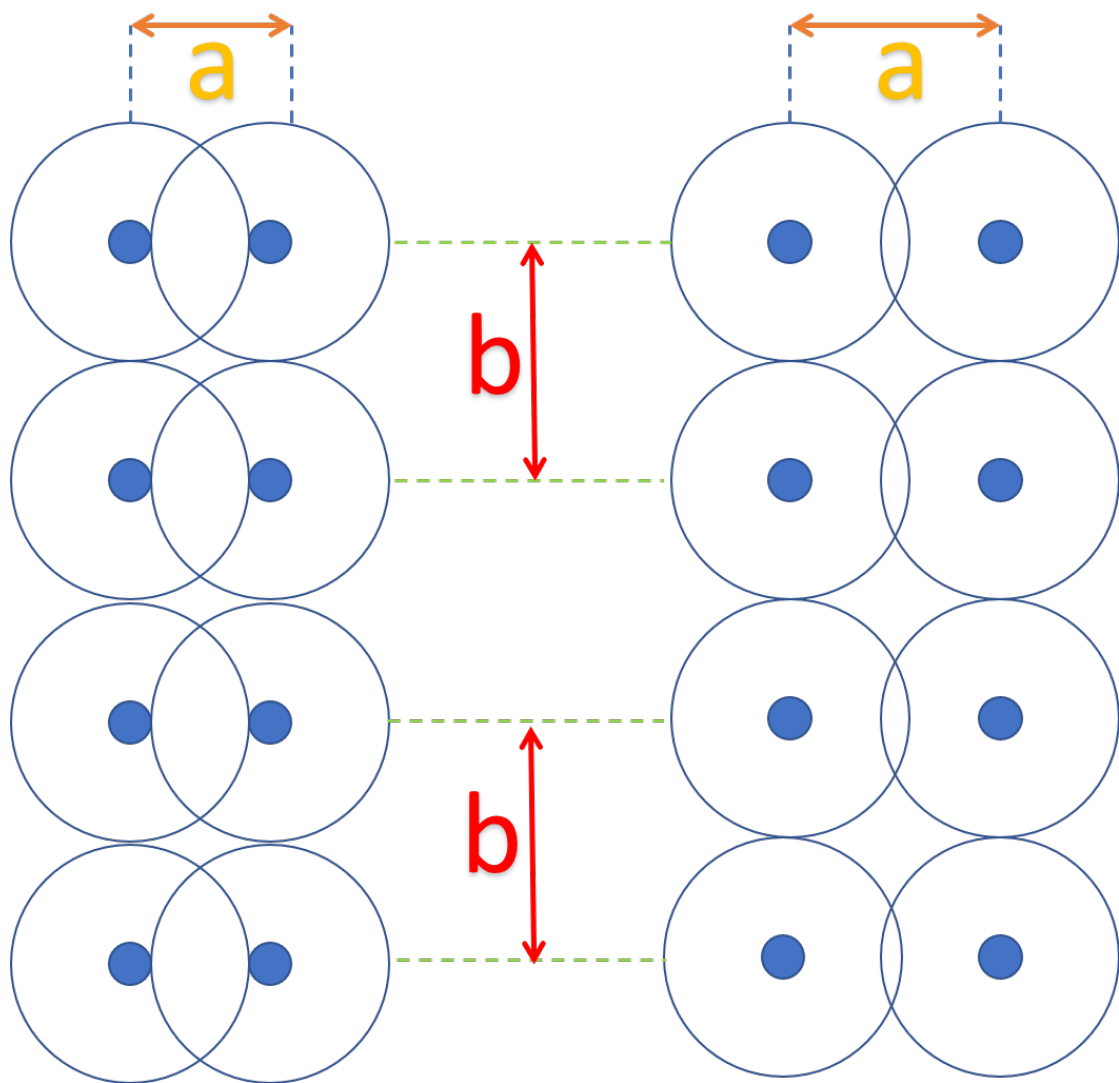


FIGURE 1.3: Diagram showing hatch spacing (a) and point distance (b)

1.4 Volumetric Energy Density

The volumetric energy density is a defined quantity that is effectively the quanta of energy deposited into the material as it is being melted by the heat source per unit volume. In the case of LPBF the heat source is either a pulsed or continuous laser source. The VED can be calculated as a function of the input build parameters as given in equation 1.1.

$$VED = \frac{P \times ET}{PD \times HS \times LT} \quad (1.1)$$

$$LS = PD \times K \times ET \quad (1.2)$$

Where VED is the volumetric energy density (J mm^{-3}) where P is laser power (W), ET is the laser exposure time (s), PD (point distance) is the distance between laser points (mm), HS (hatch spacing) is the spacing between laser melt lines (mm) and LT is the layer thickness (mm). The exposure time and point distance parameters apply only to pulsed lasers however these parameters can be combined mathematically to give the line speed quantity as displayed in equation 1.2. Where LS is line speed and K is a constant to maintain unit consistency. The line speed replaces the point distance and exposure time build parameters for continuous laser sources as the laser source is firing continuously. The VED is often quoted in literature to allow comparison between builds of the same material. The VED however is comprised of independent variables. It is possible to produce parts at identical VED's using vastly different build parameters and therefore whilst useful in the density optimisation process direct comparisons between builds and different AM machines should be treated with caution and build parameters explored individually.

1.5 Non-Build Parameters

There are of course many additional parameters in addition to the build parameters that can be modified within the build software. Some examples of these parameters are the temperature of the build chamber and the temperature of the build plate. Completing a build at an elevated build plate temperature results in a less steep thermal gradient between the build plate and the printed part, this relieves some of the residual strain of the component and reduces the risk of the component cracking [10]. The extent of this effect is largely dependant on the shape of the build as well as the build supports used.

The content of the inert atmosphere within the build chamber can lead to microstructural changes in the build. For example although nitrogen is an inert gas, conditions could exist where nitrogen can interact with the microstructure of the build and produce nitride secondary-phases within the build [11]. Subsequently the AM 400 build chamber uses an argon atmosphere. The quality of an AM build is also affected somewhat by the quality of the powder fed into the machine. The quality of the powder is determined by its size, shape, surface morphology and its composition. Having a low quality powder can result in builds having porous regions due to oversized powder particles that haven't melted fully. To prevent this powder should be sieved between builds to ensure no oversized

particles are used. LPBF uses a fine distribution of powder to improve surface finish by enabling a lower layer thickness [6].

1.6 Melt pool formation and spatter

The formation of the melt pool produced by the incident heat source in AM applications is subject to considerable research. The manipulation of the melt pool allows for the microstructure of the material to be modified. The depth, width, and length of the melt pool can all be modified by varying build parameters that in turn results in changes to the temperature reached by the melt pool, the cooling rate, the spatter ejected from the melt pool and numerous other quantities. Generally speaking, increasing the energy quanta incident on the powder bed results in increased melt pool volume [12]. Whether this increase in volume translates to an increased melt pool depth or width however is dependent on the build parameters used as well as the number of layers that influences the conduction path within the material [13]. Both the heating and cooling rate within LPBF have been shown to decrease with increasing numbers of layers [13]. Melt pool depth and width both increase with increasing laser power and decrease with increasing scanning speed, whereas increasing hatch spacing leads to increased melt pool depth and decreased melt pool width. Increasing hatch spacing decreases heat accumulation in tracks, leading to decreased width, whereas overall melt pool temperature increases with increasing hatch spacing, resulting in a nominal increase in melt pool depth [13].

Figure 1.4 gives an illustration of the formation mechanisms of all spatter types used with permission from Young et al [14]. Any medium aside from the inert gas atmosphere that the incident laser beam has to traverse results in variations to the beams properties, this can include moving the focal point, narrowing or expanding the beam width ultimately leading to unfavourable conditions at the powder bed [15] [12]. Spatter is similar to welding sparks in appearance and refers to liquid metal particles that are ejected from the material as the laser interacts with the powder bed [14]. The spatter itself can then land on and interact with either the powder bed of previously melted powder whilst still molten or having solidified resulting in defects forming within the material. There are numerous causes for spatter and the identification of which cause occurs is non-trivial due to the time step that spatter occurs within, the small scale of the liquid metal ejection, the high temperature of the environment as well as difficulties in imaging due to the inter gas atmosphere, the radiation shielding built into the LPBF machine and the gas plume given off from the powder belt during melting [14]. To overcome these barriers computer simulation, visible light and IR videography are used. Five types of spatter were analysed by Taylor et al. who conclude that solid spatter is formed due to

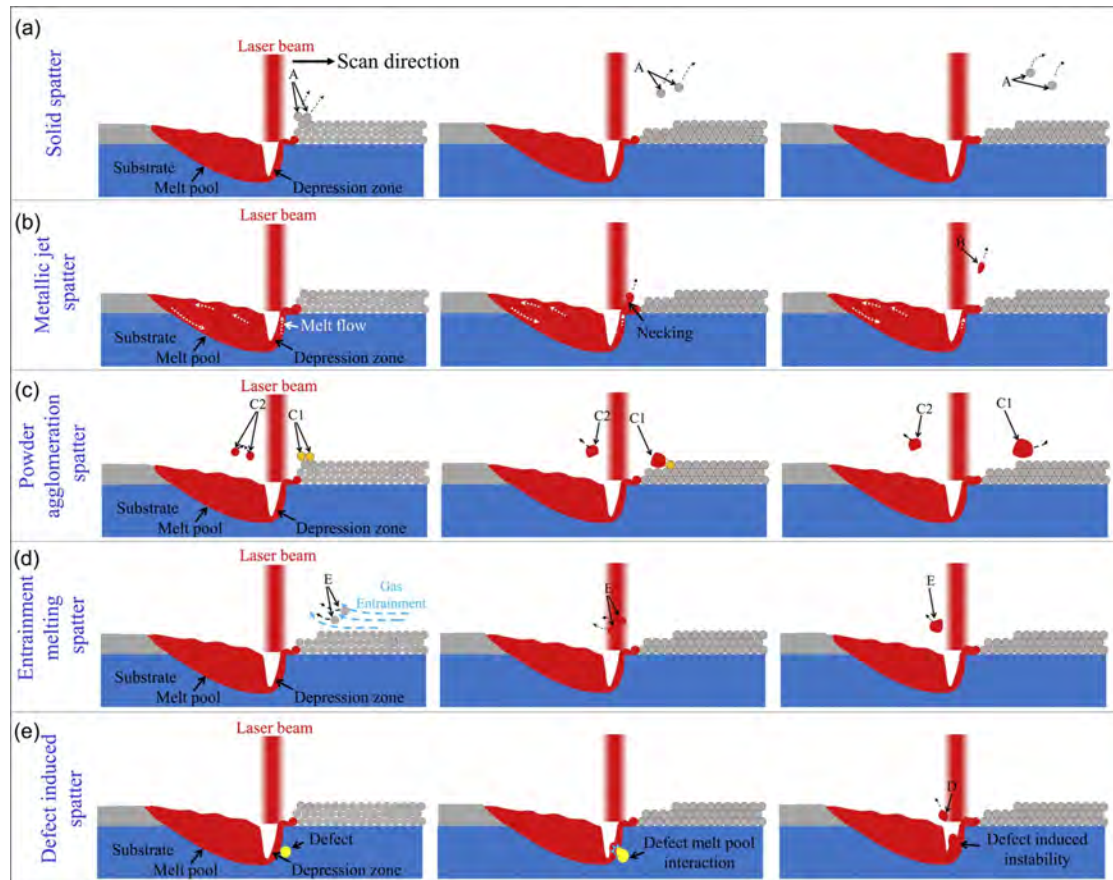


FIGURE 1.4: Schematic showing the formation mechanisms of all spatter types. (a) Solid spatter (A). (b) Metallic jet spatter (B). (c) Powder agglomeration spatter (C1, liquid-solid agglomeration spatter, C2, liquid-liquid agglomeration spatter). (d) Entrainment melting powder spatter (D). (e) Defect induced spatter (E) reproduced with permission from Young et al. [14].

unmelted feedstock powder from the bed being ejected into the atmosphere due to the intense vapour jet formed from the incident laser. Reducing the incident laser power can reduce this spatter production mechanism. Instability in the melt pool/depression zone caused by high laser power or longer than necessary laser exposure time can result in metallic jet spatter where liquid droplets from the melt pool become detached from the melt pool. Figure 1.5 below demonstrates the solid spatter and metallic jet mechanism outlined in figure 1.4 in more detail. The figure shows the incident laser melting a powder layer as the melt pool forms. This causes metal vapour emission and the vapour pressure pushes the melt surface downwards producing a keyhole weld cavity. Above the metal surface, the vapor plume becomes a jet flow to induce an upward flow of the surrounding gas and interacts with the inert gas flow of the LPBF machine. This induced gas flow causes the powder particles adjacent to the laser tracks to raise from the powder bed wherein it can be introduced into the melt pool and ejected as spatter [16].

Powder agglomeration spatter is formed through interactions between ejected spatter

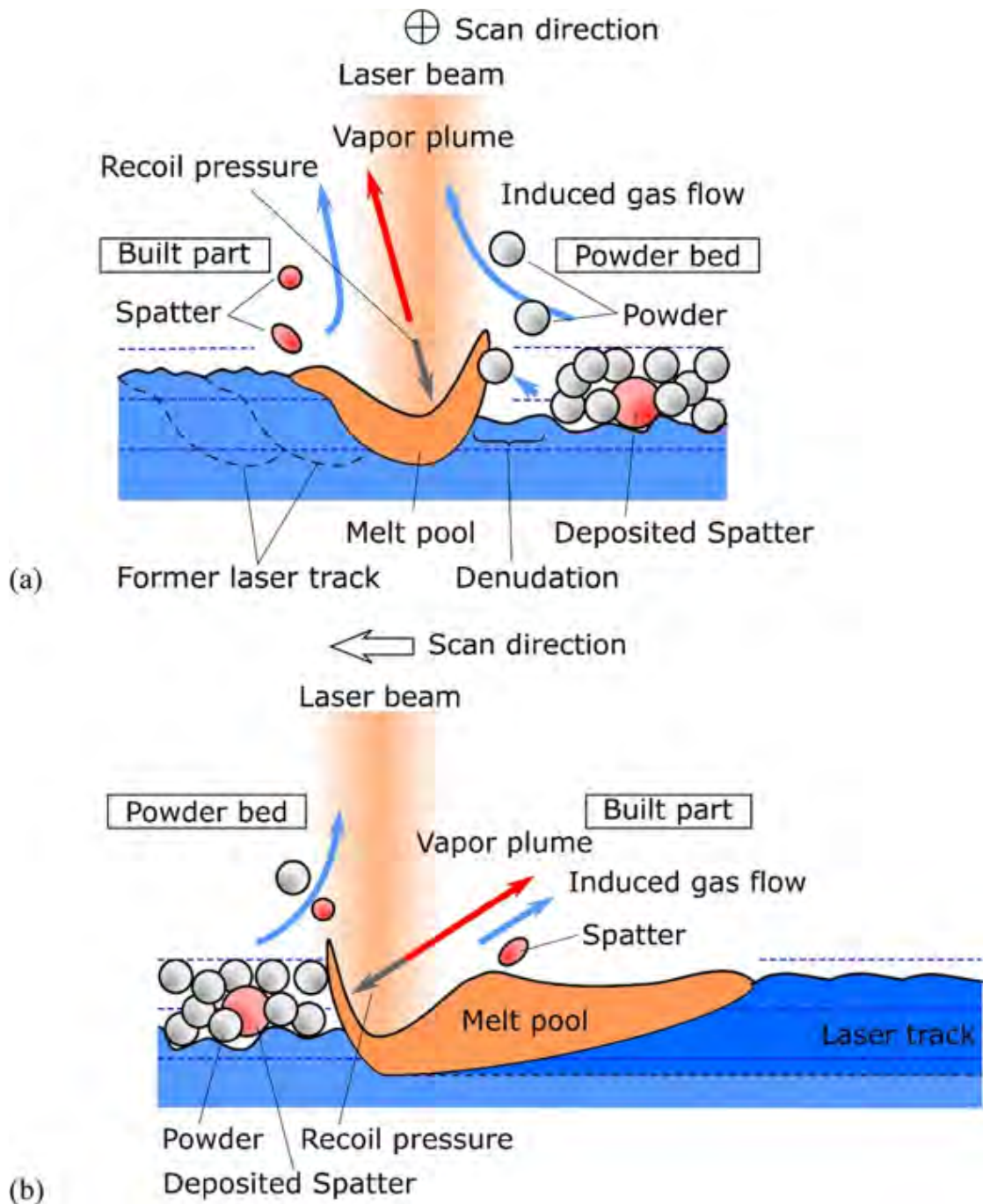


FIGURE 1.5: Schematic showing the formation mechanisms of solid spatter:(a) The transverse section of the laser scan direction and (b) longitudinal section used with permission from Ikeshoji et al. [16].

and adjacent metallic powders which can become agglomerated. Entrainment melting spatter is the melting and ejection of the entrained powders. Defect induced spatter is induced by the incident laser interacting with large defects present in previously built layers [14]. Figure 1.6 below demonstrates spatter phenomena with potential defects highlighted. The figure highlights the number of potential defects that can influence spatter including gas porosity, entrapped gas in feedstock powder, unmelted powder,

open pores, cracks, micro cracks and keyhole pores.

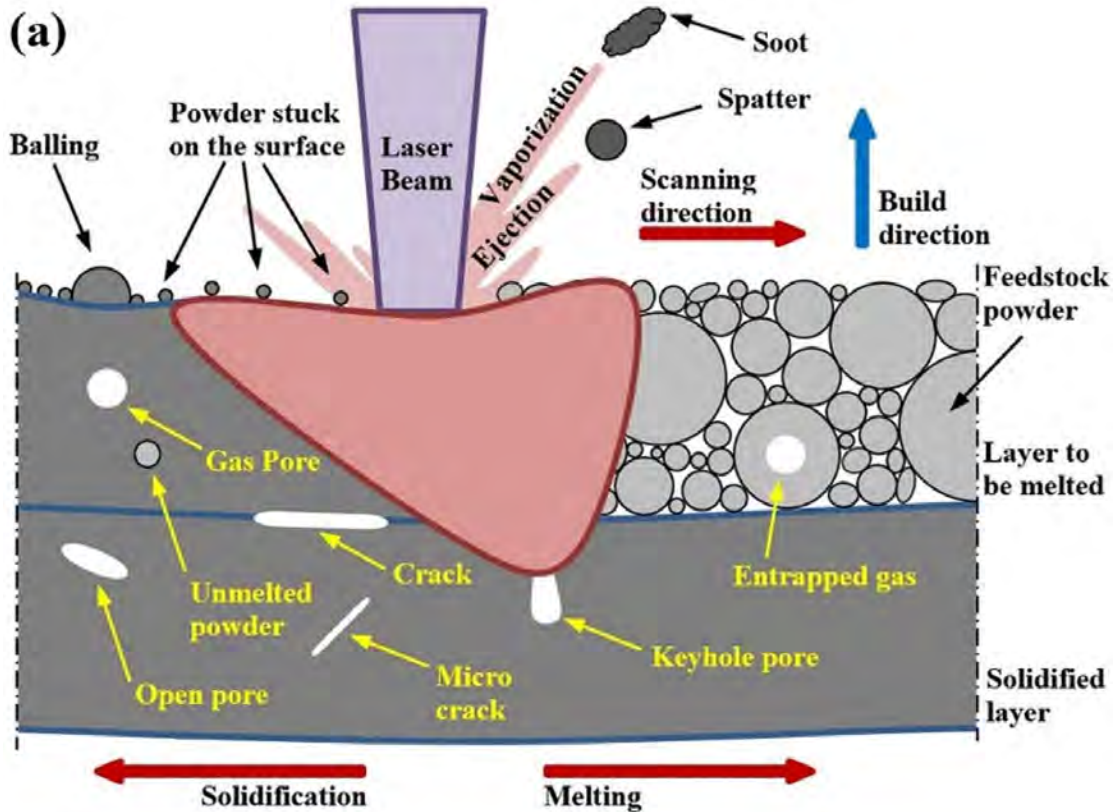


FIGURE 1.6: Schematic showing formation mechanisms of spatter in LPBF with defects highlighted. [17].

In general, high scanning speed lead to a reduction in the spatter size and an increase in the amount of spattering because of the formation of narrow melt tracks however this can also lead to unmelted regions of powder. It has also been found that high laser power lead to an increased number of ejected spatters due to deep melt pools in the “keyhole” regime [17]. In addition, low laser power also lead to more spatters trailing the laser focal spot. In summary each of the build parameters can induce the formation of spatter via numerous methods. Optimising the build process involves minimising spatter to ensure that built parts are as free form defects and spatter as possible [18].

1.7 General AM Microstructures

Due to the nature of AM processing, the microstructure of built parts have unique properties. Columnar grain structure dominates, with high amounts of grain orientation based on the build direction and scan pattern [6]. Phase formation varies across different machines and materials used. The repeated directional heating and cooling of the material result in axial variations in grain and phase formation [6]. In theory therefore it should

be possible to manipulate the microstructure of ALM parts by designing a scan pattern with the intention of purposely creating a preferred grain size and orientation. This was completed by Dehoff et al. who achieved site specific control of the crystallographic orientation of grains. [19]. This was accomplished by designing an electron beam scan strategy based on principles of columnar to equiaxed transitions during solidification [19]. There could be potential in future to develop scan strategies based off this principle to design parts that have tailor-made microstructures fit for their specific purpose.

Manipulating the formation of phases is more complex as this can be influenced by solidification and solid state phase transformations [6]. Slower scan speeds in laser melting can cause increased Aluminium segregation in Ti-6Al-4V and form Ti₃-Al, and columnar precipitate architectures have been reported in both EBM and LM by Murr et al [6][20]. Researchers have been able to rationalise phase formations due to solid state phase transformations but more work is needed to be able to predict microstructures as no work has truly demonstrated process control of precipitate formation via solidification or solid state phase transformation [6].

At a constant laser power, increasing the scan speed and the hatch spacing will reduce the size of the melt pools. This could result in insufficient overlap of the scan tracks, potentially leaving regions of unmelted powder [21]. Increasing the power of the laser while maintaining an even beam intensity profile while subsequently decreasing the exposure time can result in wider and shallower melt pools being formed. These shallower and wider melt pools result in the formation of long columnar grains growing along the build direction, when no scan rotation is used between subsequent build layers [22]. However, this method also results in a large crack density at the centre of the melt pools with cracks growing parallel to the build direction [22]. These cracks can be removed by post production processes such as hot isostatic pressing [22]. Cracks such as these can also occur in builds with a low energy density, where unmelted powder particles can adhere to the surface and the cracks that form between subsequent layers [23].

1.8 General AM Mechanical Properties

There has been significant work on determining the mechanical properties of AM parts including tensile tests to measure yield strength, ultimate tensile strength and elongation testing [23][24][25][26][27]. Once again comparing results from different work is non-trivial due to the large number of manufacturing variables that exist. For example, the quality of the feed-stock, the porosity, build direction, thermal history and the scanning pattern should ideally be quoted when discussing mechanical properties.

Figure 1.7 displays the results of tensile tests carried out on Ti-6Al-4V samples, the results show an increased UTS and YS and a decreased elongation for DMLS parts compared to cast, forged and wrought-annealed samples. The decreased elongation in LPBF samples could be due to highly non-equilibrium microstructures such as martensites. Additionally, it is possible for there to be regions with substantial residual stress which increase the strength and reduce the elongation of the AM samples [24].

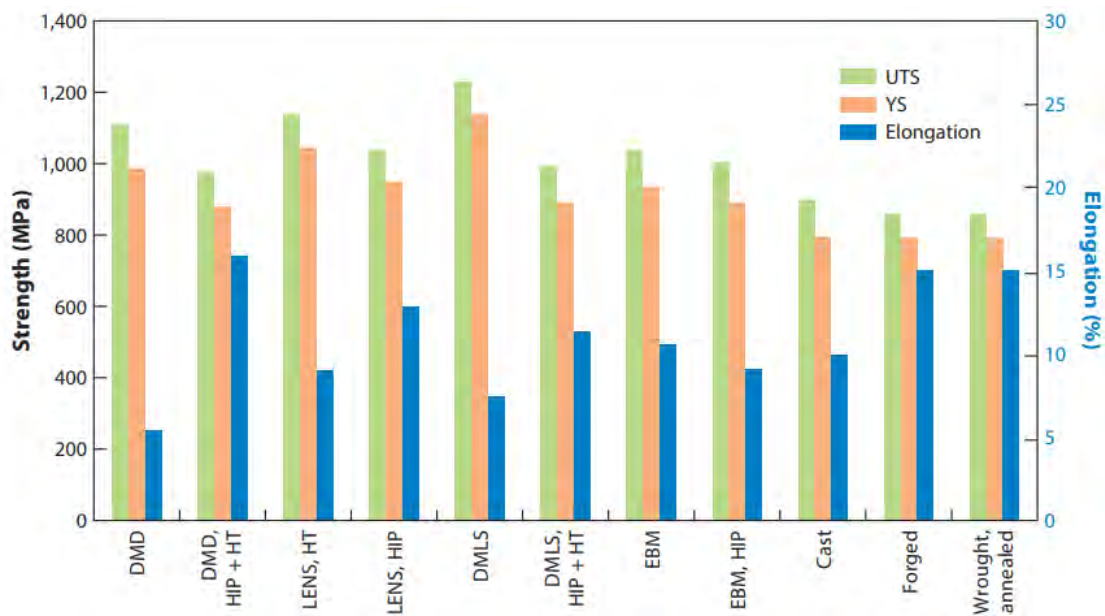


FIGURE 1.7: Summary of Ti-6Al-4V AM tensile properties. Abbreviations: DMD, direct metal deposition; DMLS, direct metal laser sintering (synonym of LPBF); EBM, electron beam melting; HT, heat treated; LENS, laser-engineered net shaping; UTS, ultimate tensile strength; YS, yield stress. Used with permission from Lewandowski et al. [24]

LPBF processed Ti-6Al-4V samples exhibit toughness values well below those of conventionally processed samples and exhibit orientation-dependent values based on machine build parameters [24]. In general, the as-built LPBF Ti-6Al4V exhibits the lowest toughness in the as-built condition. This is likely due to a combination of highly non-equilibrium microstructures, significant residual stresses and process-induced defects [24]. Some of these microstructural features can be removed by post production treatments such as heat treating and hot isostatic pressing (HIP) that can reduce harmful residual stresses, by generating more favourable microstructures and by minimising defects [24]. Despite this, other work has shown that AM 316L can be produced comprising of a single austenitic microstructure that remains stable during tensile deformation [28]. Other work has shown that the tensile deformation behaviour of laser fused ALSi10Mg and Ti6Al4V was limited by inherent brittle mechanisms [29]. High ductility has also been recorded in 316L, with considerably higher yield strength and strain hardening than in wrought, annealed 316L [29].

The fatigue strength of LPBF parts is significantly limited by the quality of the surface finish [26][29]. The reason for this is that the toughness of a material is defined as the energy per unit volume that a material can absorb before rupturing. Rupturing in materials occurs due to cracks spreading throughout the material. A poor surface finish results in peaks and troughs on the materials surface. Surface defects, such as voids and irregularly-shaped fusion features can act as crack initiation sites and can increase the chance of cracks forming, thus increasing the materials susceptibility to fail under load [29]. Post processing techniques such as polishing can be used to reduce the surface roughness. If the surface roughness issues are removed then the focus is shifted to residual porosity, where porous regions are inherently weak spots within the material. For high density parts with a perfect surface finish the fatigue strength of AM parts does not reach that of conventionally fabricated materials [26]. The exact reason for this is unknown however a possible reason lies in the generally higher oxygen content of the matrix material, reducing the mechanical load capability of the steel matrix [26]. This oxygen could arise in the material as a result of gas filled pores that oxidise within the material and despite HIP these oxidised regions still remain within the component. Additionally, the build direction has been shown to influence the fatigue strength of LPBF stainless steels. Wherein 316L and 17-4PH fabricated in the horizontal orientation have demonstrated fatigue strengths between 85% and 95% of corresponding wrought materials [29]. Corresponding parts built in the vertical direction can be prone to fatigue fractures developing prematurely by separation of the material across the build planes, resulting in significantly lower fatigue strengths [29].

The flow stress of a material is defined as the instantaneous value of stress required to continue plastically deforming the material. The rate of crack propagation is inversely proportional to the flow stress of a material and as such is an important parameter in the fatigue failure of ductile materials. 316L AM parts have been found to have a flow stress 1.7 times greater than wrought materials [25]. This has been credited to the AM part having a 2.5 times higher dislocation density compared to wrought 316L. However further work is needed in order to fully understand how the initial dislocation structure in AM parts differs from those induced by simple isothermal deformation [25].

1.9 Post production treatments

1.9.1 Vacuum Heat Treating

Vacuum heat treating is the process of heating a component up whilst under vacuum. The vacuum environment prevents oxidation, reduces the chances of contamination occurring and prevents heat loss from the component via convection. The various treatment options can effect changes in grain size, grain orientation, precipitate phases, porosity, and mechanical properties. The heat treatment temperature and time have large impacts on the grain structure of the material as both increased treatment temperature and time generally result in larger grain sizes [6].

Heating AM metal in a furnace to effect changes in microstructure is the general goal of thermal post-processing [6].

1.9.2 Hot Isostatic Pressing (HIP)

HIP is a manufacturing process used to reduce the porosity of materials, to improve the material's mechanical properties and workability. The process involves subjecting a component to elevated temperatures and isostatic gas pressure in a high pressure containment vessel. Typically, an inert gas such as argon is used. Time at elevated temperature and pressure allows for plastic deformation, creep and diffusion to occur. AM parts can be treated with HIP to close internal pores and internal cracks. Pores occurring at the surface of a part are referred to as open pores. Open pores caused by surface defects are a problem for post-processing, as they allow deeper infiltration into material from air during high heat cycles [6]. Ensuring the correct HIP cycle is used is crucial as there have been instances with AM components where HIP has changed the geometry of a pore from spherical into a long thin strip that is effectively a crack.

1.10 Introduction to corrosion

The corrosion of materials refers to the natural degradation of materials over time due to chemical or electrochemical reactions that take place that are dependant on the materials environment. The susceptibility of a material to corrosion is one of the factors that determines the lifetime of a metallic part in applications where corrosive environments are ever present, for example oil/gas refineries and the shipping and construction industries. It was estimated in 2016 that the annual global cost of corrosion was \$ 2.5 trillion, equivalent to roughly 3.4% of the world's gross domestic product that year [30].

Pitting is an example of localised corrosion occurring whereby material is selectively removed at particular regions or zones on a metal surface where a pit acts as an anode and the metal surface acts as the cathode. The exact mechanisms that take place during pitting corrosion are not completely understood. There are several different theories proposed, however the ability to confirm any one theory as being true is unlikely due to limitations in experimental techniques. Some of these proposed mechanisms will be discussed in section 1.11. The method and logical thinking used in quantifying a materials resistance to corrosion can vary based on the specificity's of the individual component. In general the rate of mass loss of metal due to corrosion can be used. However in some applications the mass loss rate may not be relevant if any loss of metal would result in a failure of the part and therefore maintaining a constant passive layer is required. For such an application the durability and thickness of the passive layer can be investigated via cyclic potentiodynamic polarisation. Some metallic elements and alloys form a passive layer that provides some resistance to corrosion. These oxide layers form naturally on the metal surface, are usually a few nanometers thick and greatly reduce the rate of corrosion of the metals [31]. For example chromium is added to steel as it readily reacts with oxygen to produce a passive layer. This passive layer is electrically insulating and prevents electrons and aggressive ions from diffusing through the layer and attacking the metal. Chloride ions are particularly effective at infiltrating the passive layer due to their small size and high diffusivity [31].

1.10.1 Dissimilar metals corrosion and electrode potentials

When a metal is immersed in a conducting liquid it takes up an electrode potential determined by the equilibrium between the anodic and cathodic reactions occurring on the surface of the metal. Dissimilar metal corrosion can occur when two metals with different electrode potentials are in electrical contact with one other whilst immersed in an electrically conducting environment. This corrosion occurs naturally as electrons flow from the metal with the more electro-negative potential (the anode) to the metal with the higher potential (the cathode). The reaction that occurs on the metal with the lower potential is similar to that which would occur without electrical contact to a higher potential metal, however the rate of the reaction is increased. Therefore the corrosion rate of the material with the lower potential (the anode) is increased and the corrosion rate of the higher potential metal (the cathode) is decreased [32]. The corrosion rate is governed by the electrically conducting environment, the difference in potentials between the materials and the relative exposed surface areas of the metals. This phenomena can be used to decrease the corrosion rate of metals by placing them in electrical contact with a sacrificial metal with a lower potential. The galvanic series lists

metals alongside their potential. This series can be used when selecting materials for applications to minimise the risk of dissimilar metal corrosion occurring. The discovery of dissimilar metal corrosion led to the creation of the galvanic cell. The galvanic cell is an electrochemical cell wherein two separate materials with different potentials are immersed in an electrically conductive solution and separated via a porous membrane. These metals are electrically connected outside of the solution. The porous membrane allows for anions to flow in the solution as spontaneous oxidation-reduction reactions occur on the surfaces of the immersed metals and electrons flow from the anodic material to the cathodic material via the electrical connection, generating an electric current [33].

1.10.2 Gibbs free energy and Nernst equation

The Gibbs free energy (G) is a thermodynamic quantity that can be used to calculate the maximum amount of reversible work that can be done by a thermodynamic system at a constant temperature and pressure. Whether a metal corrodes spontaneously or not can be characterised by the change in Gibbs free energy for a given corrosion reaction. Negative changes ($\Delta G < 0$) indicate a spontaneous reaction can occur and vice versa [34]. For the case of an electrochemical cell as discussed previously, the maximum amount of energy that can be delivered by an electrochemical cell in a given state is equivalent to the change in Gibbs free energy condition under general conditions

$$\Delta G = -nFE \quad (1.3)$$

where n , is the number of moles of electrons exchanged, F is Faraday's constant and E is the cell potential [34]. Under standard conditions the Gibbs free energy equation can be written as

$$\Delta G^0 = -nFE^0 \quad (1.4)$$

when E^0 is positive, the reaction is spontaneous and when E^0 is negative, the reaction is non-spontaneous. The Gibbs energy change under non-standard conditions can be related to the Gibbs energy change under standard equations via

$$\Delta G = \Delta G^0 + RT \ln[Q] \quad (1.5)$$

where Q is the reaction quotient of the reaction, R is the ideal gas constant and T is the temperature. Substituting equations (1.3) and (1.4) into equation (1.5) and rearranging yields

$$E = E^0 - \frac{RT}{nF} \ln[Q] \quad (1.6)$$

which is referred to as the Nernst equation which indicated that the critical potential of a cell depends on the reaction quotient Q of the reaction. As the redox reaction takes place, reactants are consumed and thus the concentration of reactants decreases and the concentration of the products increases. Therefore, the cell potential gradually decreases until an equilibrium is reached where $\Delta G = 0$ and $Q\Delta G = -nFE$. The Nernst equation cannot be used to calculate the corrosion rate of a material as given in equation (1.6).

1.10.3 Butler-Volmer equation

The Butler-Volmer equation (1.7) can be derived from the simultaneous cathodic and anodic reactions [32]. The equation shows that the electrical current through an electrode is dependent on the voltage difference between the electrode and the bulk electrolyte for a simple, unimolecular redox reaction, given that both a cathodic and an anodic reaction occur on the same electrode [32]. At equilibrium, the net current is zero, and the electrode is known to adopt a potential based on the bulk concentrations of oxidation and reduction as dictated by the Nernst equation (1.6). The Butler Volmer equation (1.7) is given as

$$j = j_0 \left[e^{\frac{\alpha_a n F \nu}{RT}} - e^{-\frac{\alpha_c n F \nu}{RT}} \right] \quad (1.7)$$

where j is the current density, j_0 is the exchange current density, α_a and α_c represent the anodic and cathodic charge transfer coefficient respectively, ν is the activation over potential and n is the number of electrons involved in the electrode reaction. Equation (1.7) relates the external current density as a result of an applied potential (j) to the exchange current density when the electrode is at open circuit potential. The positive exponential term dominates and describes the change in current as the potential shifts towards oxidative (anodic) conditions. The negative exponential term dominates and describes the current as the potential shifts towards reductive (cathodic) conditions [32]. An increase in the anodic term is accompanied by a decrease in the cathodic term and vice versa. The Butler-Volmer equation can be manipulated by dividing both sides of the equation by the exchange current density producing equation (1.8) below

$$\frac{j}{j_0} = e^{\frac{\alpha_a n F \nu}{RT}} - e^{-\frac{\alpha_c n F \nu}{RT}} \quad (1.8)$$

Plotting $\frac{j}{j_0}$ against ν the activation over potential between -0.1 and 0.1 produces the curve shown in figure 1.8 below. Wherein α_a and α_c were set to 0.5 and the Faraday

constant, temperature and ideal gas constant were taken to be 96485 C mol^{-1} , 298 K and $8.314 \text{ J k}^{-1} \text{ mol}^{-1}$ respectively. The curve demonstrates symmetric logarithmic behaviour within the boundaries given. When the net current flow is zero, the case for equilibrium the anodic and cathodic currents are equal and opposite.

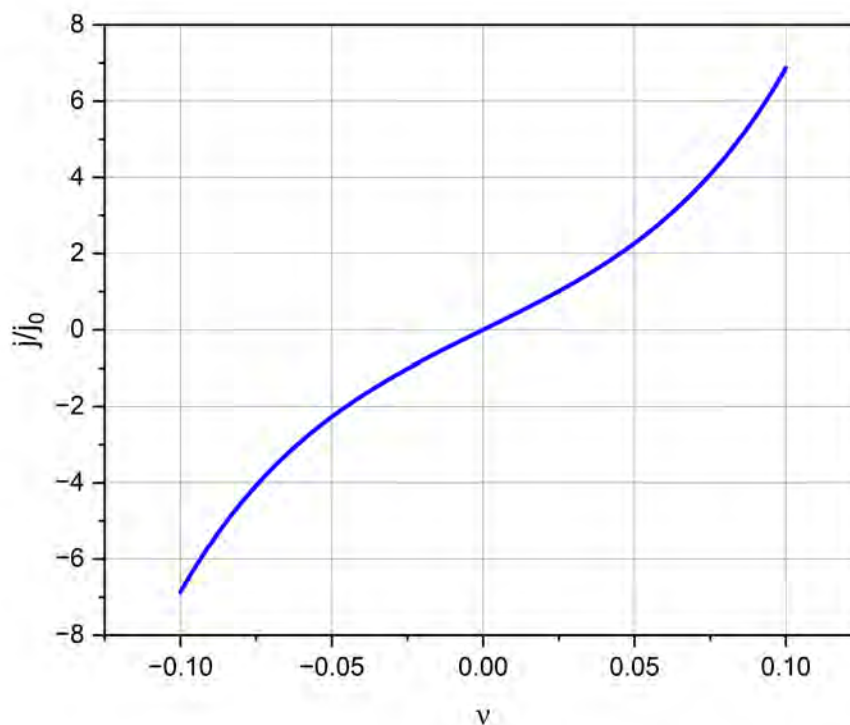


FIGURE 1.8: Plot of the Butler-Volmer curve showing anodic and cathodic branches
 $\alpha_a = \alpha_c = 0.5$

The plot demonstrates that a linear increase in applied over potential produces an exponential change in the current which is expected given equations (1.7) and (1.8). It's worth noting that the symmetric behaviour demonstrated is due to setting α_a and α_c to 0.5. Examples showing α_a and α_c at different values are given in figure 1.9.

Whilst the Butler-Volmer equation is useful in considering simple electrochemical reactions, the equation has its limitations in that it only holds if the reaction rate is charge-transfer controlled and only one oxidation and reaction is occurring. The equation assumes that the concentrations at the electrodes are practically equal to the concentrations in the bulk electrolyte, allowing the current to be expressed as a function of potential only.

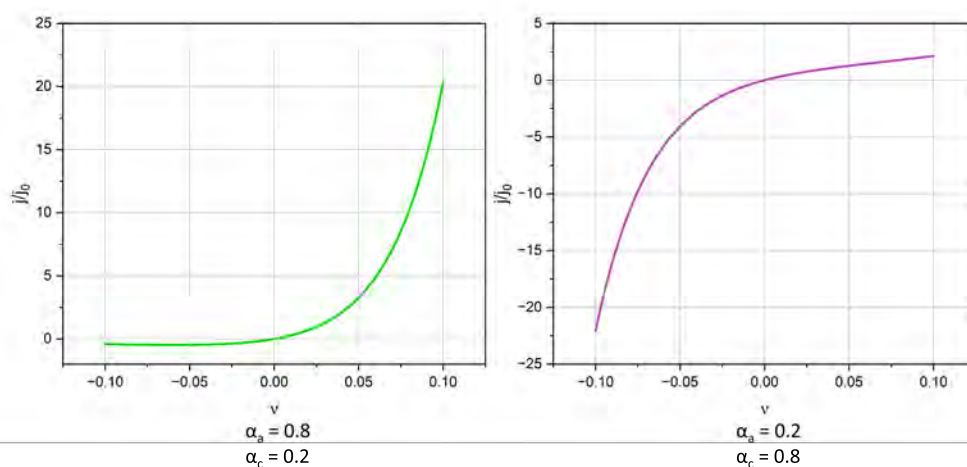


FIGURE 1.9: Plots of the Butler-Volmer curve showing anodic and cathodic branches for varying α_a and α_c values.

1.10.4 Tafel plot

The Tafel plot is a simplification of the Butler-Volmer equation which involves plotting the activation over potential ν against the $\log_{10} \left(\frac{j}{j_0} \right)$ and the over potential at high current is regressed linearly to the x- axis. The point of intersection on the x axis of the extrapolated graph as shown in figure 1.10 gives the value of the exchange current density. The gradient of the tafel plot gives information about the number of electrons transferred in the rate determining step. In reactions involving multiple stages and the transfer of several electrons the Tafel plot will be determined by the rate-determining step in the reaction. The Tafel slope allows for determining whether the rate-determining step involves an electron transfer or not, as well as the number of electrochemical (involving an electron transfer) and chemical (not involving an electron transfer) steps that precede it [32].

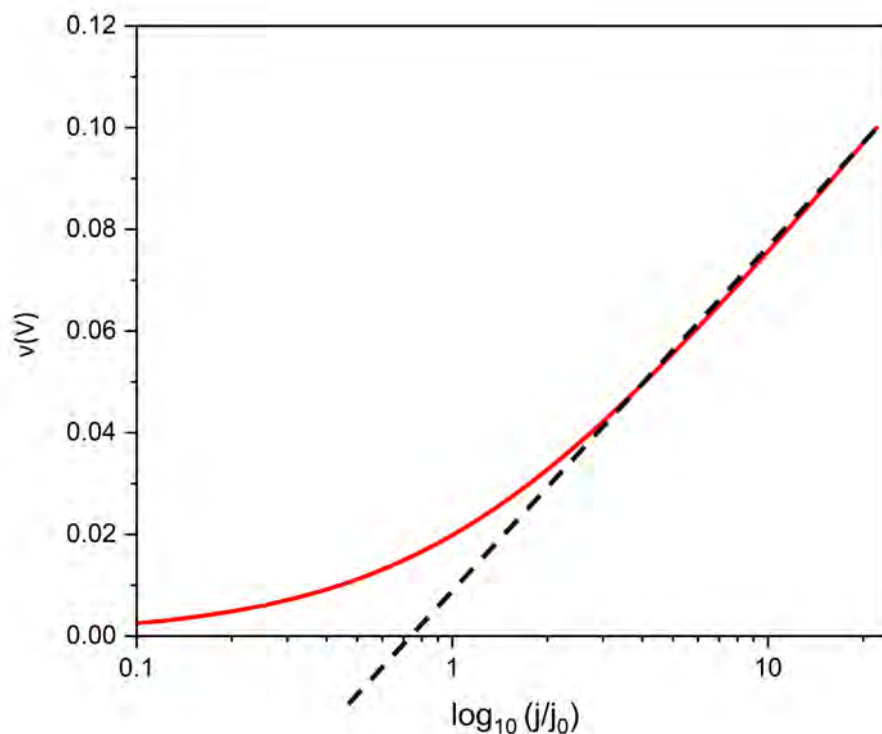


FIGURE 1.10: Example of a Tafel plot

1.10.5 Pourbaix diagrams

Pourbaix diagrams display the possible equilibrium phases of an aqueous electrochemical system as a function of pH of the electrolyte solution [35]. The vertical axis is the electrode potential of a hydrogen or non-interacting electrode relative to the standard hydrogen electrode. The lines in Pourbaix diagrams represent redox and acid-based reactions, and are the parts of the diagram where two species can exist in equilibrium [36]. The dotted lines on a diagram typically indicate water redox reactions as a guideline, liquid water is stable only in the region between the dotted lines. Below the lower dotted line, water is unstable relative to hydrogen gas and above the upper dotted line water is unstable with respect to oxygen. Pourbaix diagrams have their shortcomings as they do not display reaction rates and do not account for unstable or metastable compounds that can form under certain conditions however they are a useful tool for evaluating the state of a metal given the potential and pH are known. Figure 1.11 displays a Representative Pourbaix diagram of iron in a non-complexing aqueous medium. The grey region represents where solid iron is stable and no corrosion occurs. In the Fe^{3+} , Fe^{2+} and FeO_4^{2-} regions iron actively corrodes. The light blue region where Fe_2O_3 forms is a passivation region wherein the corrosion product film offers the base metal protection from further corrosion, in a

process known as passivation. Using figure 1.11 at pH 8 and an applied potential of 0.4 V iron will readily oxidise, forming Fe_2O_3 . The conditions then change and the pH of the water is now 4. Due to the passivation of the iron surface, the amount of Fe^{2+} that would form from the material would be less than if the surface was exposed solely at the same potential at a pH of 4.

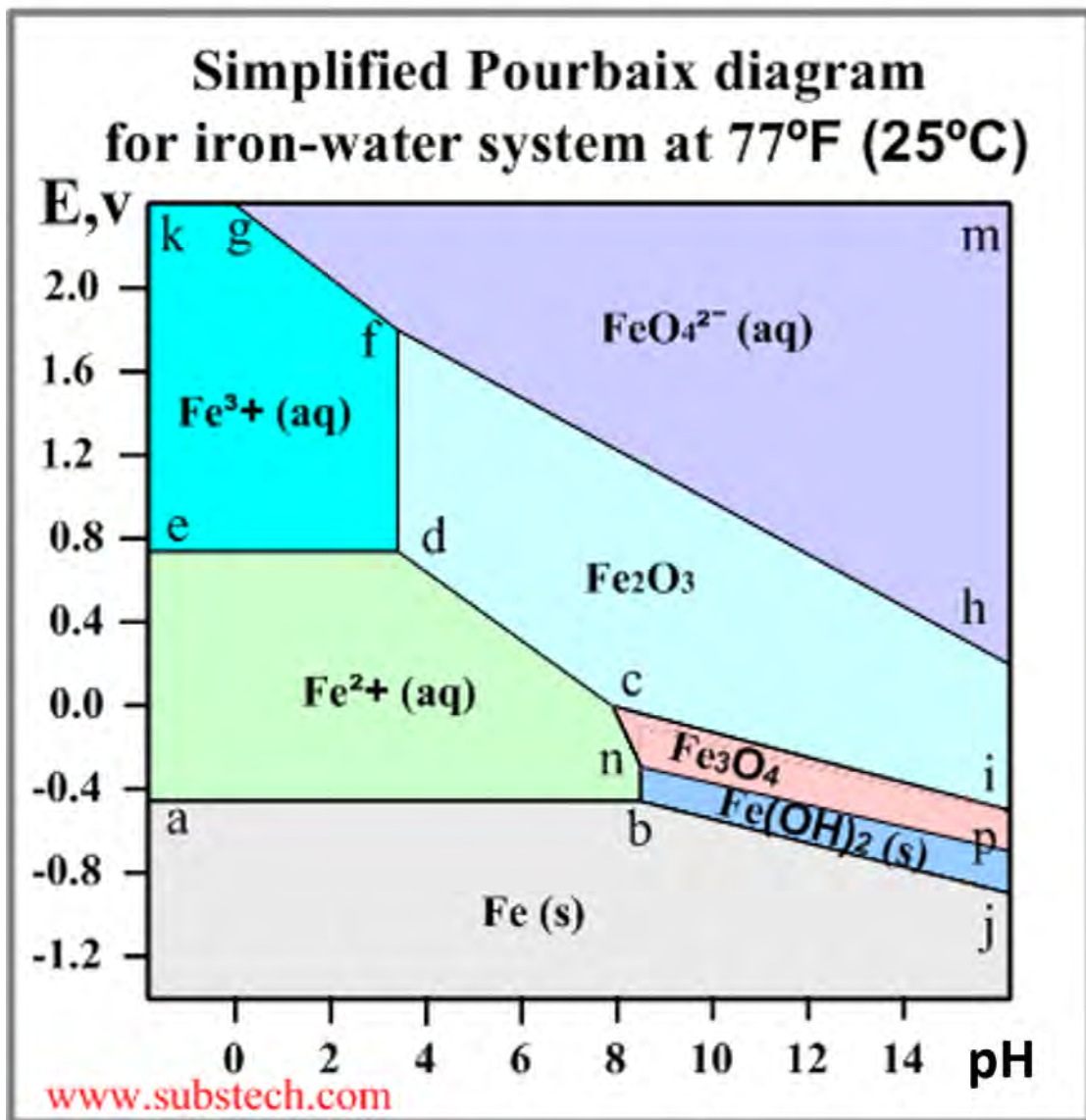


FIGURE 1.11: Representative Pourbaix diagram of iron water system at room temperature [37]

1.11 Pitting Corrosion

Pitting corrosion occurs due to the localised breakdown of a metals passive layer in the presence of aggressive anions, most notably halides. Active pits can perforate a structure, or act as initiation sites for cracks leading to a reduction in the structural integrity of components [38]. The implementation of materials without consideration of their corrosion resistance can lead to parts failing sooner than expected, requiring them to be replaced. There are numerous theories as to the exact mechanisms that govern pitting corrosion including the pitting potential model of José R. Galvele [39], the point defect model of Macdonald et al. [40] and percolation of defects theory by Williams et al. [41].

Historically, modelling has been used to describe the propagation of corrosion pits in stainless steels under potentiodynamic conditions. Laycock et al. proposed a model wherein salt film precipitation, electrolytic migration, and transport outside the pit were each considered explicitly. Numerical simulations of pit growth were used to reproduce the experimentally observed characteristics of pitting, including development of a pit cover, spontaneous repassivation of metastable pits, increased stability at higher applied potentials, and a tendency for pits to become dish-shaped rather than hemispherical [42]. Figure 1.12 below used with permission demonstrate the cross sections through a model pit grown at 190 mV at varying time intervals. The figure demonstrates that the model produced clearly reproduces the formation of a perforated pit cover as presented by Laycock et al. [42]. The work by Laycock et al. indicated that at relatively low applied potentials, modelled pits are sometimes short lived and do not always precipitate a salt film during this limited time. Consequently, their cross sections remain similar to that of the initial cavity. But in simulations where the applied potential is sufficient to stabilise pit growth for a sustained period of time, a salt film is always precipitated and the pits become increasingly dish shaped, as shown in Figure 1.12. The work demonstrated that the development of a porous pit cover can arise from the concentration of corrosion products at the pit mouth falling below the critical level required to prevent repassivation. Further to this for stable pits, a salt film will eventually precipitate over the majority of the corroding surface given sufficient time.

In recent years, the development of imaging technology has allowed for animated radiographs showing corrosion pits growing over time as shown by Davenport et al. [43]. It is highly recommended that readers view videos published by Davenport et al. as cited in this work. Davenport et al. used synchrotron X-ray radiography to observe the evolution of 2D pits growing at the edge of stainless steel foils in chloride solutions. The

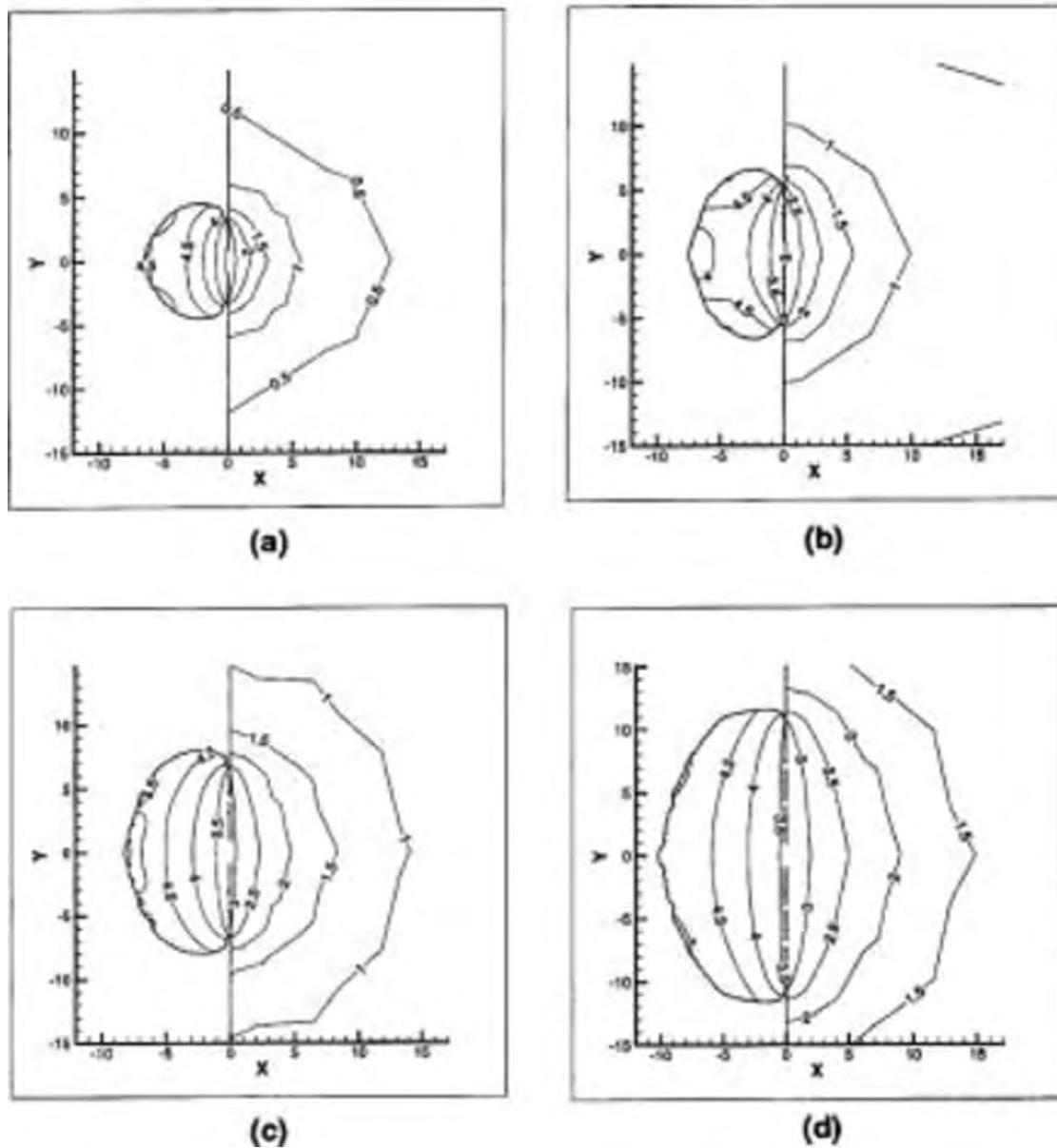


FIGURE 1.12: Cross sections through a model pit grown at 190 mV, after (a) 0.5, (b) 1.0, (c) 1.5, and (d) 2.5 s. The contour lines indicate the concentration of dissolved metal ions. The axis units are micrometers. Used with permission. [42]

chloride concentration was modified under both current and potential control. The presented radiographs confirm that pits grown under potentiostatic control at relatively high potentials develop via lobes through an undercutting process that perforates the metal surface and gradually modifies the pit shape from semi-circular to dish-shaped as growth occurs. This confirmation aligns with work presented by Laycock et al. [42]. The work concludes that in the early stages of pit growth under galvanostatic control following initiation under potentiostatic control, pits propagate by lobes undercutting the metal in a similar way to potentiostatic growth. As the pits propagate under constant current, however, the potential decreases and they tend to approach a circular shape with a rough

etched surface at the bottom, which is likely to grow close to the critical concentration required for propagation, without a salt layer. The change in growth mode may also be associated with a result of the gradual decrease in potential as the pit grows [43]. Figure ?? below shows the Variation of pit current with time in a potentiostatic measurement carried out on 304 at 650 mV (Ag/AgCl) in 0.005 M NaCl solution, together with radiographs showing the appearance of the pit at different times; the current increases as the pit grows and periodically drops due to perforation of the cover and local passivation.

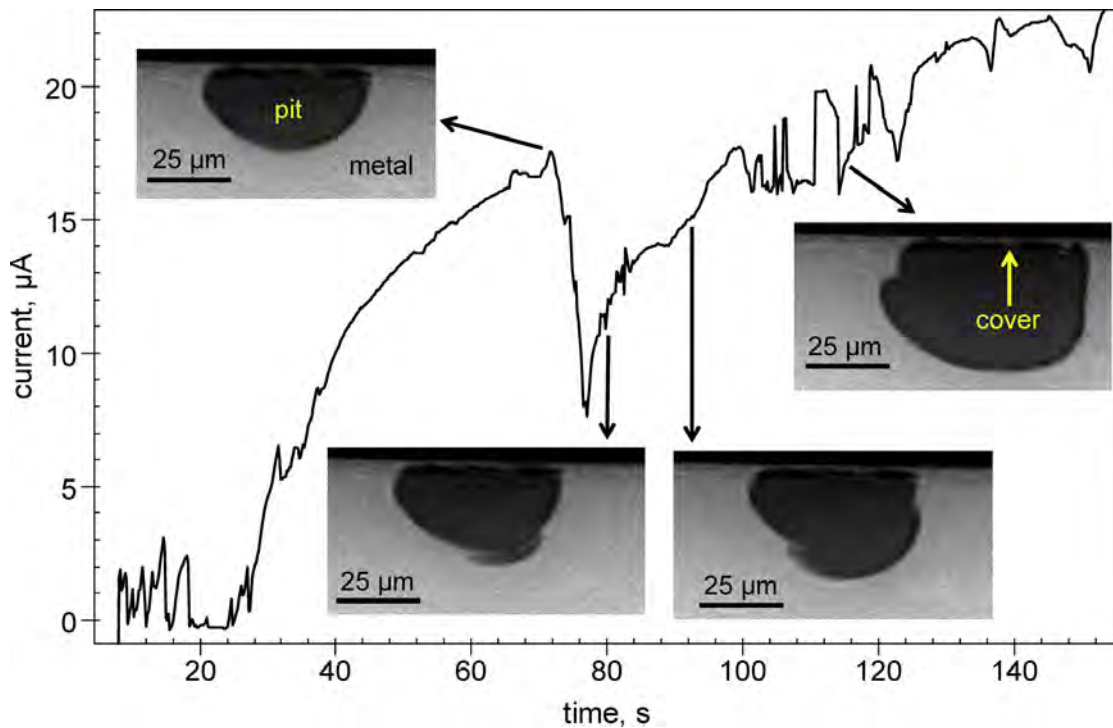


FIGURE 1.13: Variation of pit current with time in a potentiostatic measurement carried out on 304 at 650 mV (Ag/AgCl) in 0.005 M NaCl solution, together with radiographs showing the appearance of the pit at different times; the current increases as the pit grows and periodically drops due to perforation of the cover and local passivation.

[43]

It can be seen that, after a period of initiation, the current generally increases approximately according to $t^{\frac{1}{2}}$ but strong fluctuations are imposed upon this trend. The radiographs also show that a dish-shaped pit with a very thin perforated metal cover gradually grows through period of relatively fast local growth followed by a decrease in growth rate and eventual passivation of some of the (previously active) surfaces, accompanied by the development of fast growing regions ('lobes'), generally growing sideways. Further pit growth results in an increased current until 70 seconds when the current drops suddenly due to the formation of a new perforation that allows metal ions to escape from the pit, diluting the pit solution and leading to local passivation. After 5 seconds the current increases again with lateral pit growth at the bottom of the pit. The

continual development of new pits results in the appearance of a "lacy" perforated pit cover.

Figure 1.14 below shows typical growth of a pit grown in galvanostatic conditions at a current of $10 \mu\text{A}$ following pit initiation under potentiostatic control at $+650 \text{ mV}$ (Ag/AgCl) for a period of 10 seconds. The area of the pits is seen to increase across each of the pits, but once the sample was switched to galvanostatic control, the smaller pits repassivated and only one pit survived and continued to grow. This phenomena was repeatedly observed wherein only one or two pits survived the switch from potential to current control. These surviving pits would continue to grow at the same rate. This highlights that whilst uncommon it is possible for active pits to survive the switch from potential to current control and to continue to grow after the switch. This leads to

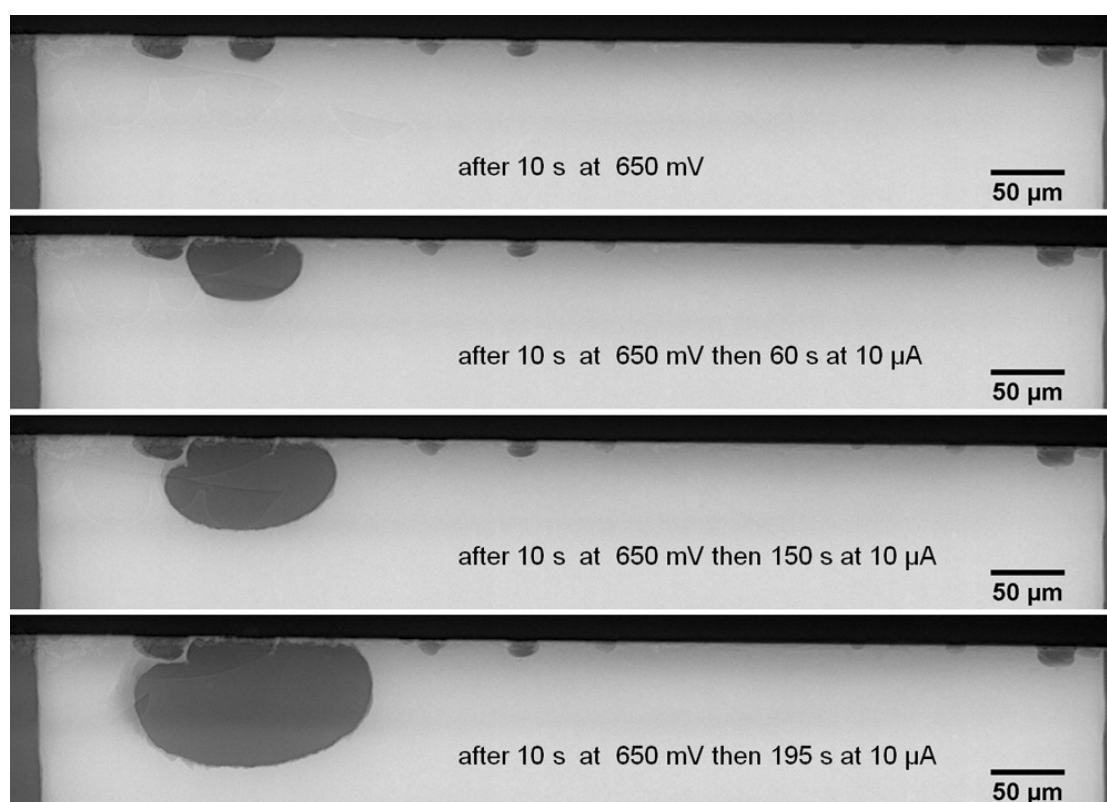


FIGURE 1.14: A series of radiographs of a 2D pit growing at the edge of $20 \mu\text{m}$ foil of 304 stainless steel that was initiated in 0.1 M NaCl at $+650 \text{ mV}$ (Ag/AgCl) for 10 s then propagated galvanostatically at $10 \mu\text{A}$. The time at which each radiograph is taken is shown ($+650 \text{ mV}$ (Ag/AgCl) was applied at $t = 0$). [43]

the claim the lateral growth of pits is controlled by the conductivity of the solution for both potential and current controlled regimes. The work highlights that the movement of the pit boundary (which can be measured via imaging techniques) coincides with the local current density along the pit perimeter. The current density within a pit under potentiostatic control remains almost constant during growth, whereas it shows significant decrease during galvanostatic pit growth. For both potentiostatically and

galvanostatically grown pits, a linear relation exists between the square of the pit depth and growth time, and is independent of the bulk chloride concentration, which suggests that increase in pit depth is under diffusion control, and the pit bottom is covered with a salt layer.

1.11.1 Stages of Pitting

1.11.1.1 Passive film breakdown

Breakdown of the passive film occurs during the initiating stages of pitting corrosion. In this case a very small area of the passive film breaks down extremely rapidly making direct observation of this phenomenon extremely difficult. The exact nature of the passive layer can vary depending on the environment, the material itself, the history of the material and other parameters. Typically however passive layers are extremely thin; on the order of a few nanometers and can support an extremely high electric field (10^6 V/cm) [31]. At low temperatures the diffusion of ionic species in solid oxide is very slow. Therefore, ion movement and hence oxide film growth is controlled by the electric field across the oxide [44]. Passive film breakdown and pit initiation can be categorised into three main mechanisms: the penetration of the passive film by ions, adsorption/ion displacement leading to passive film thinning or mechanisms that support breaking the film [31].

Figure 1.15 illustrates the penetration mechanisms for pit initiation that involve the transport of the aggressive anions through the passive film to the metal/oxide interface, where aggressive dissolution is promoted [45]. The films high electric field assists in the anion migration. This electric field was first given by Mott in 1947 [46], and depends on the hypothesis that a strong field is present in the oxide film, due to a contact potential difference between metal and adsorbed oxygen, which enables the metal ions to move through it at low temperatures [44]. The transport of anions through the metal/oxide interface is supported by the existence of an induction time for pitting following the introduction of chloride into an electrolyte. However, the estimated induction times exceed measured values by orders of magnitude [45]. Marcus and Herbelin used x-ray photo-electron spectroscopy and radiotracer measurements to show that chloride ions are in Nickel passive films [47]. However, there exists no evidence of chloride in passive films [48][49]. However it has been reported that Cl^- enter the outer hydroxide layer and remain there at low temperature and can enter the inner oxide layer at high potential. The article concluded that the intrusion of the Cl^- ions into the inner part of the passive film are the precursors of pit initiation[47]. Seemingly there is a general consensus that there is the potential for facilitated movement of Cl^- ions to travel into the inner oxide

layer however there is some ambiguity with regards to the induction time of these ions as discussed by Bardwell et al [49].

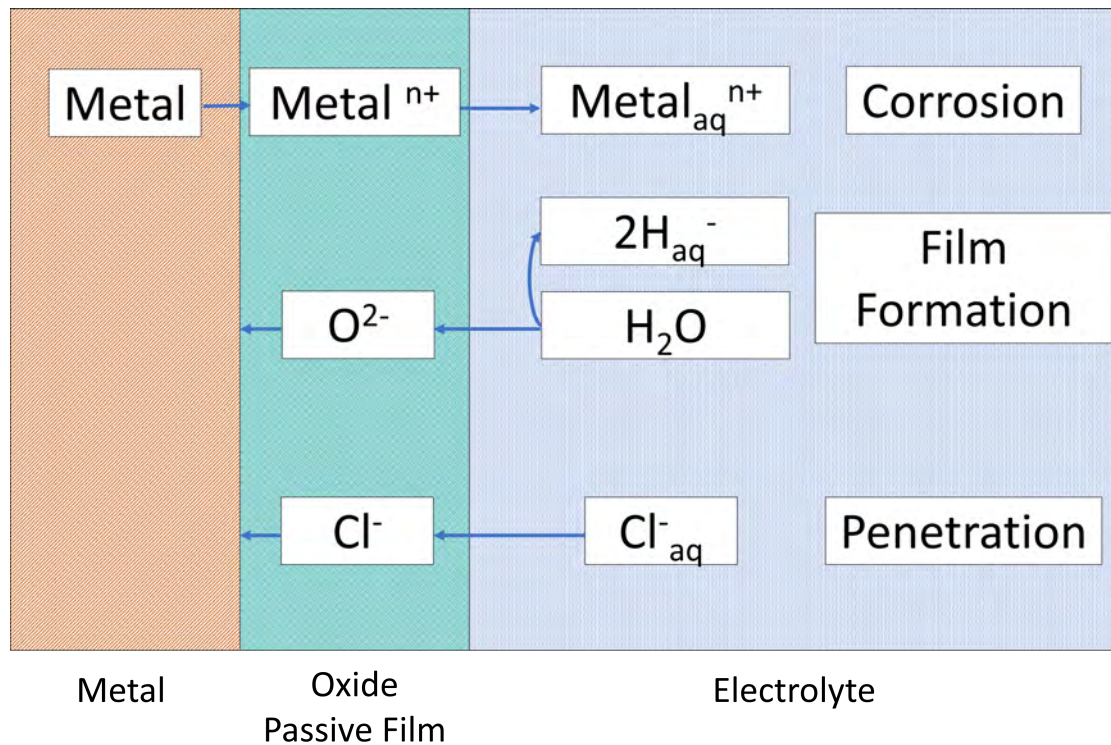


FIGURE 1.15: Penetration Mechanism diagram

The point defect model developed by Macdonald and coworkers describes passive film growth by the movement of point defects under the influence of an electrostatic field [50]. The term point defects refers to metal and oxide vacancies, electrons and holes. This view suggests that the film growth is controlled by the transport of vacancies across the film. This model has been used to explain pit initiation by assuming that aggressive ion adsorption and incorporation at the outer surface of the barrier oxide-layer results in the formation of cationic vacancies [40]. These vacancies are then said to diffuse to the metal/oxide surface where they are annihilated by the oxidative injection of cations from the metal [31]. However the rate of annihilation would therefore be limited by the available flux of cations. Once the flux of cations is unable to match the rate of vacancy diffusion vacancies are able to condense at the metal/oxide interface and a void is formed. The point-defect model has been fitted to experimental data describing the statistical distribution of pitting potentials, the induction time for pitting and the influence of alloying on the pitting potential [51]. Since metastable pits can initiate at potentials far below the pitting potential and during the induction time prior to stable pit growth the pitting potential and induction time relate to pit stability and growth rather than pit initiation [31]. Criticisms of the point-defect model have focused on the handling of the electrode potential and its role in influencing vacancy concentration and migration [48].

More recent work has suggested that voids can form at the metal/film interface by the Kirkendall effect as exhibited by oxides formed during room temperature oxidation of Fe nano-particles [52]. Additionally a study found migration of chloride into oxide and thinning at high potentials under conditions of metastable pitting in aluminium [53].

Adsorption initiation theories as displayed in figure 1.16 were originally founded upon the notion of competitive adsorption of chloride ions and oxygen, however we now know that the passive layer is comprised of several monolayers [31]. However aspects of the model are still relevant. XPS techniques were used to determine two distinct Cl^- species present as an adsorbed species within the passive oxide layer formed on polycrystalline (99.9995 %) Al foils that were polarised below the pitting potential [53]. Chloride was found to be present as an adsorbed species at the surface, as well as an incorporated species within the passive oxide [53]. There is also evidence that the migration of Cl^- ions occurred from the solution/metal oxide interface into the passive film prior to pit initiation once a critical potential was reached. Oxide thinning followed the migration of anions, as determined by XPS, and can be attributed to metastable pitting events or a general oxide dissolution [53]. Additionally XPS measurements have shown that under exposure of Fe to halides the passive layer will become thinner, once again under conditions where stable pitting had not been initiated. This has been described as the catalytically enhanced transfer of cations from the oxide to the electrolyte [48].

The film breaking mechanism as displayed in figure 1.17 presents the idea that the passive layer is in a state of continual breakdown and repair [54]. Suggesting that weak sites or flaws in the layer resulting from electrostriction and surface tension effects may cause localised breakdowns. However these localised breakdowns are able to heal rapidly in non-aggressive environments [31].

This model assumes that breakdown and repair are occurring continuously. Consequently, the ability of the film to repassivate will be limited due to the presence of the aggressive chloride ions. However, this model also implies that breakdown will only lead to pitting under conditions where pit growth is possible [31]. This was controversial at the time of discovery as it implied that pit initiation relies on having the conditions for pit growth in order for pit initiation to occur. To address this Galvele suggested that a critical, material dependant factor is required for pit stability [39]. Galvele then proposed that the nucleation of pitting corrosion of metals in aqueous halide solution depends on the rate at which metal can dissolve where the passive film has failed locally rather than the quality of the passive film. Essentially, penetration of the passive film by the electrolyte is not sufficient to initiate pitting [55]. This development by Galvele had massive implications on the understanding of pitting corrosion and implies that reducing the number of pits has greater importance than the quality of the passive film [55].

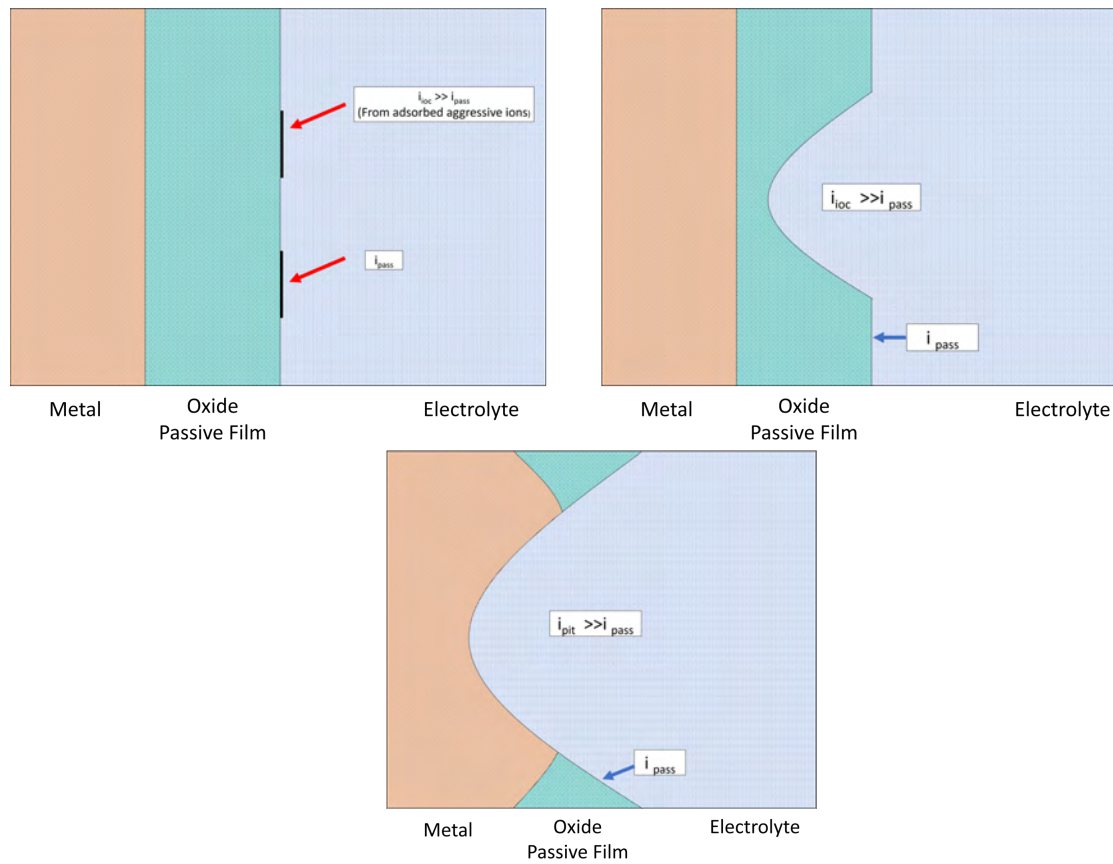


FIGURE 1.16: Adsorption Mechanism steps from left to right

Considering Al, if a freshly initiated pit at the instant of film breakdown has a depth on the order of nanometers, then current densities of around 10^8 A/m² are required for the breakdown to stabilise [31]. This does not imply that the pit will progress past the metastable stage to become a stable growing pit. Similar arguments have led some to conclude that salt films form on the pit surface at very early stages of pit growth [56]. In some cases the effective pit depth may be greater than the passive film thickness if there is some scratching or other disturbance to the metal surface. This would result in a lower current density being required for stable pit growth, the use of a spatially dependent technique to map and measure potentials could be used to determine this. A technique of this kind is detailed in section 3.7. Despite requiring a lower current to initiate pitting at the instant of film breakdown, the required current is still high and requires a high local chloride concentration for the case of stainless steels [31]. There is a theory that counters this by suggesting that the migration of chloride ions to the metal/oxide interface forms a metal chloride phase that is able to crack the overlying oxide as a result of its larger specific volume [57].

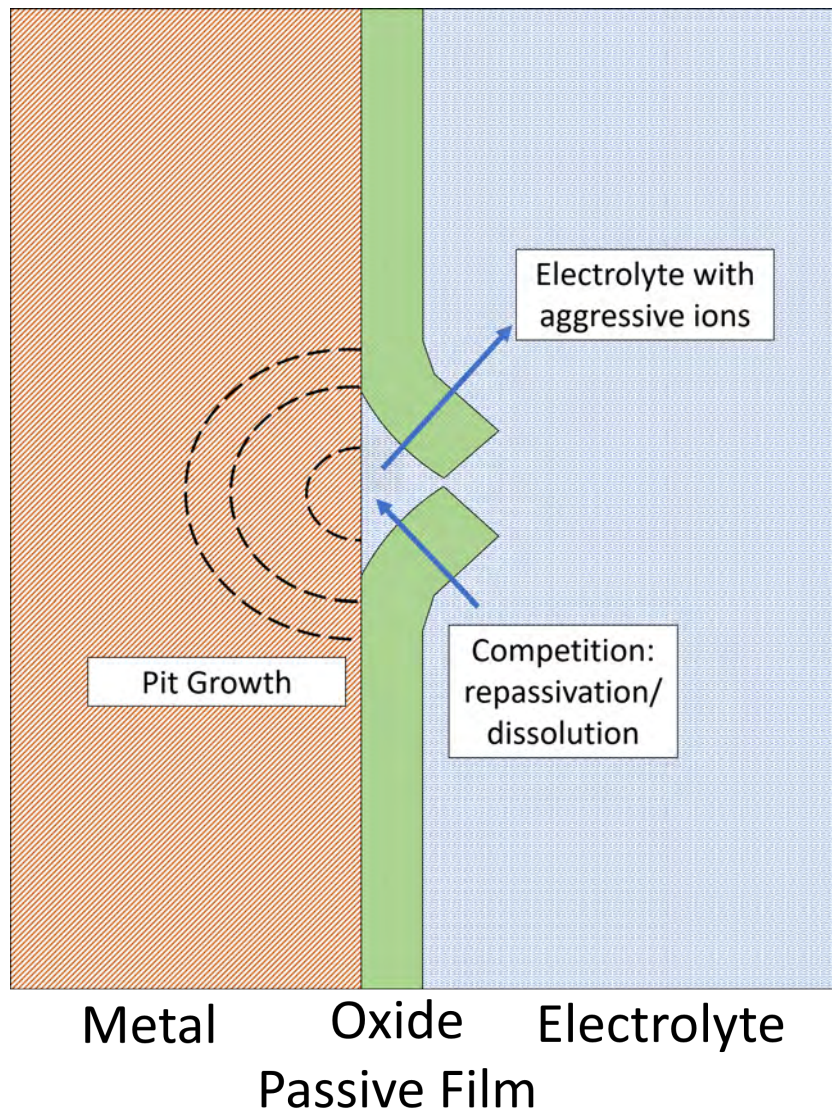


FIGURE 1.17: Film Breaking mechanism diagram

1.11.1.2 Metastable Pitting

Traditionally metastable pits are considered to be small pits of micron size at most with a lifetime less than one second [31]. Metastable pits can form at potentials far below the pitting potential and during the induction time before the onset of stable pitting at potentials above the pitting potential [31]. These events can be characterised using techniques such as Cyclic Potentiodynamic Polarisation which will be detailed in section 1.13.2. Attempts have been made to quantify the growth of pits from metastable to stable stages via a stochastic approach. The probability of the formation of a propagating pit in stainless steel can be expressed as the probability of nucleation of a metastable micropit and a transition probability from metastable to stable propagation [58]. This fundamental approach opened the door for more modern and advanced mathematical

approaches to quantifying both metastable and stable pitting [59]. However, despite the proposition in stochastic approaches that the frequency of stable pitting is related to the frequency of metastable pitting, [58] but this has never been proved [38]. Without the presence of a crevice, it is highly unlikely that metastable pitting observed many hundred mV below the pitting potential could ever stabilise [38]. A new perspective has been proposed by G.S. Frankel et al. to unify the passive film breakdown and pit-stabilisation by suggesting that both must occur for pitting to be a concern and that either can be a limiting factor [38]. They propose that under conditions that include exposure to an aggressive environment and/or a material with a susceptible microstructure, passive film breakdown would be frequent such that pit stability considerations would not be the determining factor in whether pitting were to occur or not. Consequently, in conditions where a less susceptible microstructure and/or less aggressive environment, passive film breakdown would be difficult and rare and the passive film properties and protectiveness become the critical factors. For the second scenario, it is likely that pit growth would be rapid due to the auto-catalytic nature of pitting [38].

1.11.1.3 Pit Growth and Stability

Pitting is considered to be auto-catalytic in nature; once a pit starts to grow, the conditions that are created are such that further pit growth is promoted. The growth rate of a pit depends on material composition, pit electrolyte composition and the potential at the bottom of the pit. The mass-transport characteristics of the pit influence pit growth kinetics through the electrolyte concentration. The local electrolyte concentration will change as the developing pit cavity will become the focal site of anodic metal dissolution with cathodic oxygen reduction occurring where oxygen diffusion is most facile [31]. Very low pH conditions will form in the pit and localised, aggressive pit chemistry is maintained by the salt film, the formation of a cover of corrosion products over the pit. This salt film assists in restricting oxygen diffusion into the pit whilst permitting the diffusion of smaller anions such as chloride stabilising it [31]. The pit becomes enriched in metal cations and the anionic species which migrate into the pit to maintain charge neutrality by balancing the charge associated with the cation concentration [31]. The resulting acidic chloride environment is aggressive to most metals and promotes further pit growth [31]. There are however multiple competing factors that determine the change in the rate of pit formation. For example, the anodic current emerging from each pit acts to lower the corrosion potential thus suppressing the initiation and progression of further pits. From a real world point of view while in application pits are most often associated with inclusions or second-phase particles which result in localised weaknesses in the the passive film [31].

1.12 Scanning Electron Microscopy and Energy Dispersive X-Ray Spectroscopy (SEM)(EDX)

SEM is a characterisation technique where a focused beam of high-energy electrons are fired at a specimen. These electrons lose energy when they interact with the sample as they are repeatedly scattered and absorbed by the specimen. The electrons that comprise the incident beam are known as primary electrons [60]. The type and magnitude of the interaction depends on a number of factors including, but not limited to, the electrons landing energy, the specimen's density and the temperature of the specimen [60]. These various factors impact the energy and direction of the electron beam which can be detected by various specialised detectors. Secondary electrons originate from the surface of the sample due to inelastic scattering interactions between the primary electron beam and the sample.

For the purposes of this work, SEM will be used primarily to characterise the microstructure of AM parts. This will allow comparison to steels manufactured using traditional methods. Further to this, work can be carried out to assess how modifying various build parameters as discussed in section 1.3 can modify the resulting microstructure. Additionally, many modern SEM's have the ability to determine the elemental composition and mapping of samples using Energy-dispersive X-ray Spectroscopy (EDX/EDS). In general, methods for determining elemental composition rely on incident particles such as electrons interacting with the sample causing excitation that results in x rays being released from an element which will have a unique energy bandwidth dependant on the electron shell configuration of the element. These specific energy x-ray's can be correlated based on a database of test data to identify the specific element. Elemental mapping is achieved using the same mechanism but in a raster scan fashion where the elemental map is produced by progressively rastering the beam point by point over the area of interest of the sample. Examples of this mapping are displayed in figure 1.18 [61]. Comparing the composition of the powder loaded into the AM machine with the composition of the final product could allow any elemental contamination that occurs during the printing process to be identified and potential sources determined.

1.13 Corrosion Techniques

1.13.1 Polarisation Scanning

Potentiodynamic polarisation scanning allows for considerable information on electrode processes to be acquired. The DC polarisation technique allows information on the

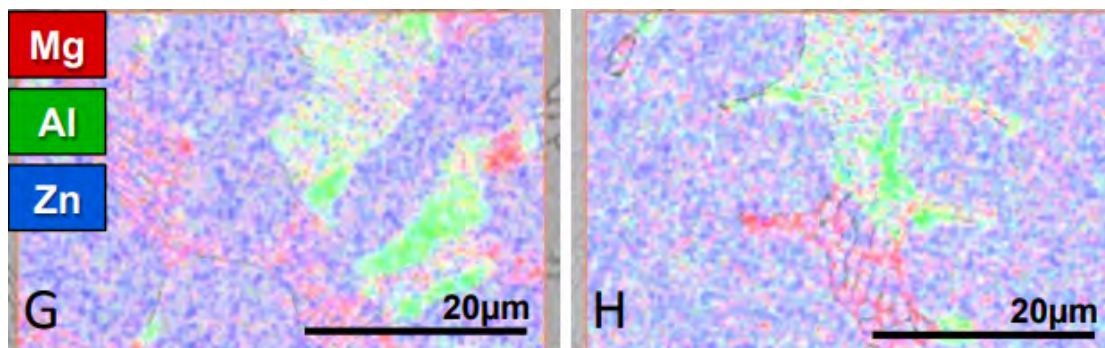


FIGURE 1.18: Example of elemental mapping used with permission [62]

corrosion rate, pitting susceptibility, passivity, as well as the cathodic behaviour of an electrochemical system to be determined [63]. In order for an electrochemical process to take place, there must be an anode and a cathode with both an ionic and electrical conduction path between the two. When performing a DC polarisation scan, the ionic conduction path is provided through the solution separating the working and counter electrodes, while the electrical conduction path is provided through the potentiostat that controls the voltage difference between the working and reference electrode [63]. There are two different scans that can be used in this technique; an anodic or cathodic scan. For both of these scans the driving force is controlled and the net change in the reaction rate (the current) is observed. The potentiostat measures the current that must be applied to the system in order to achieve the desired increase in driving force, this is known as the applied current [63]. Therefore at the open circuit potential (potential at which the total anodic current is equivalent to the total cathodic current) the measured/applied current will be zero [63]. During the potentiodynamic scanning of stainless steels in concentrated chloride environments the rate limiting step of the reaction is often the rate of oxygen diffusion within the electrolyte. This occurs as oxygen is consumed at the cathode at a greater rate than oxygen can diffuse to the cathode. The limiting current decreases with increases in chloride concentration due to lower oxygen solubilities [32]. The interpretation of the Butler-Volmer equation for anodic scanning is that the exponential term governing the anodic reaction is dominant over the exponential term governing the cathodic reaction. However it must be noted that as discussed previously, the Butler-Volmer equation only holds if the the reaction rate is charge-transfer controlled and only one oxidation and reaction is occurring.

Figure 1.19 is an example of an anodic scan starting from point 1 and terminating at point 2. Point A on this line is the potential value where the sum of the anodic and cathodic reaction rates on the electrode surface is zero, known as the open circuit potential [63]. Region B is termed the active region and within this region metal oxidation is the dominant reaction taking place. Point C is known as the passivation potential and

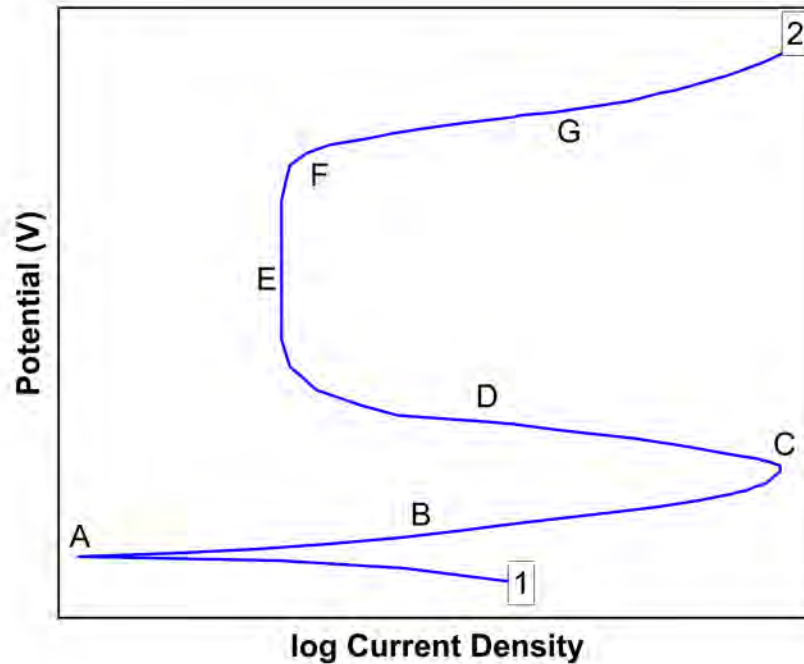


FIGURE 1.19: Theoretical anodic polarisation scan [63]

increasing the applied potential beyond this value results in a decrease in current density. This is due to the nature of the passive film where a thicker film results in charged particles having further to diffuse through the layer, thus decreasing the current density as a result of fewer particles having sufficient energy to transverse the layer. The vertical line represented by region E is known as the passive region where the potential increases rapidly with no change in current density due to the thick passive film preventing charged particle diffusion. Once the potential is sufficiently high the current density begins to increase as the passive layer begins to be broken down. The potential at which this occurs is called the breakdown potential labelled point F. Beyond the breakdown potential the applied current rapidly increases as the passive film has been broken down completely.

In a cathodic polarisation scan, the potential is varied from point 1 in the negative direction to point 2 as shown in figure 1.20. The open circuit potential is located at point A, with the same definition as previous. Region B may represent the oxygen reduction reaction based on the dissolved oxygen concentration in the solution as well as the pH. The oxygen reduction reaction will be limited by the supply of oxygen and therefore the rate of oxygen diffusion. Therefore there will be an upper limit on the rate of this reaction, known as the diffusion limiting current density [63]. Therefore further decreases in the applied potential result in no change in the reaction rate, represented by the vertical line

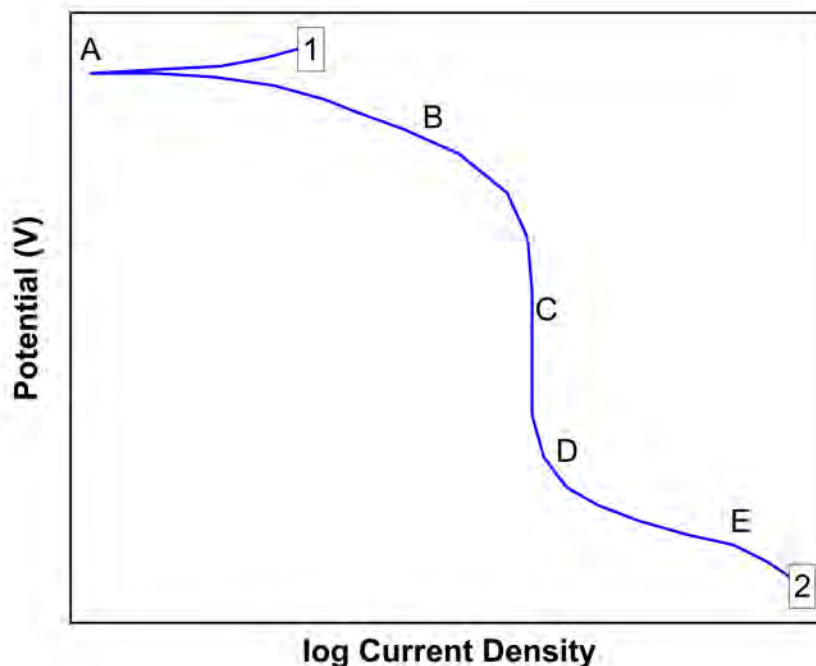


FIGURE 1.20: Theoretical cathodic polarisation scan

labelled C. A point is reached where the applied potential is sufficiently negative to allow another cathodic reaction, hydrogen reduction to take place, this occurs at point D. As the potential and the driving force continue to increase the reaction becomes dominant as displayed at the region labelled E [63].

1.13.2 Cyclic Potentiodynamic Polarisation (CPP)

Cyclic Polarisation tests involve both anodic and cathodic polarisation occurring in a cyclic manner and are typically used to evaluate the pitting susceptibility of metals. An idealised CPP curve is displayed in figure 1.21 with the regions of interest labelled [64]. Where E_{zc} is the zero current potential measured on the forward scan. E_{max} is the peak current potential, the potential at the active peak prior to passivation. E_{pit} is the pitting potential, the potential at which stable pits initiate on the forward scan. E_{repass} is the repassivation potential, the potential at which pits passivate and stop growing on the reverse scan. i_{corr} is the corrosion current density, which is related to the corrosion rate by Faraday's law. i_{pas} is the current density in the passive region. CPP tests typically start at or just below E_{cor} and scan upwards to high potentials. The scan reversal criterion must also be selected prior to testing, once this criterion is reached the scan

direction is reversed and the the final potential is usually the original E_{corr} value or lower [64]. Following testing it is important to examine the tested sample to look for any clear evidence of pitting corrosion on the free surfaces or any unwanted crevice corrosion where the specimen is attached to the specimen holder.

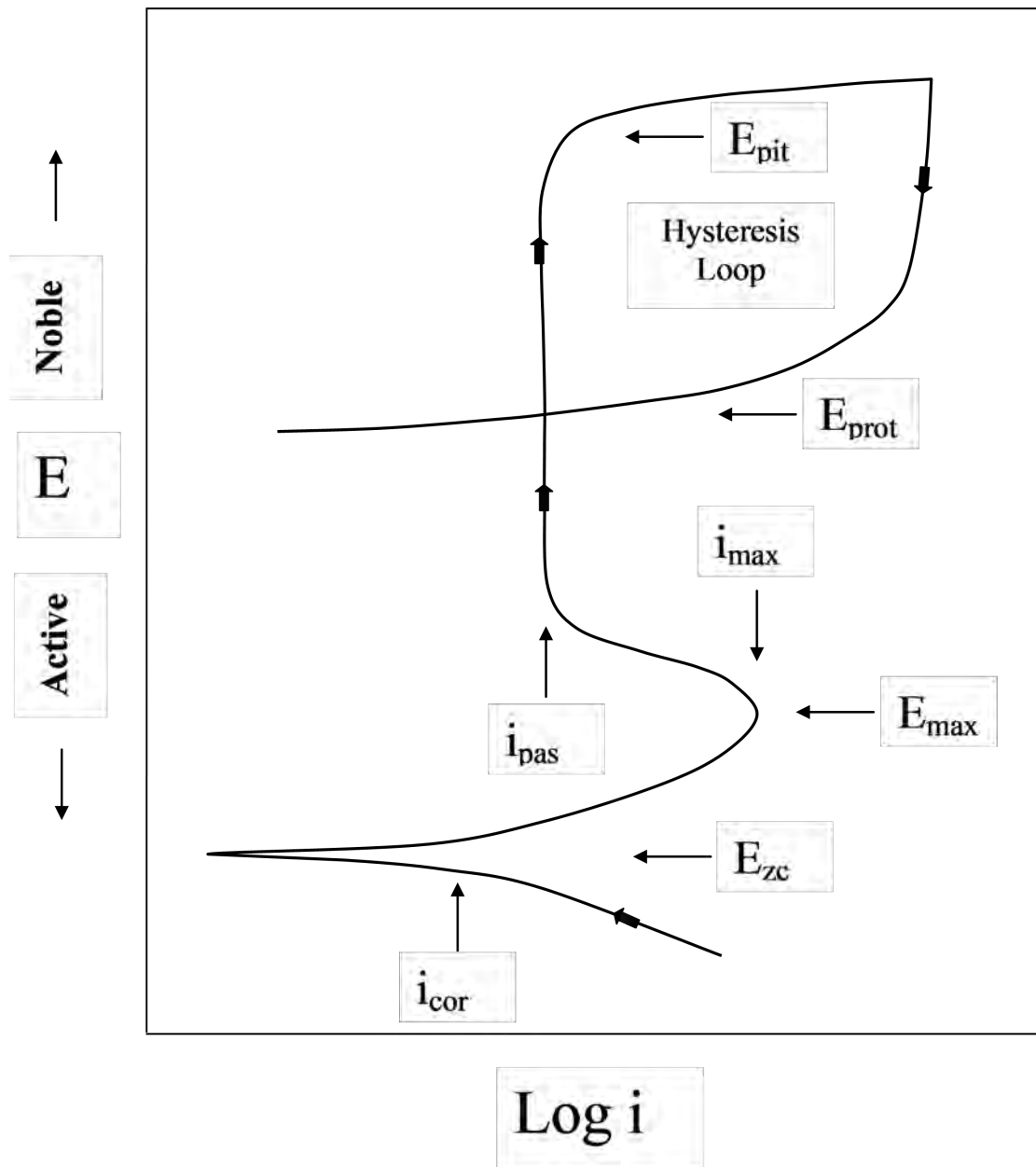


FIGURE 1.21: Idealised CPP Curve [64]

E_{corr} (the open circuit potential) is the potential of a specimen measured under open circuit conditions where the specimen is connected solely to a high impedance voltmeter. E_{corr} is measured for a period of time prior to starting the scan and the scan is then begun some 100 mV below this value [64]. If the sample is corroding actively at E_{zc} , the current will increase exponentially, represented by a straight line on the logarithmic axis. Samples susceptible to pitting must be passive, so an active/passive transition resulting

in a peak current density, i_{max} , will be observed. For the case of a spontaneously active alloy, the current will reach a relatively constant value just above E_{zc} such that i_{max} is not observed. In the passive region the current i_{pas} is usually almost constant [64]. The pitting potential is determined as the potential at which the current increases rapidly due to the onset of stable pitting. Usually it is straightforward to identify the pitting potential due to a sharp increase in the corrosion current. This is not always the case however, as the current increases gradually rather than rapidly, for such cases the pitting potential is defined as a value with a corresponding current density [64]. The shape of the hysteresis curve gives insight into the severity of pitting corrosion. For example negative hysteresis is indicative that the environment is not capable of promoting pitting of the alloy [64]. Whereas the result detailed in figure 1.22; a positive hysteresis curve with a noble pitting potential, but with the protection potential near the zero current potential indicates that pitting "can/will" occur.

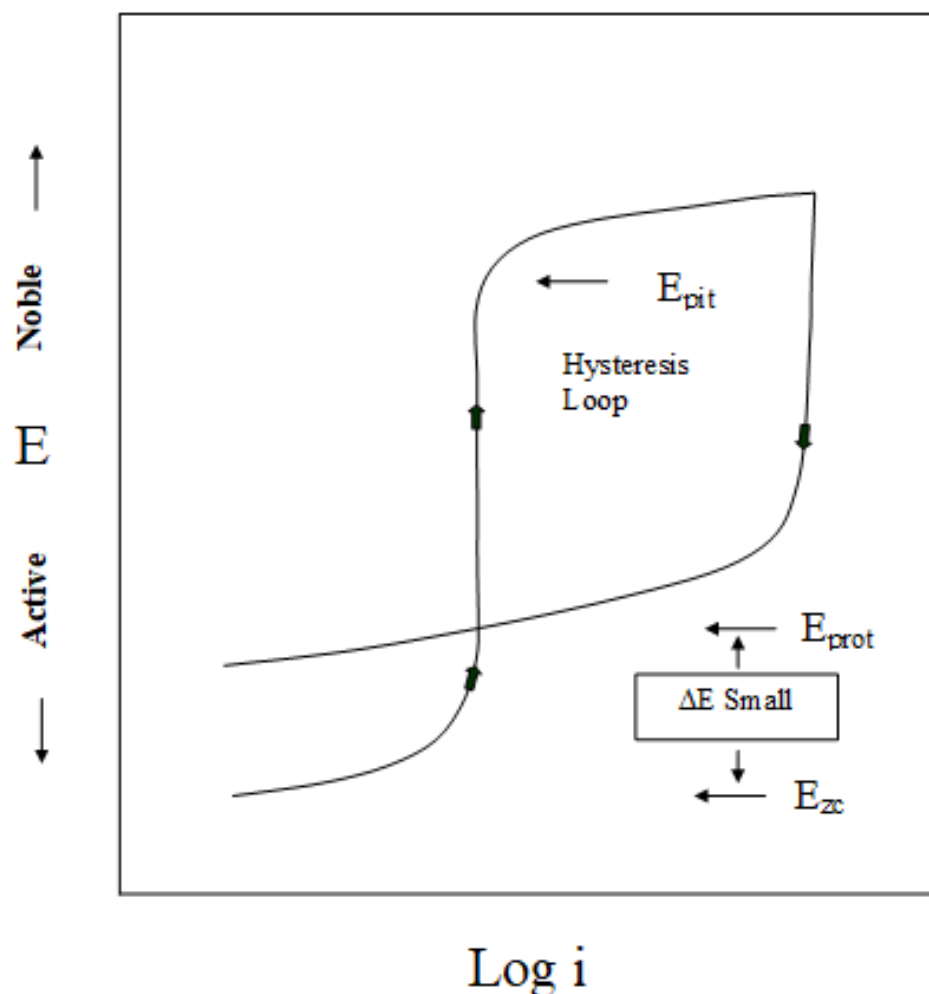


FIGURE 1.22: Representative CPP curve [64]

Pitting is likely to occur in this case even tho the E_{pit} may be quite close to noble in this case localised corrosion likely to eventually initiate when E_{zc} lies close to or is more noble than E_{repass} . It is worth noting that the examples of potentiodynamic curves given in this section are illustrations produced to highlight key features and in reality scans can deviate from these illustrations significantly due to noise, variations in environments and generally the nature of experimentation work.

1.14 The corrosion performance of Invar

Invar® is an austenitic iron nickel dual alloy consisting of 36 % nickel 64 % iron [65]. The alloy is used primarily in precision instruments that require mechanical stability under a range of temperatures. This is due to the alloys low coefficient of thermal expansion that is a result of an anomalous contraction upon heating that counteracts the normal thermal expansion which arises from the anharmonicity of lattice vibrations when thermal energy is introduced to the system [66]. Invar is used in satellites where geometric stability is maintained upon the satellite being thermally cycled as it moves in and out of the suns line of sight. The cost and energy requirement to send satellites into orbit is heavily dependent on their mass, the mass reducing capabilities that additive manufacturing offers therefore make Invar a material worth investigating. Whilst there has been considerable work investigating the mechanical properties of additively manufactured Invar [67][68] [69] its corrosion properties have not been investigated and compared to the corrosion behaviour of its wrought counterpart. The material is not stainless and is more susceptible to corrosion attack than the other alloys investigated in this work. The material readily breaks down in 1 % NaCl solutions as shown in section 4. Therefore the majority of the work reviewed in this section refers to the corrosion performance of traditionally manufactured Invar.

The corrosion behaviour of different iron nickel alloys was investigated by Gehrman et al. Nickel additions were made to iron ranging from 35 and 82 % [70]. Materials corrosion performance was determined by the mass loss recorded after exposure to thermal cycling. The work found that increasing the nickel content and improving the surface finish of the alloys improved the corrosion resistance of the materials. This was credited to nickels ability to protect itself by the development of a passive oxide film, which reduces the rate of corrosion [70].

Potentiodynamic polarisation was used to study iron nickel alloys in sulphuric acid solutions by Dale O. Condit [71]. Ten high-purity Fe-Ni alloys were tested with nickel concentrations of 0, 5, 10, 20, 25, 30, 45, 50, 65 and 100 atomic %. Specimens were

given twenty minutes to attain a steady-state corrosion potential before anodic or cathodic polarisation. X-ray analysis was also carried out on specimens to determine their structure. Alloys up to and including 25 atomic % nickel were body-centered cubic while all the alloys containing more than 25 atomic % nickel were face-centered cubic. The authors suggest that the kinetics of hydrogen evolution for the material is dependent on the nickel concentration. The gradients of the Tafel slopes obtained in the work fall into three categories; nickel concentrations from 0 - 10, 20 - 45 and 50 - 65 atomic %. This is presented as being due to changes in the metallurgical phases as the proportions of ferrite, martensite and the γ -phase vary with the variation in elemental composition. This however is countered by the fact that the values of potential indicate that the cathodic curves for all alloys from Fe-25Ni to pure nickel are nearly coincidental, despite the slight changes in the Tafel sloped. This leads the authors to suggest that the hydrogen evolution behaviour is more likely to be a function of the crystallographic structure of the material. Regression of the cathodic curves determined that increased nickel concentrations resulted in a decreased steady-state corrosion rate [71]. This is in alignment with results presented by Gehrman et al. [70] and aligns with modern general knowledge and operational experience wherein nickel based alloys are used in place of iron based alloys when the corrosion performance of iron based alloys is not sufficient for the given environment [72]. The authors continue by observing that in their investigations, the active peak critical current was not a simple function of the nickel concentration. This suggests that the active anodic behaviour of all the alloys tested up to 50 atomic % nickel are controlled by iron in the sulphuric acid solutions. This fact is in agreement with data presented by Condit in earlier work [73] on the dissolution properties of some of these alloys in the active region, that is, that proportionately more iron than nickel dissolves from low nickel, iron nickel binary alloys. As the nickel concentration is increased above 50 atomic %, the active peak decreases significantly which is evidence of the ease of passivation of high-nickel alloys [71]. The curves for the reverse potential demonstrate the protective nature of the passive film formed on the alloys. The occurrence of the current oscillations, and the high current peaks of the reverse curves for low Ni alloys indicate a film of low integrity which is easily reduced in materials where the atomic % of nickel is below 30. For nickel contents above this point the oscillations disappear and the peaks become significantly lower than those observed during the forward anodic scans, this is illustrative of the formation of a higher integrity passive film or there remain portions of the metal surface where film is still present thus, reducing the effective area for dissolution [71]. This is supported by the fact that the film formed on pure nickel is not reduced even at potentials wherein hydrogen gas is reduced on the surface of the film [71]. The authors conclude that the cathodic polarisation behaviour appears to be dependent on the crystallographic structure; whereas, the anodic polarisation behaviour

is strongly affected by the relative composition of the two components for iron nickel alloys in sulphuric acid [71].

Alharthi et al. investigated the corrosion resistance of iron nickel alloys in concentrated hydrochloric acid pickling solutions for 36 and 45 weight % nickel, iron nickel alloys. Potentiodynamic cyclic polarisation was carried out starting at a potential of -1.2 V to 0.8 V (Ag/AgCL) at a scan rate of 0.003 V/s. EIS experiments were carried out at the OCP after immersing the iron-nickel alloys after their immersion in 1M HCl solutions for 2400 seconds, the range of the frequency for the EIS was scanned from 100KHz to 100mHz [74].

The authors reported that the general and pitting corrosion performance of the higher nickel alloyed material was superior to that of the lower nickel alloyed material. The recorded current and size of the hysteresis loop obtained for Fe-36 % nickel alloy were much higher than those obtained for Fe-45 % nickel alloy. This indicates that the iron-nickel alloys under investigations suffer pitting corrosion and the intensity of pitting is lower for the alloy with higher nickel content. The potential at OCP was lower for the lower alloyed nickel alloy as the acid solution dissolved the surface of the alloy over time. SEM EDS analysis was carried out on the surface of both materials after immersion in 1M HCL for 96 hours. Both alloys were seen to have undergone uniform corrosion as localised pitting was not reported on either of the materials surfaces. EDS reported a an iron content of 49.88 weight %. The authors suggest that this lower than bulk concentration of iron is due to the dissolution of iron, whilst a recorded oxygen weight percent of 5 indicates that the corrosion product layer may contain FeO and Fe₂O₃ oxides which may offer some passivation to the surface of the alloy. Accurate identification of these oxides could be achieved using XRD or XPS techniques. The authors note a thicker oxide was formed on the higher nickel content alloy, from surface SEM micrographs. Analysis of the cut edge would help to validate this assumption. They record an oxygen content of 15 weight % and conclude that the oxide film is continuous across the surface of the higher nickel content alloy and that this offers some protection to the metal from corrosion. The work concludes by demonstrating that the higher nickel content alloy demonstrated absolute current values than the lower nickel content alloy in EIS measurements [74].

1.15 Additively Manufactured 316L

1.15.1 General

Austenitic stainless steels are formable, weldable and can be used across a range of temperatures. They can be formed using the same tools as carbon steel and can be cold

worked up to yield strengths of over 200 MPa [75]. Grade 316 and its low carbon version 316L are austenitic stainless steels commonly used in a wide range of applications, due to their durability, corrosion resistance and high performance in high-stress environments. The composition for 316/L is essentially that of general purpose 304 with a slight reduction in chromium but an increased molybdenum and nickel content. Commenting on the effects of individual elements within an alloy can be difficult, for example it is well known that the addition of chromium, molybdenum and manganese in general increase the pitting corrosion resistance of steel alloys in chloride environments. However, understanding the role of each element within the passive film which provides the protection and explaining the structure of the passive film requires sub nano-scale measurements as the thickness of the 316L passive layer for example has been reported as being 2.2 nm thick with outer and inner layers of 0.7 and 1.5 nm thickness, respectively. [76]. Comments can be made based on accepted literature however this field is developing as equipment and technological improvements allow for more precise measurements to be made on these tiny scales. Whilst this information is as accurate as possible at the time of writing technological improvements in future may render some of this text invalid. Nickel is less readily oxidised than iron and chromium, the role of Nickel in the passive film has been reported to bring down the overall dissolution rates of iron and chromium [77]. Scanning tunnelling microscope (STM) results indicate that the passive film formed on austenitic stainless steels shows a higher degree of long-range order within a shorter time span than the corresponding ferritic alloy [78]. However despite this, other studies on 316L have found that Nickel was below the detection limit of XPS in the passive layer of the material [76]. Instead Nickel was found to be enriched in the alloy underneath the oxide film (26 at% instead of 12 at% in the bulk alloy). This could mean that whilst nickel is not a major component of the passive layer it is still essential in the natural production of the passive layer. Molybdenum is frequently added to ferritic and austenitic stainless steels to improve their resistance to pitting corrosion in chloride media, according to literature the element can reduce the surface enrichment of chlorides and sulphates in iron chrome alloys and can help stabilise the passive layer [77]. When used as an alloying element within stainless steel, molybdenum has been found to be incorporated into the passive film, demonstrating a complex oxide chemistry with different states of oxidation [79]. Concerning molybdenum in 316L, the calculated composition shows that it is enriched in the native oxide film (4 at% globally and 13 at% in the oxide outer layer instead of 1.6 at% in the bulk alloy). It is also found enriched in the alloy underneath the oxide film (4 at% instead of 1.6 at% in the bulk alloy) [76].

1.15.2 316L LPBF Inert Atmosphere

The inert gas used when building austenitic stainless steel 316L parts has also been investigated in the literature. There is a large body of published literature wherein 316L was built both in argon [80], [81],[82] [83] and nitrogen build atmospheres [84], [85], [11]. The reported effects of using argon include producing manufactured specimens with a more heterogeneous structure compared to building with nitrogen [86]. Using nitrogen in place of argon has been documented to lead to an increase in weight percent of nitrogen within the as-built material resulting in increased material hardness [86]. The residual oxygen levels within the process atmosphere differ when building in argon or nitrogen. When building with a nitrogen atmosphere higher levels of nitrogen dissolution are observed [84]. Pauzon et al. state that differences in oxygen and nitrogen dissolution appeared to have little effect on the mechanical properties of the material [84]. In addition to this, Pauzon et al. presented parts built to near complete densification under both nitrogen and argon atmospheres with relative densities of $99.96 \pm 0.02\%$ [84]. Work presented by Aversa et al. states that an increase in yield strength and fracture elongation is possible when building within a nitrogen environment with these effects attributed to the different size of manganese-silicon oxide particles and different nitrogen content within built parts [85]. It is also possible to modify the elemental composition of 316L powder via gas nitriding processes. One such process as outlined by Boes et al. involves nitriding 316L powder in a pure nitrogen environment at a temperature of 675°C at a pressure of 3 bar [11]. This process allows for the powder to "pick up" nitrogen from the surrounding nitrogen atmosphere. Samples built in a nitrogen atmosphere from a blend comprising of this modified and traditional composition 316L powder demonstrated an increased yield and tensile strength without a large change to the fracture elongation [11]. However, during the LPBF solidification process it is possible for outgassing of nitrogen to occur during melt solidification, resulting in a lower specimen density. These reduced density samples suffer from a reduction in the positive effects attributed to the increased nitrogen content on the mechanical properties [11]. This work outlined in this article use the conventional argon atmosphere for the build process which is still widely used in academic and industrial settings.

1.15.3 Corrosion Behaviour of AM 316L

The corrosion behaviour of AM 316L is an emerging topic with new results and discussions being published rapidly. The general conclusions from literature are that AM stainless steels such as 316L have demonstrated both enhanced and reduced corrosion

performance compared to wrought 316L. These contrasting views traverse different experimentation methods and corrosion environments [87] [88] [89] [90] [91] [92] [93]. There have been instances where 316L LPBF produced parts have experienced Mo microsegregation to grain boundaries [94]. A localised region depleted in Mo or Cr can result in a defect in the passive film at a particular point in the build. This localised region could be significantly more vulnerable to pitting corrosion than other regions which are abundant in Cr and Mo [31]. These results were attained on ALM produced parts which approached a relative density of 99.5 % compared to wrought 316L [94]. It has also been reported in literature that the increasing the energy density of a 316L steel build results in an increase in the % weight of Mo accompanied by a decrease in Mn and Ni [23]. This can result in a diminished passive range and an increased passive current density for printed alloys, indicative of a reduced corrosion performance [94]. Additionally AM parts have been found to be susceptible to intergranular corrosion, where corrosion has attacked grain boundaries which can promote intergranular stress corrosion cracking. This has been attributed to heterogeneous compositional changes caused by elemental segregation, specifically the microsegregation of Mo to grain boundaries. The microsegregation of elements present in low quantities within 316L could have a greater effect than segregation of more abundant elements. For example even if there is segregation of chromium from one region to another there may still be sufficient chromium throughout the microstructure to prevent a noticeable localised difference. Despite these findings other literature has reported the microsegregation of Mo to be a positive effect in terms of material properties such as hardness and susceptibility to dislocations [95]. For instance, the local enrichment of Mo accompanied by the formation of Cr-Silicate nano inclusions in the austenitic lattice of 316L can induce a fine network of dislocation tangling which can retard or in some cases block the migration of newly formed dislocations. Effectively turning a soft austenite microstructure to that of a hardened steel [95]. Further to this, it has been demonstrated that the local oxidation of active elements chromium and silicon yielded the formation of spherical nano-inclusions of an amorphous chromium-containing silicate. The mechanism for forming these oxide nano-inclusions can pave a way for cleaning the oxygen contamination that may be present in the starting powder [95]. In deep-sea chloride environments Zhao et al. have reported an increased resistance to corrosion in SLM 316L [91]. This improvement is accredited to the small grain size and high density of grain boundaries within their material. They state that the high densities of grain boundaries enhances the formation of stable oxides controlled by the electromigration process [91]. Further to this, they determined that whilst the SLM and wrought material are comprised of the same metal oxides that the SLM material had a greater fraction of stable Oxide Cr_2O_3 in comparison to the wrought part. However their work made no comment on the repassivation of the material. Further work investigating the passive layer of 316L and the corrosion performance of AM 316L in a 3.5 % NaCl

environment was presented by Nie et al.[96]. They proposed that difference in corrosion performance between wrought an AM 316L was in essence due to the microstructure of the material. They suggest that although both wrought and AM 316L have dual-layer passive films composed of Cr and Fe oxides and hydroxides that the large number of sub-grain boundaries and the high dislocation density of the AM material promote the formation of a more compact and thicker passive layer compared to wrought 316L [96]. Whilst this more compact layer leads to improved general corrosion resistance the low hydroxide content in the passive film accompanied by a proposed micro-galvanic coupling effect between sub-grain boundaries and sub-grains due to Mo segregation lead to a weakened resistance to pitting corrosion in the AM part [97].

Interesting results are presented by Duan et al. who investigated the pitting behaviour of SLM 316L in chloride environments of different concentrations. They specifically looked at the pitting mechanism induced by gas pores [87]. Their work reported that the shapes of the potentiodynamic curves recorded on both the SLM and wrought 316L were similar, suggesting that the electrochemical process governing both conditions were largely the same despite small differences in some examples [87]. The work also showed that localised corrosion was most likely to initiate at manufactures defect sites wherein gas pores were the most common site. Across the range of environments tested several phenomena suggested that the influence of the typical microstructures on the corrosion behaviour of SLM 316L was dependent on the aggressiveness of the environment used [87]. Birbilis et al. has attributed the enhanced corrosion properties of AM 316L to to the absence of MnS inclusions within the material that occur as a result of rapid solidification during the build process [97] [98]. This explanation however does not apply in some conditions [87]. One explanation for this can be found published by Frankel et al. pre-dating the MnS theory, wherein it is proposed that that the pitting resistance of metals depends on the properties of passive film in less extreme environments and is related to the pit stability in aggressive conditions [38].

Duan et al. also presents results indicating that that the evolution of metastable pits into active pits occurs more easily on SLM material compared to wrought 316L [87]. Ultimately, the work presented by Duan et al. states that the SLM material displays a decreased resistance to corrosion in aggressive solutions such as (1M NaCl, pH 1 and 3M NaCl, pH 3) whilst under less aggressive conditions the SLM material displays an increased corrosion resistance compared to wrought 316L. The immersion testing revealed that the wrought material had a higher frequency of metastable pitting however the metastable pits formed on the SLM material transitioned more easily to stable growth [87]. The work concludes that the different pitting mechanisms associated with the materials resulted in the difference in pitting corrosion behaviour. Pitting always initiated at MnS inclusions in wrought 316L and initiated preferentially at gas pores in the SLM

material. The density and chemical activity associated with the MnS inclusions within the wrought material were larger than that of the gas pores for which pitting corrosion nucleated the SLM sample. Metastable pit growth following the preferential dissolution of MnS inclusions occurred in the mode of active state dissolution of the metal [99], the current density of which was much larger than that of electrochemical dissolution of the passive film [87].

To summarise the in-depth and detailed work presented by Duan et al into the most relevant paragraph possible. In aggressive conditions, the rate controlling step for pitting in 316L is the transition from metastable to stable active pits. SLM 316L has an easier transition pathway than wrought 316L. Therefore in aggressive conditions the pitting performance of SLM 316L is inferior to that of wrought 316L. As the aggressiveness of the environment decreases the rate controlling step for pitting in 316L becomes the pitting nucleation relating to passive film breakdown. Duan et al. credit SLM 316L with having a more stable passive film and therefore superior pitting corrosion resistance compared to wrought 316L in less aggressive solutions (0.01M – 1M NaCl, pH 3; 1M NaCl, pH 3–11) [87]. In significantly less aggressive solutions (1M NaCl, pH 13) the rate determining step of pitting corrosion is the nucleation process [87]. Whilst the work focuses in great detail on gas porosity it does not evaluate the pitting behaviour of materials with lack of fusion porosity. It is possible that materials with large irregular lack of fusion porosity present will perform badly in localised corrosion corrosion regardless of the manufacturing method. Larger irregularly shaped porosity features can act as initiation sites for localised pitting corrosion due to the restricted diffusion of oxygen into these regions as per the Fontana Greene mechanism of crevice corrosion [100] [101] [102] [93].

Work by Chen et al. investigated the corrosion behaviour of LPBF manufactured 316L after modifying the surface of the material using laser polishing [89]. This work is interesting in that it aims to address the issues associated with porosity and surface level defects on the initiation of localised corrosion. Chen et al. were able to remove the majority of surface defects including residual powder particles, partially melted particles and asperities. The treatment they used also refined the microstructure of the material wherein columnar grains were refined into cellular structures [91]. The treatments also resulted in a higher corrosion potential and lower corrosion current density than their as-printed samples, demonstrating that laser polishing is effective in improving the corrosion performance of as-built LPBF 316L [91]. Despite the improvements in corrosion potential however Zhao et al. did not comment on the repassivation potential of the material or the effects of the treatment on this parameter.

Ultimately when considering the pitting performance of a material the Review of the Critical Factors and Passive Film Breakdown vs Pit Growth Stability by Frankel are still relevant [31] [38]. Despite the unique and recently developed microstructures attainable by cutting edge AM techniques ultimately the chemical reactions and the fundamental principles governing the initiation and growth of metastable and active pits remains unchanged [87].

1.16 The effects of HIP treating on Additively Manufactured 316L

For AM parts to be successfully integrated into supply chains the mechanical and corrosion performance of the materials must be predictable and repeatable, and comparable to that of their wrought counterparts. Post-processing treatments such as heat treating, hot isostatic pressing (HIP) and surface treating are commonly used throughout the majority of manufacturing processes to remove defects, alleviate anisotropy and improve mechanical and corrosion performance [103] [104].

1.16.1 HIP Process

HIP treatments commonly use an inert gas at elevated pressures to exert an isostatic force on a material at elevated temperatures. This process can reduce the total volume of porosity and heat treat the part in a single process. The increased pressure associated with HIP treatments increases the solubility of gases trapped within pores; these gasses then drift to the surface of the part wherein the internal pore then collapses and closes [105]. Whilst this mechanism can remove gas filled porosity it is uncertain whether the conditions necessary to consolidate unmelted powder particles trapped within the material can be met. This phenomenon has been reported in other materials but not in 316L [106]. Additionally HIP treatments are unable to remove porosity that is connected to the external surface of a part due to the ingress of the HIP treatment gas into that porosity during the treatment [106]. The importance of this is that parts can be HIP treated wherein porosity is diffused outward from the centre of the material. Following this, the outer region of the sample can be machined away to remove any remaining surface breaking porosity. Several studies have been carried out investigating the effects of HIP treatments on reducing the presence of porosity, and how it can manipulate changes to the microstructure and resulting mechanical properties of AM 316L [107]. Cegan et al. found that using higher scanning speeds resulted in irregular lack of fusion porosity being produced in their parts. Their HIP process significantly reduced the presence of

internal closed porosity but had a minor effect on open porosity [108]. The importance of the optimisation of the HIP process is detailed by Liverani et al., who reported that increasing HIP pressure from 105 to 200 MPa has no influence on final sample density suggesting that there is a cut off point wherein increasing the pressure of the cycles further has no benefit if porosity is the primary concern [109]. The temperature of the HIP cycles carried out in the work was also sufficient to allow for complete recrystallization of the materials grains removing the microstructural features associated with the as built AM microstructure. Simultaneously resulting in an increased ductility at the expense of yield strength and hardness [109].

1.16.2 Sensitisation of Stainless Steels

Stainless steels can suffer from sensitisation at elevated temperatures wherein chromium carbides precipitate at grain boundaries leaving the material vulnerable to intergranular corrosion. Both the chromium and the carbon must diffuse to the grain boundaries to form the precipitates, which leaves a chromium-depleted zone adjacent to the grain boundary. Consequently, this grain boundary region is now highly susceptible to corrosion. This corrosion mechanism is displayed in figure 1.23.

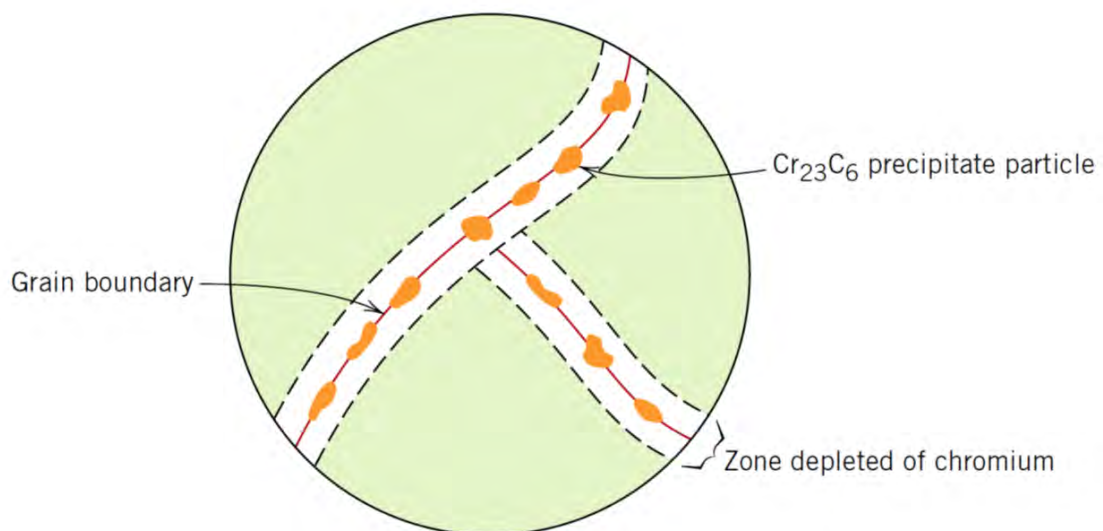


FIGURE 1.23: Illustration of the sensitisation process taken from "Callister, Materials Textbook eighth edition" [72]

Despite 316L being designed as the low carbon sibling of 316, sensitisation is still possible under certain conditions. The sensitisation temperature range for 316L varies across literature however the general region is considered between 500 – 950°C depending on the soak time [110] [72], [111]. Increasing the soak time gives the chromium carbides more time to precipitate and become mobile within the microstructure. This presents an issue

as the HIP used for this work does not have the capability for active cooling through the means of gas quenching. Thus, the cooling rate of the materials after being HIP treated is slow enough for sensitisation to occur as the samples cool within the HIP chamber as the cooling process can take several hours in this setup. The three most widely used methods to prevent sensitisation are as follows: 1) To modify the alloys composition to include metals such as niobium or titanium which have a greater tendency to form carbides than chromium does. 2) Lowering the carbon content below 0.03 wt %. 3) to subject the material to a high-temperature heat treatment in which all the chromium carbides are redissolved and rapidly cooling the alloy in a time frame that prevents the precipitation of chromium carbides at grain boundaries [72].

1.16.3 Tensile Performance of AM 316L

The tensile data reported by Cegan et al. suggests that their HIP process reduced the yield strength of their printed parts across all of their HIP processes while also reducing the deviations between individual samples as printed [108]. The work presented by Puichard et al. agrees with the tensile data reported previously wherein their HIP process resulted in a decrease to the yield strength of their material attributed to a recrystallisation of 50 % of their grains and the removal of dendritic cells [107]. There is not significant literature investigating the effects of post production HIP treatment on the pitting performance of AM 316L in sodium chloride environments. However, Laleh et al. investigated the variation in corrosion performance in a sodium chloride environment as a result of high temperature thermal post processing via solution annealing and water quenching [112]. This study presented a decrease in pitting corrosion resistance in parts treated at temperatures of 1100 °C and 1200 °C compared to the as-built SLM-produced specimen and those heat-treated at 900 °C and 1000 °C [112]. The large error bars presented in the treated parts also suggests a large degree of variability in the pitting performance of the parts compared to their as-built control [112].

1.16.4 Fatigue Performance of AM 316L

The fatigue performance of both traditionally and AM 316L is well documented in literature. The general consensus is that additively manufactured 316L has superior low cycle fatigue strength properties than traditionally manufactured 316L [113] [114] [115] [116] [29] [117] [118]. Literature is in agreement in that the improved low cycle fatigue performance is credited to the presence of the sub granular cellular structure present within AM 316L microstructures. These sub granular cells offer effective dislocation against dislocation slip and crack initiation [116]. The boundaries between these cells

are not standard high-angle grain boundaries but are in fact reported as dislocation structures of 100–300nm in thickness. The exact size of these cells depends on the build parameters used during the manufacturing process [115]. From a fatigue perspective, grain size and dislocation networks play an influential role in determining the fatigue life, especially on the crack initiation behaviour. Cui et al investigated the cells further using post-deformation TEM observations on as-built L-PBF 316L. This revealed that the "cell structures serve as the soft barriers for the movement of dislocations during the entire fatigue process. The partials are the main carrier for plastic deformation, and their motion can be temporarily trapped, but not fully stopped by the cell walls [118]. The cell structures are stabilized by the segregated atoms and the misorientation between the adjacent cells, and their configuration is retained even if significant stress concentrations are formed at the final rupture stage. Hence, cell structures can continuously interact with dislocations, promote the formation of nano-twins, and provide a massive twin–twin, twin–dislocation, and dislocation–cell structures 3D network obstacles to the dislocation motion" [118]. It is reported that these cells are stable up to temperatures of 800–900 °C [115]. This suggests that if it is necessary to heat treat a sample with the idea of maintaining the low cycle fatigue life treating below this temperature range is required. However if the desire is to improve performance in very high cycle fatigue at lower stress regime then the aforementioned cells are detrimental. The microstructure attained from HIP treating or full annealing leads to coarse grain microstructures and increased ductility which are reported as being beneficial in high cycle fatigue testing [116][114]. Zhang et al. suggests that in the high cycle fatigue regime where the bulk deformation mode is elastic the impact of defects and microstructural heterogeneities are increased compared to the lower cycle fatigue regime [119]. They go on to state that high temperature annealing crack initiation occurs at thermally induced defects if the microstructural defects have been removed by recrystallisation and grain growth and that HIP treatments can also cause previously benign defects to be exposed [119].

Figure 1.24 presented by Lai et al. shows an SN curve generated from high cycle fatigue testing across LPBF manufactured 316L investigating the impact of machining and polishing on fatigue performance. A characteristic SN curve was produced which demonstrated that a significantly lower fatigue life was found on samples that were simply polished as opposed to machined and then polished. They also demonstrated that a stress relief heat treatment at 900 °C improved the fatigue performance of the material if tensile residual stress is present in the as-built material [120]. Treatment at this temperature is on the limit to which sub granular cells are reportedly stable in LPBF 316L [118] [104].

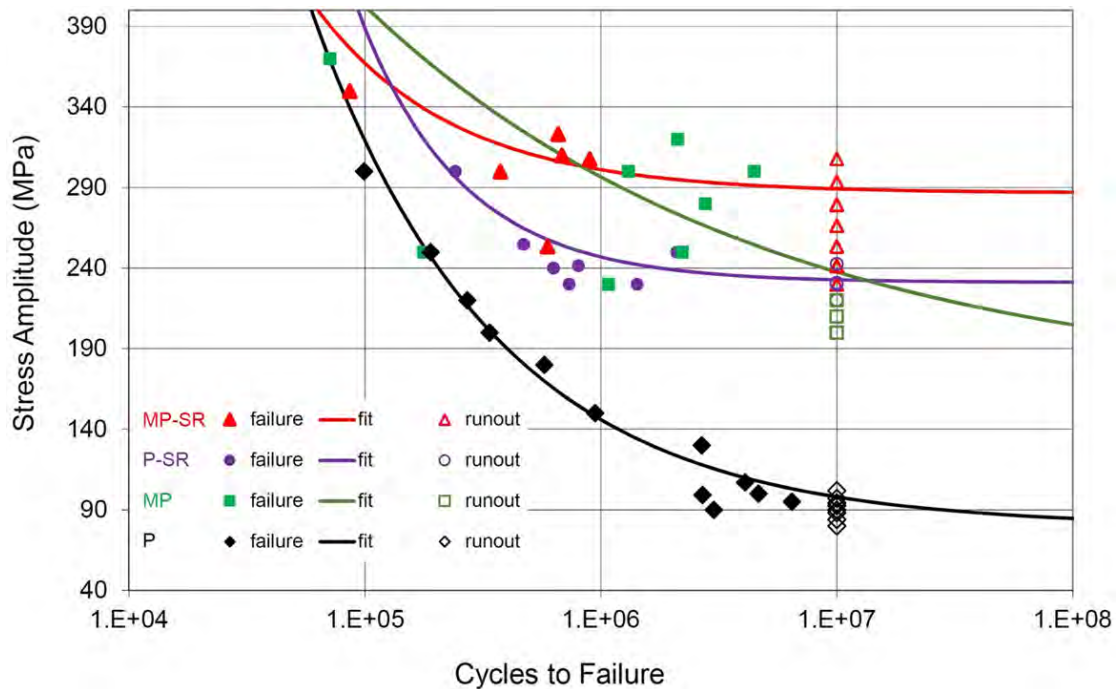


FIGURE 1.24: Fatigue S–N curves of L-PBF 316L reproduced with permission [120]

1.17 Additively Manufactured 17-4PH

1.17.1 Introduction

17-4PH is a widely used precipitation-hardening stainless steel wherein the name represents the 17% chromium and 4% copper content of the steel. The material is commonly used in environments that require wear resistance accompanied by high levels of strength and hardness including chemical and food processing plants, offshore petrochemical sites and the aerospace industry [121]. Precipitation hardenable alloys demonstrate a change in hardness, yield strength or other mechanical properties after rapid cooling from a higher treatment temperature [122]. This change in mechanical properties is brought on by a change in the materials phase matrix which is induced intentionally by the formation of specific precipitates within the material which are dependant on the elemental composition of said matrix [72]. For example solution followed by vacuum heat treating can result in a martensitic microstructure with increased hardness due to highly dispersed copper rich precipitates within the microstructure. However increasing the copper content beyond a certain threshold would result in increased values of micro-strain throughout the material and an unwanted increase in brittleness [123]. 17-4PH built by LPBF has been shown to require heat treatment to enhance its tensile strength to that of its wrought counterpart, this contrasts the behaviour of 316L wherein LPBF demonstrate superior tensile properties to their wrought counterparts without any post

processing [124]. The main body of literature on the corrosion performance of 17-4PH consists of a handful of papers, the relevant ones can be summed up as following[125]. In sodium chloride conditions the active corrosion of AM 17-4PH in 0.6M NaCl has been reported to occur as a result of crevice corrosion occurring within LoF voids [126]. Similar findings were presented at the Solid Freeform Fabrication Symposium in 2019 [101].

1.17.2 Pitting performance of additively manufactured 17-4PH

The performance of wrought and post-build heat treated, additively manufactured SS17-4PH stainless steel was investigated by Stroudt et al. [127]. 17-4PH was manufactured using two different AM machines, one using a nitrogen environment and one using an argon environment. These materials were then compared to a wrought part. The nitrogen-atomized cube was built at NIST using an EOS M270 1 LPBF system using an Yb-fiber laser, a laser power of 195 W, a laser scan speed of 800 mm/s, a laser energy density of 97.5 J/mm², an approximate powder layer thickness of 20 μ m, and a nitrogen build atmosphere. The argon-atomized cube was built at The Pennsylvania State University using similar build parameters to those used for the nitrogen sample with the exception of the nitrogen build atmosphere. The electrochemical behaviors were evaluated in three aqueous environments each containing 0.5 mol/L of chloride ions but with a varying pH (0, 3.5, 7). The authors found differences in the phases of the samples was dependent on the elemental composition of the powder used in the build process rather than the manufacturing method. The authors found that the free corrosion potential estimates made in their work have less scatter and lower values in the strongly acidic solution, this is credited to the pH affect wherein lower solution pH tends to make surface films less stable, resulting in higher overall corrosion rates. The OCP curves are not reported in the work however the data analysis is presented. The OCP recorded had a large variation in each of the samples with ranges from 0.119 - 0.501 V. This large variation is not discussed in the work however randomly distributed porosity could be a contributing factor as this would impact the surface conditions of the material. The density of the produced samples is also not mentioned in the text.

The performance under free corrosion conditions in naturally aerated solutions revealed that the free corrosion potential for the nitrogen-atomized alloy was consistently higher than that of the argon-atomized alloy in all three solutions. The differences between the argon-atomized and the wrought alloy were not statistically significant however the differences between the nitrogen-atomized and wrought compositions were statistically significant in the neutral (pH=7) and the strongly acidic solutions (pH=0), but were not in the moderately-acidic solution (pH = 3.5) [127].

Cyclic potentiodynamic scans were not carried out therefore there is no comment on repassivation potential of the materials. Potentiodynamic polarization revealed that while both the wrought and nitrogen-atomized alloys exhibit relatively similar performance over the passive range, the nitrogen-atomized alloy exhibited a higher pitting potential than both the wrought and the argon-atomized alloys in the neutral pH environment. Metastable pitting was not recorded on any of the samples in any of the solutions used. The difference in pitting potential between the argon-atomized and nitrogen-atomized compositions was on the order of 100 mV in both the neutral and moderately acidic environments. This affect however could be a result of the lower Mo and Mn contents in the argon-atomized composition. It is difficult to draw any meaningful conclusion from this work due to the variation in elemental composition of the materials used in the different manufacturing methods presented. This issue is common in AM literature wherein the elemental composition of powders is modified to increase ease of printing. Additionally, the authors state that both AM materials were manufactured using similar but not identical parameters on different machines. This adds additional uncertainty in terms of the materials thermal history variations to the work presented.

The pitting corrosion of 17-4PH manufactured by laser beam melting was compared to that of the wrought material by Barroux et al. [128]. The weight percent of chromium of the AM parts was higher than that of the wrought in this work (16.2 - 15.4), with the opposite relation for nickel (4.1 - 4.5). Parts were fabricated from 17-4PH nitrogen-atomised powder with an average diameter of 33 μm . Corrosion samples were taken from the centre of printed parts. This is worth noting as when molten porosity can diffuse outward through the metal leaving the Central regions more defect free than the outer regions of the material. The AM parts were also subject to annealing at 1040 °C for 30 minutes followed by immediate air quenching. Subsequently materials were aged at 480 °C for 1 hour, corresponding to H900 ageing. It is likely that these treatments would remove some of the exotic AM microstructure features such as melt pool boundaries and any properties resulting from it. Despite this the authors did note non-negligible differences between the wrought and AM microstructures. This included a larger proportion of the gamma phase in one orientation of the AM part. Additionally, the structure of NbC precipitates was found to differ between Am and wrought parts, in the wrought material the precipitates were coarser with an elliptic shape compared to spherical shape in the Am material. Additionally, Si-rich oxide inclusions were not detected in wrought MSS but formed during the AM production process despite the use of protective gas. Such inclusions, considered as manufacturing defects, were characterised by several authors on 316L stainless steel [128]. The martensitic lath was also found to be finer on the AM structure in comparison to the wrought material. Fine copper rich

precipitates were found in both materials, which act as facilitation sites for grain growth and result in increased hardness in 17-4PH [128].

OCP results showed similar behaviour between wrought and AM 17-4PH, given the assumed lack of porosity in the samples as a result of the heat treatments and removal of outer layer the similar behaviour of the OCP curves is not unexpected. Despite this, unlike the wrought material the AM material did not reach the steady state condition within 24 hours of immersion. However no pitting was noted on the surface of either sample after 24 hours of immersion within the 0.5 M NaCl solution. A one-hour OCP measurement was performed before either cathodic or anodic polarisation curves to reach the near steady state conditions before the polarisation. Clearly defined current density plateaus were observed on all cathodic scans. The samples all showed similar behaviour with breakdown at 0.2 - 0.3 V rel. SCE. Metastable pitting was observed on all samples, with increased frequency on wrought compared to the AM samples. However significantly higher pitting and corrosion potentials were measured for AM samples in comparison to wrought. Larger variations in corrosion and pitting potentials were noted for AM parts compared to wrought. These results suggested a better corrosion behaviour for the 17-4PH MSS manufactured by LBM than for the wrought one for the same heat treatment (H900). Variations in pitting potential were noted at different sample orientations, owing to the inhomogeneous microstructure of AM parts. This is unexpected given the heat treatments would reduce some of these orientation affects. Results showed that, independent of the forming process, the pit propagation was dependent on the microstructure. This could be associated to the lower pH at the bottom of the pits, due to the anodic reactions and subsequent hydrolysis of the cations. Such an acidic electrolyte can lead to the preferential dissolution of both the grain boundaries and the matrix surrounding the NbCs. Therefore, these observations could suggest that NbCs might act as preferential pit initiation sites [128]. Further work is needed to clarify this due to the small size of NbCs. The authors reported that lack of fusion porosity was present within the AM parts and acted as preferential pit initiation sites. However due to the low number of these sites they did not influence the pitting corrosion resistance of the material. It would be interesting for an overview of the number of porosity features present in the material to be presented by the authors in the outer surface as well as within the central regions of samples they tested. This would allow for determination if the heat treatment methods they used alleviated porosity or if it was down to the build parameters used. Unfortunately, the build parameters were not given in this work. The authors provide discussion on the differences in the nature of metastable pitting between wrought and AM materials. They postulate that if pores were preferential sites for metastable pitting to initiate those pits could grow into active pits leading to high current due differential aeration within the pore. However considering the number of stable pits formed near a

pore was very low they assume that the passive film would reform with the pore. The issue with this however is that the nature of porosity is not necessarily spherical in nature and at lack of fusion porosity if pluming is present the occluded region would not be able to repassivate. The authors continue that the passive films formed on the different samples might be slightly different and therefore might present differences in terms of stability, at least during the first stages of immersion of the samples in the electrolyte. This aligns with the results found in their work and is consistent with conclusions that could be drawn by considering the cumulative probability curves they present for the nucleation time of metastable pits. The curves show a variation in this parameter as a function of orientation as well as the materials manufacturing method. They conclude that overall a stronger evolution of passive film is formed on AM samples in compared to wrought based on their findings [128]. In conclusion the presence of pores inside the LBM samples could not be neglected and the differences in elemental composition of the wrought could contribute to the differences in corrosion behaviour noted in this work. This work is inherently interesting and thorough and presents numerous non-trivial arguments. A significant proportion of the references however point to work carried out on austenitic stainless steels, namely 304 or 316. It would be beneficial for more literature to be published and presented on 17-4PH as to discern differences between the austenitic stainless steels and 17-4PH due to their fairly significant elemental composition (copper, nickel, chromium and molybdenum specifically) and vastly different post production heat treatments.

The influence of microstructure and manganese sulfides on corrosion resistance of selective laser melted 17-4 PH in acidic chloride medium was investigated by Alnajjar et al. [129]. The AM material was studied both in the as-built condition and after a re-austenization heat treatment at 1050 °C for 1 hour followed by a water quench. The composition of the wrought and AM materials were nearly identical with marginally more nickel present in the wrought samples (4.95 - 4.16 wt %). Electrochemical testing was carried out in deionized water with 30 g /l NaCl and was deaerated with a continuous flux of nitrogen gas. The pH varied between 1.5, 2.5 and 3.5. The open circuit potential was measured for an immersion time of 5 hours and anodic scans were repeated 3 times on each specimen and at each condition. Scans were initiated from -600mV vs.SCE, slightly in the cathodic region, and continued until an anodic current of 1 mA was reached. The scan rate applied during testing was 0.1 mV/min. The wrought 17-4 PH steel was studied after a solution heat treatment at 1050 °C C for 1 hour followed by a water quench and was found to be fully martensitic with a mean grain size of 3.3 μ m. EDS measurements revealed a homogeneous distribution of elements along with the presence of MnS and NbS inclusions of approximately 1 μ m in diameter. The as built AM microstructure was found to be ferritic with a mean grain size of 9.2 μ m. The AM samples post re-austenitized had

a grain mean grain size of $2\mu\text{m}$. In contrast to the wrought steel, the microstructure of as-built AM material does not show a typical martensitic microstructure with packets and blocks. The microstructure consists mainly of coarse grains having an average grain size of $9.2\mu\text{m}$. Since the majority phase has a BCC structure, the authors suggest the material has a delta ferrite microstructure. This phenomenon was also reported by Alnajjar in previous work [130]. This ferritic microstructure is due to the high cooling and heating rates experienced during SLM which do not allow the austenite phase to be formed, as if the delta phase bypasses the austenite phase [129]. After the re-austenization heat treatment at $1050\text{ }^\circ\text{C}$ for 1 hour followed by a water quench the AM material displays a martensitic microstructure, meaning the delta ferrite to martensitic transformation occurred during cooling. The EBSD map shows, that the martensitic lathes are gathered into packets inside prior austenitic grains. For each pH, the corrosion potential for both SLM-ed steels is similar and varies between -405 and -455 mV/SCE . The general corrosion behaviour of the materials is very similar across the range of pH values tested despite the differences in microstructure of the materials. The authors credit this similar behaviour due to both materials having near identical elemental compositions [129]. There were differences in the pitting potentials however wherein the as-built AM sample demonstrated higher pitting potentials than the re-austenitized material. The authors credit this to the martensitic microstructure having a higher dislocation density and grain boundary density increasing the probability of pit initiation [129]. A similar theory was postulated by Grech et al. who investigated the corrosion performance of AM 17-4PH produced by LPBF [101]. In addition, the MnS inclusions present in the re-austenitized AM steel, which have been proven to be preferential sites for pitting, could be also the cause of the lower pitting potential. However, this assumption is questionable because, as it will be shown later, the MnS inclusions did not have any effect on the pitting potential of the wrought steel. Despite the compositions of the AM and wrought samples being near identical the increased sulfur content of the wrought material is significantly higher in this work ($0.021 - 0.008$) wt %, resulting in larger and more numerous MnS inclusions being present in the wrought material which promote the destabilisation of the passive film [112][129][97][98]. The authors continue by remarking that despite the increased MnS presence in the wrought parts that overall the pitting potentials across all materials were similar. They postulate this is due to the slow anodic scan rate used there was sufficient time for MnS inclusions to dissolve and for the material to passivate before reaching the pitting potential [129]. A possible explanation for the slightly lower pitting potential for the re-austenitized AM steel would be its higher grain boundary density, since it has smaller grains, and the presence of porosity suggesting that grain boundaries and porosity sites could be pit initiation sites [101] [104] [129].

In conclusion, higher pitting potentials were recorded in the as-built condition than the

re-austenitized one. This was associated with the higher grain boundaries and dislocation densities. The wrought steel was more corrosion resistant than the AM re-austenitized steel, with the authors crediting this to the higher grain boundary density and the presence of porosity in the martensitic re-austenitized AM material. From these conclusions it seems that the sulfur content in the wrought material contributed significantly to lower the pitting potential of the wrought part. In order to fully compare the differences between wrought and AM components it is required to maintain as constant elemental composition across materials as possible. This however is difficult due to reasons discussed repeatedly in this work.

The effects of hydrostatic pressure on the pitting corrosion of 17-4 PH martensitic stainless steel was investigated by Ma et al [131]. Samples were ground using 2000 grit SiC paper before being degreased with acetone, cleaned with distilled water and dried in compressed hot airflow. Tests were carried out in 3.5 % NaCl solutions. Before all electrochemical measurements, the specimens were initially reduced potentiostatic at -1 V for 120 s to remove the air formed oxides from the metal surface. For the polarization curve measurements, the specimens were kept in 3.5% NaCl solution until a stable corrosion potential was attained and then relative to OCP from the cathode - 0.3 V to the current density reached 1 mA/cm² at a scan rate of 0.333 mV/s. The results indicated that the pitting corrosion performance of the material increases as a function of hydrostatic pressure with the pits forming at higher pressures having larger diameters than at lower pressures. The variation in pitting potential at different pressures is stated to be as a result of the effects of hydrostatic pressure on the passive film. The growth rate of the passive film at 15 MPa is faster than that at 0.1 MPa, which means that the thickness of the passive film under high hydrostatic pressure is thicker than that at 0.1 MPa at the same time. The XPS results presented show indicate that a more stable and thicker passive film is formed at higher hydrostatic pressures [131].

1.18 Literature Review Summary

Generally literature has reported that AM parts perform better than traditional manufactured parts with regard to mechanical properties. Post processing techniques have been shown to improve some of these properties at the expense of others. Research in AM is very specific and as such some findings cannot be readily applied generally. This is also true with regards to the corrosion performance of AM parts due to the wide range of experimental setups available and the varying methods of characterising corrosion performance. It seems that literature suggests that generally materials with holes in them are more vulnerable to corrosion attack than materials without holes. Therefore

removing these holes is crucial to truly investigate the corrosion performance differences between wrought and AM parts aside from the inherent porosity present within the AM parts. There are still large areas of work yet to be carried out which will increase the knowledge of AM further and allow it to transition into industrial applications.

1.19 Aims and objectives of this work

The manufacture and mechanical properties of additively manufactured parts are significantly better understood than the corrosion behaviour of additively manufactured materials. The aims and objectives of this work were to investigate the corrosion performance of additively manufactured parts. If the behaviour of these materials differed from the traditional wrought counterparts then the reasons as to why will be investigated. This involves investigating whether the corrosion performance of the material is dependent upon the build parameters used during its manufacture or the resulting microstructure resulting from the build process. In addition to this, post production techniques that aim to improve the corrosion performance of additively manufactured materials will be investigated. The materials investigated and the reasoning behind their inclusion is given below:

- Invar: Invar is a single phase iron-nickel alloy with a low coefficient of thermal expansion. This material was investigated initially as the material is metallurgically simplistic and is suited to additive manufacturing. Ease of printing allowed for familiarity with the equipment to be obtained quickly resulting in the production of high density parts. Producing near 100 % parts would allow for insight into whether reasons apart from density could result in the corrosion performance of wrought and AM parts being different.
- 316L: Austenitic stainless steel 316L is one of the most commonly used steels in the world and there is operational experience of additively manufacturing the material. The material is used in a range of industries and its performance in corrosive aquatic environments is of great interest to the corrosion community worldwide, particularly within the gap in knowledge that exists within additively manufactured material.
- 17-4 PH: The precipitation hardened stainless steel is widely used in industry where a range of post production heat treatments are used to tailor the microstructure to a given application. This material was of interest as the complex thermal histories induced by additive manufacturing results in exotic microstructures. The material

is not easy to print and the elemental composition of the material can be modified to increase the ease of printing.

2. The additive manufacturing process

2.1 Introduction

This section details and outlines the key steps and stages that were performed with the Renishaw AM400 to produce parts for this work. The steps outlined are not all encompassing as the intricate details and extra steps are beyond the purposes of this section. An extreme example is the recommended torque to remove different types of screws found within the machine is detailed in the user manual however information such as this is omitted to preserve the sanity of the reader and the author. The author would like to highlight the importance that all of the work carried out with metallurgical powders was within all health and safety guidelines and that personnel were appropriately trained prior to beginning any work. Metallurgical powder is harmful to humans and the environment and must be contained, stored and disposed of appropriately.

2.2 Printing material

2.2.1 Planning steps

2.2.1.1 Initial steps

The quality of the feedstock used in any AM is crucial to producing high quality parts. Generally, powder should be spherical in geometry, as high purity as possible and manufactured within the atmosphere of a suitable inert gas usually nitrogen or argon. Powder should be delivered and stored in an inert gas environment.

If an optimised parameter set is not available from the machine manufacturer it is preferable to find a material of similar elemental and phase composition either from previous builds, the AM machines manufacturer or other personnel who use the AM machines. Manufacturers often test novel materials on their AM machines and will support the user in selecting build parameters for similar materials. These build parameters can be used

as a starting point for printing in the new material. The starting point parameter set is then varied by a set percentage deviation both above and below to print cuboid parts. One useful way to find an optimal parameter set for a given material is by implementing the use of an L9 orthogonal array. This method is outlined further in section 3.4.

2.2.1.2 Software steps

Typically the part that requires printing in is known prior to starting this process and CAD designs already exist. If not these CAD designs need to be produced and exported into the correct format for the AM machine being used. In this case the software package, QuantAM is used. STL files exported from CAD software are imported into QuantAM which produces an AMX file. The AMX file contains the STL information in a format that allows the user to configure the build plate and modifying build and machine parameters using QuantAM. This includes manipulating the placement of parts on the plate, adding build supports to parts to ensure they build successfully and stacking parts in the vertical plane. Once the parts have been positioned and checked the build parameters are assigned including the scan pattern strategy and layer thickness. When the build parameter changes have been confirmed the file can be exported into an MTT file that the AM machine is able to interpret to commence the build.

2.2.2 Feed stock material change over

Once the feed stock powder has arrived, been added to the database and stored correctly the AM machine can be prepared for the new powder to be added. The previous feed stock is be removed from the AM400, sieved under an inert gas and then stored appropriately. The machine is then disassembled somewhat with the main hopper, feed stock removal pipes, the doser, gas filters and other parts removed for deep cleaning. Components must then be cleaned thoroughly such that there is no trace of the previous feed stock material and there is no cross-contamination. This includes careful cleaning of the delicate laser lens. The powder sieve and any other machines that have come in contact with metallurgical powder must also be fully disassembled and cleaned thoroughly. Some parts within certain machines such as the filters within the sieve are material specific and must be stored and kept separate for each feed stock material used. Once the cleaning process has been completed and machines have been reassembled the new feed stock material can be loaded into the machine. Powder is typically delivered in 10kg tubs and the maximum capacity of the main hopper is approximately 150kg for 316L but varies by material.

2.2.3 Build preparation

At this stage the AM machine should be fully clean with the feed stock powder fully loaded and additional powder handling machinery should be clean and ready for operation. An appropriate material build plate is selected and the thickness of the plate measured either side of each corner of the plate. The plate is then loaded into the machine and the thickness of the plate is entered into the AM machine (assuming an equal thickness across the plate). Once the build plate is inserted a fresh wiper blade is fitted and adjusted to run smoothly across the surface of the plate. The build chamber is then sealed and pumped to low vacuum pressure whilst the heat soaking procedure is started. During the heat soak the build plate will move sequentially through the build chamber to ensure there are no obstacles or mechanical motor driver issues.

At this stage the build file can be selected and the build process can begin. Whilst the build is proceeding it is important to regularly check on the machine to ensure there are no errors and the build is progressing correctly. The powder level of the machine is monitored as the build progresses. The overflow powder is blown by the argon gas flow into the overflow vessels. These vessels must also be monitored to ensure they do not overflow. When they are nearing capacity vessels must be emptied and powder sieved before being returning the vessels to the machine. The material that is being sieved under argon can then be re-loaded into the main hopper whilst the AM machine is building. This ensures that feed stock powder levels are maintained to complete the build. The volume of powder needed per build is largely dependent on the height of the printed parts. It is possible to run multiple full plate builds without sieving but it is best practise to continuously sieve powder to prevent a backlog and overflowing of the overflow vessels.

2.2.4 Build completion and removal

Once cooled, left over powder in the build chamber is processed into the overflow vessels. The glove box on the front of the machine is then used to brush any leftover powder into the overflow chute. Once the vast majority of the powder has been recycled into the overflow chute the build plate can be removed. Additional vacuuming is required to remove any loose bits of powder still remaining on the build plate. At this stage the build has been fully removed and the system is ready to be cleaned for the next build.

3. Experimental methods

3.1 Introduction

This chapter describes and illustrates all of the experimental techniques that were used throughout the scope of this work. Detailed content is provided for techniques used frequently throughout this work as well as for niche techniques not used commonly. More widely used techniques such as optical and electron microscopy are not discussed in detail as there is a plethora of information on these techniques available in literature and online.

3.2 The additive manufacturing process

This section details and outlines the key steps and stages that were performed with the Renishaw AM400 to produce parts for this work. The steps outlined are not all encompassing as the intricate details and extra steps are beyond the purposes of this section. An extreme example is the recommended torque to remove different types of screws found within the machine is detailed in the user manual however information such as this is omitted to preserve the sanity of the reader and the author. The author would like to highlight the importance that all of the work carried out with metallurgical powders was within all health and safety guidelines and that personnel were appropriately trained prior to beginning any work. Metallurgical powder is harmful to humans and the environment and must be contained, stored and disposed of appropriately.

3.2.1 Planning steps

3.2.1.1 Initial steps

The quality of the feedstock used in any AM is crucial to producing high quality parts. Generally, powder should be spherical in geometry, as high purity as possible and manufactured within the atmosphere of a suitable inert gas usually nitrogen or argon. Powder should be delivered and stored in an inert gas environment.

If an optimised parameter set is not available from the machine manufacturer it is preferable to find a material of similar elemental and phase composition either from previous builds, the AM machines manufacturer or other personnel who use the AM machines. Manufacturers often test novel materials on their AM machines and will support the user in selecting build parameters for similar materials. These build parameters can be used as a starting point for printing in the new material. The starting point parameter set is then varied by a set percentage deviation both above and below to print cuboid parts. One useful way to find an optimal parameter set for a given material is by implementing the use of an L9 orthogonal array. This method is outlined further in section 3.4.

3.2.1.2 Software steps

Typically the part that requires printing in is known prior to starting this process and CAD designs already exist. If not these CAD designs need to be produced and exported into the correct format for the AM machine being used. In this case the software package, QuantAM is used. STL files exported from CAD software are imported into QuantAM which produces an AMX file. The AMX file contains the STL information in a format that allows the user to configure the build plate and modifying build and machine parameters using QuantAM. This includes manipulating the placement of parts on the plate, adding build supports to parts to ensure they build successfully and stacking parts in the vertical plane. Once the parts have been positioned and checked the build parameters are assigned including the scan pattern strategy and layer thickness. When the build parameter changes have been confirmed the file can be exported into an MTT file that the AM machine is able to interpret to commence the build.

3.2.2 Feed stock material change over

Once the feed stock powder has arrived, been added to the database and stored correctly the AM machine can be prepared for the new powder to be added. The previous feed

stock is removed from the AM400, sieved under an inert gas and then stored appropriately. The machine is then disassembled somewhat with the main hopper, feed stock removal pipes, the doser, gas filters and other parts removed for deep cleaning. Components must then be cleaned thoroughly such that there is no trace of the previous feed stock material and there is no cross-contamination. This includes careful cleaning of the delicate laser lens. The powder sieve and any other machines that have come in contact with metallurgical powder must also be fully disassembled and cleaned thoroughly. Some parts within certain machines such as the filters within the sieve are material specific and must be stored and kept separate for each feed stock material used. Once the cleaning process has been completed and machines have been reassembled the new feed stock material can be loaded into the machine. Powder is typically delivered in 10kg tubs and the maximum capacity of the main hopper is approximately 150kg for 316L but varies by material.

3.2.3 Build preparation

At this stage the AM machine should be fully clean with the feed stock powder fully loaded and additional powder handling machinery should be clean and ready for operation. An appropriate material build plate is selected and the thickness of the plate measured either side of each corner of the plate. The plate is then loaded into the machine and the thickness of the plate is entered into the AM machine (assuming an equal thickness across the plate). Once the build plate is inserted a fresh wiper blade is fitted and adjusted to run smoothly across the surface of the plate. The build chamber is then sealed and pumped to low vacuum pressure whilst the heat soaking procedure is started. During the heat soak the build plate will move sequentially through the build chamber to ensure there are no obstacles or mechanical motor driver issues.

At this stage the build file can be selected and the build process can begin. Whilst the build is proceeding it is important to regularly check on the machine to ensure there are no errors and the build is progressing correctly. The powder level of the machine is monitored as the build progresses. The overflow powder is blown by the argon gas flow into the overflow vessels. These vessels must also be monitored to ensure they do not overflow. When they are nearing capacity vessels must be emptied and powder sieved before being returning the vessels to the machine. The material that is being sieved under argon can then be re-loaded into the main hopper whilst the AM machine is building. This ensures that feed stock powder levels are maintained to complete the build. The volume of powder needed per build is largely dependent on the height of the printed parts. It is possible to run multiple full plate builds without sieving but it is best

practise to continuously sieve powder to prevent a backlog and overflowing of the overflow vessels.

3.2.4 Build completion and removal

Once cooled, left over powder in the build chamber is processed into the overflow vessels. The glove box on the front of the machine is then used to brush any leftover powder into the overflow chute. Once the vast majority of the powder has been recycled into the overflow chute the build plate can be removed. Additional vacuuming is required to remove any loose bits of powder still remaining on the build plate. At this stage the build has been fully removed and the system is ready to be cleaned for the next build.

3.3 Renishaw 400

Figure 3.1 is a simplified internal diagram of the Renishaw 400 system. The section labelled A represents the laser source, B the powder source/doser, C the rubber wiper that spreads the powder across the build plate. The region labelled D represents the build plate, with the dotted region representing the next layer that will be printed once the build plate has moved down. The rectangle labelled E represents a previously printed layer which has been lowered to allow the subsequent layer to be printed. The laser source for this system is a single 400W laser whose beam is focused using a convex lens. The build chamber is pumped to obtain an inert atmosphere that prevents the laser from acting as an ignition point for the highly pyrophoric powder [132]. This atmosphere is maintained by a pumping system wherein the argon gas is recirculated throughout the system, once the gas leaves the build chamber it passes through a filter system before returning to the build chamber. The pumping system allows for condensate (small metal nano-particles formed when an evaporated melt pool suddenly condenses in cold gas) to be removed. Additionally the atmosphere prevents the powder from oxidising while also stopping oxide forming at the level of the melt pool which could embrittle the build [132].

3.4 L9 orthogonal arrays

The L9 orthogonal array method is used commonly in experimental design to optimise the performance of a given characteristic of a process and is based on the theory of factorial designs. The process uses a matrix whose columns have the property that in every pair of columns each of the possible ordered pairs of elements appears the same number of times

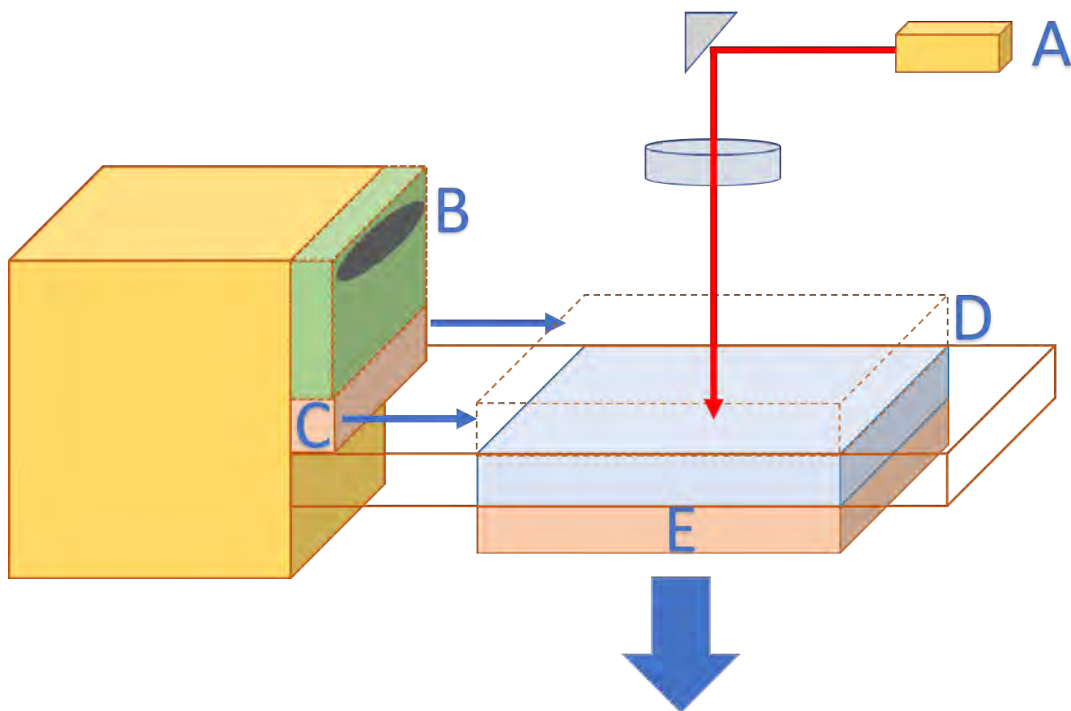


FIGURE 3.1: Internal diagram of Renishaw 400 (not completely to scale)

[133]. The method allows for parameter optimisation without carrying out experiments using every possible combination of parameters. In this work this method provided a systematic and efficient method to study the effects of varying build parameters on the density of AM components. Build parameters were varied around a mid point which was selected for each of the build parameters based on either the machine manufacturers guidance or knowledge from manufacturing on similar materials. An example of an L9 orthogonal array is provided in table 3.1. Parameters 1,2 and 3 could be exposure time, hatch spacing and laser power. The 1,2 and 3 values given within the table themselves represent low, medium and high values for each of those parameters.

3.5 Taguchi Analysis

Taguchi methods were carried out on the data obtained in chapter 6 in order to elucidate the impact of varying temperature and pressure on the mechanical and corrosion properties of AM 316L treated using a range of HIP treatments. The particular method used in this work is trivial and involved comparing the mean values recorded for each setpoint in both the temperature and the pressure setpoints used in the HIP treatment. Plotting the mean values obtained at each set point with respect to the set point for both temperature and pressure allows for variations associated with either temperature

Test number	Parameter 1	Parameter 2	Parameter 3
1	1	1	3
2	1	2	2
3	1	3	1
4	2	1	2
5	2	2	1
6	2	3	3
7	3	1	1
8	3	2	3
9	3	3	2

TABLE 3.1: Table showing an example of an L9 orthogonal array experimental design

or pressure to be visually evident. This common method is explained in more detail in literature [133] [134] [135].

3.6 Time lapse microscopy

Swansea University have pioneered an in-situ imaging technique that allows for time-lapse images as corrosion takes place [136]. The equipment setup is intentionally minimalistic and consists of a standard optical microscope with the lens surrounded by a protective shroud. The lens can then be lowered into an electrolyte as displayed in figure 3.2. Images are captured at set intervals and are spliced together to produce videos. This technique is extremely useful as it allows for corrosion to be visually observed and for regions susceptible to corrosion to be identified. This information can then be used to fine tune materials microstructures to maximise corrosion resistance.

3.7 Scanning Vibrating Electrode Technique (SVET)

An SVET apparatus diagram is displayed in figure 3.3. The microtip is controlled mechanically by a tri-axial micro-manipulator platform and an oscillator and amplifier are used to drive the probe. A detector is used to measure and amplify the signal recorded by the probe. The microtip itself is a key component of the apparatus. The electrical impedance of the microtip electrode exerts a considerable influence on the levels of electrical noise picked up from the environment [138]. A high impedance microtip will exhibit inherently high noise characteristics which will limit the overall SVET sensitivity

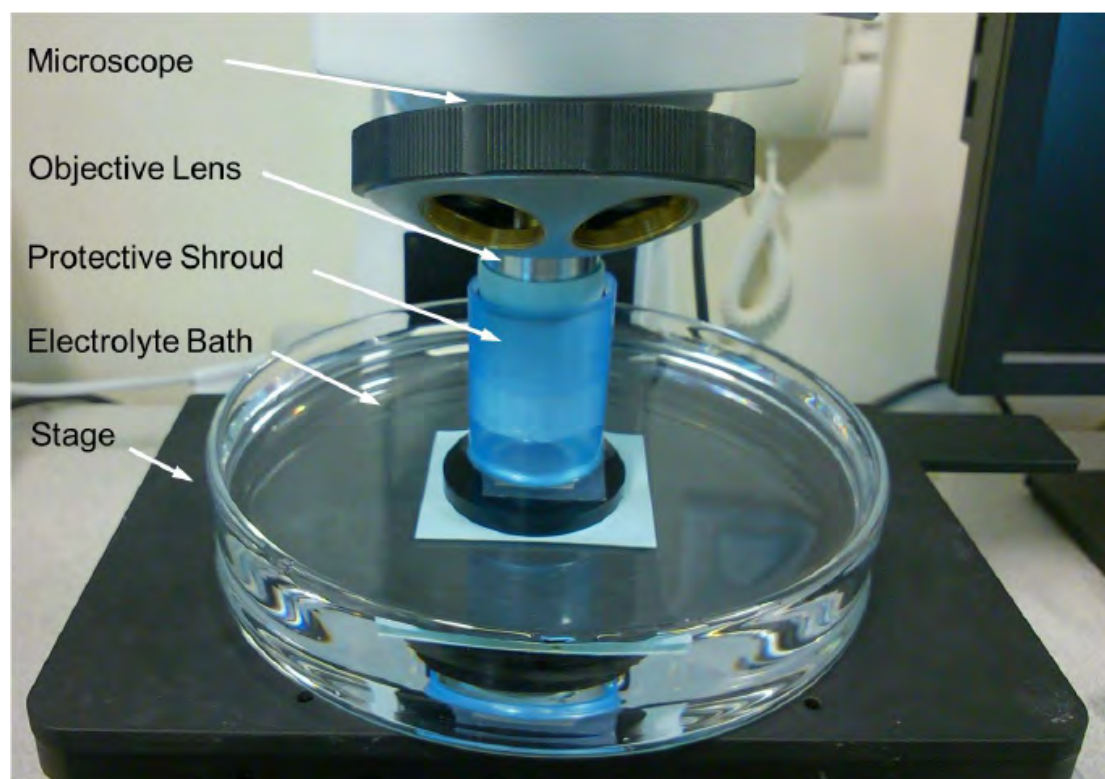


FIGURE 3.2: In-situ optical microscope [137]

[138]. Metal microdisc electrodes are the most widely used SVET microtips as they can be miniaturised relatively easily and can be coated with colloidal metal. This increases the electrochemical surface area and reduces the microtip impedance. The spatial resolution of the SVET technique is inversely proportional to the distance between the microtip and the sample which is logical and given by equation 3.1.

$$whm = 1.533z \quad (3.1)$$

where whm is the width half maximum (effectively the resolution) and z is the distance between the microtip and the sample surface. A lock-in amplifier is used to select the desired signal using electronic frequency filters and phase sensitive synchronous detection, this allows for very weak signals to be detected and reduces noise from unwanted frequencies [138].

The SVET technique uses a piezoelectric driver to mechanically vibrate the microtip electrode at a constant amplitude and frequency in the vertical plane [138]. As it vibrates, the SVET microtip electrode registers an alternating potential at the vibration frequency that is proportional to the electric field strength in the direction of vibration (vertical plane) [138]. For a corrosion experiment the sample will be immersed within an electrolyte solution. This alternating potential arises from the oscillation of the microtip in

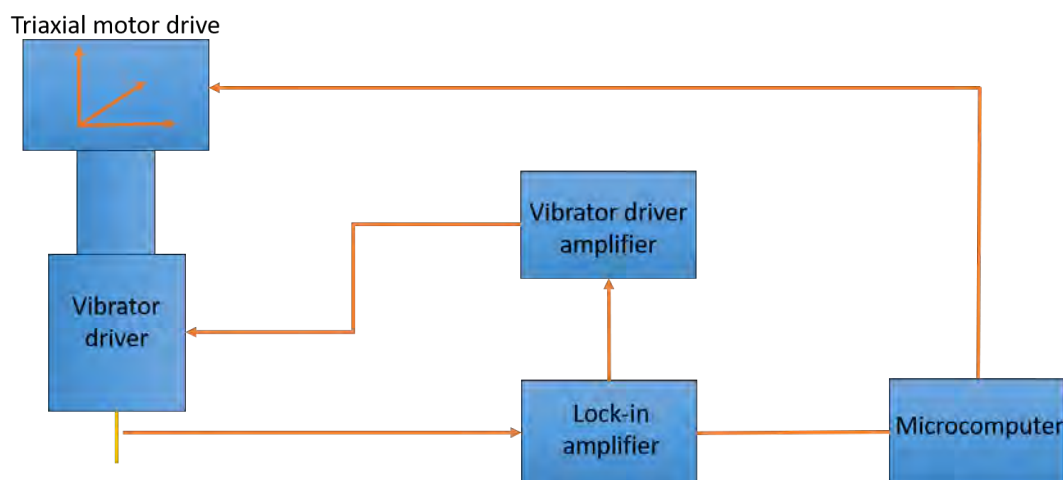


FIGURE 3.3: Apparatus diagram for SVET measurements

the potential field which is generated ohmically by the ionic current flux passing through the electrolyte solution. The recorded SVET signal is therefore directly proportional to the component of the ionic current density in the direction of probe vibration (vertical plane)[138]. The SVET will then make individual measurements in a raster scan fashion across the entirety of the sample producing a 2-d array full of measurements at specific points. These individual data points are then knitted together using custom-made software which produces a map of the tested sample with the anodic and cathodic regions identified as well as the individual “intensities” of each region as displayed in figure 3.4. The SVET was calibrated prior to each use using a two compartment tube cell wherein a known current is passed through a known cross sectional area. The vibrating microtip is lowered into a cylinder of known diameter in which there is a flux of ionic current. The probe is then moved in the z direction to until a stable signal is recorded. At this stage the the lock-in amplifier is auto-phased; such that the speaker and amplifier are synchronised. The reference electrode is then placed within the perspex tank. A nanogalvanostat supplies a user selected current between two Pt electrodes; one of which is within a perspex beaker, the other is connected to the outside of this. As the two electrodes are separated by a significant distance, the only route for current flux is through the vertical tube. Assuming that the current flux is constant across the tube of known diameter and parallel to the motion of the tip in the z direction, a current density can be obtained. Taking the gradient of a plot of the supplied current and the corresponding SVET detection signal a calibration factor is obtained. This calibration factor must then be combined with the raw data produced by the SVET measurement.

To resolve local point current sources a constant probe height above the sample must be maintained throughout scanning. For ground and level polished samples as used throughout this work the most appropriate method was deemed to be the interpolation

the height between corner points on rectangular surfaces. Simply put the probe was manually lowered at each corner of the sample to the surface.

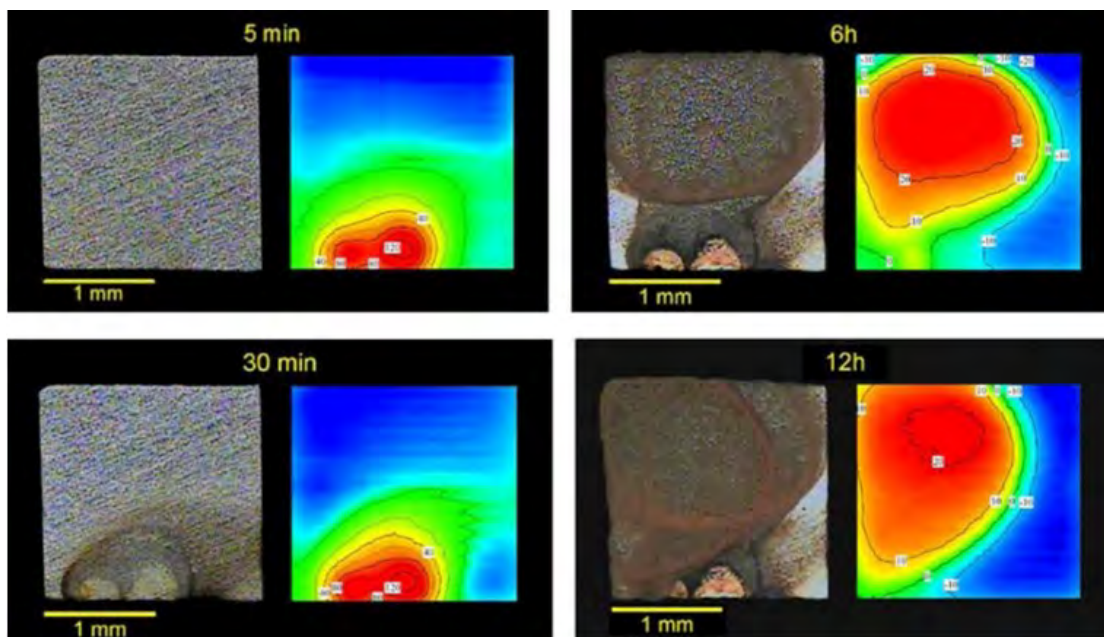


FIGURE 3.4: Example of an SVET measurement on a corroding mild-steel sample [139]

Further to this the data from an SVET measurement can be processed to produce a 3-d plot with the intensity of anodic and cathodic regions represented by peaks and troughs respectively, an example of this is figure 3.5.

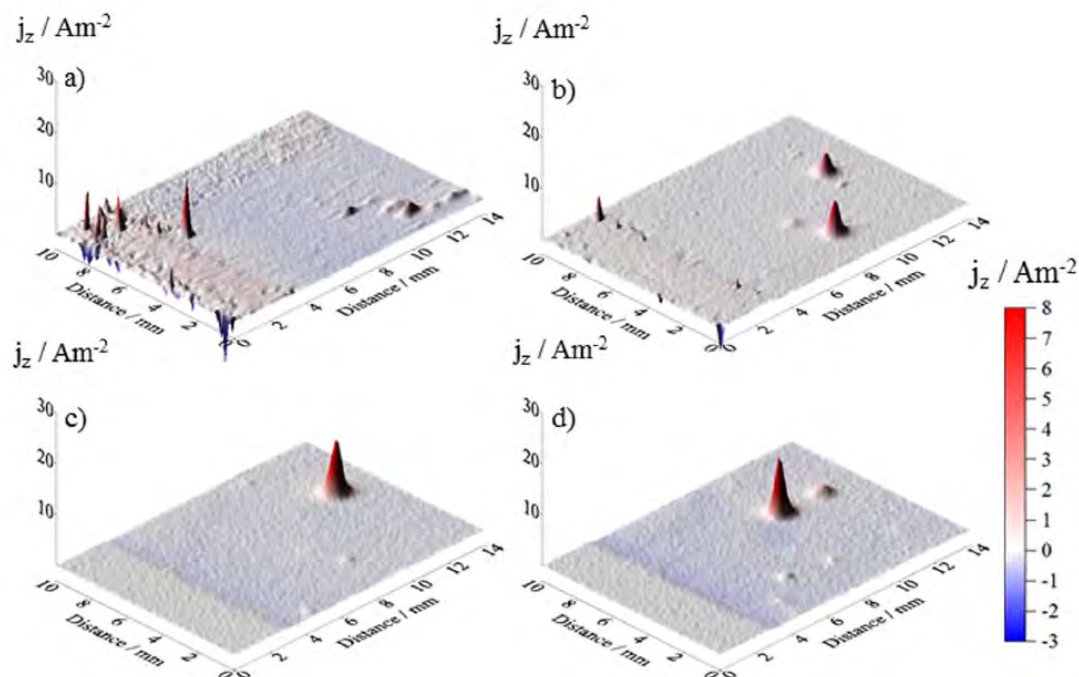


FIGURE 3.5: 3-d data produced from SVET measurements [140]

3.8 Potentiostat experiments

Potentiostat based experiments were carried out using a combination of Solatron 1287A and 1281 and Gamry 12070 and 600+. The specific make and model was kept consistent across any given material. Unless stated otherwise measurements were carried out using a standard three electrode setup as detailed in figures 3.6 and 3.7 [63]. Wherein a saturated calomel electrode was used as the reference electrode and a platinum plated electrode as the counter. The reference electrode is placed as close to the working electrode as possible. Conversely the counter electrode is placed as far away from the working electrode within the confines of the system. For deaerated experiments the test beaker was sealed using parafilm and the solution was deaerated by purging with nitrogen gas for 15 minutes. Once purging was complete nitrogen was slowly pumped into the atmosphere of the test throughout the experiment. Unless stated otherwise the flow of nitrogen did not perturb the surface of the solution and the electrolyte was not stirred during testing. The electrolyte used in potentiodynamic work in this thesis was 3.5 % NaCl, which was prepared freshly either the day prior or the day of testing using analytical grade chemicals and deionised water.

3.8.1 OCP recording

Recording the OCP of materials was carried out using a standard three electrode setup as these measurements would take place prior to potentiodynamic scanning. The OCP was recorded for 15 minutes before initiating potentiodynamic scanning.

3.8.2 Potentiodynamic scanning

Whilst the start, end and reverse current points of the scan were varied across materials and samples the scan rate was kept at a constant of $0.16667 \text{ mV s}^{-1}$ (10 mV min^{-1}). In general however scans were started at a potential below the OCP upwards to a set potential before reversing the scan direction and returning the potential to the initial value. The point at which the applied potential is reversed can be set at a fixed potential or whenever a desired current density is recorded [63]. Whilst there is an ASTM standard current density turnaround value after carrying out a number of experiments it becomes clear that the value is not constant across materials. For example to investigate pitting mechanisms on stainless steels there must be sufficient current density to allow for active pitting to occur. However this current density will not be suitable to investigate a less corrosion resistant alloy. For cyclic potentiodynamic testing on 17-4PH and 316L scans was started at their respective OCP values $-0.1V$. The turning point was set as at

$10^{-3}(\text{Acm}^{-2})$. This turning point was chosen based on preliminary experiments carried out on 316L and parameters taken from literature. Understanding and interpreting the resulting potentiodynamic scans is non-trivial and is outlined in section 1.13.1.

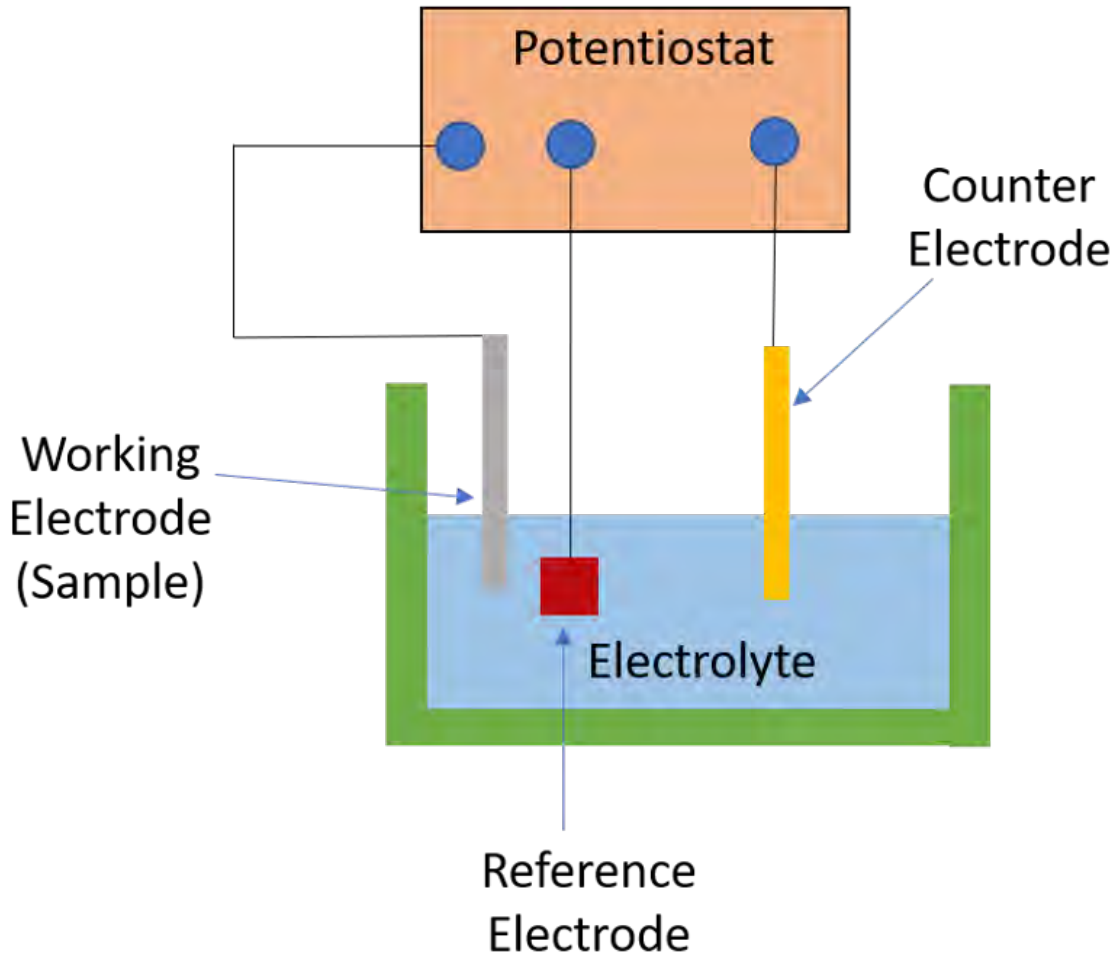


FIGURE 3.6: Three electrode aerated potentiodynamic setup

3.8.3 Potentiolapse

This technique is a fusion of time lapse microscopy and potentiodynamic testing. The setup is a combination of the setups displayed in figures 3.2 and 3.6. This configuration facilitates the visual monitoring of the breakdown of more corrosion resistant alloys whilst simultaneously producing electrochemical data. The video and data outputs can be used to great effect as visual aids in presentations.

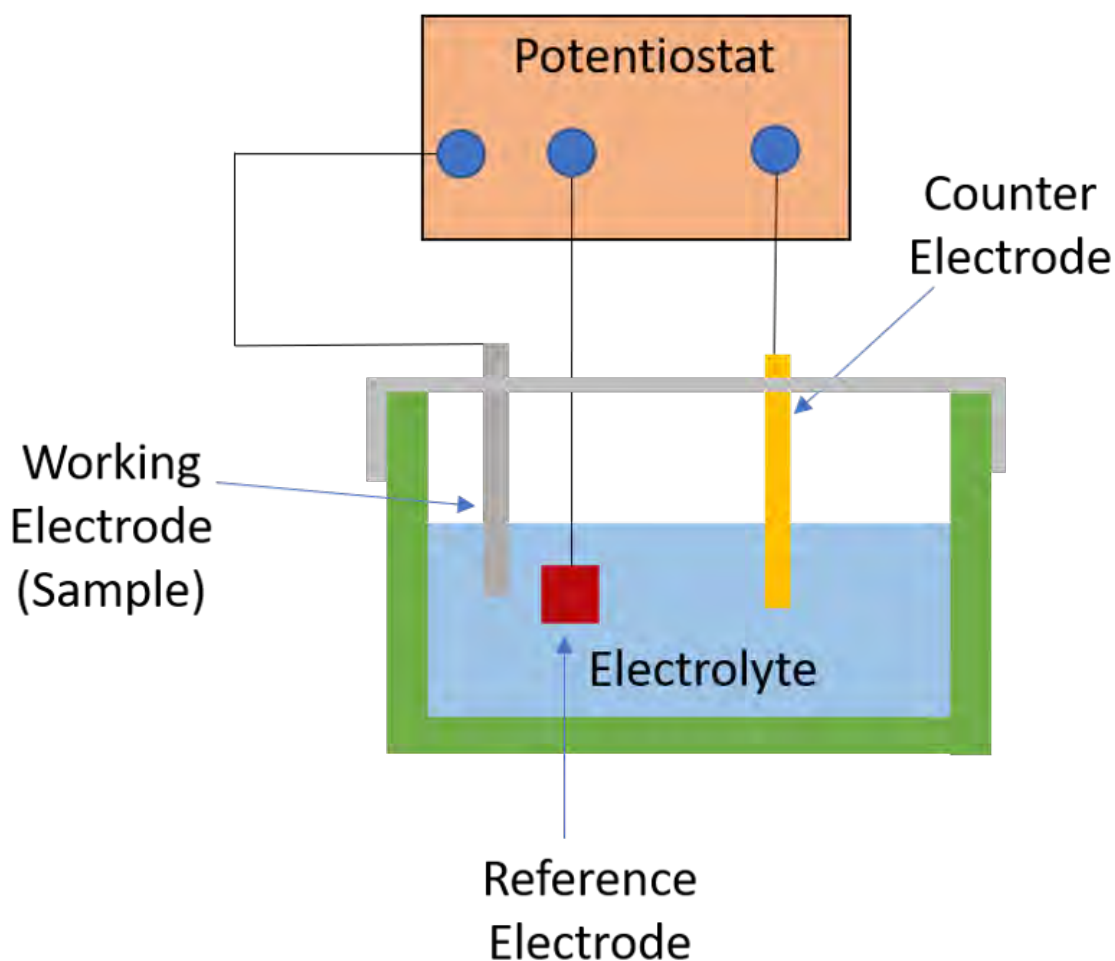


FIGURE 3.7: Three electrode deaerated potentiodynamic setup

3.9 Etching

Across this work a variety of etching techniques were trialled for each material. For immersion etching the method involved using a set concentration and then immersing the samples within the etchant for five second increments whilst driving and observing the sample under a microscope at each interval. The reason for the short time increment is that it ensures that the ideal etching time is not missed. Electrolytic etching involves the added variable of the potential difference driving force through the etching solution and subsequently the current density going through the sample that is dependent on the surface area of the sample as well as the distance of the sample edge from the mounting compound edge. To make the process repeatable it is necessary to produce samples of the same dimension, mounted directly in the centre of the same volume of conductive mounting compound each time. Ultimately despite best efforts it is not possible to replicate methods identically each time and a degree of common sense is required when etching. The recipes best favoured and used in this work are displayed in table 3.2.

Material	Etchant	Method
Invar	Kallings 2	Immersion or swab for 20 - 40 s Very easy to over etch, dilute kallings with water if necessary
316L	70 % Nitric acid Electrolytic 1 minute at 10V	Grains appear suddenly close to 1 minute for AM parts, ~90 seconds for wrought

TABLE 3.2: Etching details

3.10 Density measurements

Measurements were carried out using One Attension force tensiometer that employs the Archimedes principle to calculate the density of printed parts. It is important when carrying out these measurements to ensure the temperature of the water and the room due not vary significantly due to the density of air and water being dependent on their respective temperatures, if only to ensure additional time isn't needed due to slightly varying densities when analysing the data. Samples are printed into cube shapes with a notch allowing for easy attachment to the tensiometer hook. Cubes can be directly attached to the hook or some light string or floss can be used as long as the mass of the floss is accounted for. Beneath the hook a beaker containing a known volume of distilled water is placed on the platform. The tensiometer is then programmed to increase the height of the platform at a select velocity until the entirety of the cube is submerged within the water held by the beaker. The mass of the cube is recorded initially whilst dry and when fully submerged. The mass of the dry and soaked cube can then be input into the following basic equation:

$$\rho = \frac{(m_{air}\rho_w)}{(m_s - m_{sup})} \quad (3.2)$$

Where ρ is the density of the part, m_{air} is the mass of the part in air, ρ_w is the density of water used, m_s is the mass of the submerged sample, m_{sup} is the mass of the string or support used to submerge the sample. The recommendation of this equation and the method is outlined in ASTM B962- 08 [141].

3.11 Porosity analysis

Analysing the size and morphology of porosity withing an AM material can give an insight into whether the build parameters selected are appropriate in addition to simply measuring the overall density of the sample. To carry out optical porosity analysis samples are cut, mounted, ground and polished to a $1\mu m$ finish. Optical images are then

captured of the sample surfaces at magnifications in the region of x50– x200 and then stitched together to cover the entire surface of the sample. A custom made macro was made which would use the ImageJ software pack that would return the requested parameters including, number or porosity points, mean porosity point area, the circularity of each porosity point etc. The macro would also allow for this data to be exported and saved as either a .csv or .txt file at the preference of the user. Figure 3.8 displays a flow chart which summarises the process.

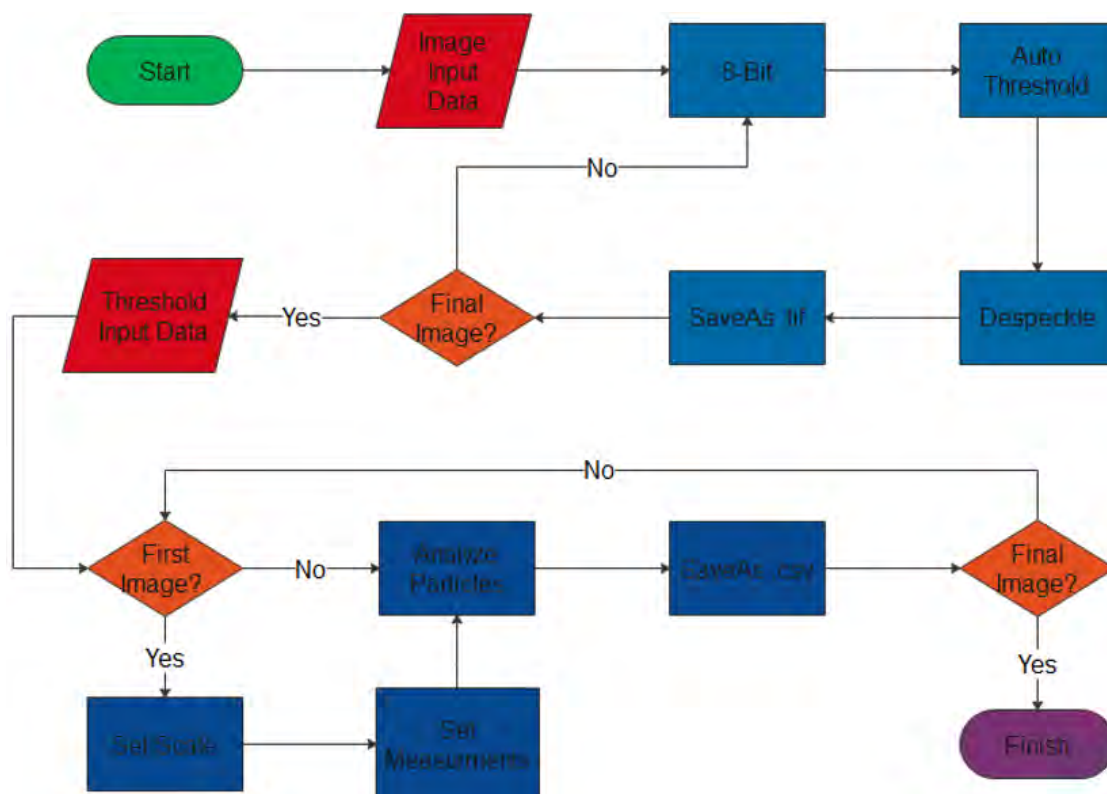


FIGURE 3.8: Flow chart showing porosity analysis macro steps

3.12 X-ray diffraction

XRD measurements were carried out on flat, mounted samples polished to a $1\mu\text{m}$ finish. Scanning was carried out using a BRUKER D8 DISCOVER XRD equipped with a Lynxeye 1D detector using a standard copper K-alpha source. A slit width of 0.3mm with a 2mm collimator was used. The angle scanned through was varied based on the material being investigated.

3.13 CT Scanning

Samples were machined into rectangles of 10mm length with a base of side length 3mm and were scanned using a ZEISS XRADIA 520 VERSA XRM with a voxel size of $1\mu\text{m}$. The process for converting the as-received .txm files into final images is outlined in Figure 3.9. The process as outlined also allows for porosity morphology's to be determined. The three initial steps given in the top row refer to the physical processes required to manufacture and then CT scan samples. The second row refer to the steps required to convert the raw data outputted from the CT scanner into a sequence of images which can be used for data extraction. This includes converting the image to the correct format whilst maintaining the scale of each image. The images can then be made binary and thresholded resulting in an image comprised of fully white and fully black regions only. The third row and steps in gold represent the data analysis processes. Analysing particles is a script that is run within ImageJ software which performs a set of measurements on either fully black or fully white regions of each image. This data can then be exported and the data analysed using a range of software. The step referred to as "Apply fiddle" highlights one of the shortcomings of the method implored to calculate porosity data wherein the thresholding of the image and the filtering of data is subjective to the user carrying out the work. Due to the total CT scan area encompassing the entirety of the cuboidal CT slices there should not be any issues with clipping at the edge of the samples. This also allows for the samples outer surface roughness to be visible on the final images.

Figure 3.10 demonstrates the region on the sample where the sample was machined to produce the cuboidal shaped sample for CT scanning. The centre image in figure 3.10 shows an imported raw .txm file. The hyperstack plugin for ImageJ then allows the user to modify defined layers or the entire stack of files included in the .txm file. After completing image thresholding and cropping to remove unwanted scan regions each layer within the stack resembles that shown in the right image of figure 3.10. It is then possible using software such as 3D slicer to export the finished 3d image as a range of files including an STL. The free software Slicer available at <https://www.slicer.org/> was also used to export images and STL files from the CT scan data.

3.14 Hot Isostatic Pressing

Hot isostatic pressing treatments were carried out using an AMERICAN ISOSTATIC PRESSES AIP 10-30H, with a 150mm diameter x 300mm long hot zone using a molybdenum furnace. The HIP was run under argon gas and a temperature ramp rate of 2.5 K

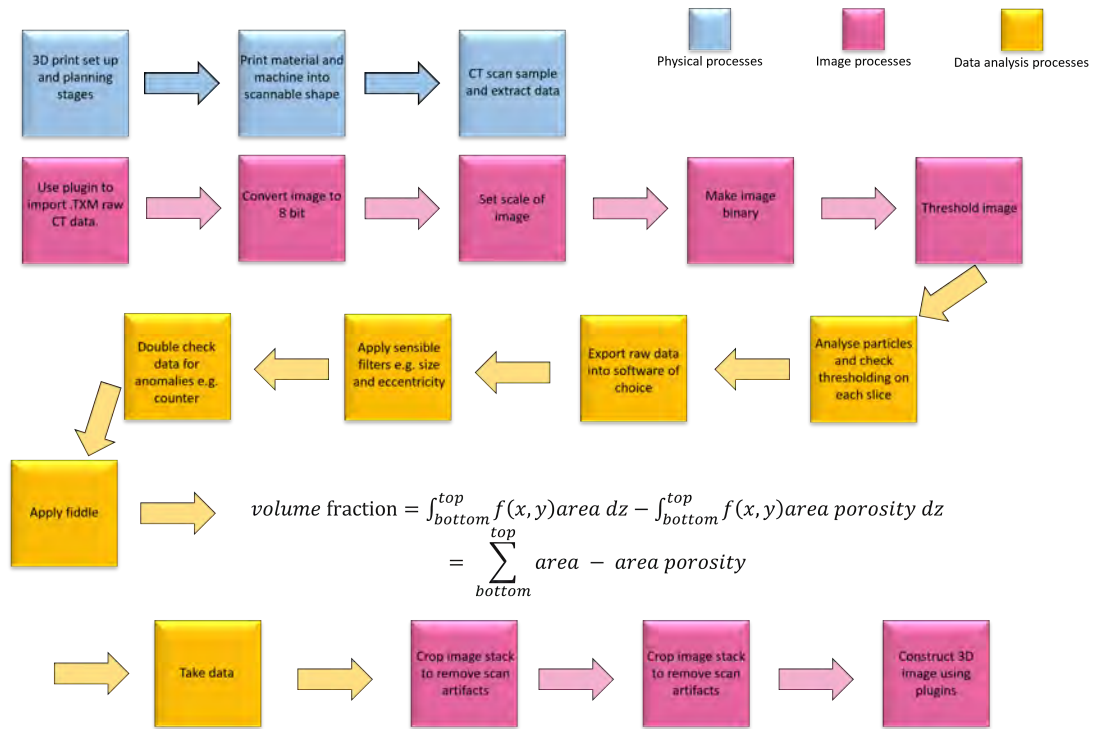


FIGURE 3.9: Flow chart outlining CT scanning process

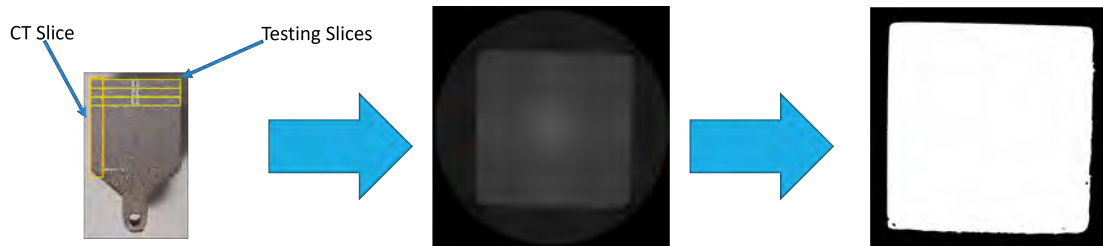


FIGURE 3.10: Images showing the CT image recreation process

per minute was used with a 4 hour hold once the temperature and pressure setpoint were reached. The programme running the HIP was set up in a way such that allowed for the pressure and temperature set points to be reached at the same time during treatment cycles. In order to hold the parts in the HIP chamber a custom made 99.5 % alumina oxide (Al_2O_3) sample holder as shown in figure 3.11 was designed and created to hold each part vertically upright. The areas of the parts that were contained within the sample holder were removed via machining. The stand allowed for 1 cube, 3 tensile specimens and 2 cylinders to be treated in one HIP cycle. The HIP cycle temperature ramp and cooling rate was 2.5 K/minute and the hold time was 4 hours. The HIP cycles were assigned a low, medium and high parameter for both temperature and pressure as well as a long hold cycle held for 60 hours. One condition, 12 - HIP (T700 P200 - quench) comprised of treatment 7 - HIP (T700 P200) followed by a subsequent furnace treatment and water quench. The additional furnace treatment comprised of placing the set of parts in a pre-heated argon filled furnace at 1125 °C for 2 hours followed by immediate water

quenching to room temperature. The temperature points chosen for the HIP cycles were 50 % (700°C), 80 % (1125 °C) and 85 % (1200 °C) of the melting point of 316L with the aim of medium and high points being either side of the phase transition line between the gamma and gamma + delta regions in the material's phase diagram. Throughout this article conditions have been labelled as # - HIP (Tx Py) - A wherein # represents the condition number, x and y represent the HIP treatment temperature (°C) and pressure (MPa) and A represents any additional notes (long hold and quench condition).

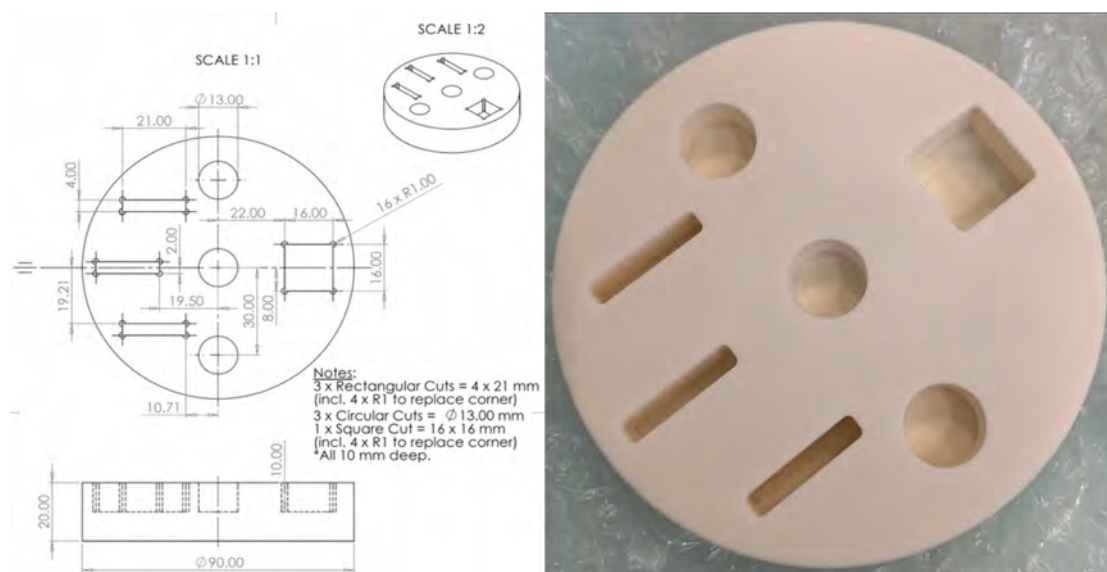


FIGURE 3.11: Engineering drawing and final alumina sample holder for HIP treating, note 1:1 and 1:2 scale not accurate.

3.15 Hardness testing

Hardness testing was carried out using a Wilson VH3300 hardness tester equipped with a diamond tip. Hardness measurements are performed on flat polished samples surfaces. The machine is frequently calibrated using calibration samples to minimise any measurement uncertainty by ensuring the accuracy of test equipment is within the tolerances of the manufacturer. The probe applies a user defined amount of force which penetrates through the surface into the sample for a set period of time. The hardness of the sample surface is related to the depth that the probe penetrates. The probe penetration depth is calculated using the built in varifocal microscope and a corresponding hardness value is reported. The machine can be set up to perform multiple measurements in various patterns to measure at various locations across the sample surface. In this work multiple lines of 25 indents were carried out with a spacing of 0.4 mm and a force of 9.81N on each sample in various directions.

3.16 Tensile testing

Tensile testing was carried out using a Tinius Olsen H25KS with a 25k N load cell and a Tinius Olsen optical non-contact video extensometer. The video extensometer is calibrated at a set distance and numerous lines are fitted across the tensile specimen. As tensile specimens are pulled apart the extensometer tracks the fitted lines and an elongation across the sample is measured. This method also allows for slow motion video of the tensile testing to be recorded. The dimensions of the sample correspond to subsize samples as displayed in figure 3.12a with experimentation being carried out following the processes and guidelines laid out in ASTM /E8M - 13a [142]. The initial speed used in the elastic region was 0.47 mm/minute and the speed to break was 12.61 mm/minute which gives the required strain rate for the specimen.

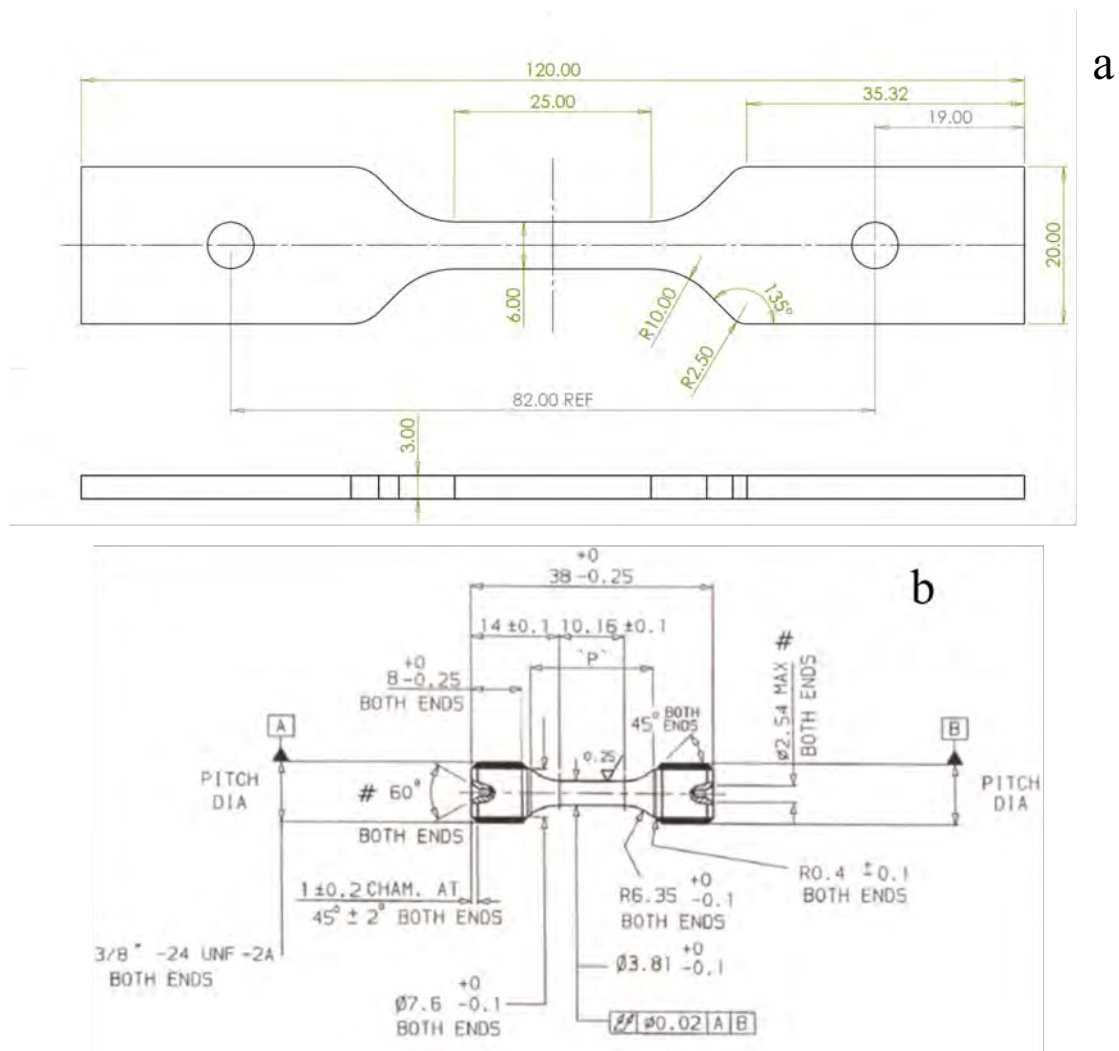


FIGURE 3.12: Tensile and fatigue specimen drawings

The yield strength from the tensile data was estimated by plotting a straight line of equal gradient to that of the tensile curve in the elastic region. This straight line was

horizontally shifted to begin at the point where the strain was equal to 0.2 %. The point at which this line crossed the real tensile curve was taken as the yield strength.

3.17 Fatigue testing

Fatigue samples were machined from cylindrical printed parts to the dimensions given in figure 3.12b. Force controlled low cycle fatigue tests were carried out under two applied maximum stress levels, namely 330 and 375 MPa respectively, with a run-out limit of 100,000 cycles. An R of -1 triangular waveform with a frequency of 0.25 Hz was employed for all tests, and performed in accordance to BS EN 6072:2010 and ASTM E466-21. All tests were performed at ambient room temperature in a controlled laboratory environment.

4. The corrosion performance of additively manufactured Invar [®]

4.1 The Invar build process and introduction

Build parameter optimisation was carried out by varying the build parameters of 15 x15 x 15 mm density cubes according to an L9 orthogonal array. The orthogonal array method is one approach used to understand the effect of varying 4 independent factors each having 3 factor level values as detailed in section 3.4. The array varies the parameters by a given percentage across 9 samples. These L9 arrays were then built at various locations across the build plate to minimise any build plate location based density variations. Figure 4.1 illustrates the build plate layout and one of the completed Invar builds. The powder used to manufacture Invar within this work was sieved and then re-loaded back into the machine for printing. The three builds used in this work was powder recycled 4, 5 and 6 times and the entirety of the builds were complete within the space of 2 weeks. Invar was the first material investigated in this PhD and as such the purpose this work was to produce samples of high density as possible with minimal variation. Subsequently, samples taken from material produced with the highest density and lowest variation were investigated in detail to ascertain if the performance of the "best possible" AM part was comparable to that of the wrought material. The AM invar samples that were corroded in this chapter were all taken from cube 28 as labelled in figure 4.1. This cube was produced with build parameters that yielded a VED of 64.84 J mm^{-3} produced the highest density measurement with the lowest variation. $(99.81 \pm 0.03)\%$.



FIGURE 4.1: Left: Invar build layout. Right: One of the completed Invar builds

4.2 Material characterisation

4.2.1 Powder Analysis

Figures 4.2 and 4.3 display SEM micrographs of the virgin nitrogen gas atomised Invar powder used in the Invar work detailed in this thesis. Observing powder morphology's at lower magnification as displayed in figure 4.3 allows for a general powder quality overview to be made. The powder particles shown are mostly spherical with measurements ranging from $28\text{--}50\mu\text{m}$ in diameter. Whilst there are some examples of prolate spheroids "potato particles" the vast majority of powder particles are spherical. Whilst there are examples of powder satellites within the micrographs however these are very rare with the majority of powder particles being free of satellite particles.

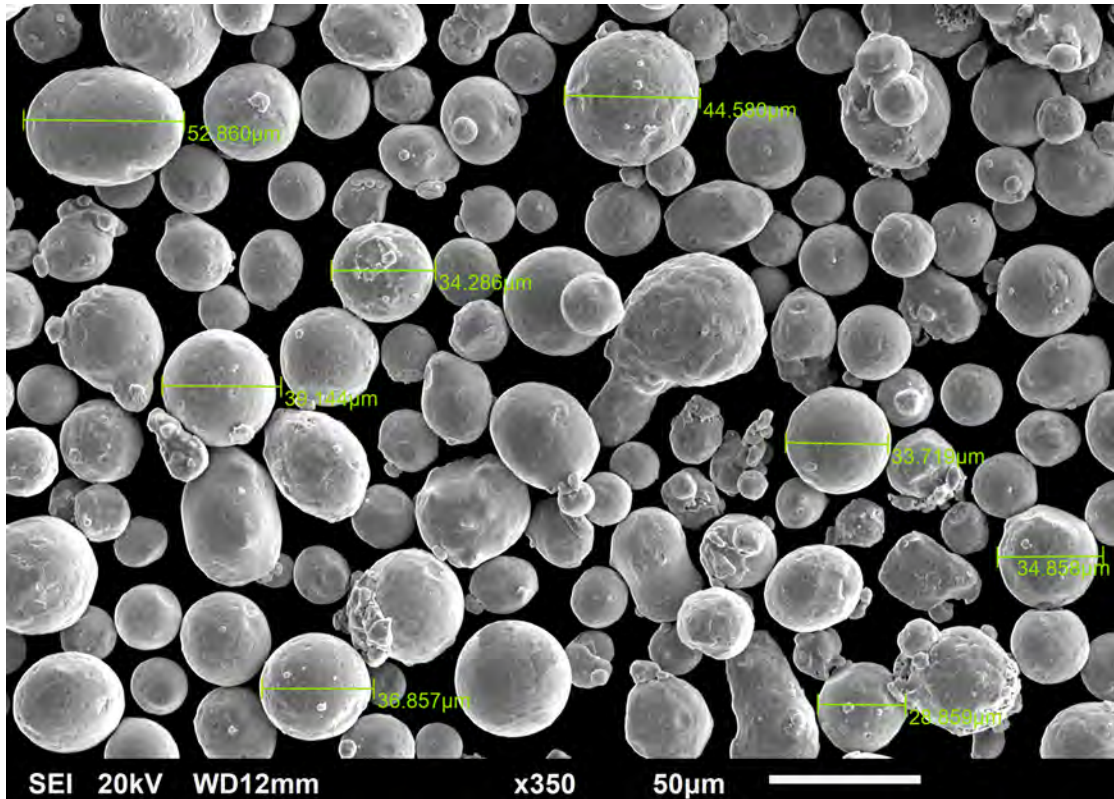


FIGURE 4.2: SEM micrograph showing virgin Invar powder with particle size measurements.

4.2.2 Density measurements and porosity analysis

The density results for as printed Invar components from three builds, each containing 9 different build parameters are displayed in figure 4.4 measured using the Archimedes principle. The error bars on each point represent repeated measurements made at a particular set of built parameters. There are a total of 27 data points presented in the figure, each data point corresponds to a cube printed using a specific set of build parameters. Every cube built using specific build parameters was built multiple times across the build plate with the point shown in figure 4.4 being the mean value of those measurements. Therefore each point displayed in figure 4.4 contains 9 repeat readings from different regions across the build plate. There are no errors in the x value as the value for VED is computed from set build parameters rather than measured. Whilst the VED is a useful parameter for combining the various build parameters involved when producing material via LPBF one must be aware of the workings of the equation as expanded upon in section 1.4. The plot in figure 4.4 has three distinct regions: The first region $30 - 48 Jmm^{-3}$ can be thought of as the geometry region where insufficient energy is being provided to the powder bed to melt the powder sufficiently. This results in physical gaps between melted regions and the resulting low density. The material is joined in this region via conduction welds wherein there are unmelted regions of powder

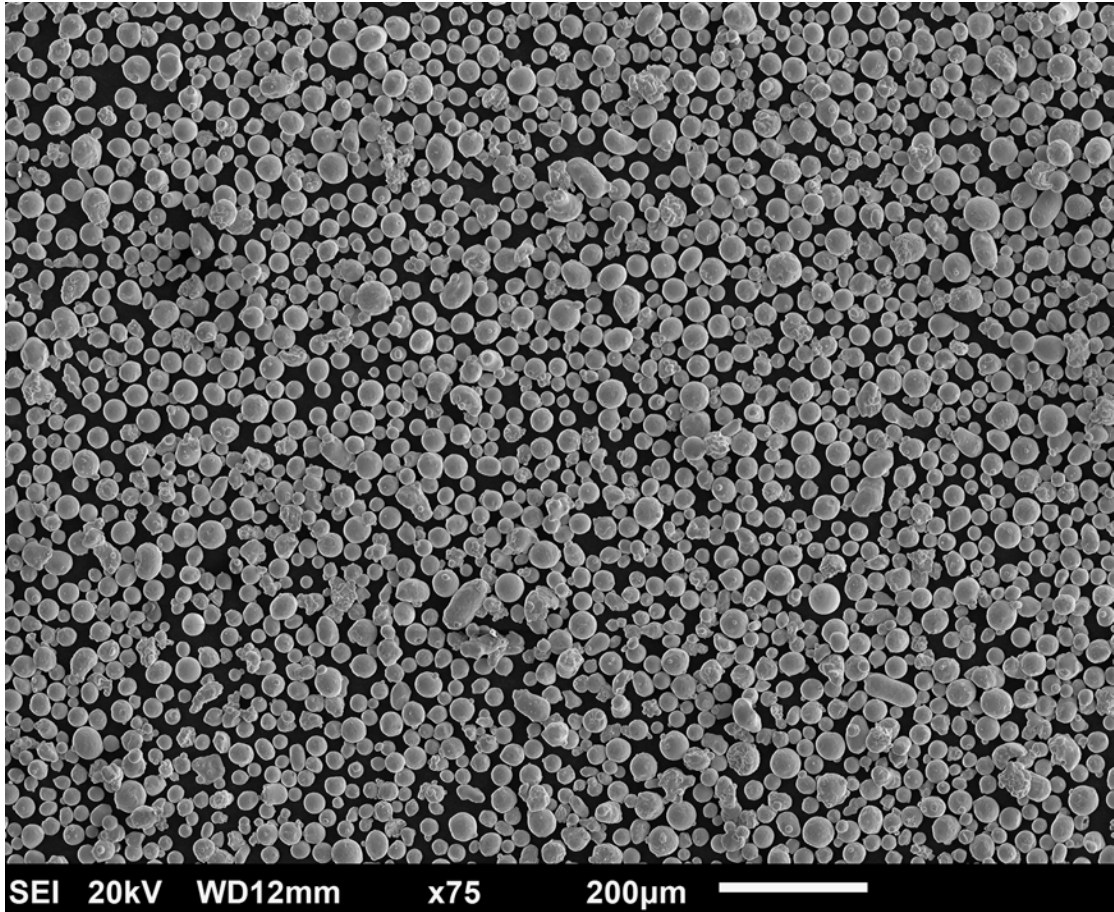


FIGURE 4.3: SEM micrograph showing low magnification virgin Invar powder.

throughout the part. Region 2 between $48 - 72 Jmm^{-3}$ is effectively the Goldilocks region, the region within which sufficient energy is being applied by the laser to melt all of the powder on the build plate and not too much energy being supplied such that excess spatter is not being ejected from the melt pools as solidification occurs. This is crucial to producing parts of higher densities (98.5%+). This region is generally the operating zone for this material and components produced should be within this VED as a rough guide. The third region $> 72 Jmm^{-3}$ is where too much energy is being deposited into the powder bed by the laser and the welds are transitioning into keyhole welds and spatter is being ejected from the melt pool. Spatter that is ejected from melt pools during the build process can induce inhomogeneity's and cause porosity formation throughout the material via a number of mechanisms as expanded upon in section 1.6.

Samples taken from cubes 27, 23 and 21 with lower (97.18%) , mid range (99.59%) and higher (99.77%) densities respectively as measured using the Archimedes principle as outlined in section 3.10 were imaged and the porosity was analysed as outlined in section 3.11. These samples were selected at random to investigate the difference in measured densities between the Archimedes and optical density methods. An example image is

shown in figure 4.5 of the 99.77 % density with some of the porosity features labelled. Small spherical porosity induced by gas and large irregular porosity induced by the building process are visible and highlighted within the image. The image highlights that despite the sample having a density of 99.7 % there still exist large irregular porosity features within the material. Porosity image analysis on images revealed there were 348 pores that exceeded $50\mu\text{m}^2$ in area across these images equivalent to an average of 14.61 large pores mm^{-2} with values ranging from 0.00 to 20.11 large pores mm^{-2} across all samples. The sample densities as calculated using optical microscopy were 96.73%, 99.35 % and 99.85%. The samples with the low, medium and highest densities were consistent across both the optical and Archimedes methods however the values themselves vary between methods. This is likely due to the fact that the optical microscopy technique gives the density of a single slice and the Archimedes principle gives a measurement for the entirety of the dipped sample.

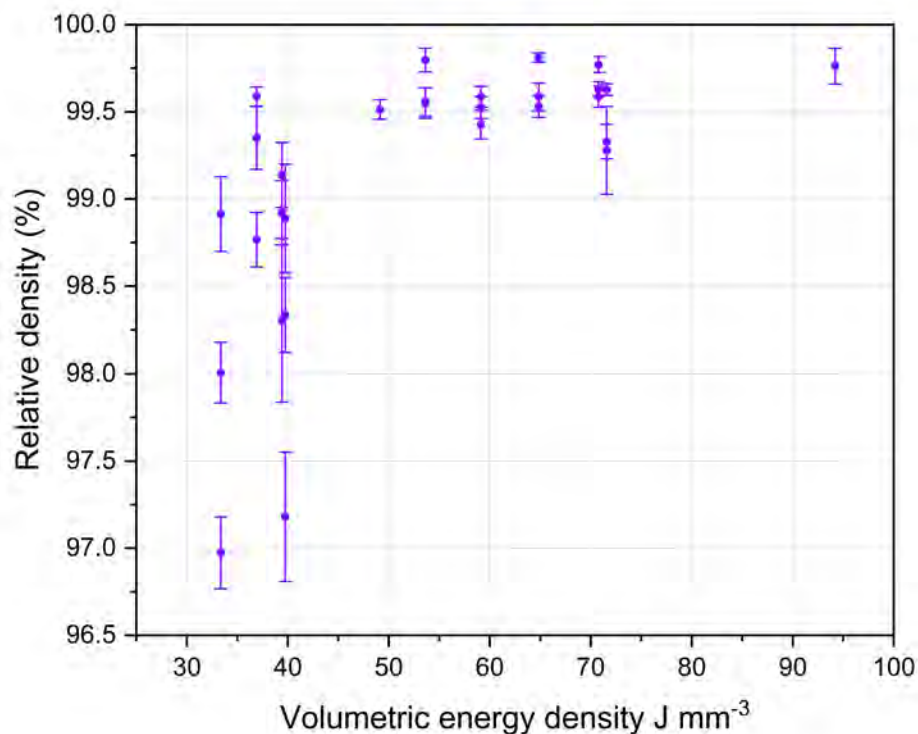


FIGURE 4.4: Invar density against VED for every AM Invar sample.

The Archimedes method is useful but it is crucial to understand the output of the technique. The optical method is able to produce a density value for any given slice imaged. This is inherently different to the method as outlined in section 3.10 which effectively produces a density measurement as an average across the entirety of the sample. The nuance being that each result has its benefits and its short comings.

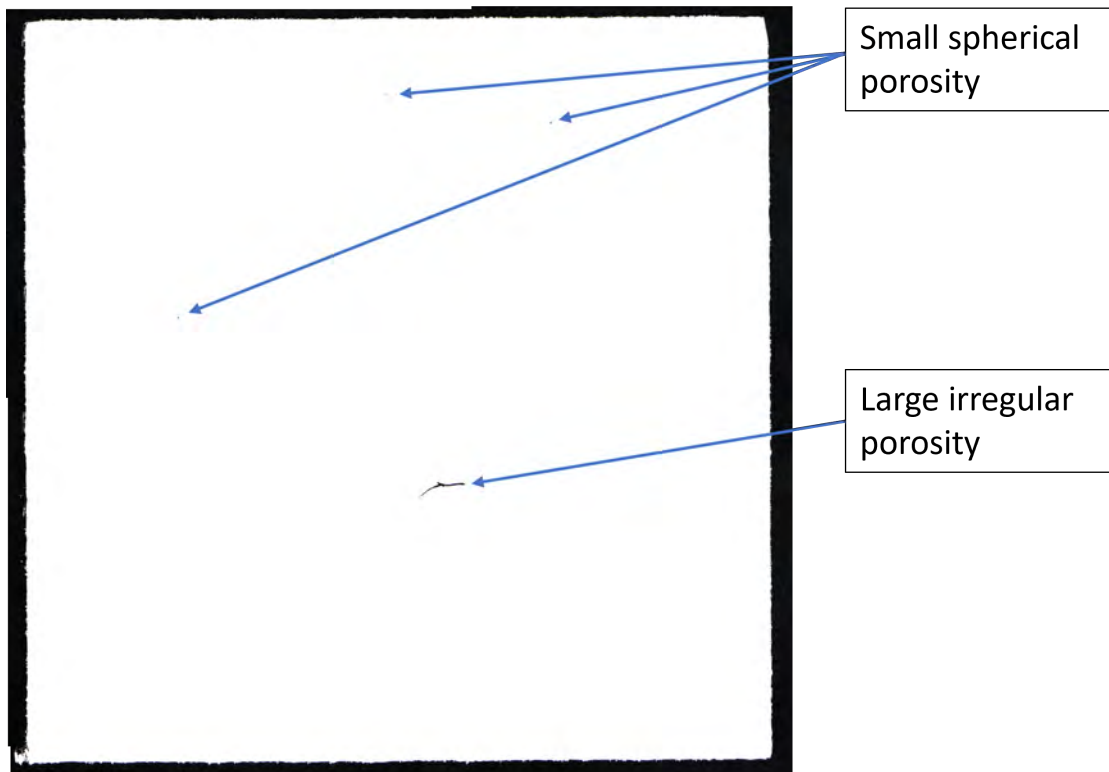


FIGURE 4.5: Example image showing porosity in an Invar sample taken from cube 27.

4.2.3 Microstructure

Figure 4.6 shows representative optical images of a) AM and b) wrought Invar[™] samples after sectioning, polishing and etching. The melt tracks induced by the AM laser melting process are clearly visible within the microstructure of the AM sample with spherical porosity highlighted (blue dotted circles) and larger irregular porosity points (red circles) are also shown. The structure imparted by the AM process is radically different to that of the wrought Invar[™] shown in figure 1b, that generally has an equiaxed grain morphology.

Figure 4.6 shows an SEM image of an AM invar[™] sample obtained after etching using Kalling's 2 as outlined in section 3.2. The melt pool boundaries were visible in the SEM image in Figure 4.7 with the spectrum labels indicating the points at which EDX measurements were made. Spectra 1, 3 and 4 were taken at the melt pool boundary whereas spectra 2 and 5 were from within the melt pool. The atomic weight data corresponding to the measured spectra is found in 4.1, the error values represent the standard deviation taken from the EDS scan. There was no significant variation in the atomic composition across the spectra taken. This indicates that there was no elemental segregation in the finished part and that any variation observed in corrosion performance across the microstructure is not due to elemental segregation. EDX scans were performed on multiple samples across various regions and elemental segregation associated with the

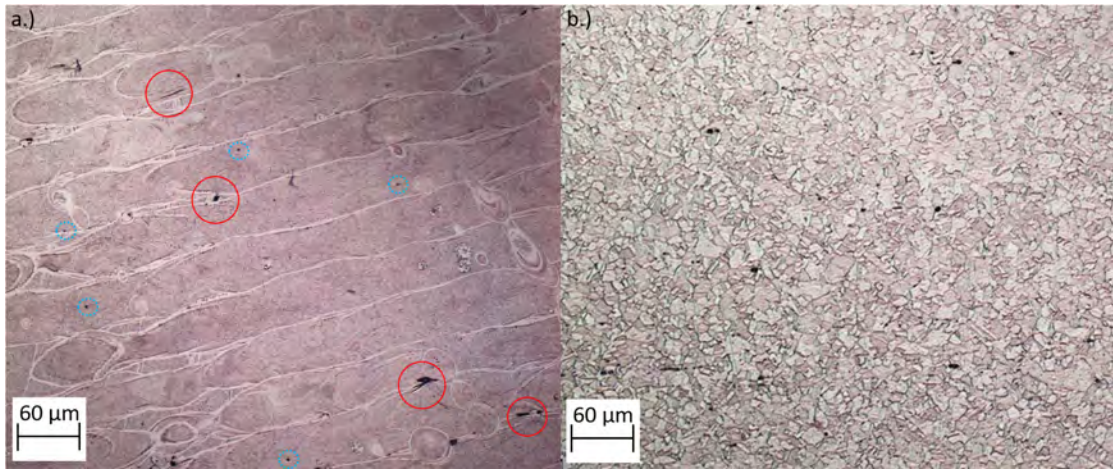


FIGURE 4.6: Optical image showing AM Invar (cube 28) (a) and wrought Invar (b) with spherical porosity highlighted (blue dotted circles) and larger irregular porosity points (red circles).

AM microstructure was not reported in any of the tests. Throughout all of the EDX scans the Nickel content measured did not deviate by more than 0.8 wt.%. The iron content varied slightly more at a maximum of 1.1 wt.% across samples however neither of these values demonstrate a considerable variation.

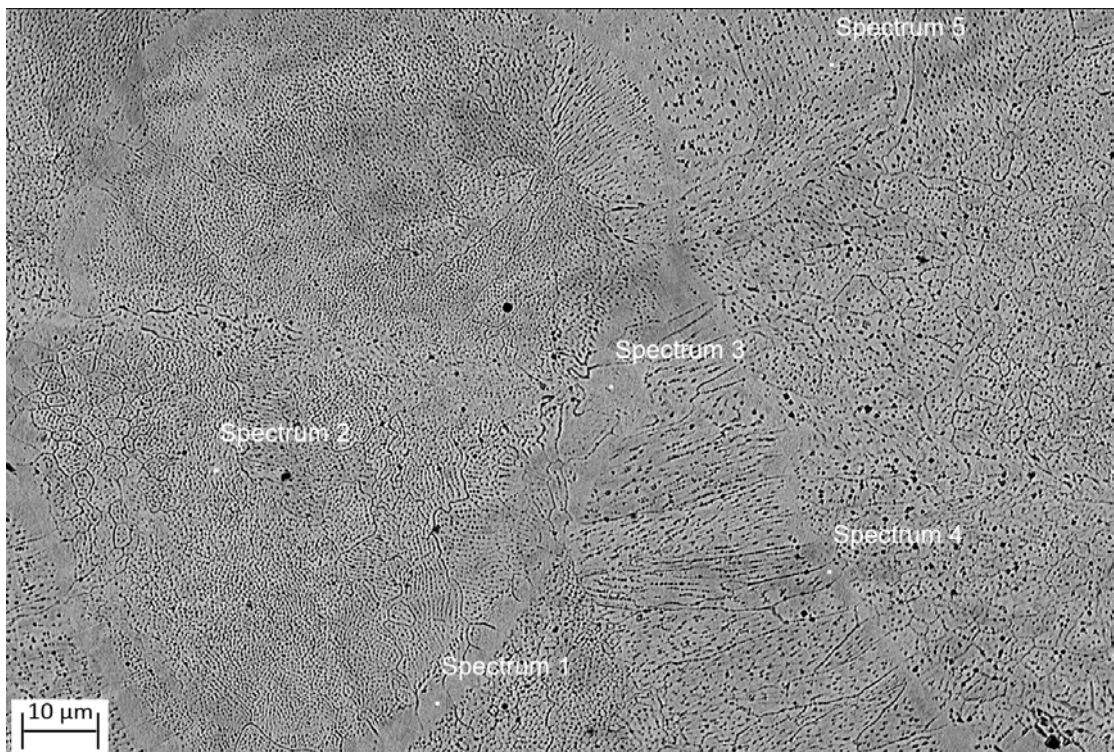


FIGURE 4.7: SEM image on sample from cube 28 showing AM Invar with EDS measurement locations. Locations 1,3 and 4 are melt pool boundaries and points 2 and 5 are within melt pools.

The EBSD scan shown in Figure 4.8a demonstrates the non-uniformity in grain size

Spectrum	Iron (wt%)	Nickel (wt%)	Oxygen (wt%)	Chromium (wt%)	Silicon (wt%)	Manganese (wt%)
1	62.5±0.3	37.3±0.3	0	0.2±0.3	0	0
2	62.0±0.3	37.4±0.3	0.5±0.3	0	0.1±0.3	0
3	61.7±0.3	37.6±0.3	0.6±0.3	0	0.1±0.3	0
4	61.5±0.3	36.9±0.3	0.8±0.3	0.3±0.3	0.2±0.3	0.3±0.3
5	62.3±0.3	37.7±0.3	0	0	0	0

TABLE 4.1: Table showing EDS data from SEM image shown in Figure 4.7.

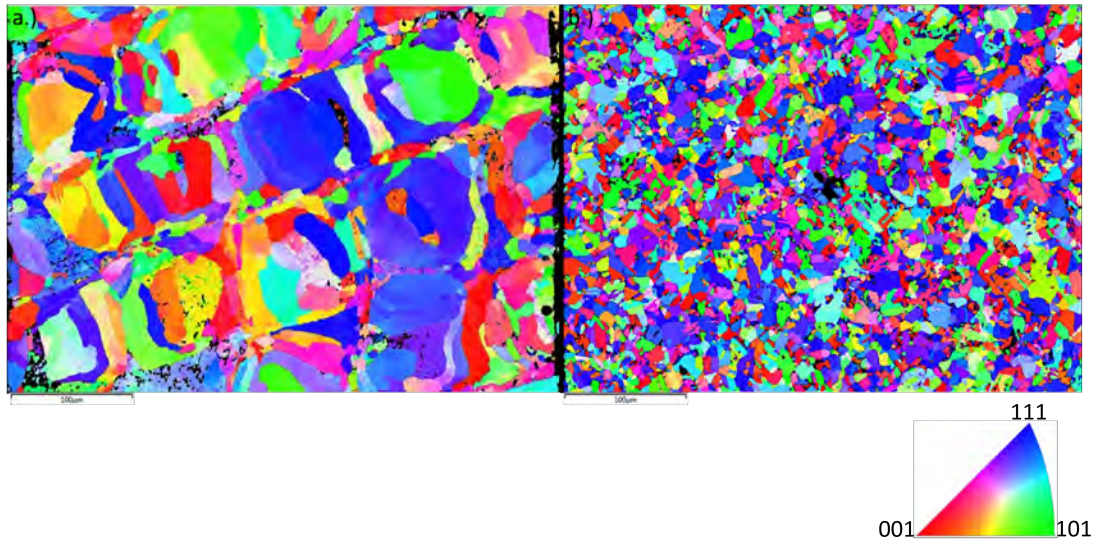


FIGURE 4.8: EBSD image showing AM Invar (cube 28) (a) and wrought Invar (b).

and orientation of the AM microstructure. Melt pools regions are characterised by long ($50\mu\text{m}$) but narrow grains ($10 - 20\mu\text{m}$) traversing most of the width of the melt pools, with smaller equiaxed grains ($10\mu\text{m}$) forming at the melt pool boundaries. The AM sample was found to have an average grain size of $29\mu\text{m}$ with a standard deviation of $14\mu\text{m}$. This non uniformity in the grain size and orientation within the microstructure of AM components has been reported elsewhere in literature [143]. The existence of the irregularly shaped grains at melt pool boundaries is due to the repeated heating and cooling that the melt pool boundaries receive as the laser rasters across the powder bed. These melt pool boundary grains cool rapidly as they grow and come into contact with preexisting melt pool bulk grains and solidify. The spacing between melt pool bulks is sufficient that rasterisation of powder in parallel tracks is not sufficient to re-melt powder, resulting in a longer cooling time for melt pool bulk regions. Grains are shown to be distributed throughout the melt pool track with nucleation points likely related to the pulsing of the laser source. The sample demonstrates a lower proportion of grains in the [001] orientation. Comparing to what is shown in figure 4.7, spectrums 1, 3 and 4 are located at smaller irregularly sized grains at melt pool boundaries. Spectrums 2 and

5 are located at larger grains within the melt pool bulk. The wrought sample (Figure 4.8b) was found to have a much finer and more uniform grain structure in comparison with an average grain size of $12\ \mu\text{m}$ and standard deviation of $5\ \mu\text{m}$. The crystallographic orientation of grains is consistent throughout the material with no preferential crystallographic orientation. The larger standard deviation in the AM sample illustrates the increased variation in grain size compared to the wrought sample.

4.2.3.1 White light interferometry

White light interferometry was carried out in order to investigate the size of porosity present in the LPBF Invar material and to identify whether there are any height differences across melt pools and melt pool boundaries. Figure 4.9 displays a surface image and then a corresponding white light surface measurement for an AM Invar sample. There are numerous porosity regions located throughout the surface image captured. The two deepest porosity points visible are approximately 0.2 mm in depth. There was no visible height difference observed across a range of sample surface measurements using white light interferometry.

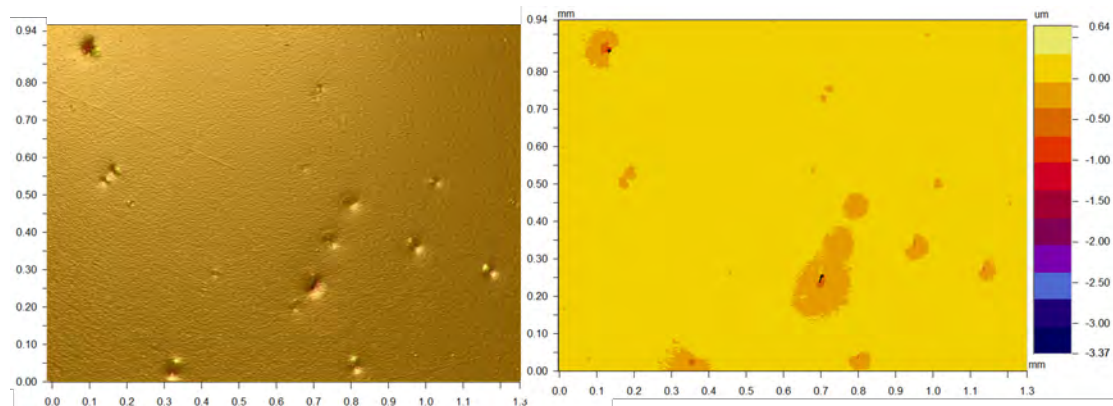


FIGURE 4.9: Invar cube 28 images showing surface topography (left) and surface height (right).

The instrument used to carry out the white light measurement presented the data using proprietary software and would not export any 3D data. Therefore in order to prepare the 3D images shown in figure 4.10 and 4.11 a script was written to export the x-z data at every y interval. This data was then reconstructed using Python into the desired format for exporting into Matlab for 3D plotting.

White light interferometry is excellent in investigating the depth and location of build defects within materials as long as there is a clear path for the light to reach the desired surface and return to the detector. However if porosity defects were to plume in either direction then this technique would not be suitable. The data recorded from white

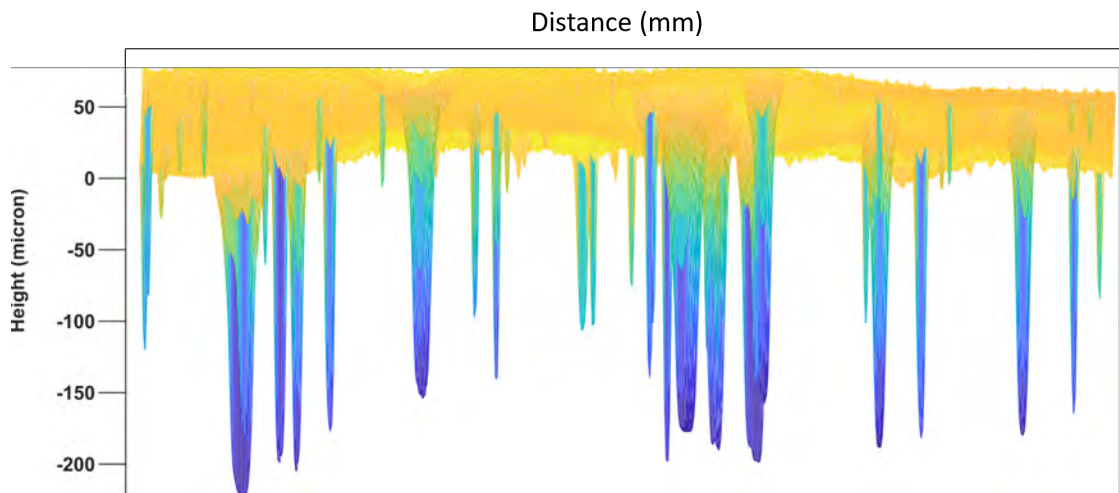


FIGURE 4.10: Invar cube 28 3D reconstructed topography front view, note the horizontal length of the sample is 1.3 mm.

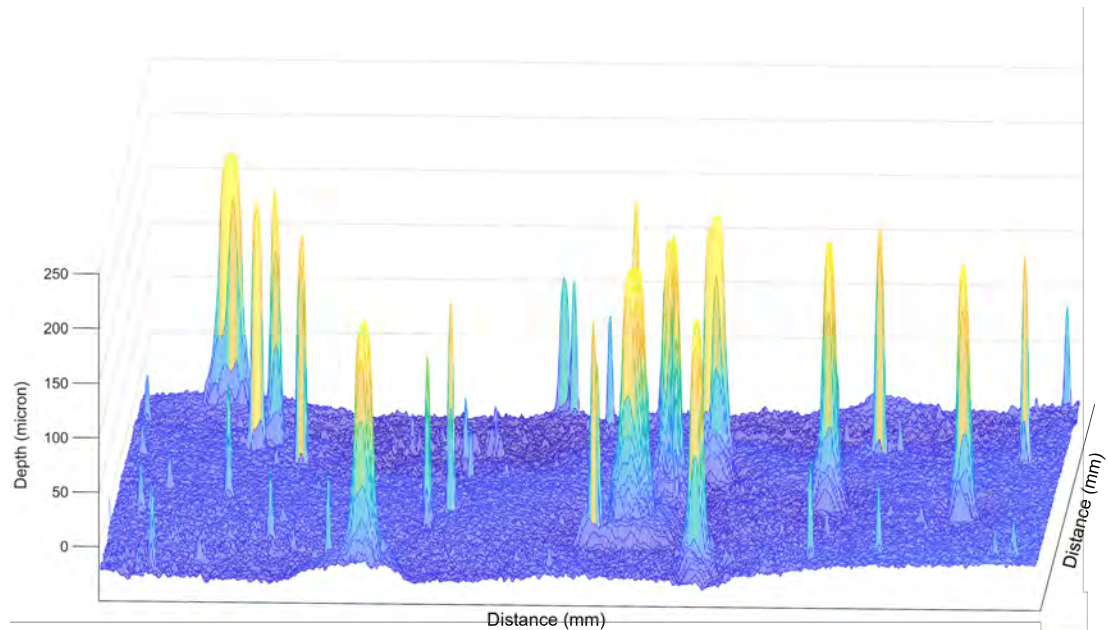


FIGURE 4.11: Invar cube 28 3D reconstructed topography flipped, note the horizontal and depth of the samples are 1.3 and 0.94 mm respectively.

light interferometry revealed that porosity defects varied in depth in clusters. With one cluster being $50\mu\text{m}$ deep, one cluster being $100\mu\text{m}$ deep and one cluster being $200\mu\text{m}$ deep. One can see from the surface image presented in figure 4.9 that the majority of the porosity has prolate spheroid morphology. The large porosity features located at (0.7,0.2) however could be a combination of numerous spherical porosity defects or on larger irregularly shaped lack of fusion defect as shown in figures 4.11 and 4.10.

4.2.4 XRD

The XRD spectra obtained from scanning wrought and LPBF manufactured Invar are displayed in figure 4.12. The spectra are enlarged to allow for individual peak intensities to be visible in figure 4.13.

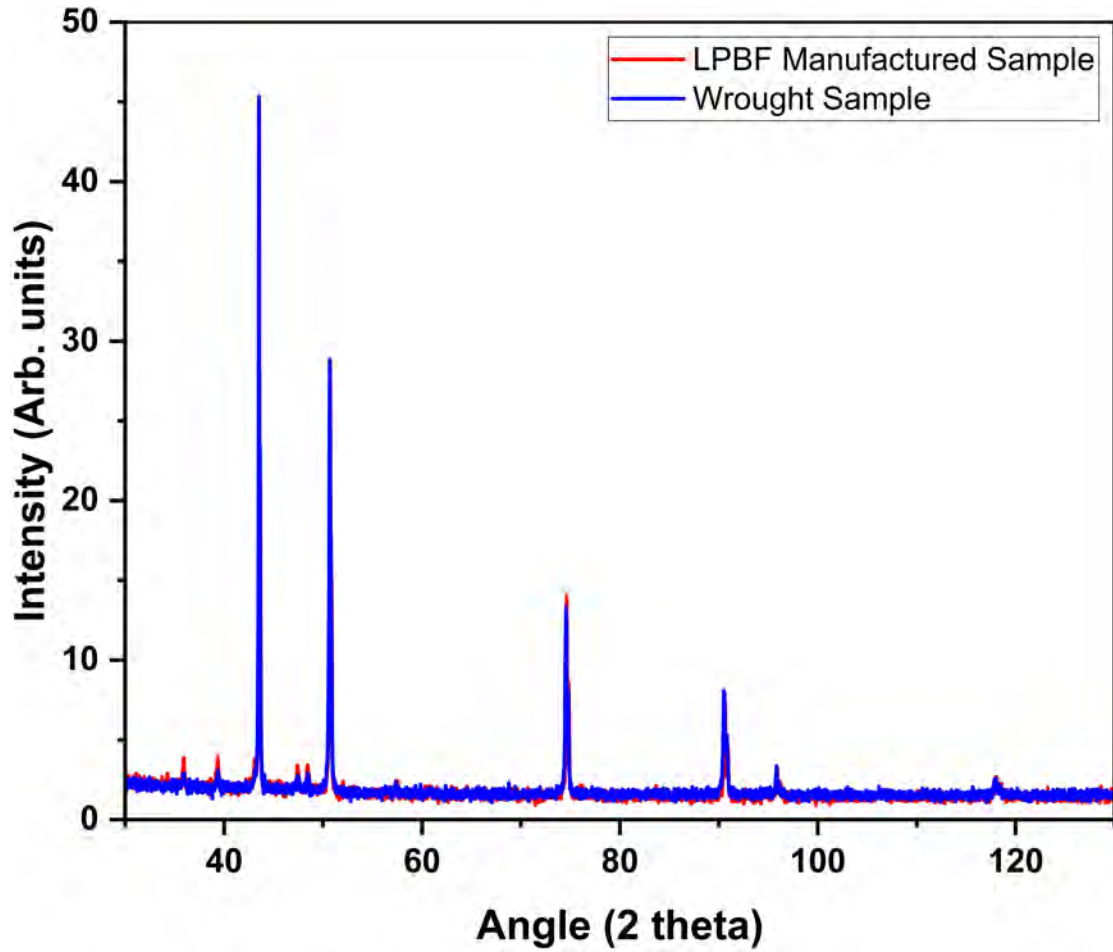


FIGURE 4.12: Invar XRD scan for wrought and LPBF manufactured (cube 28) samples.

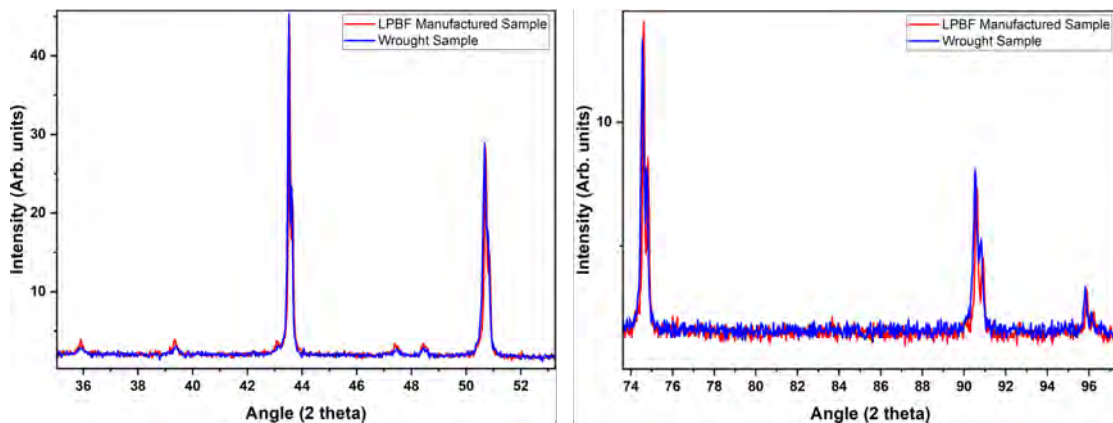


FIGURE 4.13: Enlarged XRD scans showing individual peaks on wrought and LPBF (cube 28) samples.

The displayed spectra for both the LPBF manufactured and wrought sample overlap throughout the entirety of the scans. The location and signal to noise ration of each of the peaks is comparable across the materials. There minor peaks located at $\theta = 36$ and 39° have a slightly larger signal to noise ration in the LPBF manufactured sample but such a small difference is not noteworthy and is most likely a scan artefact. The small peaks visible in the XRD profiles at around $\theta = 36, 39, 47, 48$ degrees could indicate the presence of oxides on the material surface however, it was not possible to characterise these oxides using the software available. The ratio of FCC to BCC was 75:25 for the wrought part and 74:26 for the LPBF manufactured part, effectively the same for each sample. Further to this the fitted FCC and BCC profiles produced lattice spacings of 3.597 \AA for FCC and 2.930 \AA for BCC for the wrought part compared to 3.600 \AA for FCC and 2.932 \AA BCC, calculated using Braggs law for the LPBF manufactured part.

4.3 Corrosion testing results

4.3.1 Scanning vibrating electrode technique

The corrosion behaviour of the AM and wrought Invar[™] samples was subsequently explored under immersion conditions in pH 5.5 0.17 mol.dm^{-3} NaCl. Experimental data from the SVET is presented as false colour maps in Figure 4.14 that provide time resolved intensity and spatial information regarding anodic (red) and cathodic (processes) associated with AM and wrought Invar[™] samples continuously immersed in pH 5.5 0.17 mol.dm^{-3} NaCl for 29 hours. For AM Invar[™], the initiation of localised anodic activity was observed after 2 hours. Subsequently 5 anodes were observed to have initiated after 5 hours of immersion. These localised anodic features subsequently persisted for the full duration of the 29 hour experiment. Figure 4.15 displays the current density of two localised corrosion regions that were detected by the SVET (labelled as A and B in Figure 4.14) as a function of x axis position and time. The data demonstrates that these two localised features remain active once initiated and there is a trend for increasing current density with respect to time for both anodes. In comparison, the wrought material did not display similar localised anodic attack after 29 hours. The only anodic activity in the wrought SVET derived false colour map appeared after 29 hours at the top left of the sample incident with PTFE masking tape in one experiment. This activity however was low with a recorded current density below 0.25 A m^{-2} and is thought to be a result of crevice corrosion initiating between the masking tape and the sample. In other repeat experiments localised anodic activity was not observed on the wrought samples. Post SVET scanning, red rust was visible on the surface of the AM sample in several discrete circular features (inset of second image of Figure 4.14) which corresponded to the points

of high anodic activity shown in the SVET maps. Conversely, the wrought invarTM samples displayed no visible signs of red rust after 29 hours of immersion.

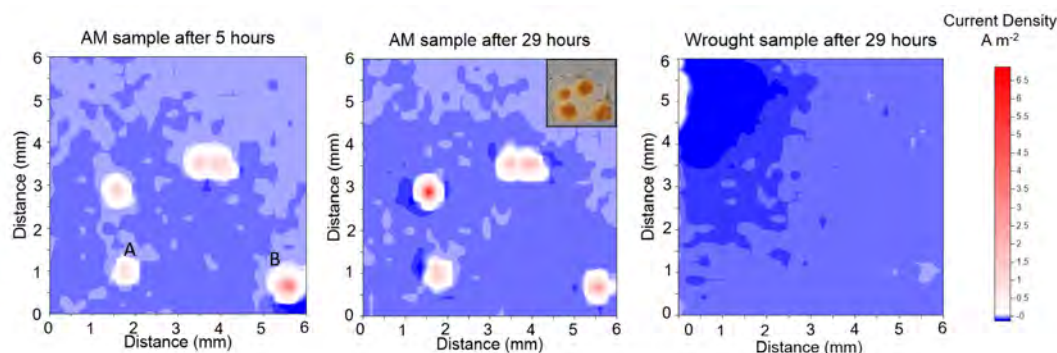


FIGURE 4.14: SVET derived false colour maps for AM and wrought InvarTM (cube 28) immersed in pH 5.5 0.17 mol.dm^{-3} NaCl solution showing corrosion current density values. An optical image of the surface is shown in the second SVET map showing that the location of red rust was coincident with the localised anodic features observed by the SVET.

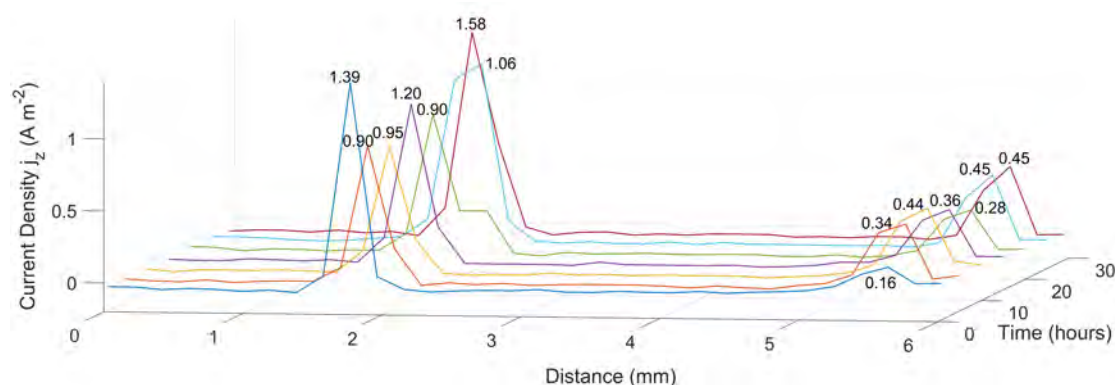


FIGURE 4.15: SVET localised corrosion intensity measurements as a function of distance at 0, 5, 10, 15, 20, 25, 29 hours from cube 28.

4.3.2 Time lapse microscopy

Figure 4.16 a- f and supplementary video 1 show the initiation and progression of corrosion on the surface of AM InvarTM immersed in pH 5.5 0.17 mol.dm^{-3} NaCl solution. Anodic features had initiated after 115 minutes of immersion. This coincides with the SVET scans wherein localised anodic activity was observed after 2 hours (120 minutes) of immersion. The initiation site corresponded with irregular process induced porosity located at a melt pool boundary (figure 6a). The succession of timelapse images at 30 minute intervals shown in figure 4.16 a – f illustrates the growth of this anodic feature over time, and the subsequent deposition of corrosion product local to the anodic feature. Interestingly, a circular region immediate to the anode remained free of corrosion product throughout the duration. This may indicate that the local chemistry of the

electrolyte in terms of pH prevented the solubility product of the corrosion product from being exceeded. The timelapse images obtained for AM Invar[™] immersed in a pH 5.5 0.17 mol.dm⁻³ NaCl electrolyte was repeated four more times and, in each case, highly localised corrosion was initiated at porosity regions located at melt pool boundaries as shown in figure 4.17. This corrosion tended to occur preferentially at non-uniform, process induced porosity regions, rather than at spherical gas induced porosity regions. This preferential initiation was observed repeatedly across the range of AM Invar[™] samples. In contrast the wrought Invar[™] samples repeatedly did not undergo visible corrosion in the control experiments in line with the observations from the SVET experiments. The majority of the sample surface shown in figure 4.17 does not appear to be actively corroding and can be considered as passive. The passivity of the material in solution is likely due to the high nickel content (37 wt%) of the material as highlighted in section 1.14.

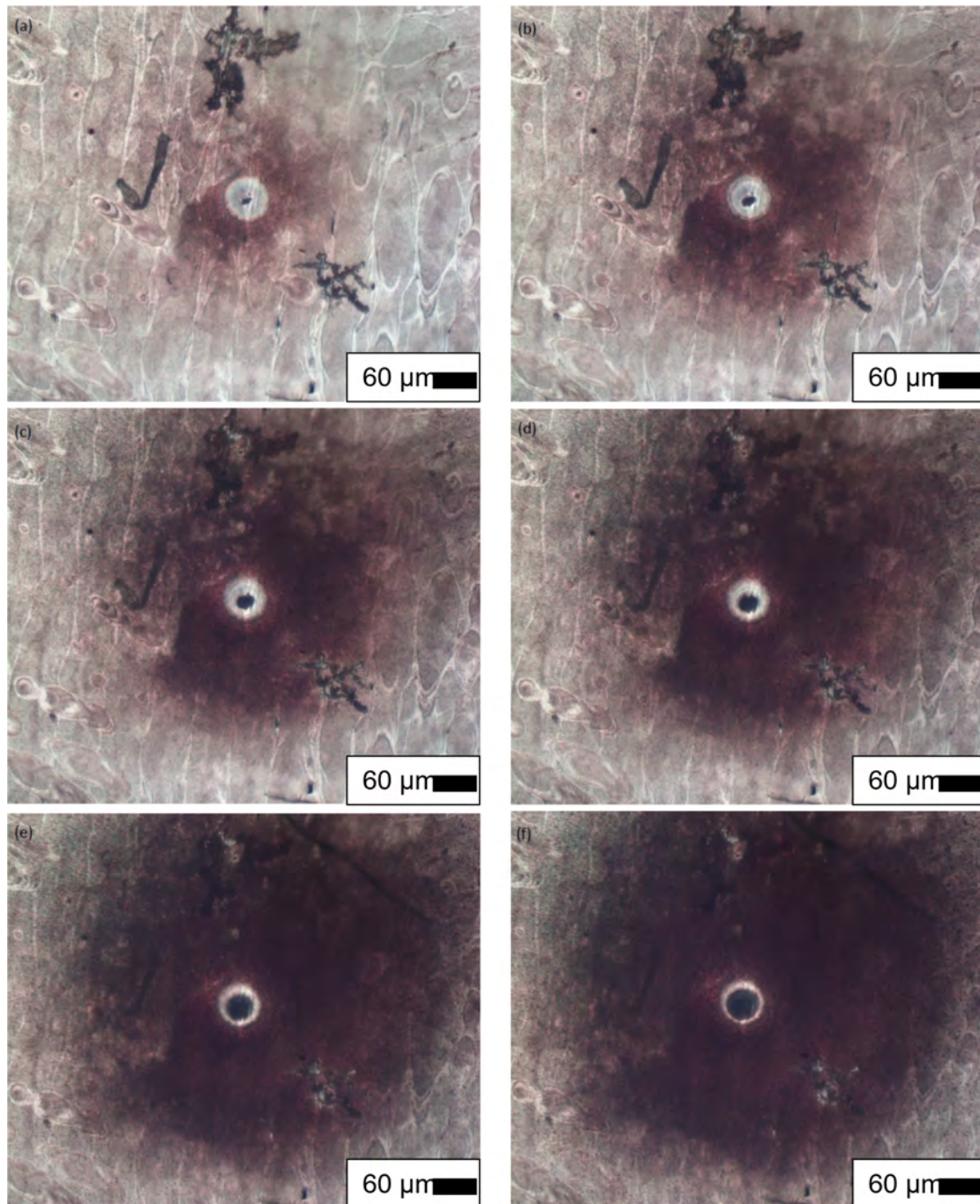


FIGURE 4.16: Images a-f showing the progression of corrosion in AM Invar (cube 28) at 30 minute intervals between 115 and 250 minutes whilst immersed in pH 5.5 0.17M NaCl electrolyte.

4.4 Discussion

The SVET and TLM data both show that AM Invar[™] was susceptible to localised corrosion in comparison to wrought Invar[™] material when immersed in pH 5.5 0.17 mol.dm⁻³ NaCl. The SVET derived false colour maps obtained in the case of an AM

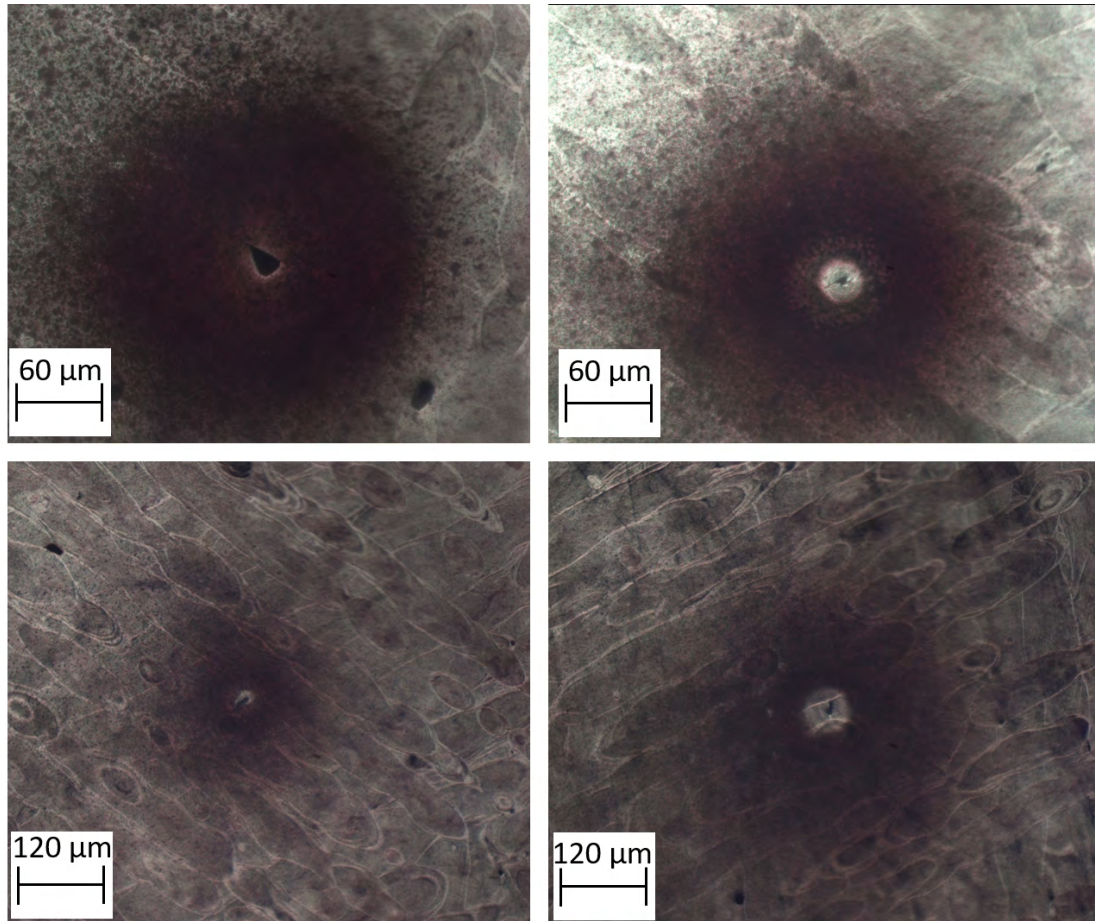


FIGURE 4.17: : Microscopy images of AM Invar™ (cube 28) immersed in pH 5.5 0.17M NaCl electrolyte, corrosion is seen to initiate at irregularly shaped porosity located at melt pool boundaries.

sample (Figure 4.14) show the areas of anodic current density to be highly localised as point anodes that persist for the duration of the 29 hour experiment. In comparison, wrought Invar™ did not display such point anode features with limited anodic activity observed for repeated experiments. These findings are in agreement with those obtained during TLM experiments (Figures 6 and 7), which show that the dissolution of AM Invar™ initiates preferentially at irregular process induced porosity regions, principally those situated at melt pool boundaries, this aligns with work presented at the Solid Freeform Fabrication Symposium in 2019 [101]. It therefore seems plausible that the increased susceptibility of AM parts to highly localised corrosion mechanisms is a result of its inherent porosity. Porosity with semi-occluded regions are more conducive to facilitating localised corrosion through differential aeration due to the restricted diffusion of oxygen into these regions as per the Fontana Greene mechanism of crevice corrosion [100]. As such, the pores at the melt pool boundaries become established as intense anodic features and the environment within the pore will become increasingly aggressive due to chloride ion ingress and hydrolysis of $\text{Fe}^{2+}/^{3+}$ ions leading to a drop in pH. These

conditions enable the anodes, once initiated, to remain active for the duration of the SVET experiments as demonstrated in figures 4.14 and 4.15. The drop in pH may be inferred from the TLM images in figure 6 where a corrosion product free region of alloy surface is maintained surrounding the mouth of the anodically active pore. The lack of precipitation of corrosion product over this region, where the flux of Fe ions emanating from the pore will be highest, suggests that a low pH is established that prevents the solubility product of the corrosion product becoming exceeded. The pores that initiated as anodes were repeatedly large features associated with process induced porosity at melt pool boundaries rather than smaller, spherical gas induced porosity defects. This suggests that the process induced porosity is generally larger with respect to volume and more complex in shape providing a more tortuous path for oxygen diffusion and thus is more likely to develop differential aeration conditions which facilitates persistent anodic activity [100] [144]. The crevice like corrosion which occurs at porosity points indicates the presence of porosity would seem to outweigh any potential differences in corrosion behaviour purely due to the differences in microstructure between the AM and wrought Invar™. Therefore, it is not possible to determine from this investigation whether microstructures of Invar™ produced through AM processing are inherently more susceptible / resistant to corrosion than wrought material. It could also be argued however that the preferential initiation of corrosion at these regions is due to the large concentration of high angle grain boundaries.

For determining the overall density of AM components a combination of optical and Archimedes principle is ideal in determining build parameters which produce parts best suited for their application. The initiation of persistent localised corrosion features at process induced porosity regions raises some important considerations for AM materials with regards to corrosion. The AM Invar™ material used has a measured density of $8.08 \pm 0.02 \text{ g cm}^{-3}$ equivalent to 99.75 % density. It would seem however that this small degree of porosity is sufficient to allow for intense localised corrosion attack due to the morphology of the pores and their susceptibility to differential aeration. The formation of pores within the microstructure is difficult to predict and certainly not uniform across the surface of the alloy which induces further uncertainty into the performance of the AM materials from part to part during production. The difficulty in predicting the formation and location of porosity is due to the complex thermal history of materials printed via AM as layers are melted and reheated upon subsequent laser passes. Further to this spatter is also difficult to predict and can cause porosity to form during the build process. The results of the porosity image analysis confirm this wherein 348 pores were recorded that had a surface area $> 50 \mu\text{m}^2$, an area comparable to that of pores where corrosion initiated in figure 7. The large variation in the number of pores per unit area as shown in section 3.1 highlights the potential difficulties in investigating the corrosion behaviour of

AM material and whether exposed surfaces are representative of the entirety of the part. Selectively choosing an area of material without porosity could lead to experimental results and conclusions that do not represent the bulk material behaviour. For example a part containing 0.5% porosity located entirely in the centre of the part would perform well in corrosion testing but would not perform well in a tensile test. Subsequently a part containing 0.1% porosity evenly distributed throughout the sample and its surface would perform well in tensile testing but poorly in corrosion testing compared to a part with no surface porosity. This addresses the variation presented in literature with regards to the performance of AM parts wherein porosity features or defects in the material can infer susceptibilities to localised anodic attack. Maximising part density through AM build parameters is therefore an important consideration, especially for mechanical properties of alloy. However, any residual porosity can potentially lead to accelerated environmental degradation. This work has demonstrated through in-situ techniques that AM materials are susceptible to localised corrosion attack regardless of the corrosion performance of its wrought counterpart. Therefore, a further processing step may be required for AM materials to eliminate the porosity entirely before AM parts can be reliably introduced into supply chains.

4.5 Conclusions

- Optical and SEM images show that AM Invar™ has a microstructure with distinctive melt pool tracks associated with the AM laser pattern with porosity often observed at melt pool boundaries and as small spherical features within the melt pools. In contrast wrought Invar™ has an equiaxed grain morphology with no comparable porosity regions.
- EBSD showed that AM parts have non-uniform microstructures, with larger, columnar grains forming in the melt pool bulk and smaller highly mis-orientated grains residing at melt pool boundaries.
- SVET false colour derived maps have shown that highly localised corrosion initiated within 5 hours on the AM samples immersed in pH 5.5 0.17 M NaCl that persisted for the 29 hour duration of the experiment. In comparison, localised anodic activity was not observed on wrought sample after 29 hours.
- Time lapse microscopy at a microstructural level repeatedly demonstrated that these anodes initiated at points of process induced porosity at the melt pool boundaries. Subsequently these features persisted as sites of anodic dissolution suggestive of a Fontana Greene crevice corrosion mechanism of differential aeration and acidification developing within the pores.

- Image analysis demonstrated that the distribution of process induced porosity is non-uniform and thus the corrosion behaviour of any one area of the material and hence from part to part in manufacturing becomes unpredictable.
- Based on the findings of this work it seems plausible that post-production treatment of AM parts is required to eliminate process induced porosity and reduce the risk of preferential initiation of localised corrosion at melt pool boundary porosity regions.

5. The corrosion performance of additively manufactured 316 L

The wrought samples referred to in this work were samples cut from 1.2mm thick annealed sheet 316L supplied from Goodfellows.

5.1 Powder Analysis

The composition of wrought 316L, the powder used to build with in this work is displayed in table 5.2.

Figures 5.2 and 5.1 display SEM micrographs of the virgin 316L powder used in the 316L work detailed in this thesis. Observing powder morphology's at lower magnification as displayed in figure 5.2 allows for a general powder quality overview to be made. The powder particles shown are mostly spherical with measurements ranging from $30 - 46\mu\text{m}$ in diameter corresponding to the measurements listed in table 5.1. Whilst there are some examples of prolate spheroids "potato particles" these particles are the minority and not abundant throughout the powder. Similarly there are examples of powder satellites within the micrographs however these are not common with the majority of powder particles being free of satellite particles.

Particle Size (μm)	Percentage (%)
>53	0.00
53>45	0.36
45>15	99.55
15>	0.09

TABLE 5.1: Particle size of virgin nitrogen gas atomised 316L powder.

Element	Weight Percent	
	Wrought	AM Powder
Chromium	16-18	16.9
Nickel	10-14	12.5
Molybdenum	2-3	2.4
Carbon	0.030 (Max)	0.019
Manganese	2 (Max)	0.67
Phosphorous	0.045 (Max)	0.02
Sulfur	0.03 (Max)	0.008
Silicon	0.75 (Max)	0.6
Nitrogen	0.1 (Max)	0
Iron	Balance	Balance (67)

TABLE 5.2: Elemental composition of 316L powder by weight percentage.

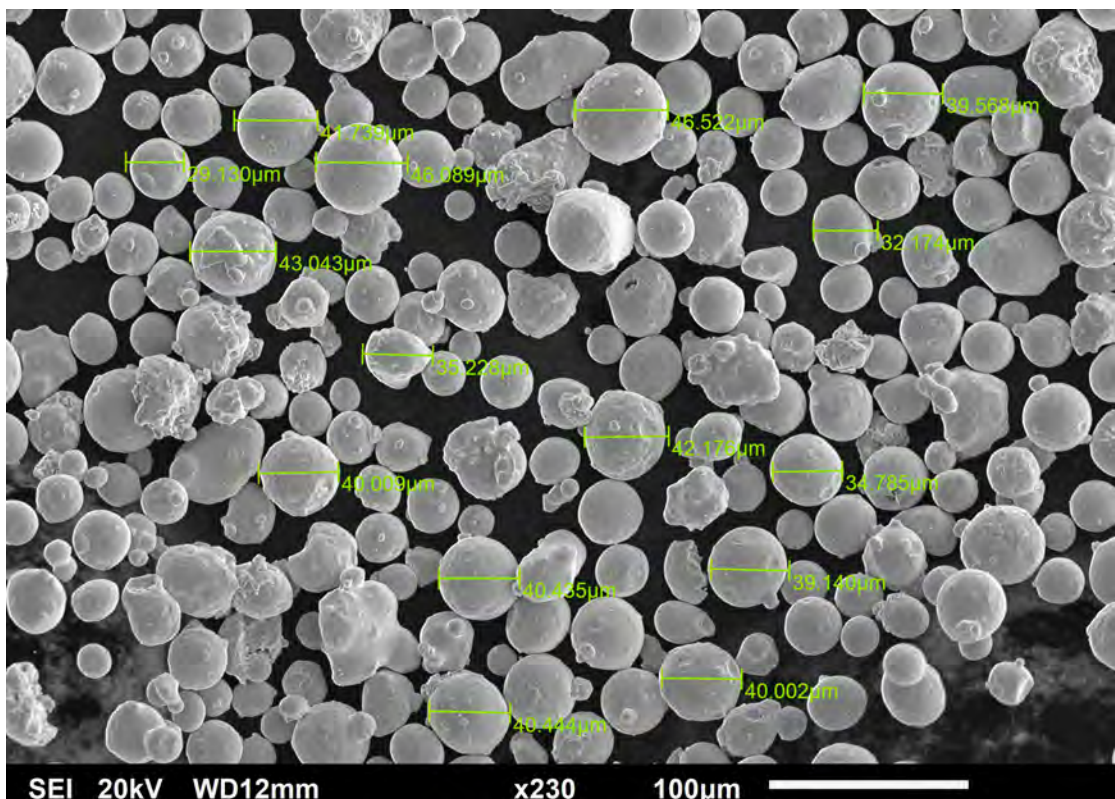


FIGURE 5.1: SEM micrograph showing virgin 316L powder with particle size measurements.

5.2 Mass and density variation across the build plate

Mass and density measurements were carried out on a set of 316L cubes of 15x15x15mm dimensions built with 2mm build supports. The cubes were assigned build parameters following an L9 orthogonal array with some modification as displayed in table 5.3 to produce predetermined VEDs. The modification to the orthogonal array was to substitute

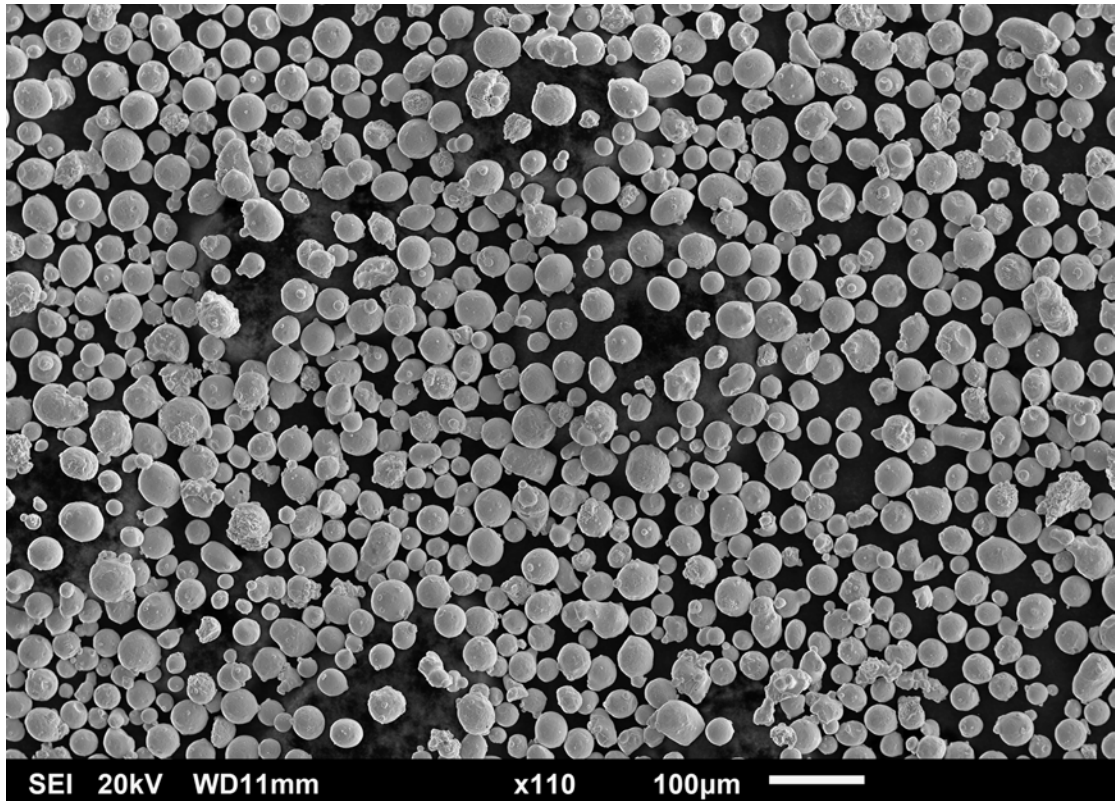


FIGURE 5.2: SEM micrograph showing an overview of virgin 316L powder.

one of the parameters with one designed to give a specific VED to investigate a VED range that was not covered in previous builds.

Sample Label	Point distance (μm)	Hatch Spacing (μm)	Exposure Time (μs)	Power (W)	VED (J mm^{-3})
1	70	110	70	205	37.27
2	70	110	80	195	40.52
3	70	100	80	195	44.58
4	60	110	80	195	47.27
5	50	100	70	185	51.80
6	60	100	80	205	54.66
7	50	110	80	195	56.73
8	50	120	90	205	61.50
9	70	100	85	200	48.57

TABLE 5.3: 316L build 3 build parameters, sample 4 are the optimum parameters from Renishaw.

The build plate was split into designated zones in order to investigate the variation in mass and density across the plate as identified in table 5.3. Group 1 of cubes had already been removed prior to optical imaging. This configuration would also allow for insight into whether particular build parameters resulted in a more significant variation in mass and density across the plate however this is unlikely to be the case.

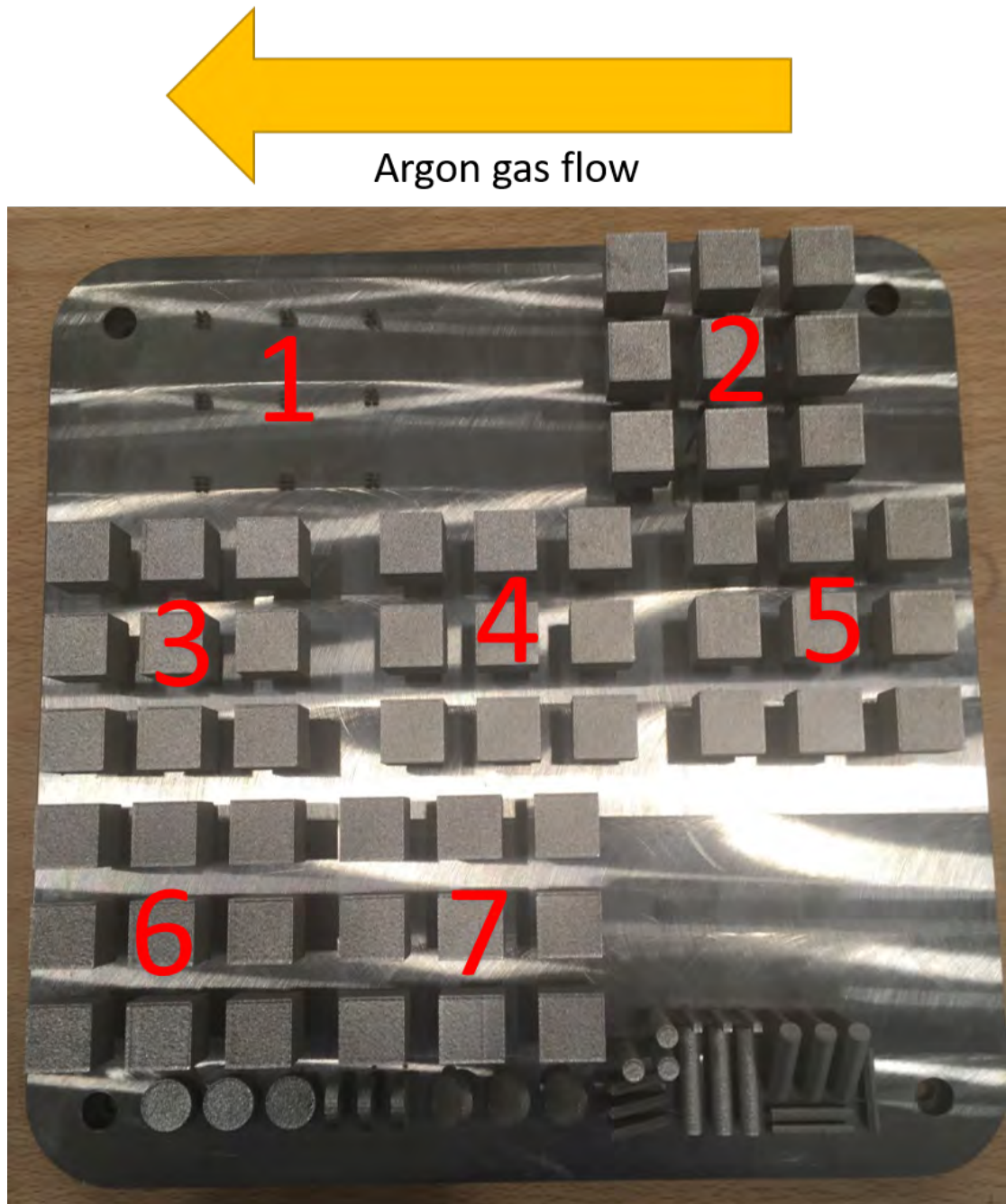


FIGURE 5.3: Build 3 with L9 arrays numbered, note sample 4 was produced using optimum parameters as supplied by Renishaw and sample 9 being the authors choice of parameters. Parameters are visible in table 5.3.

There is a small horizontal area along the bottom of the build plate containing parts for other pieces of work which are not relevant. These parts were placed in this region to minimise their affects on the remainder of the build. Ideally, a comprehensive study would not include any additional parts on the build plate. However the AM 400 is in constant use and smaller builds which take up a small percentage of build plate space are routinely placed on available space on larger planned builds. Whilst this scenario

is more akin to how an AM machine would be used in industry it is not optimum for learning and understanding the basic fundamental principles at play in AM. Mass and density measurements were carried out using a One attention force tensiometer following the methodology set out in section 3.10 on each of the printed cubes.

The mass and density measurements for each cube are displayed in tables 5.4 and 5.5 respectively along with standard deviation values across groups 1 - 9 calculated from multiple repeated measurements of each cube within that group.

Figures 5.5 and 5.6 show the mean density measurement of cubes as a representation of cube and block number respectively. The solid line displaying the average density allows the trend of the data to be visible. Figure 5.5 shows that there is significant variation in the recorded density of identical samples built with the same build parameters at different locations on the build plate. Cube 1 for example had the largest % in density across blocks as shown in table 5.5 with a measured relative density of 99.90 % within block 1 and measured relative density of 98.15% in block 3. Comparatively, cube 9 produced the lowest variation in density with respect to block location with a variation of 0.326 %. The highest recorded mean density was sample 4, the optimum parameter set supplied by Renishaw with a mean relative density of 99.64 %. Figure 5.6 displays the mean measured density of each cube plot with respect to the block that cube is located in. The block layout is visible in figure 5.3. The conclusion that can be garnered from figure 5.6 is that despite the seemingly large spread of points for each block with different cubes densities varying across blocks the overall average density across each block remains fairly constant. The mean measured density across the entirety of the blocks ranges from 99.26 % to 99.37 %. Such a small variation from block to block gives confidence to the user that the variation in density across the location in the build plate is small for the 316L powder used when building with the build parameters used in this study. Whilst the block with the highest recorded average density was block 5 at 99.37 % the mean average density across each block was 99.32 %. Such small differences in density are difficult to quantify using the equipment and method used as outlined in section 3.10. Figure 5.4 shows the average density of all LPBF printed 316L parts plotted against line speed and VED with a superimposed non-linear curve to increase the visibility of the trend. The data seems to show that there is a general inverse relationship between VED and line speed which is logical. There also seems to be a correlation wherein parts printed with higher VED and lower line speeds have the highest measured densities. The logical explanation for this is that the line speed is a product of the hatch spacing and the exposure time and the point distance, decreasing the point distance and increasing the exposure time results in a reduced line speed. This corresponds to the laser introducing more energy through heat to the system per unit area resulting in a reduction in the number of unmelted powder particles in the build. This pattern continues up until the point wherein keyhole

Sample	Block 1	Block 2	Block 3	Block 4	Block 5	Block 6	Block 7	S.Dev	Average Value (Mass)	Variation	Variation (%)
1	31.880	31.590	31.398	31.754	31.786	31.486	31.711	0.160	31.658	0.482	1.523
2	31.565	31.752	31.673	31.856	32.025	31.701	31.971	0.154	31.792	0.460	1.447
3	31.835	31.929	32.010	32.040	32.048	31.966	31.989	0.068	31.974	0.213	0.666
4	31.702	31.958	31.762	31.968	31.980	31.704	31.905	0.117	31.854	0.278	0.873
5	31.844	31.925	31.880	32.024	32.118	31.857	32.056	0.100	31.958	0.274	0.857
6	31.903	32.060	32.028	32.093	32.108	31.966	31.999	0.067	32.022	0.205	0.640
7	31.723	31.983	31.685	31.940	31.930	31.689	31.906	0.122	31.837	0.298	0.936
8	31.673	31.767	31.539	31.767	31.970	31.704	31.797	0.122	31.745	0.431	1.358
9	31.922	32.065	32.043	32.062	32.045	31.901	31.928	0.069	31.995	0.164	0.513
Mean	31.783	31.892	31.780	31.945	32.001	31.775	31.918		31.871	0.312	0.979

TABLE 5.4: Recorded 316L masses by cube and block number in grams.

welding becomes prominent and spatter is expunged from the melt pool resulting in a reduction to build density and increased elemental segregation [18][14]. Whilst the 316L parts printed in this work were not taken to high enough VED levels to visualise this effect as demonstrated by the non reduction of measured density at higher VEDs in figure 5.7. This effect is visible in the density VED curve presented for 17-4PH in figure 7.1 as the measured density decreases in the $VED > 90 \text{ J mm}^{-3}$ region.

Maybe some samples with certain build parameters are suited to different locations on the build plate or being surrounded by samples of certain build parameters??

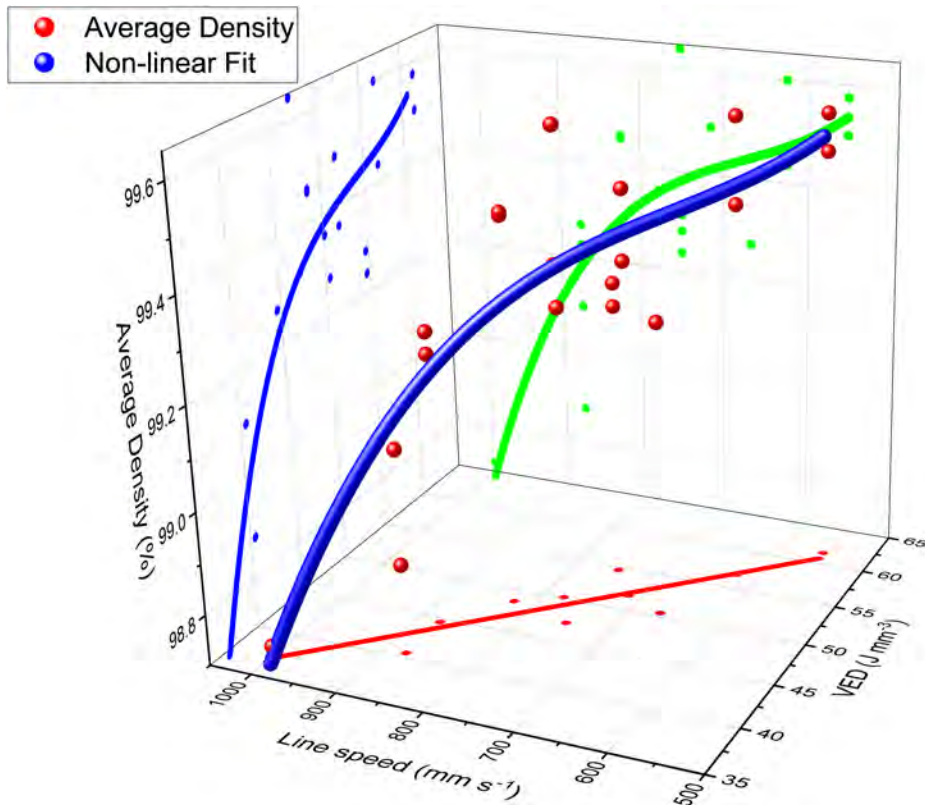


FIGURE 5.4: Mean density all LPBF 316L parts against VED and line speed fitted with a non-linear curve.

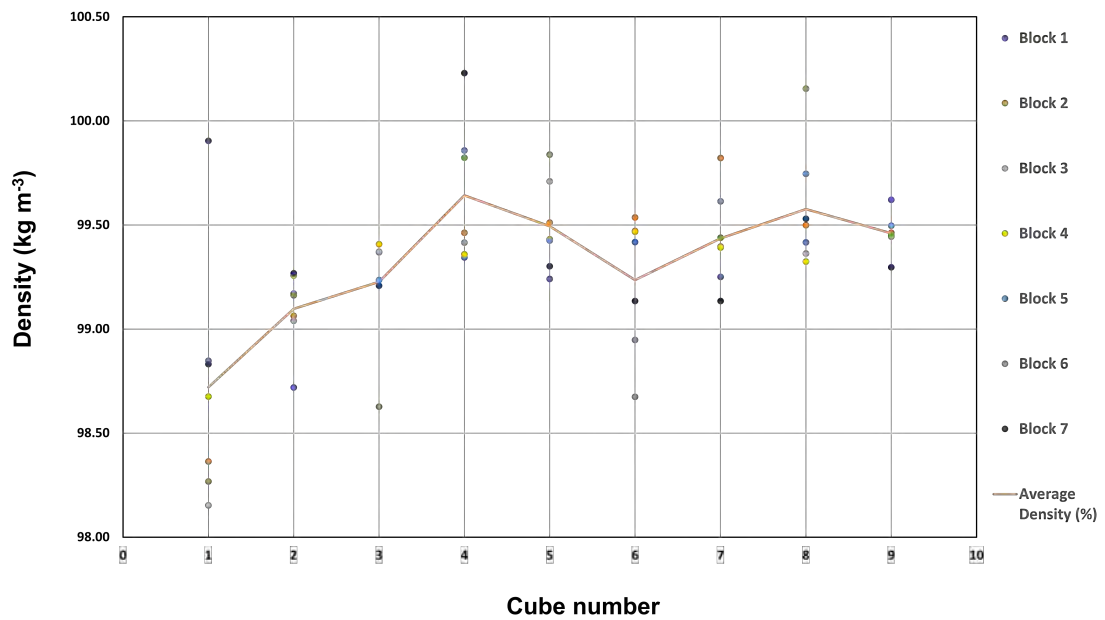


FIGURE 5.5: Density of build 3 316L parts by cube number.

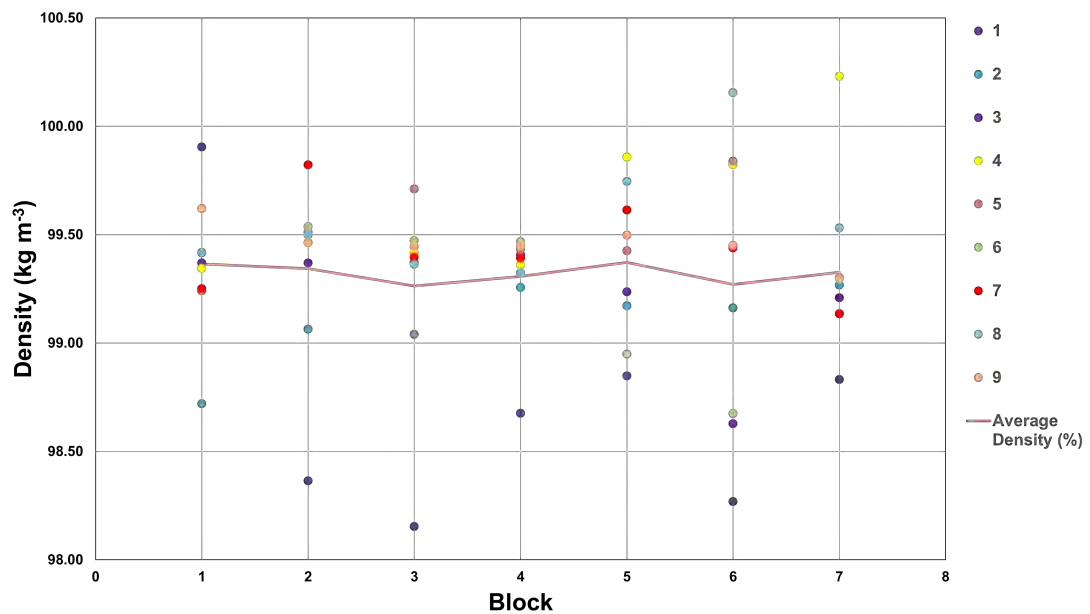


FIGURE 5.6: Density of build 3 316L parts by block.k

With regards to variation in density with respect to any given build parameter the overall impact of varying a single parameter was found to not be significant. There was however a trend relating the measure density of a part with the line speed which is a combination of the exposure time and the point distance. This trend is displayed in figure 5.8 wherein increasing the line speed results in a decreased measured density.

Sample	Block 1	Block 2	Block 3	Block 4	Block 5	Block 6	Block 7	S.Dev	Average Value	Variation	Average Density (%)	Variation (%)
1	7.982	7.859	7.842	7.884	7.898	7.852	7.897	0.044	7.888	0.140	98.72	1.774
2	7.888	7.915	7.913	7.931	7.924	7.923	7.931	0.014	7.918	0.044	99.10	0.553
3	7.940	7.940	7.940	7.943	7.929	7.880	7.927	0.020	7.928	0.062	99.23	0.786
4	7.938	7.947	7.943	7.939	7.979	7.976	8.008	0.025	7.961	0.071	99.64	0.889
5	7.929	7.951	7.967	7.945	7.944	7.977	7.934	0.016	7.950	0.048	99.49	0.600
6	7.943	7.953	7.948	7.947	7.906	7.884	7.921	0.024	7.929	0.069	99.24	0.869
7	7.930	7.976	7.942	7.941	7.959	7.945	7.921	0.017	7.945	0.055	99.44	0.691
8	7.943	7.950	7.939	7.936	7.970	8.002	7.952	0.021	7.956	0.066	99.58	0.834
9	7.960	7.947	7.946	7.946	7.950	7.946	7.934	0.007	7.947	0.026	99.46	0.326
Mean	7.939	7.938	7.931	7.935	7.940	7.932	7.936		7.936	0.065	99.321	0.8149

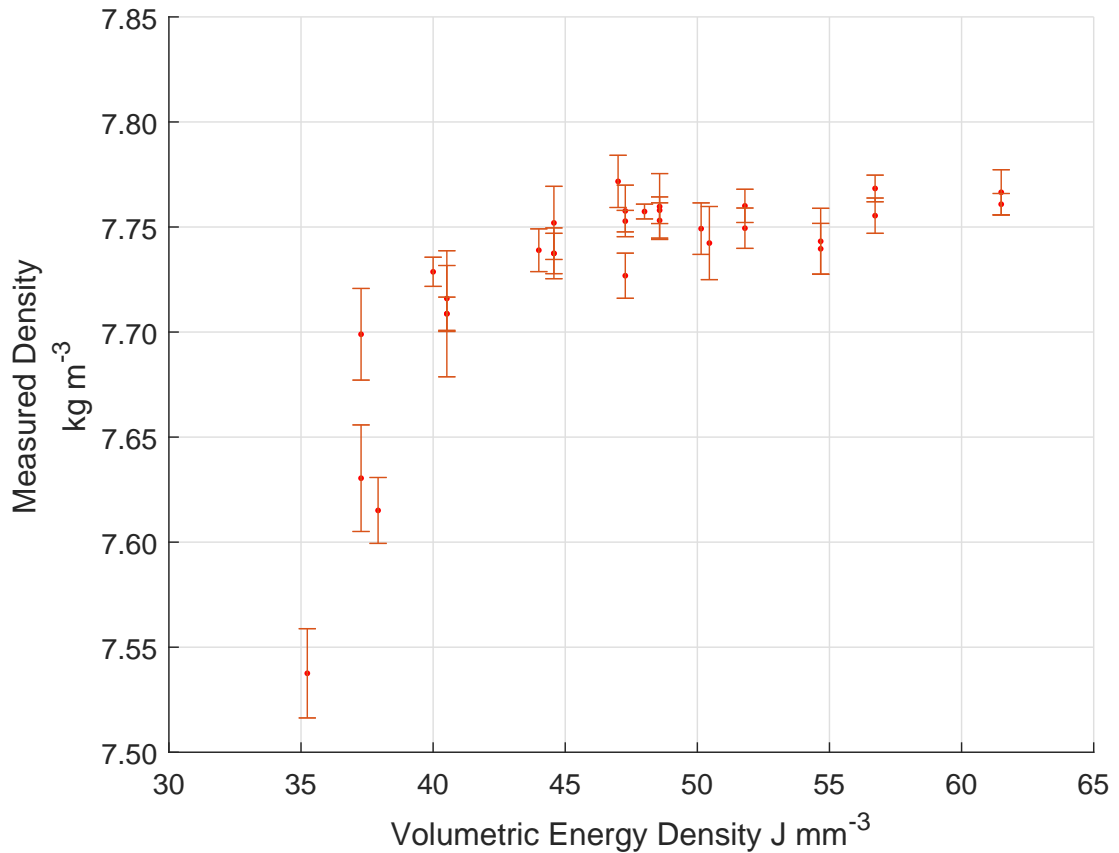
TABLE 5.5: Recorded 316L densities (kg m^{-3} by cube and block number.

FIGURE 5.7: Graph showing the density of all tested 316L parts with respect to V.E.D.

5.3 Optical porosity measurements

Optical density measurements were made following the procedure outlined in section 3.11. The values recorded alongside the relevant Archimedes density measurements and their differences are presented in table 5.6. The optical density measurements produced density measurements higher than that produced from the Archimedes method in all samples apart from samples 5 and 8. There is a considerable difference between the optical Archimedes density results with samples 2 and 3 producing differences of 0.82 % and 0.65 % respectively. There are numerous explanations that can explain the difference in the reported densities from these tests. The Archimedes method produces a density measurement on the entirety of the sample that is submerged within the liquid. The

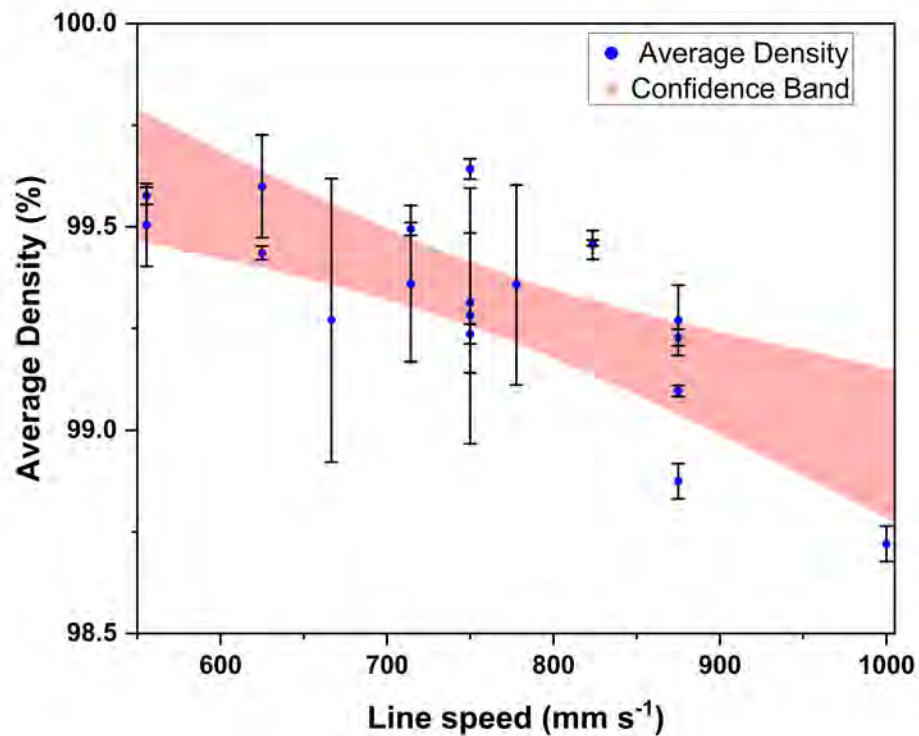


FIGURE 5.8: Line speed against relative density of all 316L parts produced by LPBF against line speed with a 95 % confidence band shown in pink.

optical method produces a density measurement of the particular slice that has been imaged. Whilst figure 5.11 shows that porosity there is a variation in the porosity distribution in each axis. Further to this the optical method are limited by their ability to resolve tiny porosity regions. Effectively the Archimedes method produces a bulk density measurement applicable to the entirety of the sample whilst the optical method produces a localised density measurement for a particular slice/cross-section. The combination of each slice without needing to metallurgically prepare samples and machine apart samples is possible using CT scanning methods. The downsides of this technique however are that expensive machinery and specific knowledge and training is required to carry out the scanning as oppose to the accessible optical and Archimedes methods.

Sample	Archimedes Density (%)	Optical Density (%)	Difference
1	98.72	98.95	0.23
2	99.10	99.92	0.82
3	99.23	99.88	0.65
4	99.64	99.19	0.26
5	99.49	99.19	-0.30
6	99.24	99.58	0.34
7	99.44	99.56	0.12
8	99.58	99.13	-0.45
9	99.46	99.57	0.11

TABLE 5.6: Density measurements from Archimedes and optical density methods.

5.4 CT scanning

CT scanning was carried out on sample built using the same build parameters as sample 4 listed in table 5.6 following the method outlined in 3.13. Figure 5.12 shows the difference between image reconstruction using the volume and projection methods. The volume method which creates a 3D render using alpha blending, with higher detail and "better looking" results coming from a larger sampling value. The projection method projects voxels using the alpha values as a weighting factor. In general, the volume method produces better images but takes considerable more time to render. In order to view only the porosity present within a sample the image thresholding must be inverted such that areas filled with gas (porosity) are marked as containing data and areas containing solids (metal) are marked as not containing any data. The CT reconstructed images as presented in figures 5.10 and 5.11 show that the majority of porosity located at the scan regions of the sample are conglomerated in the regions nearby to the 2 exterior surface of the scanned samples. Additionally, the geometry of the porosity displayed is mostly of prolate spheroid shape in nature with no large lack of fusion porosity visible in any of the reconstructed CT images. For reference an irregularly shaped lack of fusion porosity defect imaged on a lower density 316L sample is given in figure 5.9. A video representation of the 3D reconstructed CT image is shown in supplementary Video 2. Whilst there are no scale bars attached to the 3D reconstructed CT images please note that the length of each side of the scanned CT slice is approximately 3mm in length.

The data presented in 5.7 displays the density measurements as measured on the sample using the Archimedes principle as outlined in section 3.10. The table also contains calculated average and largest pore size values produced using the method outlined in 3.13. The CT data average value is identical to two decimal places to the Archimedes

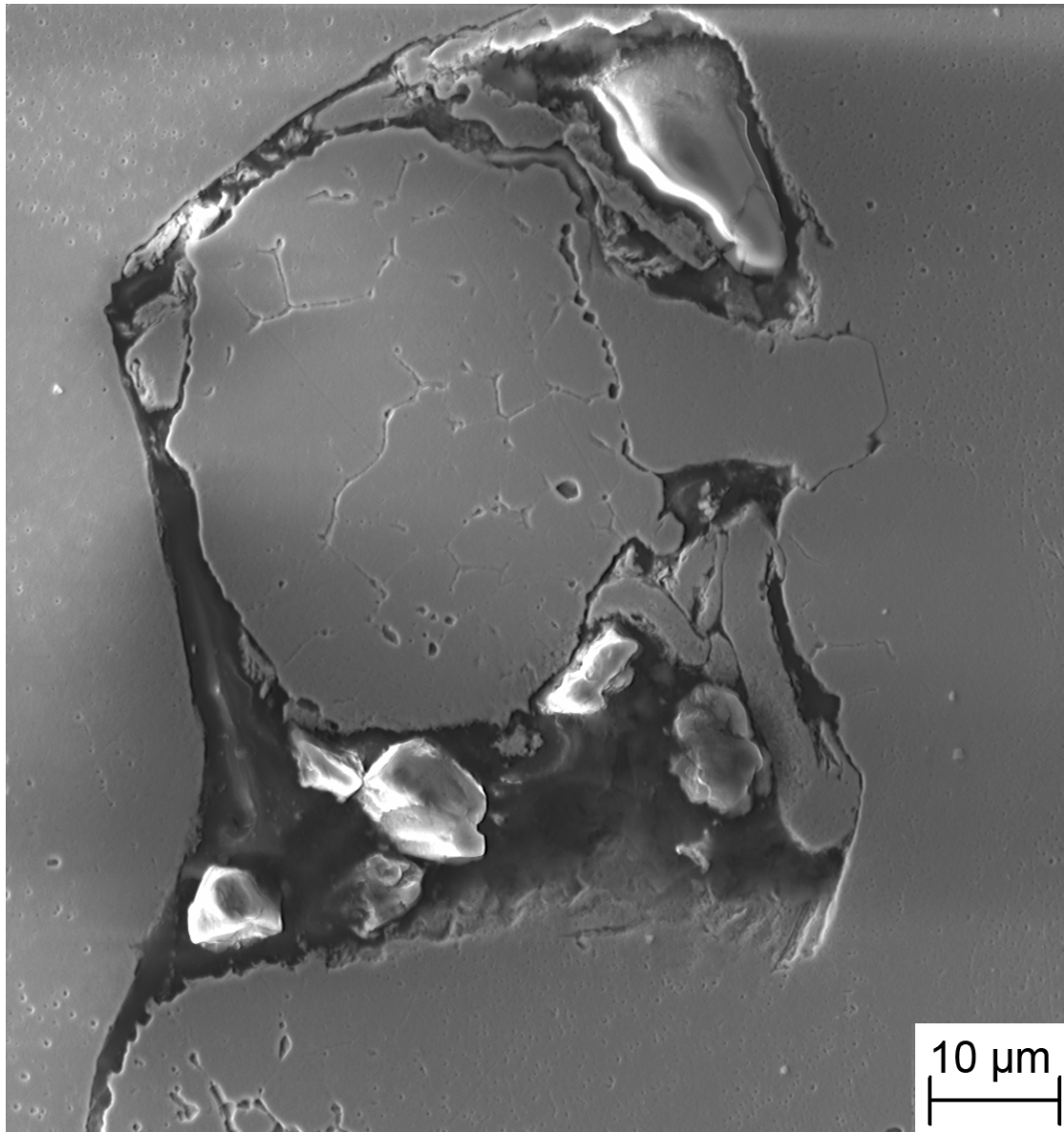


FIGURE 5.9: SEM micrograph showing a lack of fusion porosity defect in LPBF 316L with partially and/or completely unmelted powder trapped in the defect.

measurement despite the CT data being averaged across two separate scans. This suggests that both methods are able to produce density measurements to a high resolution for these conditions wherein the density of built parts is approaching 100 % density. The largest and average pore values are displayed as areas as the porosity areas are measured slice by slice on the thresholded files. The author was unable to find a way to accurately retrieve the volume of specific porosity regions using free software. Whilst an average porosity volume would be possible the reliability of this value would be low and effectively meaningless given the large discrepancy in the volume of porosity across the entirety of the samples. Given the assumption that the dominant shape of porosity in these samples is generally roughly spherical then it the task of converting an area to a

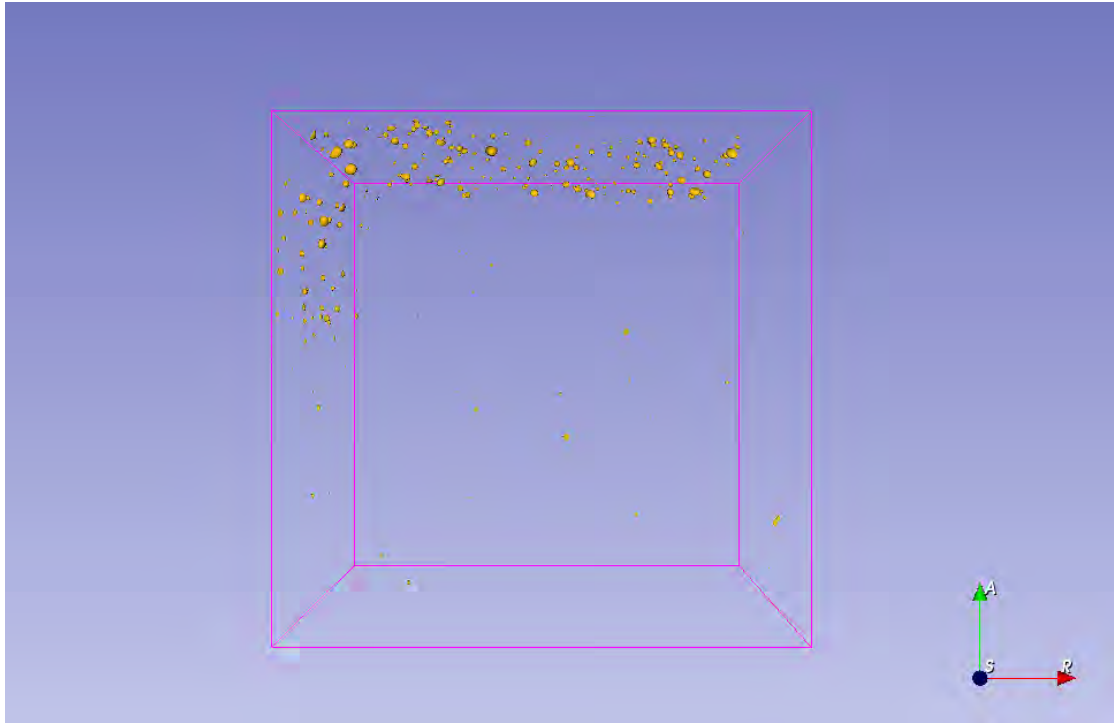


FIGURE 5.10: 3D reconstructed image of porosity within sample from top down view.

Test Method	Density(%)	Largest pore diameter (mm ²)	Average pore diameter (mm ²)
Archimedes measurement	99.86	-	-
CT data top	99.92	0.534	0.0164
CT data bottom	99.79	0.951	0.0030
CT data average	99.86	-	0.0045

TABLE 5.7: CT porosity data.

volume is trivial but the resulting values will be over estimates as spheres are the shape with the highest volume to surface area ratio of all three dimensional shapes as a consequence of the isoperimetric inequality in three dimensions [145]. In such case the largest volume porosity's for top and bottom would be 0.077 and 0.450 mm³. The largest pore area measured within the top scan was almost double that of the bottom scan, with both of the largest diameters being significantly larger than the average pore diameter. This suggests a large variation in the size of porosity spread throughout the scanned samples.

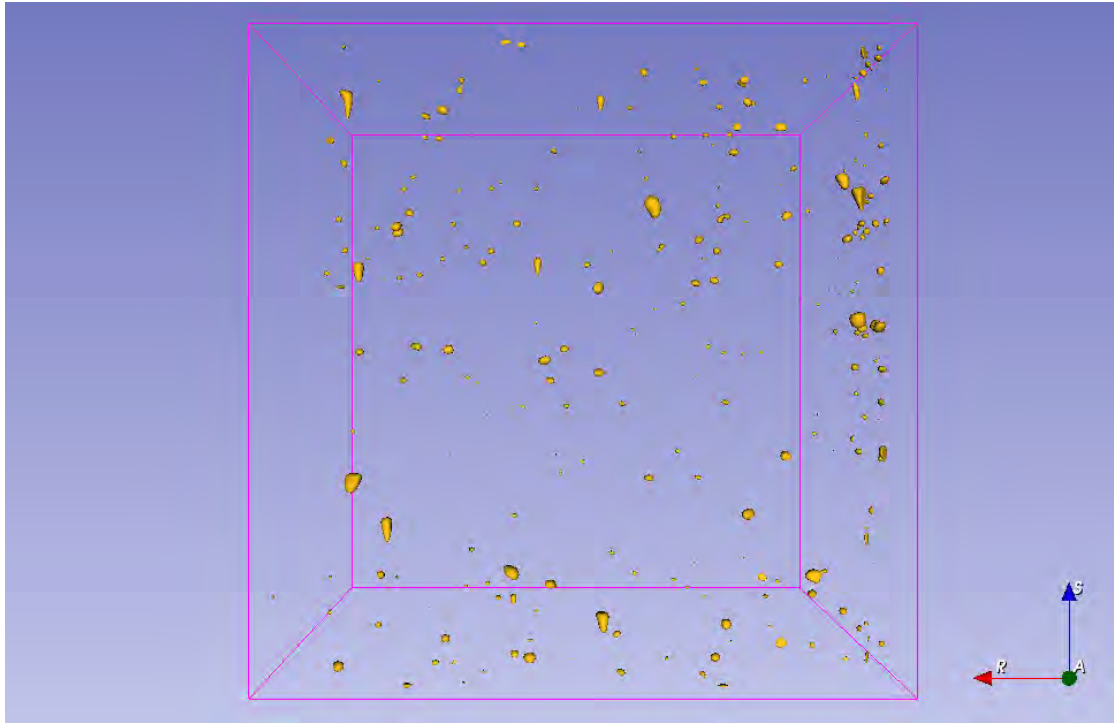


FIGURE 5.11: 3D reconstructed image of porosity within sample from side on view.

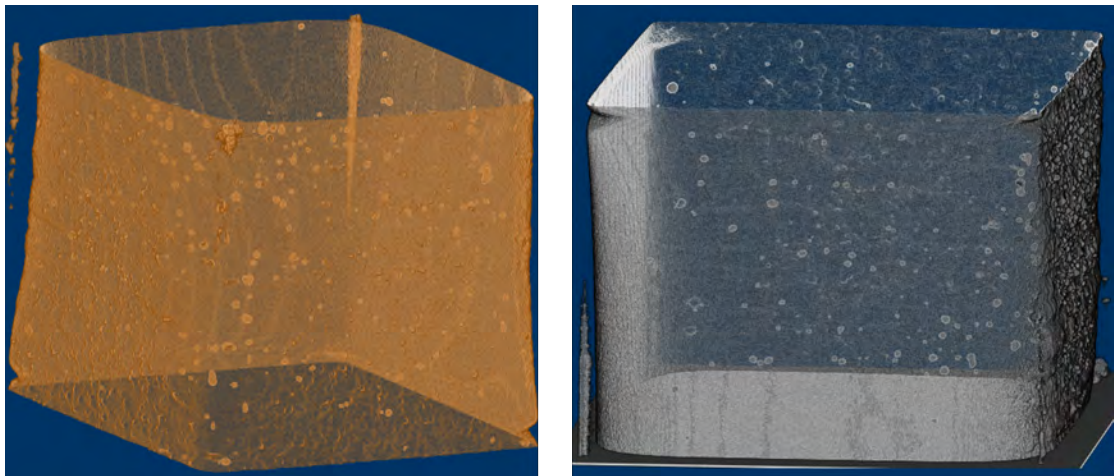


FIGURE 5.12: 3D reconstructed image of sample (bottom scan) using projection (left) and volume (right) reconstruction methods.

5.5 Corrosion testing

Deaerated potentiodynamic scanning was carried out on LPBF manufactured 316L and wrought samples following the procedure outlined in section 3.8.2 using 3.5% NaCl electrolyte. Figure 5.14 shows potentiodynamic scans from sample 1 and from the wrought sample. The behaviour of the samples is similar with each sample transitioning from open circuit potential to a passive region. The current densities recorded in these passive regions however is significantly different with the AM sample recording a current density

an order of magnitude larger than the wrought sample (5×10^{-4} vs 5×10^{-5}) Acm^{-2} respectively. This was a trend across all potentiodynamic tests in general wherein the passive region current densities were larger for AM than wrought samples. With increasing potential the scan shifts into the active region with clearly defined pitting potentials before the scanning potential is reversed. In the reversed scanning direction the wrought sample is shown to repassivate at a potential of -0.1V vs. SCE. Whilst the reversed scan on sample 1 does cross the upward scan this occurs below the passive region at a potential of -0.4V vs. SCE. Metastable pitting is not observed in either of the samples passive region. There is a difference in the current densities recorded on both materials wherein the wrought sample scan whilst having a similar loop size to Sample 1 generally recorded current densities one orders of magnitude lower than sample 1. Similar increased current densities are reported on AM 316L SS compared to wrought in potentiodynamic testing carried out in $1\text{N H}_2\text{SO}_4$ [146]. Table 5.8 and Figure 5.13 display the pitting and repassivation potential of as-built 316L samples produced by LPBF. Note that there is no repassivation potential for the sample with 99.24 % density as this sample did not repassivate in any test. Further to this, there are no error bars on the repassivation of sample with density 99.36 % as this sample only repassivated in one of its tests. The sample at 100% density is the wrought sample. Five of the nine LPBF manufactured samples produced mean pitting potentials higher than those measured on the wrought samples. These were samples 1, 2, 7, 8 and 9. Despite this, the error associated with the pitting potentials of the LPBF samples were significantly larger than that of the wrought samples. The mean standard deviation in pitting potential across the LPBF manufactured parts was 0.093 compared to 0.008 for the wrought parts. Considering the extreme values of the error bars the only LPBF manufactured part with a higher pitting potential than the wrought sample was sample 1 with a mean pitting potential of 0.709 ± 0.041 (V vs. SCE). Subsequently however this sample was only able to repassivate in one of the three tests. Figure 5.15 displays the OCP values recorded prior to potentiodynamic samples. The left image shows data taken from AM parts and the right image shows data taken from wrought samples. The OCP data is displayed on the same Y axis scale to portray the difference in values recorded not just between different samples but between the variation in OCP values as time progresses. Please note the 1 line in the left image that stops short of 900s was stopped and not potentiodynamically scanned due interference out of the authors control. The figure shows that there is low variation in the recorded OCP of the wrought samples compared to the large variation associated with the LPBF parts. The OCP values recorded for the LPBF varied significantly more over time than the wrought at a larger range of potentials. The large spread implies that some LPBF samples were actively corroding or there were in differences in surface oxides at OCP conditions. For example the presence of porosity at the surface of a sample could undergo localised corrosion immediately upon immersion in the electrolyte.

Sample	Density (%)	Pitting Potential (V vs. SCE)	Error (SD)	Repassivation Potential (V vs. SCE)	Error (SD)	OCP (V vs. SCE)	V.E.D (J/mm ³)
1	99.36	0.709	0.041	-0.260	-	-0.485	37.27
2	99.23	0.648	0.080	-0.138	0.026	-0.433	40.52
3	99.22	0.084	0.022	0.123	0.232	-0.456	44.58
4	99.64	0.480	0.055	-0.116	0.034	-0.479	47.27
5	99.49	0.356	0.047	-0.100	0.028	-0.394	51.80
6	99.24	0.639	0.132	-	-	-0.429	54.66
7	99.44	0.577	0.110	-0.096	0.089	-0.446	56.73
8	99.58	0.642	0.194	-0.087	0.067	-0.404	61.50
9	99.46	0.663	0.154	0.095	0.189	-0.444	48.57
Wrought	100	0.576	0.008	-0.103	0.0009	-0.471	-

TABLE 5.8: Table containing corrosion data from potentiodynamic scans on 316L samples produced by LPBF.

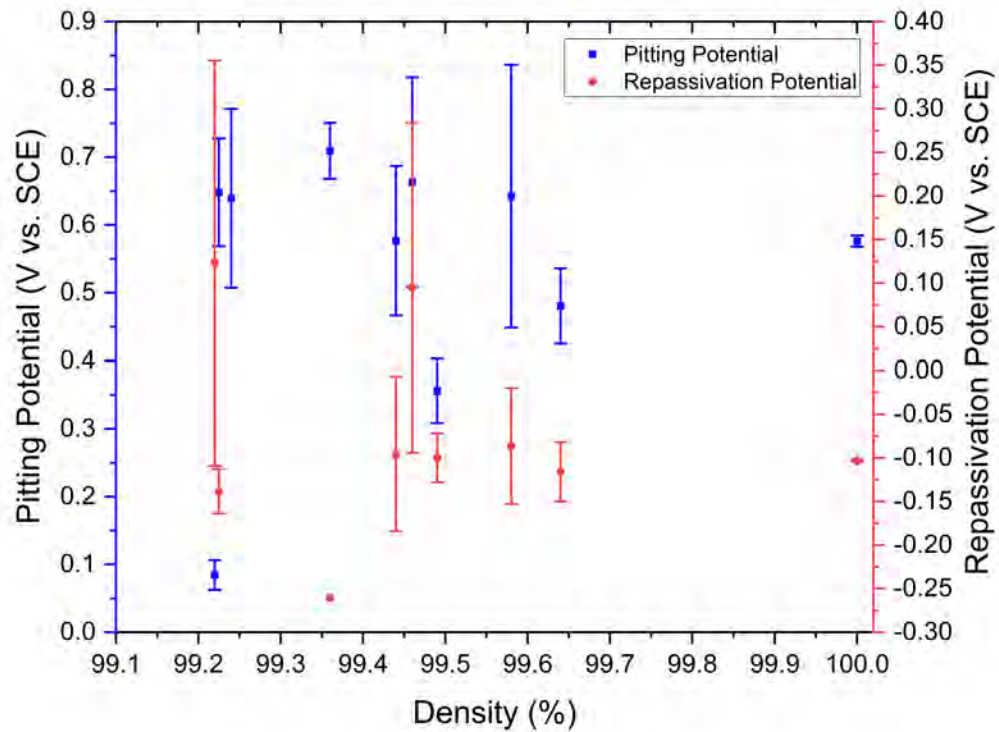


FIGURE 5.13: 316L pitting (blue squares) and repassivation (red circles) potentials plotted against relative sample density, where wrought samples have 100 % density.

The data shows that there is no clear correlation between the measured density of a sample and the resulting pitting or repassivation potentials recorded in this work. The lack of trend continues whether plotting pitting potential against volumetric energy density, open circuit potential or any build parameter (laser power, exposure time, point distance or hatch spacing). The large variation in recorded pitting potentials suggests a low confidence in the performance of the material in corrosive environments. Table 2 presented by Laleh et al. further demonstrates the low repeatability of AM 316L pitting potentials [93]. The lack of relationship and high variation is thought to be due to the nature of pitting

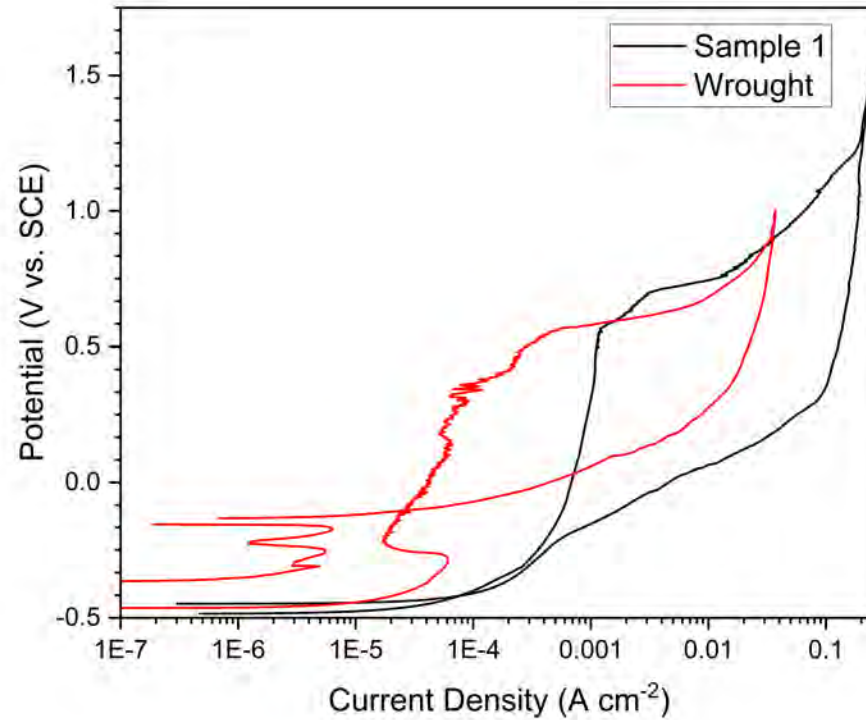


FIGURE 5.14: Potentiodynamic scan of LPBF sample 1 and wrought 316L sample.

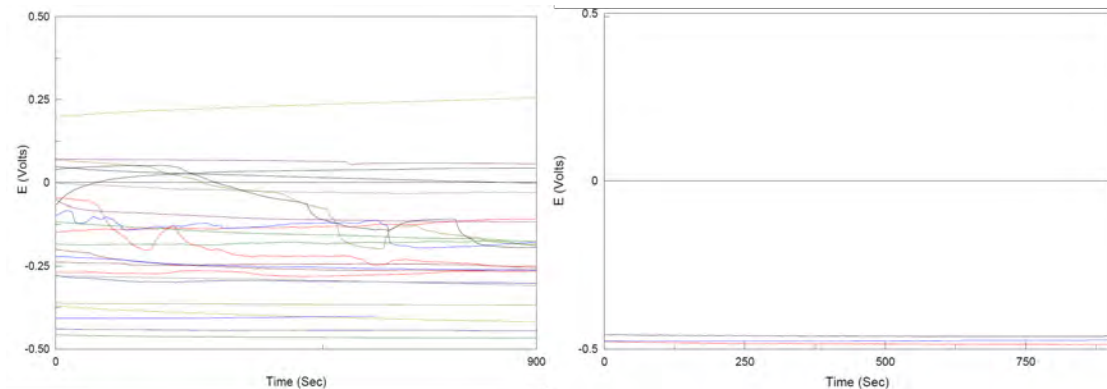


FIGURE 5.15: OCP recordings taken on samples prior to potentiodynamic scanning
Left: AM specimens, Right, Wrought specimens.

initiation wherein localised defects on sample surfaces can result in surface conditions more conducive to the facilitation of active corrosion pits [31][100]. The distribution of porosity as shown in section 5.4 is distributed randomly throughout external facing surfaces this suggests that despite the measured density of the part any localised region of porosity on a sample surface can result in localised corrosion attack. One must also consider the range of sample densities presented in this chapter. Densities range from 99.22 % to 99.64 % , a range of 0.42 % for LPBF parts. This relatively small range may

be the reason for not seeing a large variation in pitting potential against density as even the lowest density sample of 99.22 % is still comparatively high. Sander et al. concluded that once a density of 99.6% is reached that porosity is no longer a controlling factor in stable pitting in AM 316L [98]. This may be the case assuming the material consists of entirely spherical porosity however the presence of a singular large lack of fusion pore in a 99.95 % sample would be far more detrimental than an even distribution of spherical porosity in a sample of lower relative density [93]. This highlights the need for optimising build parameters in AM to produce high density parts with no lack of fusion porosity as displayed in figures 7.4, 5.11 and 5.12. Rather coincidentally sample 8 with a measured density of 99.58 % in figure 5.13 has error bars significantly larger than those of sample 4 with a measured density of 99.64 %. However the LPBF sample with the smallest error bars is that of sample 3 with a measured density of 99.22 %, the lowest recorded density in this chapter. If the porosity content on the samples surface is indeed the cause for the large variation in pitting potential of LPBF manufactured parts there are several ways of circumnavigating this issue. These include post-production treatments including furnace annealing and HIP to alleviate porosity. Additionally if the results shown in section 5.4 are found to be consistent across builds and build parameters then the solution could be as simple as machining away the outer regions of LPBF produced parts.

In summary, whilst some of the recorded corrosion metrics on LPBF 316L parts are superior to the wrought parts in general the scatter associated with these values is significantly larger than that of the wrought part. If this large variation in corrosion metrics is due to the inherent porosity located on the surface of the LPBF manufactured parts then removing this porosity via post-production methods may be necessary to provide manufacturers with the confidence that LPBF manufactured parts can perform similarly if not better than traditionally manufactured 316L in corrosive environments.

5.6 Conclusions

The work presented in this chapter has shown that the parameters used to manufacture LPBF 316L have produced parts of high density whose variation in mass and density is not significant across the build plate. The CT scan reconstructed images reveal the presence of prolate spheroidal porosity located predominantly on the outer surface regions of the sample with no large lack of fusion porosity defects visible. The corrosion testing revealed that the inherent porosity within the LPBF 316L material resulted in larger variations in the OCP, pitting potential and other corrosion metrics compared to the wrought part despite the low porosity in the parts and lack of fusion porosity defects in the material.

6. The mechanical and corrosion properties of additively manufactured 316 L treated by HIP

6.1 Introduction

As mentioned throughout this thesis and numerous academic papers porosity is a major problem with AM parts. Post production treatments can be used to optimise materials for a number of purposes and applications. HIP treatments involve using an inert gas to exert an isostatic force on a material at an elevated temperature. The intention of this process is to reduce the porosity of samples, increasing their density. HIP cycles are controlled by three main variables; time, temperature and pressure. In some cases HIP cycles involve stages at multiple temperatures and pressures. The novelty aspect of this work is that traditionally HIP cycles have been designed to optimise the mechanical properties of components whereas this work will also incorporate the corrosion performance of the HIP treated parts. Traditionally 316L parts are not subject to heat treatment, however the performance of the parts printed in this work in previous chapters suggests that this post processing is required in this work to improve the performance of the parts such that their performance is comparable to the wrought material.

6.2 Methodology

A build design was made consisting of 10 total sets of parts. Each set of parts consists of 2 cubes, 3 tensile bars and 3 cylinders which will be machined into fatigue samples post HIP treatment. It was predicted that the HIP cycle that produces the optimised mechanical properties will also produce components with the optimum corrosion performance. The cubes were sectioned into 15x15x1mm thick tokens to allow for hot mounting and polishing. These tokens were studied via optical microscopy, subject to hardness testing,

and potentiodynamic scanning. The tensile bars were treated and then pulled in a tensile testing rig and the cylinders were machined into 3 sets of fatigue samples for testing under various low cycle fatigue conditions. The details of the experimentation processes for each experiment are outlined in chapter 3.

In this work the effects of hold time were not the main consideration, instead samples were maintained at temperatures and pressures for sufficient time to allow for any microstructural changes/effects to have taken place throughout the entirety of the material. 3 temperature and 3 pressures were chosen with the intention of improving the mechanical properties and the corrosion performance of the material by reducing the porosity volume within the parts. 1 additional set was held at temperature and pressure for 60 hours to investigate the effects of a long hold. Further to this, one set was heat treated by placing the set in a box furnace heated to 1125°C for 2 hours and water quenched post HIP. The purpose of this was to benefit from the high pressure effects of the HIP whilst subsequently being heat treated and water quenched to avoid sensitisation taking place. An as-built control set was also printed which did not undergo any post-build treatments. Samples were HIP treated before being machined into their final shape for mechanical and corrosion testing. The HIP cycles and sample labels are displayed in table 6.1. The midpoint parameters chosen were based on a study carried out by Lavery et al, the temperature value of 1125°C aligns with 80% of the melting temperature of 316L [103]. The low temperature point of 700°C aligns with 50 % of the melting point of 316L. Subsequently the highest temperature achievable using the selected furnace is 1200°C. Higher temperatures are possible in this HIP system using a graphite based furnace but for the sake of fairness it was decided to use the same molybdenum furnace for each HIP run. Subsequently, the highest pressure achievable by the HIP system is 200 MPa which was selected as the uppermost pressure point for this work. The lowest pressure used of 100 MPa was selected to identify whether it is necessary to treat at a pressure above this point.

6.3 Mass and density measurements

Mass measurements were carried out on a balance with an accuracy of +/-0.0005g. Density measurements were carried out using the method outlined in sections 3.10. Since it is not possible to carry out optical microscopy on samples pre and post HIP treatment the following work uses measurements from Archimedes principle method unless stated otherwise.

It's worth noting that the values noted in table 6.2 for sample 11 were measured before the 1125°C 2 hour box furnace treatment and water quench. The results show a decrease

Number	Temperature (°C)	Pressure (MPa)
1 - HIP (T ₇₀₀ P ₁₀₀)	700	100
2 - HIP (T ₁₁₂₅ P ₁₀₀)	1125	100
3 - HIP (T ₁₂₀₀ P ₁₀₀)	1200	100
4 - HIP (T ₇₀₀ P ₁₃₇)	700	137
5 - HIP (T ₁₁₂₅ P ₁₃₇)	1125	137
6 - HIP (T ₁₂₀₀ P ₁₃₇)	1200	137
7 - HIP (T ₇₀₀ P ₂₀₀)	700	200
8 - HIP (T ₁₁₂₅ P ₂₀₀)	1125	200
9 - HIP (T ₁₂₀₀ P ₂₀₀)	1200	200
10 - As-built	-	-
11 - HIP (T ₁₁₂₅ P ₂₀₀ - long hold)	1125	137
12 - HIP (T ₇₀₀ P ₂₀₀ - quench)	700	200

TABLE 6.1: Table displaying post build treatment parameters.

Sample	316L build 4 mass and density values				HIP parameters	
	As built density (%)	Post HIP density (%)	Δ Density (%)	Δ Mass (g)	Temperature (°C)	Pressure (MPa)
1	99.24	99.53	0.29	-0.054	700	100
2	99.26	99.46	0.20	-0.045	1125	100
3	99.11	99.40	0.29	-0.048	1200	100
4	99.41	99.41	0.00	0.009	700	137
5	99.29	99.49	0.26	-0.062	1125	137
6	99.29	99.35	0.06	-0.020	1200	137
7	99.24	99.38	0.14	-0.034	700	200
8	99.18	99.46	0.28	-0.057	1125	200
9	99.11	99.42	0.30	-0.085	1200	200
10	99.27	-	-	-	-	-
11	99.35	99.19	-0.16	-0.064	1125	137
12	99.34	99.48	0.14	0.001	700	200

TABLE 6.2: Table displaying the mass and density change of cubes printed and treated using various HIP cycles measured using the Archimedes principle.

in mass of the cubes after HIP treating in all samples apart from samples 4 and 11 which show a minuscule increase in mass. Ascertaining whether these decreases in mass are due to an actual effect or just the variability of using a balance is difficult. One possible explanation to explain the decrease could be that any gas trapped inside the samples from the AM process has been removed from the samples during the HIP process.

Sample 10 which was treated with a 60 hour hold time was found to have a decrease in density after HIP treatment, this could be due to the samples being held at pressure and therefore subject to external forces for extended periods of time distorting the shape of the sample and increasing its volume resulting in a decrease in measured density. The measured density of 4 - HIP (T₇₀₀ P₁₃₇) neither increased nor decreased after the HIP treatment. Apart from this sample every set treated for 4 hours had an increased measured density after HIP treatment.

The increase recorded in density across the range of HIP parameters is fairly consistent across the range of treatments, ranging from 0.06 to 0.30 % with an average increase of 0.22 % with a standard deviation of 0.08. This indicates that the variability in the increase of density as a result of these HIP treatments is low. The highest recorded density post treatment was 99.53 %. This value is comparable to but below the highest density measurement produced in build 3 of 316l of 99.64 %. This highlights the fragility and sometimes low repeatability results when producing material using AM even when time and consideration is put into optimising build parameters. Cycle 9, with the highest temperature and pressure used produced the largest change in density however the cycle producing the overall highest density value was cycle 1, the lowest temperature and pressure used. Due to the increase in density being comparable across a large range of temperature and pressures used it is not possible to differentiate which cycle is the best overall from this data alone.

Post HIP treatment samples were also analysed using optical microscopy as outlined in section 3.11. The results of this are displayed in figure 6.1. The data shown follows the trend discussed in section 5.3 wherein the density values recorded from optical measurements are higher than those produced using the Archimedes principle method.

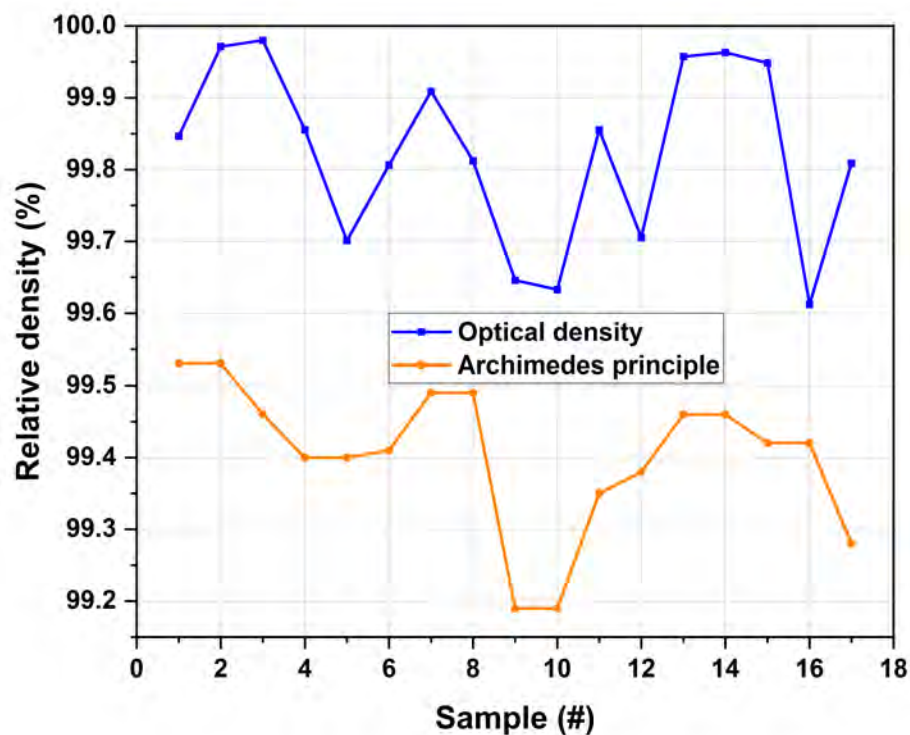


FIGURE 6.1: Comparison of density measurements made on post HIP treated samples using optical and Archimedes principle methods.

6.4 Microscopy

Each sample slice was mounted using Buehler's non conducting EpoMet fine mounting compound and metallurgically prepared by surface grinding using a Buehler Hercules SiC disc followed by polishing to a 1 μm finish using the same compound, with Buehler MetaDi supreme polycrystalline suspension for each sample. Samples were etched as detailed in table 3.2. Microstructures are displayed in figure 6.2. The wrought condition, as shown in 6.2 locations 1A, 1B and 1C demonstrates an equiaxed grain structure with no preferential directionality in grain growth. In contrast, treatment 10 - As-built, as given in Figure 6.2, locations 2A, 2B and 2C demonstrates a typical LPBF microstructure with large melt pools and melt pool boundaries that can be clearly observed. At higher magnifications (Figure 6.2 locations 2B and 2C), a sub grain cellular structure is also visible [33]. These cellular structures are less than 1 μm in length and form due to the high cooling rates experienced in the LPBF process, promoting the growth of columnar grain structures in an epitaxial manner, perpendicularly to the build plate [34].

The microstructure of treatment conditions 1 - HIP (T_{700} P_{200}), 4 - HIP (T_{700} P_{137}) and 7 - HIP (T_{700} P_{200}), which refer to the low temperature treatment, are effectively identical to the as-built microstructure with the same key features being identifiable in representative images of low temperature treatment in Figure 6.2 locations 3A, 3B and 3C.

The mid temperature treated samples, 2 - HIP (T_{1125} P_{200}), 5 - HIP (T_{1125} P_{137}) and 8 - HIP (T_{1125} P_{200}) as given in Figure 6.2 locations 4A, 4B and 4C, do not display obvious melt pools or melt pool boundaries, however it is possible to see some remnants of this structure in Figure 6.2, location 4A where larger grains run parallel to each other, surrounded by smaller grains. The sub grain cellular structure however has been removed entirely and is not visible at higher magnifications in Figure 6.2 points 4B and 4C.

The high temperature treated samples, 3 - HIP (T_{1200} P_{200}), 6 - HIP (T_{1200} P_{137}) and 9 - HIP (T_{1200} P_{200}) as displayed in Figure 6.2 locations 5A, 5B and 5C, have a noticeably larger grain size than the low and mid temperature treated samples, along with a more equiaxed microstructure. The melt pools, melt pool boundary and sub grain cellular features have been removed entirely and overall, the microstructures of the high temperature treated samples resemble that of the wrought sample in this respect. The grain size of the high temperature sample however is larger than the wrought sample. The microstructure of sample 11 - HIP (T_{1125} P_{200} - long hold), representing the long hold treatment, is portrayed in Figure 6.3 top row. The images show that this treatment produced the largest measured grain size and does not contain any of the AM microstructural associated features as discussed previously. Finally, in sample 12 - HIP (T_{700} P_{200} - quench), where the HIP treatment was followed by a furnace treatment and water quenching, the microstructure is similar to that of the mid temperature treated samples. Whilst the features associated with the AM microstructure are largely removed there remains some directionality in the microstructure as visible in Figure 6.3 bottom row. Additionally, there is a large variation in the grain size within this sample as seen in Figure 6.3 bottom row. The measured grain sizes for each of these heat treated variants are displayed in ascending order in Table 6.3 and Figure 6.4, together with their respective errors.

Sample	Grain Size (μm)
1 - HIP (T_{700} P_{100})	$16.7 \pm 4.6 \mu\text{m}$
12 - HIP (T_{700} P_{200} - quench)	$17.0 \pm 11.1 \mu\text{m}$
Wrought	$20.1 \pm 7.2 \mu\text{m}$
10 (as-built)	$32.5 \pm 7.2 \mu\text{m}$
5 - HIP (T_{1125} P_{137})	$45.0 \pm 9.7 \mu\text{m}$
9 - HIP (T_{1200} P_{200})	$58.2 \pm 9.7 \mu\text{m}$
11 - HIP (T_{1125} P_{200} - long hold)	$66.0 \pm 11.2 \mu\text{m}$

TABLE 6.3: Sample grain size (with error values) in ascending order error.

Figure 6.5 displays an SEM micrograph taken from sample 1 - HIP (T_{700} P_{200}) alongside a table showing the EDS data corresponding to the point displayed in the micrograph. Note that the error values associated with each measurement are not included because the values are small and comparable within elements across different points. The atomic percentages of iron, nickel, chromium and molybdenum remain fairly constant across each point. EDS was carried out on all samples and revealed that there were no significant examples of elemental segregation excluding build defects on samples treated at low and medium temperatures. Further to this the values displayed for carbon and oxygen are not accurate values and are for comparison purposes only. Points 1, 2, 6 and 7 were selected to be within grains, points 3, and 4 were selected to be on melt pool boundaries and point 5 was placed on a grain boundary within a melt pool.

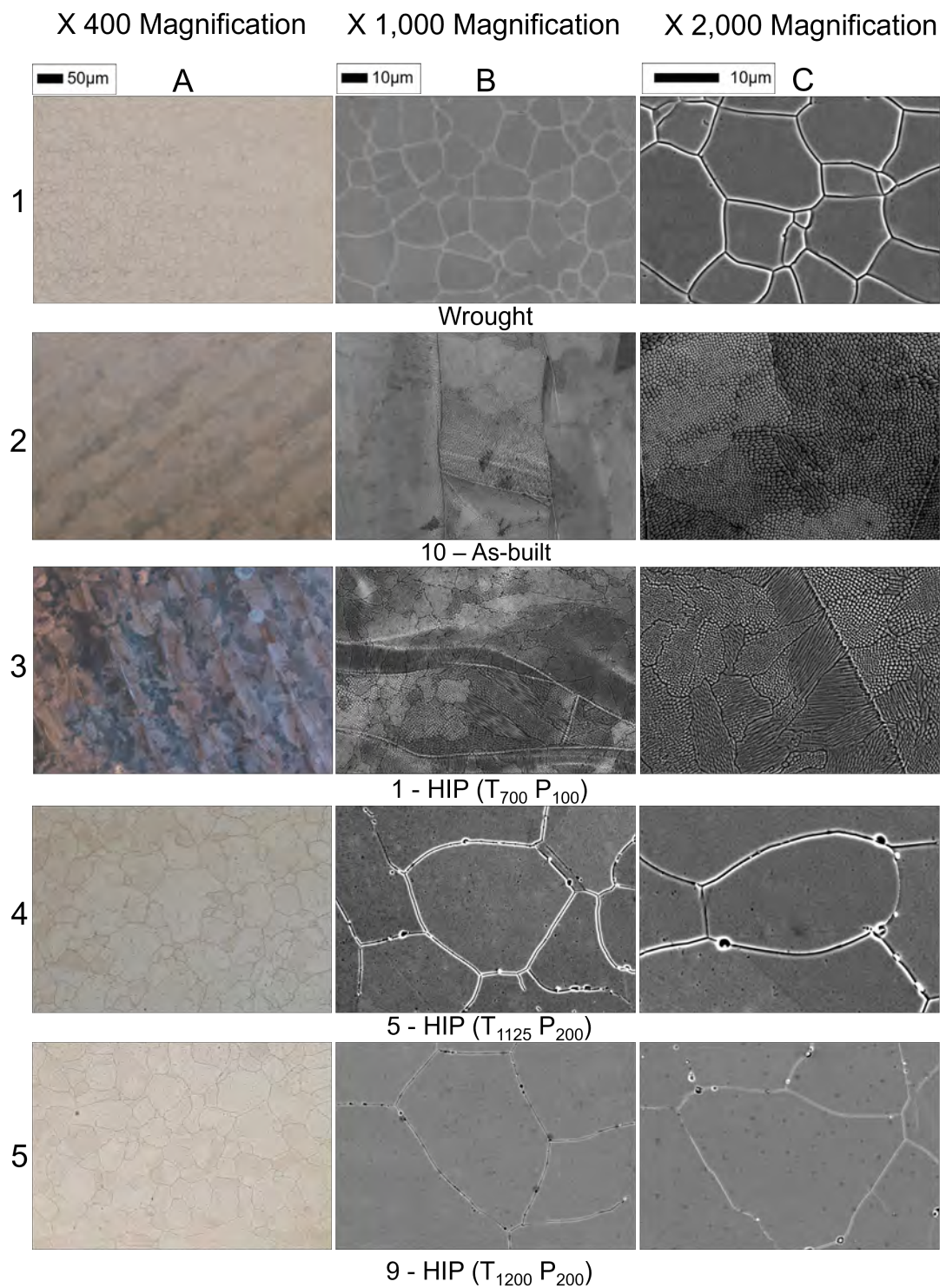


FIGURE 6.2: Microstructures of X-Y plane, parallel to the build plate for wrought, conditions 10 - As-built, 1 - HIP ($T_{700} P_{100}$), 5 - HIP ($T_{1125} P_{137}$) and 9 - HIP ($T_{1200} P_{200}$).

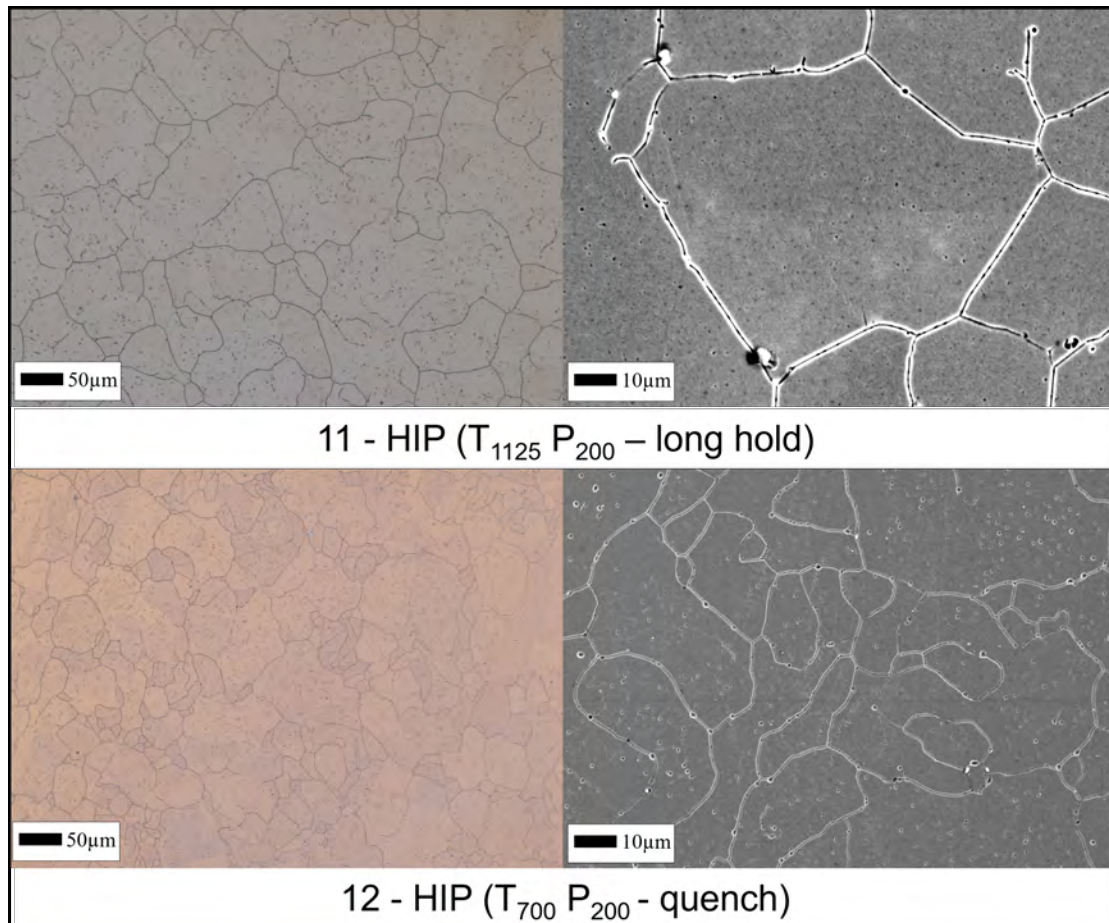


FIGURE 6.3: Microstructures of X-Y plane, parallel to the build plate for conditions 11 - HIP (T_{1125} P_{200} - long hold) and 12 - HIP (T_{700} P_{200} - quench).

There were however examples of elemental segregation found in the samples treated at the high HIP temperature point and the long hold sample. The SEM micrographs displayed in Figure 6.6 contains several white spherical objects distributed throughout the material. The elemental composition of the white spherical objects is presented in figure 6.6 at points 1 and 5. Points 2 and 4 are located within grains and point 3 is located at a grain boundary. Once again whilst the absolute values displayed of carbon and oxygen are not accurate it is evident that points 1 and 5 have significantly increased carbon and oxygen values compared to points 2, 3 and 4. Points 1 and 5 also measured a decrease in chromium, iron and nickel at these regions. This pattern is also present in the long hold sample 11. These spherical objects could also be related to the etching process due to the reduced resistance of heat treated materials to etching.

The images presented in figure 6.7 display an SEM micrograph with accompanying EDS maps taken on sample 9 - HIP (T_{1200} P_{200}). In the bottom right quarter of the SEM micrograph a round spherical object is present similar to those presented in figure 6.6. However the EDS maps reveal that this spherical object contains noticeable higher levels

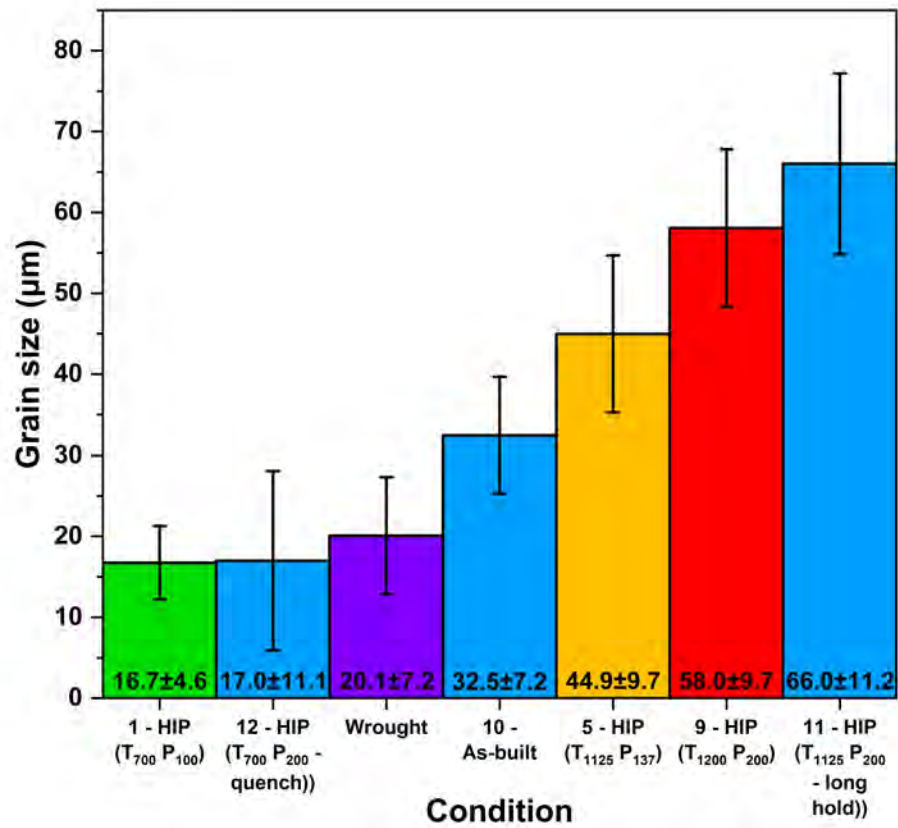
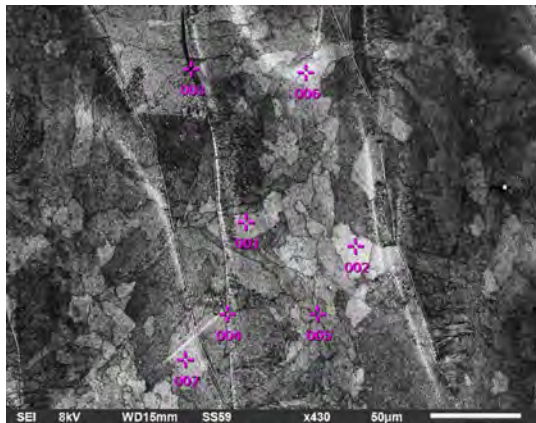


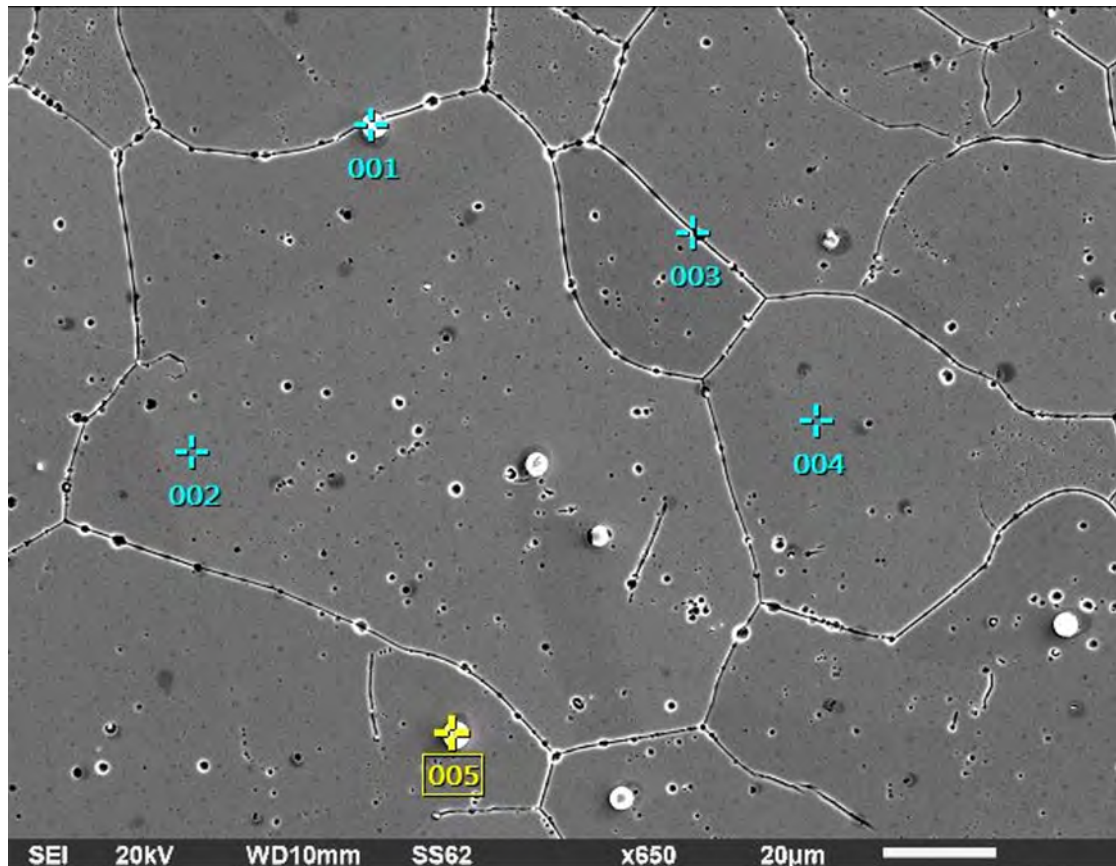
FIGURE 6.4: Measured grain sizes of samples.



Element	Atomic (%)						
	Point 1	Point 2	Point 3	Point 4	Point 5	Point 6	Point 7
Carbon	4.63	5.16	6.71	6.46	6.36	6.58	7.44
Oxygen	10.33	8.39	9.68	7.08	7.28	8.06	8.04
Silicon	1.13	0.97	0.99	0.95	0.92	0.81	0.92
Chromium	22.94	21.92	22.19	20.69	20.30	20.86	21.03
Iron	49.44	51.08	48.93	52.38	52.41	51.34	50.41
Nickel	10.62	11.56	10.55	11.59	11.88	11.57	11.39
Molybdenum	0.92	0.92	0.95	0.87	0.86	0.78	0.77
Total	100.01	100.00	100.00	100.02	100.01	100.00	100.00

FIGURE 6.5: SEM micrograph and EDS data from sample 1 - HIP (T₇₀₀ P₂₀₀).

of chromium, carbon and oxygen than the rest of the image. The spherical object is also shown to be depleted of iron. The iron EDS map also suggests a depletion of iron running along grain boundaries however the chromium map does not duplicate this at first glance.



Element	Atomic (%)				
	Point 1	Point 2	Point 3	Point 4	Point 5
Carbon	41.92	12.76	11.38	13.32	43.57
Oxygen	22.44	0.00	0.00	0.00	24.72
Silicon	0.44	1.15	0.41	0.93	0.39
Chromium	6.06	16.09	17.57	16.11	5.56
Iron	25.22	60.75	62.49	60.63	22.43
Nickel	3.69	9.26	8.15	9.01	3.33
Total	99.77	100.01	100.00	100.00	100.00

FIGURE 6.6: SEM micrograph and EDS data from sample 9 - HIP (T_{1200} P_{200}).

There is the indication of the presence of rounded particles along the grain boundaries in the SEM micrograph presented in figure 6.7. The spherical object could be contamination potentially an intermetallic from either the building process, the HIP treatment or the etching process such as chromium oxide. Further discussion on these oxides is presented in section 6.5

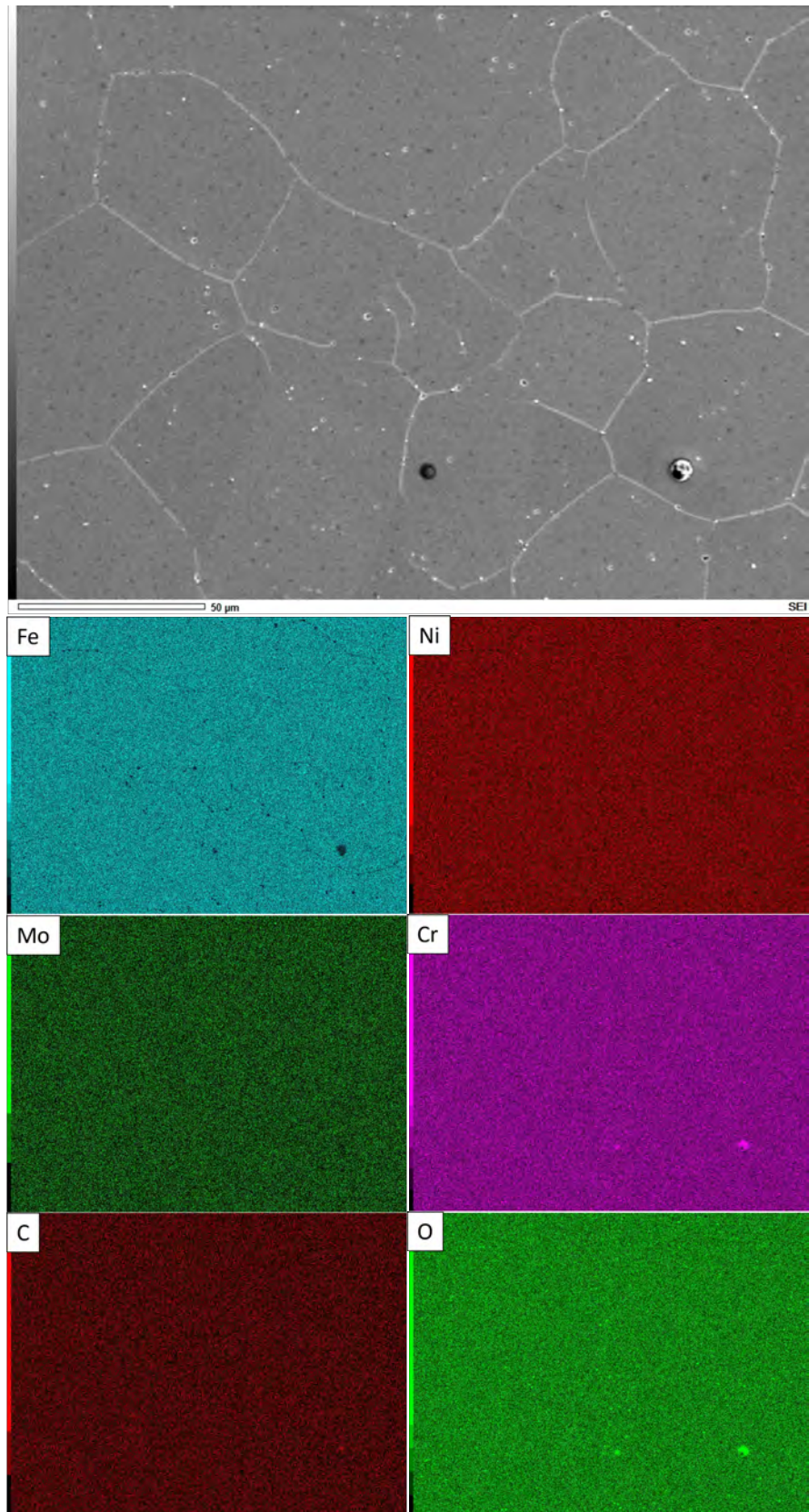


FIGURE 6.7: SEM micrograph and EDS data from sample 9 - HIP (T_{1200} P_{200}).

6.5 XRD Analysis

XRD analysis was carried out following the procedure outlined in section 3.12 to identify whether or not there was any change in materials phase as a result of the HIP treatments. Figure 6.8 displays the XRD spectra in their entirety's. With respect to the location and ratio of peak height the spectra displayed is more characteristic of a ferritic rather than fully austenitic structure. One would expect a purely austenitic structure to have the dominant peak located at $2\theta = 74^\circ$. The dominant peak in the presented spectra demonstrate a dominant peak at $\theta = 43.5^\circ$ demonstrates a mixture of austenitic and ferritic phases [147]. This suggests there could be a small proportion of delta ferrite within the material. The delta phase labelled $\delta(110)$ is present in all HIP treated parts likely due to the slow cooling of the material during HIP treatment. To maintain a fully austenitic structure quenching from high temperatures is required. Small peaks that are not intrinsic to the austenitic or ferritic phases could be due to the presence of oxides e.g. the small peak at $\theta = 119^\circ$. Oxides can be observed within the SEM micrographs shown in figures 6.6 and 6.7. The phase composition of austenitic stainless steels produced by additive manufacturing has been investigated in literature wherein multi phase structures have been reported in materials which are single phase when produced traditionally [148]. A review by Astafurov et al. concluded that the phase composition of AM austenitic stainless steels is highly dependent on the thermal history of the material. This thermal history is modified by the chemical composition of the steel, the AM method used, the process parameters chosen for a given AM method as well as any post production heat treatments. The combination of these factors impacts the properties of the final built material and can result in the material being purely austenitic or of heterophase structure comprising of austenite, ferrite, σ -phase, and elemental segregations of alloying elements on interphase boundaries [148]. The lattice parameters produced by Rietveld refinement produced values of ranging from 3.952 to 3.955Å. The lattice parameter did not change significantly for any scan and the value presented corresponds well to literature values [149].

With respect to the displayed spectra there are no major differences with no shift between samples and there is a slight increase in the signal to noise ratio of sample 10. There are however slight differences in the peaks which become apparent upon closer inspection as shown in Figure 6.9 showing an enlarged view of individual peaks. The peaks at $2\theta = 43.5^\circ$ as visible in the top left box in Figure 6.9 are very similar across all samples, the peaks at $2\theta = 44.4^\circ$ have a slight difference wherein each sample apart from sample 10 (as-built) demonstrates a slight peak of very low intensity. Due to the low signal to noise ratio of this peak it is difficult to determine whether this is a real effect or an artefact. The top right box of Figure 6.9 shows the second major peak of the spectra

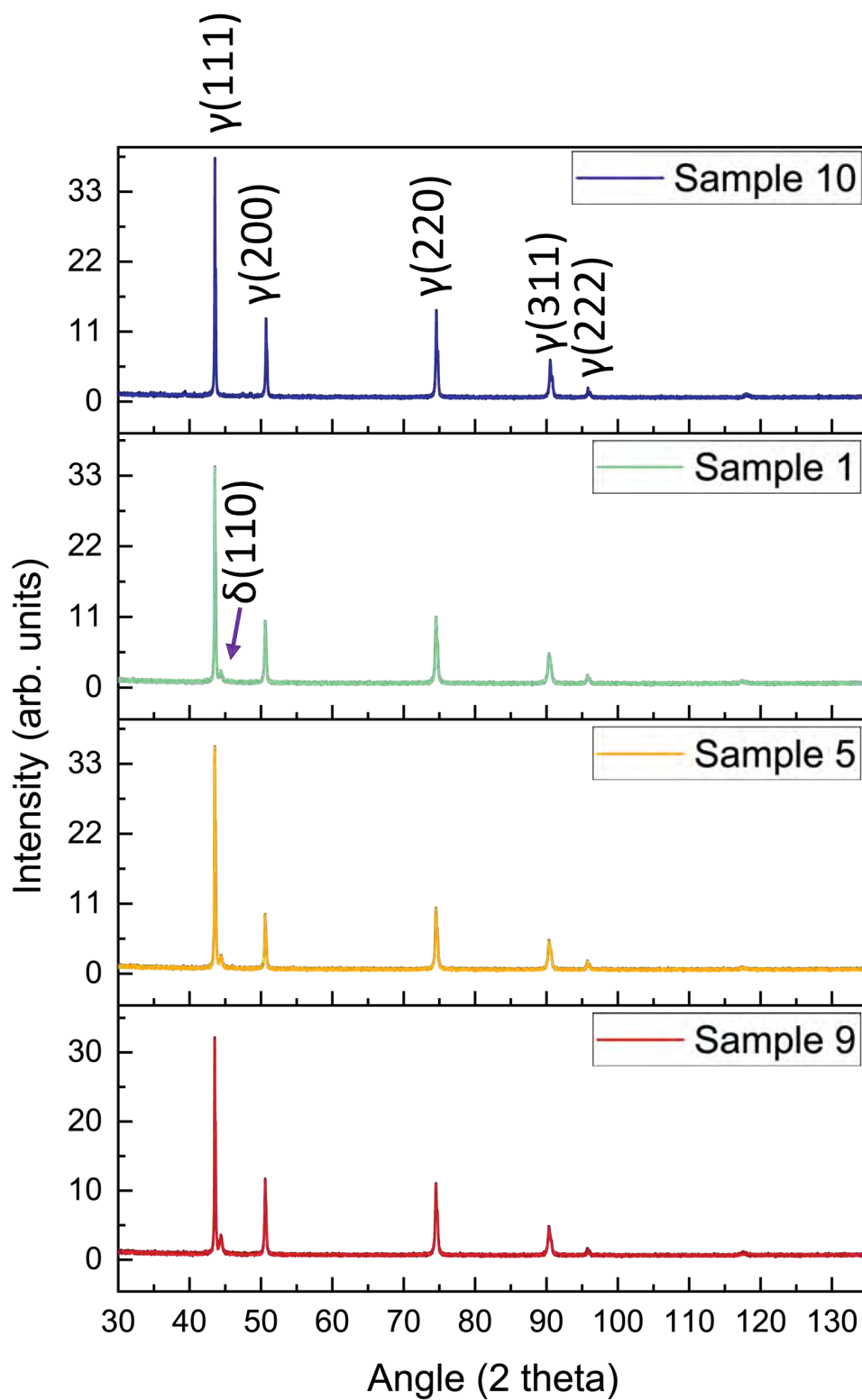


FIGURE 6.8: XRD peaks for sample 10 as-built, low, medium and high temperature treated HIP samples.

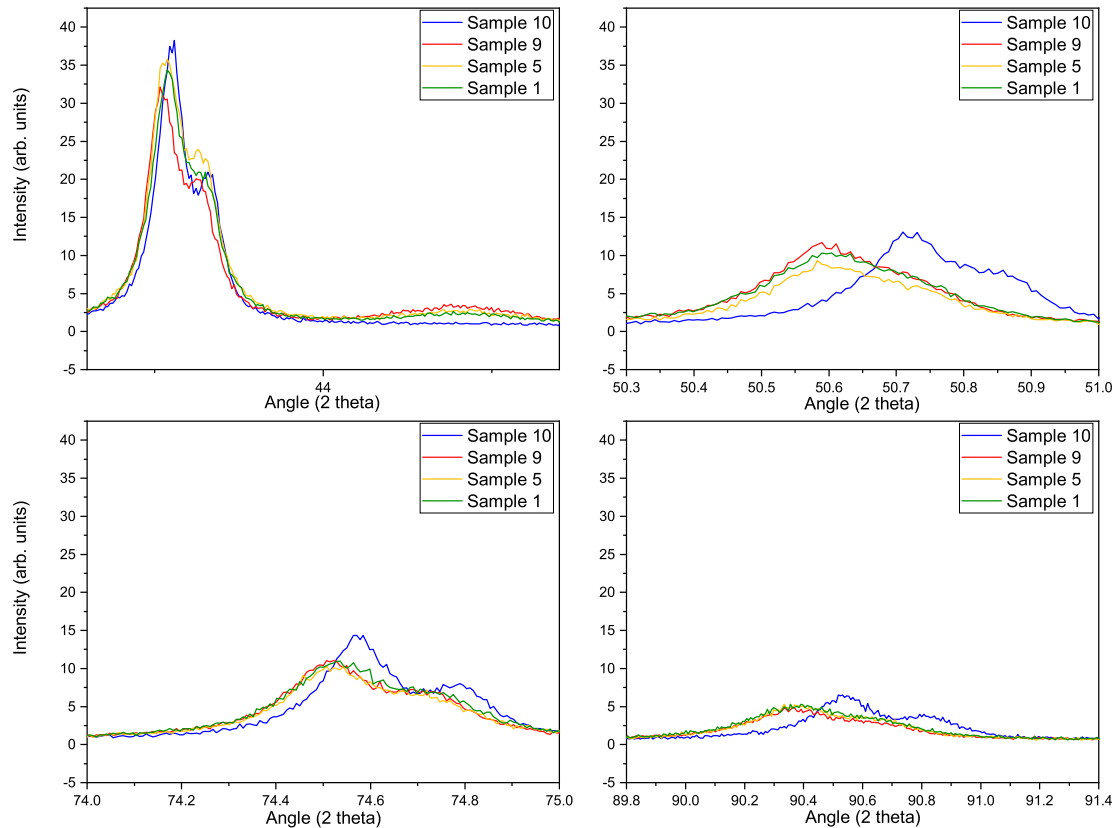


FIGURE 6.9: XRD peaks for sample 10 as-built, low, medium and high temperature treated HIP samples.

wherein the treated sample peaks (1, 5 and 9) are located at a lower angle than the as-built sample 10 peak. The bottom boxes in Figure 6.9 each share the same characteristics wherein in the treated sample peaks (1, 5 and 9) are located at a lower angle than the as-built sample 10 peak with reduced signal to noise ratios. Further to this it appears that the resolved peak in sample 10 in the peaks located at $2\theta = 43.5^\circ, 50.6^\circ, 74.5^\circ$ and 90.5° have separated into two peaks. This peak splitting could be due to a number of factors including inhomogeneity in the as built samples crystallographic orientation or a scan artefact. However, the fact samples 1,5 and 9 all do not show this peak splitting improves the likely-hood of the splitting not being due to a scanning artefact.

6.6 Hardness testing

Hardness testing was carried out on each of the samples subject to HIP treating the results of which are displayed in table 6.4. Details on the experimental procedure can be found in section 3.15. The wrought samples value of $162 \pm 8HV$ aligns with the accepted value of $155HV$ [150] [151]. The as built sample had the highest recorded hardness value. The error values are consistent across each of the samples apart from sample 11 which demonstrates a lower error than every other part. This could suggest that the extended treatment time allowed for the microstructural changes induced by the treatment to occur throughout the sample. The counter to this argument would be that the error on the wrought part was consistent with the printed and treated values without undergoing a HIP treatment. The hardness values themselves are then seemingly separated into 3 groups based on the HIP treatment temperature. Samples 1, 4 and 7 demonstrated values close to overlapping when considering their respective errors with the highest hardness values post HIP treatment. Samples 2, 5 and 8 which show a slight reduction from the samples treated at the lowest temperature. Samples 3, 6, 9 and 11 which show a further reduction in hardness. It is possible that despite sample 11 being treated as the mid temperature set-point the increased hold time has resulted in the increased reduction in hardness from sample 5 which was HIP treated at the same temperature and pressure.

The results of the hardness testing reflect the measured grain sizes and generally agree with the Hall-Petch relationship which proposes an inverse relationship between grain size and material hardness [72]. The as-built sample has the highest measured hardness; this increased hardness compared to the wrought counterpart is common across AM materials and is duly associated with the high cooling rates of the manufacturing process [152]. The sub grain cellular features also contribute to the increased hardness of the AM sample wherein each cell is analogous to a grain [143]. Thus, whilst the lower temperature HIP cycles did not remove the cellular structure entirely, it could have removed the structure in some regions of the microstructure. Increasing the time and temperature of treatment removes the inherent AM microstructural features, but coarsens the grain structure resulting in a decrease in hardness [116]. Sample 12 has an outlying hardness value between the higher and lower hardness samples. It is suggested that this is due to the effect of the additional furnace treatment, competing with quenching. The first stage in the post processing was the low temperature, high pressure HIP. At this point the hardness value of the sample is expected to be similar to samples 1,4 and 7. However the addition of the subsequent 2 hour furnace treatment has resulted in the final hardness value decreasing further.

Sample	Hardness (Vickers)	Standard deviation
1 - HIP (T ₇₀₀ P ₁₀₀)	216	6
2 - HIP (T ₁₁₂₅ P ₁₀₀)	166	7
3 - HIP (T ₁₂₀₀ P ₁₀₀)	150	5
4 - HIP (T ₇₀₀ P ₁₃₇)	223	8
5 - HIP (T ₁₁₂₅ P ₁₃₇)	163	6
6 - HIP (T ₁₂₀₀ P ₁₃₇)	164	6
7 - HIP (T ₇₀₀ P ₂₀₀)	215	7
8 - HIP (T ₁₁₂₅ P ₂₀₀)	162	6
9 - HIP (T ₁₂₀₀ P ₂₀₀)	155	4
10 - As-built	234	8
11 - HIP (T ₁₁₂₅ P ₂₀₀ - long hold)	155	3
12 - HIP (T ₇₀₀ P ₂₀₀ - quench)	180	7
Wrought	162	8

TABLE 6.4: Hardness data taken on all samples in HIP study.

6.7 Tensile testing

The data generated from the tensile tests is displayed in Table 6.5, with the most representative curves for each variant displayed in Figure 6.10. The treated sample results are separated into two distinct groups. Group A represents the samples treated at the lowest HIP temperature (1, 4 and 7) and group B represents the remaining collection of samples. The group A samples, or samples 1, 4 and 7, can be seen to have increased ultimate tensile strength (UTS) and proof strength (PS) properties, exhibiting mean values of 584 MPa and 220 MPa respectively. Additionally, their fracture elongation (El) values are very similar to the wrought value (50%) [153] with a mean value of 47.82 %. The remaining samples, group B, all demonstrated an increased El value relative to the wrought values (50%) with an average El value of 59.03 %. However, the group B samples demonstrated a decrease in UTS with a mean value of 542 MPa compared to the wrought value of 560 MPa [153]. Group B samples also suffered from a decrease in PS and fracture strength (f) properties compared to Group A samples. Whilst there are variations in the data which could be linked to changes in the treatment pressure the significance of these effects is not dominant. Furthermore, it is possible to separate the data into 2 further groups from A and B respectively. As compared to group A, the as-built samples achieved a higher stress value whilst in the elastic region 510 MPa compared to samples 1, 4 and 7 (440 MPa). Whilst, within group B a similar trend exists where the samples that were treated at the high temperature point and the long hold samples (3, 6, 9 and 11) demonstrate a lower maximum stress value in the elastic region compared to all other group B samples. Further to this Figure 5 displays the relationship between hardness and ultimate tensile strength. The data is once again separated into two sections with the quenched sample at 180 HV being the outlying point. Group A consists

of the samples treated at low temperatures and the as built sample. Group B contains samples of lower hardness and ultimate tensile strength (UTS). Microstructurally the difference between group A and B is the presence of the intrinsic AM features, the sub grain cellular structure, the presence of clearly visible melt pools and the anisotropy of the grains.

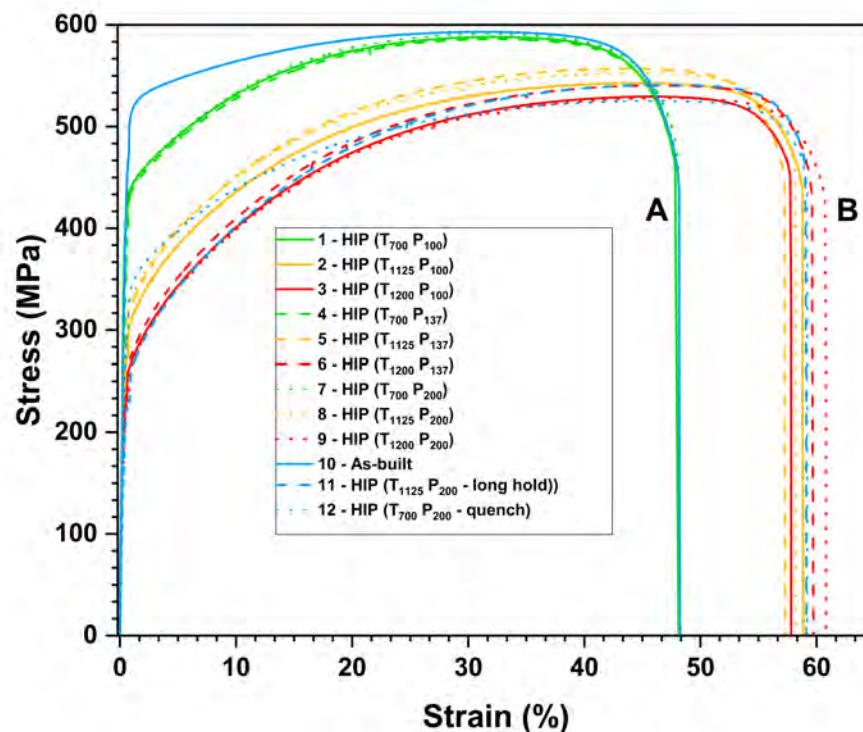


FIGURE 6.10: Representative tensile curves of the different samples from each treatment. The colours blue, green and red represent low, medium and high temperature setpoints respectively. Solid, dash and dotted lines represent low medium and high pressure setpoints respectively. The yellow lines represent samples 10, 11 and 12 with solid dash and dot lines to differentiate between them respectively. Groups labelled A and B represent samples with and without the presence of the intrinsic AM microstructural features

The separation of the tensile data into two distinct groups aligns with the two groups reported in the hardness and microscopy findings. Samples 1, 4, 7 and 10, whilst peaking at a higher σ_{UTS} and attaining a higher σ_{PS} , suffered from fracture at a reduced E_l than all other samples. This aligns with results documented in literature that found that as-built AM 316L components have demonstrated high strength but lower ductility than wrought components to various degrees, depending on the build parameters and post-production treatments used [143] [103]. Despite the hardness data generally following the standard Hall-Petch relationship a modified Hall-Petch relationship is more suitably applicable to AM 316L. This relationship as proposed by Cui et al. allows for the

Treatment	El (%)	UTS (MPa)	YS (MPa)	FS (MPa)
1 - HIP (T ₇₀₀ P ₁₀₀)	48.0	582.7	399.4	463.3
2 - HIP (T ₁₁₂₅ P ₁₀₀)	58.0	538.8	304.6	444.8
3 - HIP (T ₁₂₀₀ P ₁₀₀)	58.8	535.8	228.3	445.9
4 - HIP (T ₇₀₀ P ₁₃₇)	47.2	585.3	398.2	475.6
5 - HIP (T ₁₁₂₅ P ₁₃₇)	57.5	554.4	296.0	446.9
6 - HIP (T ₁₂₀₀ P ₁₃₇)	59.7	541.7	272.1	441.1
7 - HIP (T ₇₀₀ P ₂₀₀)	48.1	585.1	428.3	449.5
8 - HIP (T ₁₁₂₅ P ₂₀₀)	59.7	549.8	294.6	455.7
9 - HIP (T ₁₂₀₀ P ₂₀₀)	60.1	530.8	230.6	442.6
10 - As-built	48.0	588.2	474.3	452.6
11 - HIP (T ₁₁₂₅ P ₂₀₀ - long hold)	59.5	538.5	221.9	451.7
12 - HIP (T ₇₀₀ P ₂₀₀ - quench)	59.0	532.1	300.2	446.0

TABLE 6.5: Table showing average tensile data values across all treatments.

prediction of yield strength values using $\sigma_{YS} = \sigma_0 + \sigma_{GB} + \sigma_{SS} + \sigma_p + \sigma_{Dis}$ [154]. Where the contribution from friction stress σ_0 is 15 (MPa) [155] [156] [157], $\sigma_{Dis} = M\alpha K\sqrt{d}$ is the contribution from strain boundary strengthening, and $\sigma_{Dis} = M\alpha Gb\sqrt{\rho}$ is the contribution from dislocation strengthening [154]. M, the orientation factor is taken as 2.20, α as 0.30, G, the shear modulus as 78 GPa, b the Burgers vector as 2.5×10^{-10} m, K the Hall-Petch parameter is approximately $300 \text{ MPa } \mu\text{m}^{-0.5}$ and d being the average grain size $32.5(\mu\text{m})$ [154] [158]. The contributions of σ_p the precipitation hardening and σ_s the solution strengthening are taken as 12.50 and 96.60 from Cui et al. [154]. Assuming that the dislocation density of 10 - As-built is $6 \times 10^{14} \text{ m}^{-2}$ as per Bahl et al. [43]. Then the calculated yield strength for the as-built condition using the grain size measured in this work is 492 MPa. This value is in strong agreement with the value of $474.3 \pm 12.3 \text{ MPa}$ recorded in this work in Table 6.5. Increased σ_{YS} values have been attributed in literature to the fine granular structure and a high dislocation density present in as-built AM samples [159]. In some work the increased σ_{UTS} and σ_{PS} of the as-built sample was attributed to the microstructure being comprised of small grains with large misorientation angles [107]. The further differentiation of groups within this work is notable in that the tensile behaviour of the samples subjected to the high temperature HIP cycle is near identical to the behaviour of the long hold HIP cycle despite the long hold being carried out at the midpoint temperature. This suggests that for an application requiring a high level of ductility, then either a high temperature HIP cycle or a long hold at a lower temperature is advisable. The likelihood however is that the cost associated with a long hold is greater than that required for a higher temperature cycle and therefore the long hold is not recommended. In addition to this the mean El value achieved by the midpoint temperature treated parts (58.40 %) is comparable to the high temperature average (59.53 %) whilst maintaining a σ_{PS} of 186.36 MPa compared to the high temperature average of 160.35 MPa. The significance of this is that

for an application wherein a high elongation as well a high σ_{PS} is required, this work suggests that the midpoint temperature and pressure HIP cycles are more favourable than HIP treating at a higher temperature. Increased σ_{PS} values have been attributed in literature to the fine granular structure and a high dislocation density present in as-built AM samples [159]. This correlates with the conclusions drawn from microstructural observations made in this work. For HIP cycle optimisation, assuming the same volume of gas is used per HIP cycle, ultimately the overall cost of the HIP cycle is determined by the treatment temperature and the length of cycle. The tensile results obtained in this work suggest that the high temperature treatments are only required for an application wherein attaining absolute maximum possible elongation is crucial. Samples containing melt pool, melt pool boundaries and cellular microstructural features were found to result in increased performance in some of the tensile parameters, however they also suffer from reduced fracture elongation. Additionally, the as-built sample has the marginally highest σ_{UTS} and highest σ_{YS} whilst condition 4 - HIP (T_{700} P_{137}) produced the highest outright σ_f value.

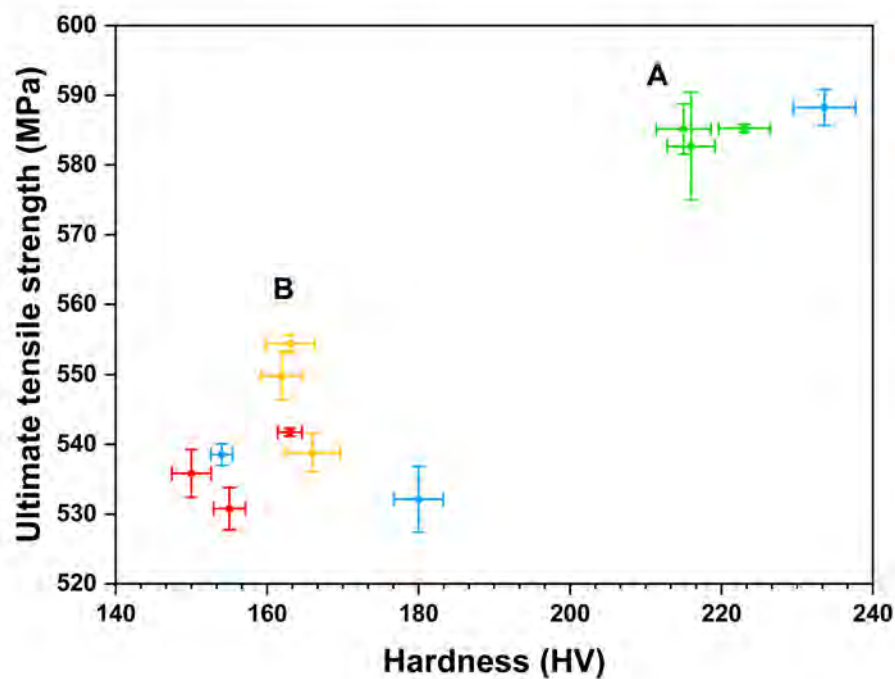


FIGURE 6.11: Hardness plotted against UTS. The colours green, yellow and red represent low, medium and high HIP temperature setpoints respectively. The colour blue represents treatments, 10, 11 and 12.

6.8 Fatigue testing

The results from the testing carried out at applied stresses of 330MPa and 375MPa are displayed in table 6.6 below.

Treatment	σ MAX (MPa)	Nf	σ MAX (MPa)	Nf
1 - HIP (T ₇₀₀ P ₁₀₀)	375	47,911	330	100,000
2 - HIP (T ₁₁₂₅ P ₁₀₀)	375	699	330	5,674
3 - HIP (T ₁₂₀₀ P ₁₀₀)	375	1,297	330	4,807
4 - HIP (T ₇₀₀ P ₁₃₇)	375	100,000	330	100,000
5 - HIP (T ₁₁₂₅ P ₁₃₇)	375	1,428	330	5,936
6 - HIP (T ₁₂₀₀ P ₁₃₇)	375	2,155	330	4,446
7 - HIP (T ₇₀₀ P ₂₀₀)	375	66,761	330	100,000
8 - HIP (T ₁₁₂₅ P ₂₀₀)	375	1,507	330	2,136
9 - HIP (T ₁₂₀₀ P ₂₀₀)	375	1,720	330	1,382
10 - As-built	375	74,064	330	100,000
11 - HIP (T ₁₁₂₅ P ₂₀₀ - long hold)	375	1,380	330	8,238
12 - HIP (T ₇₀₀ P ₂₀₀ - quench)	3375	1,173	330	10,191

TABLE 6.6: Fatigue test results across the two stress regimes for each treatment.

In the samples subjected to the lower of the two maximum applied stress (σ MAX) values (330 MPa), the low temperature (1, 4, 7) and as-built samples (10) reached the run-out limit and did not fail during testing. The remaining samples all failed within the order of 10,000 cycles. In the higher σ MAX regime (σ MAX = 375 MPa), 4 - HIP (T₇₀₀ P₁₃₇) was again able to reach the run-out condition, surpassing 100,000 fatigue cycles. The as-built sample (10) and sample 7 were the next best performing samples, failing between 65,000–75,000 thousand cycles. This was closely followed by treatment 1 - HIP(T₇₀₀ P₂₀₀) which failed just under 48,000 cycles, whilst the remaining samples all failed within 2,155 cycles. The results in their entirety are displayed in Table 6. Post-test fractographic assessments of the fatigue samples revealed that cracking predominantly initiated at the surface of the gauge length and propagated towards the centre of the samples, thus indicating that the presence of any potential internal defective regions had minimal influence on the crack initiation life of these samples. Despite the compressive nature of the loading ratio (R=-1) fatigue striations are visible on several of the fracture surfaces, tracking perpendicularly to the growth direction of the crack in figure 6.13. Some indicative examples of the observed fractures are presented in Figure 6.12. This figure shows the fractures for sample 9, which represents the high temperature, high pressure HIP condition, and sample 10, which is the as-built equivalent. These samples saw contrasting behaviours under fatigue loading, with sample 10 significantly outperforming sample 9, despite not being subjected to a post-process HIP cycle. Like that seen for the hardness and tensile results, this can be attributed to the smaller grain size observed in the X-Y plane in the as-built material (32.49 μ m), as compared to

58.07 μm in sample 9, and the greater presence of porosity defects in the HIP sample which are heavily populated in close proximity to the secondary crack running through the structure. Together with fractographic images displayed in 6.12 a and b, where minimal evidence of any defective regions can be seen in the as-built sample, this clearly indicates that the as-built material already had a high degree of consolidation and the high temperature, high pressure HIP operation has only predominantly acted to promote grain growth in the material, to the detriment of the sample's hardness, tensile and fatigue performance.

The fractographic images captured as shown in figures 6.12, 6.13 and 6.14 are comparable across each of the tested specimens with no major differences appearing. Fractographic microscopy reveals that the fatigue surface is covered in dimple like features as seen in figures 6.13 and 6.14. Whilst these dimple ruptures can be caused by overload in the case of these sample fractographic analysis rules this out as cracks were seen to clearly initiate at the surface of samples and travel inward [160]. These dimples are indicative of highly ductile materials and are visible throughout the fracture surfaces. The fractographic images as displayed in figures 6.12, 6.13 and 6.14 show that the samples surfaces are devoid of unmelted powder particles. The presence of unmelted powder particles and porosity within the microstructure can be detrimental to fatigue life when cracks initiate at these localised regions [113]. There are a number of explanations as to why there are no visible unmelted powder particles or porosity regions visible on the samples fracture surfaces including.

1. The samples as-built from the AM process are free from porosity and un melted powder.
2. None of the images show these features by coincidence alone and they are present throughout the material just unobserved.
3. The HIP process has re-melted any unmelted powder from the build and removed any porosity from the samples.

For point 1 the results displayed in sections 5.7 and 6.2 suggest that there is porosity within the sample. Whilst there is no evidence showing there is unmelted powder within the samples it is highly likely that not every single particle of powder was fully melted given the density measurements made. For point 2 whilst it is possible that no cracking initiated from un melted powder in any of the samples by chance this is unlikely to occur across the 24 tests and 19 fracture surfaces analysed. It's important to recall that these fatigue samples were machined from larger cylinders after being HIP treated. The HIP process as outlined in section 1.16.1 is effective in increasing the density of materials via

the diffusion of gas filled pores outward from the centre of the sample [105]. Therefore if the HIP process has allowed for the diffusion of porosity away from the centre of the sample to occur then the machining process which removes the outer regions of the sample would leave only central part of the sample remaining which is the region most likely to be porosity free.

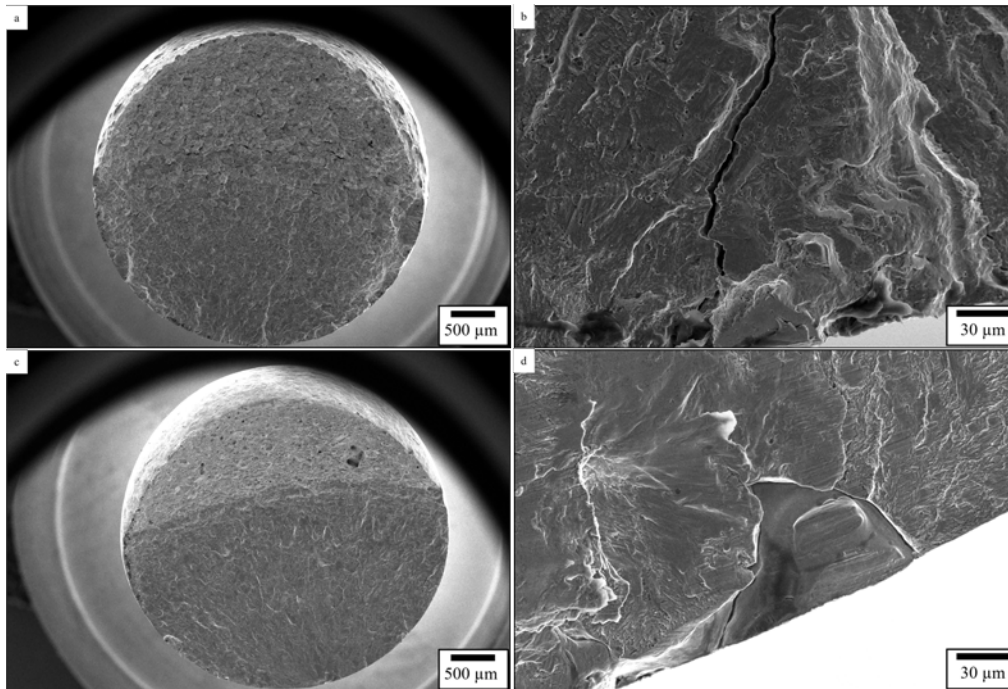


FIGURE 6.12: SEM fractographic images of a. Treatment 9 at low magnification, b. Treatment 9 at high magnification, c. Treatment 10 at low magnification and d. Treatment 10 at high magnification.

The results of both the higher and lower stress regime fatigue tests align with the previous mechanical results wherein the as-built sample and those treated at low temperature tend to outperform the remaining conditions. Further performance differentiation between the low temperature HIP treated and as-built samples can be considered for the tests subjected to the higher σ_{MAX} value (330 MPa). Since conditions 4 - HIP (T_{700} P₁₃₇)'s sample reached the run-out limit, the failure point is unknown making it difficult to estimate the full potential fatigue life of this sample. Whilst unmelted powder and inclusions contribute to a higher defect volume and subsequently a shorter fatigue life, the high ductility of 316L lends to its fatigue performance being influenced heavily by the material's microstructure [116]. It has been shown that retention at high temperatures and slow cooling rates have led to a high reduction of dislocation density, the removal of sub grain cellular structures and subsequently, reduced strength in AM 316L [115]. This is in agreement with the results presented in this work wherein the fatigue performance aligns heavily with the differences in microstructures between the samples and pore-induced failure is not observed in the fracture surface of any sample. This work indicates

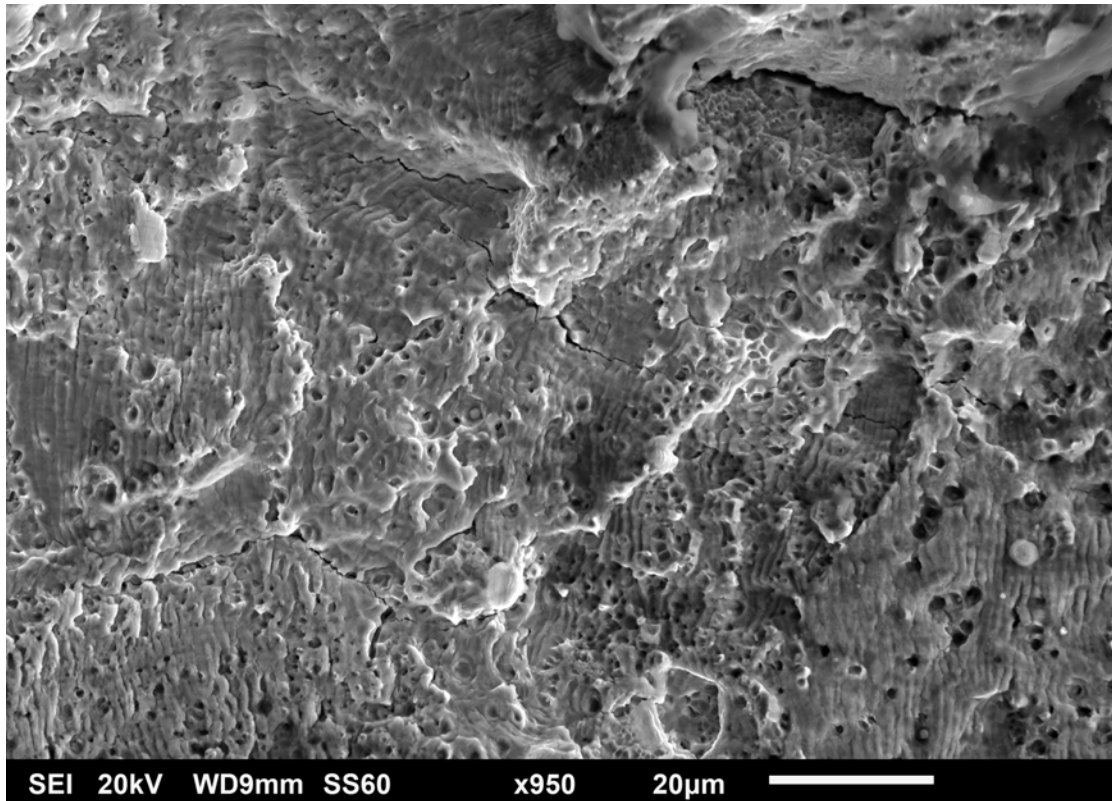


FIGURE 6.13: SEM fractograph showing striations tracking perpendicularly to cracks and dimples throughout the surface.

that a sweet spot in HIP treatment pressure exists for 316L which lies between the lower (100 MPa) and the higher (200 MPa) pressure thresholds. The performance of the as-built sample highlights the importance of optimising HIP parameters. Running a HIP cycle at the optimum temperature but a non-optimum pressure can result in a decrease in fatigue performance due to the microstructural grain growth, whereas treating at the optimum temperature and pressure results in an increased fatigue performance compared to the as-built part.

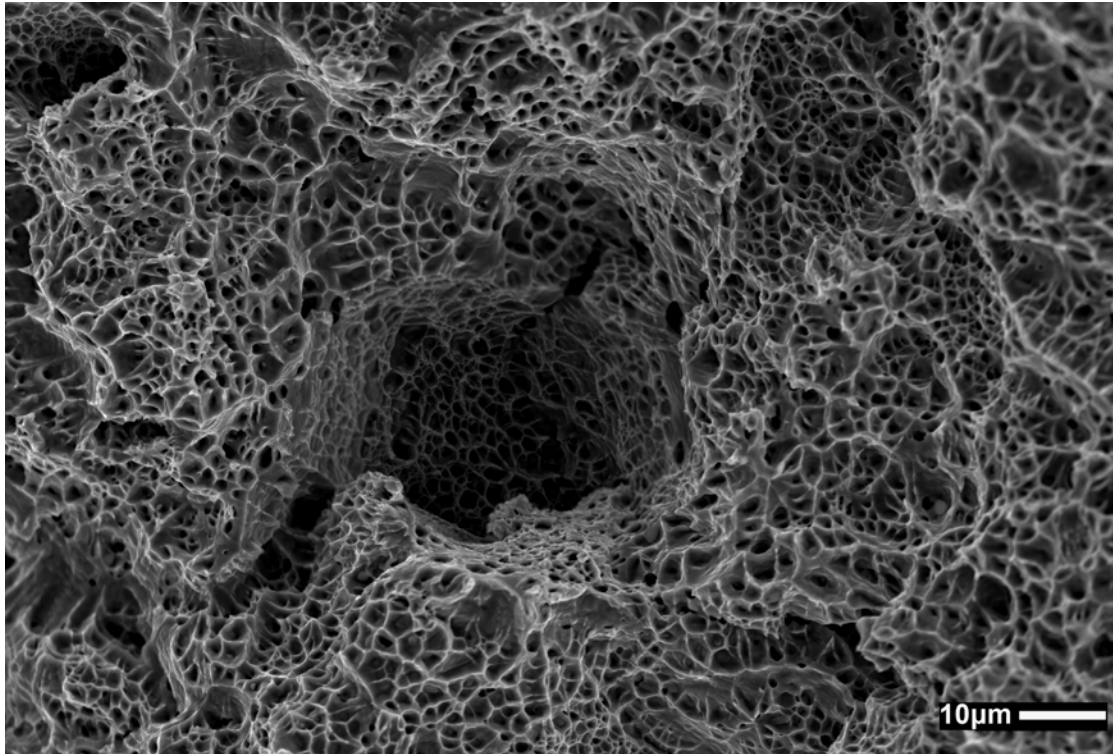


FIGURE 6.14: SEM high magnification fractograph showing a dimple characteristic of ductile material failure.

6.9 Corrosion testing

The potentiodynamic curves obtained from the first scan of each condition are displayed in figure 6.15 below. Each of the scans was started at their respective OCP values $-0.1V$. The turning point was set as at $10^{-3}(Acm^{-2})$. The scan shown for condition 5 however continued beyond this point, this however does not affect the data significantly. Breakdown had occurred with the sample showing a very diminished passive layer with repassivation failing to happen on each of the repeats on this condition. The curves are separated by temperature setpoints with comparison to the wrought curve in each plot. The wrought scan demonstrated a clear passive region at a current density of $5 \times 10^{-5} A cm^{-2}$ with a clearly defined inflection point marking breakdown at a potential of $0.56 V$ vs. SCE. On the reverse scan direction the wrought sample repassivated at a potential of $-0.01V$ with a current density of $8 \times 2.5^{-5} A cm^{-2}$. This behaviour is characteristic of traditionally manufactured 316L. The recorded open circuit potentials vary between each condition and between repeats for all AM samples. The curves show that conditions 11 - long hold and 12 - quench are the worst performing conditions with high current densities being reached at potentials lower than all other conditions. The scan reverse current density was met by both of these samples before a volate of $0.2 V$ vs. SCE was reached on the forward direction scan. Metastable pitting is showing in conditions 9 - HIP(T_{1200}

P₂₀₀), 2 - HIP(T₁₁₂₅ P₁₀₀) and 8 - HIP(T₁₁₂₅ P₂₀₀). The passive currents presented are highly variable ranging from 10^{-8} – 5×10^{-4} A cm⁻². The highest pitting potential was recorded in condition 1 - HIP(T₇₀₀ P₂₀₀) with a pitting potential of 0.93 V, despite this however the sample was unable to repassivate during this test. The size of the hysteresis loop was large with an approximate value of 10^5 (Acm⁻²), indicative of low resistance to pitting. Similarly large hysteresis loops were observed across numerous other conditions including conditions 2 - HIP(T₁₁₂₅ P₁₀₀), 5 - HIP(T₁₁₂₅ P₁₃₇), 7 - HIP(T₇₀₀ P₂₀₀) and 9 - HIP(T₁₂₀₀ P₂₀₀). Samples treated at pressures of 137 and 200-MPa respectively at this temperature point had pitting potentials of 0.70 and 0.61 V vs. SCE respectively.

A repeat potentiodynamic curve taken from condition 1 - HIP(T₇₀₀ P₂₀₀) is displayed in figure 6.16 alongside the wrought sample. The reason for highlighting this curve is that the sample did not seem to undergo pitting corrosion during the potentiodynamic scan as there is no clear inflection marking the start of breakdown. The current density continued to increase as the scan direction was reversed before eventually decreasing once the potential dropped below 0.45 V vs. SCE. The reverse direction scan crossed the forward direction scan at a voltage of -0.09 V vs. SCE, since this sample did not show breakdown it is unclear whether this can be considered as repassivation or not. This is the only repeat across any sample wherein this behaviour was observed. It is unclear whether the results of this test are coincidental or demonstrative of an increased resistance to pitting at this condition.

The potentiodynamic curves shown for conditions 2 - HIP(T₁₁₂₅ P₁₀₀) and 5 - HIP(T₁₁₂₅ P₁₃₇) undergo breakdown at comparatively low recorded current densities in the region of 1×10^{-7} A cm⁻². However the curve shown at the same temperature point treated at the highest pressure is shown to breakdown at a significantly higher current density of 8×10^{-5} A cm⁻². This is not a consistent trend across all temperature points as the curve displayed for a sample treated at condition 9 - HIP(T₁₂₀₀ P₂₀₀) shows breakdown at a comparatively low current density of 1×10^{-7} A cm⁻². Upon examination of the curves it is apparent that the curves shown for samples treated at conditions 2 - HIP(T₁₁₂₅ P₁₀₀) and 9 - HIP(T₁₂₀₀ P₂₀₀) display similar behaviour in the positive scan direction with similar breakdown current densities and similar pitting potentials whilst both samples failed to repassivate. This similar behaviour could be due to the samples having comparable surface porosity features or it could be coincidental. The curve shown for condition 8 - HIP(T₁₁₂₅ P₂₀₀) demonstrates a clear passive region at a current density of 1×10^{-5} A cm⁻². The horizontal lines in the scan at the higher potential region of the passive region indicate the formation of metastable pitting before the sample pits at a voltage of 0.56 V vs. SCE which is comparable to the wrought sample. Whilst the area of the hysteresis loop is smaller than other conditions shown the sample was unable

to repassivate in the test shown, however repassivation was recorded in 2 of the 3 tests carried out on samples in this condition.

The behaviour of curves from samples at conditions 3 - HIP(T₁₂₀₀ P₁₀₀) and 6 - HIP(T₁₂₀₀ P₁₃₇) are very consistent with overlapping regions throughout the scans. The scans have overlapping passive regions with current densities of approximately 5×10^{-4} A cm⁻² before breakdown occurs at potentials of 0.64 and 0.61 V vs. SCE respectively, each higher than the wrought sample displayed. Despite these samples from conditions 3 - HIP(T₁₂₀₀ P₁₀₀) and 6 - HIP(T₁₂₀₀ P₁₃₇) only repassivated in 2 of their respective tests.

The curve of the sample from condition 10 - As built is the most similar to that of the wrought part. Both scans demonstrate inflection points at comparable voltages, 0.56 and 0.61 V vs. SCE respectively. The current densities at breakdown are similar and the current densities recorded on the reverse scan overlap significantly. The wrought part demonstrated repassivation in each of its tests in comparison to the as-built condition achieving repassivation in 2 out of its 3 tests. The curve presented for condition 4 - HIP(T₇₀₀ P₁₃₇) demonstrates a "two-step" breakdown. This behaviour is similar to that presented by Monteiro et al. in a study on the corrosion behaviour of 316L in hot caustic aqueous environments [161]. Monteiro et al. attribute the behaviour seen in their work to the exposure of stainless steel to NaOH shows the occurrence of several active to passive transitions [161].

Corrosion parameters as well as their standard deviations derived from deaerated potentiodynamic scanning of each HIP condition are given in table 6.7 below. Each condition was scanned three times on three separate samples following the method outlined in section 3.8.2. The results of the corrosion testing are plotted in Figure 6.17. The wrought samples demonstrated a pitting potential of 0.576 ± 0.007 V rel. SCE. The low standard deviation of the pitting potential on the wrought sample justifies that the larger uncertainties measured on AM parts are a feature of the sample and not due to experimental error. The as-built parts mean pitting potential was 0.570 ± 0.389 V rel. SCE, representing a pitting potential close to the wrought value but with a larger associated error. The treatment with the highest recorded pitting potential was treatment 1 - HIP(T₇₀₀ P₂₀₀) with a mean pitting potential of 0.970 ± 0.026 V rel. SCE, an increase in pitting potential of 68% relative to wrought. The variation in recorded values varies significantly in the AM parts in comparison to the extremely small variation reported in the wrought counterpart. Repassivation was recorded in each of the experiments carried out on the wrought parts at a mean value of -0.103 ± 0.002 V. Repassivation was recorded for all repeats on samples from treatment 3, 12 with mean values of -0.274 ± 0.110 and -0.266 ± 0.086 respectively.

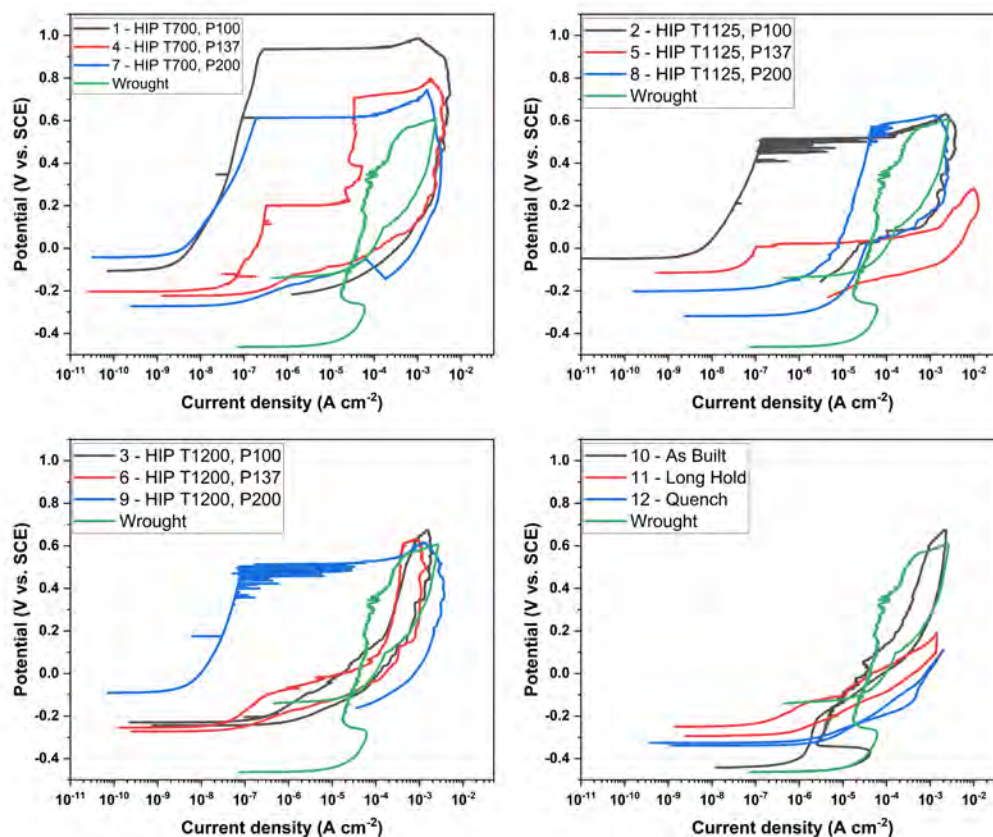


FIGURE 6.15: Cyclic potentiodynamic scans of all conditions compared to wrought 316L. Scans are separated into plots comparing samples treated at the same HIP temperature.

Interpreting the corrosion data is non-trivial as although having the highest possible pitting and repassivation potentials are preferential, the variability of results is equally important. This importance is due to the severe effect that pitting corrosion has on the structural integrity of a sample. Pitting corrosion can lead to the onset of stress corrosion cracking which can lead to the sudden failure of normally ductile alloys when subject to tensile stresses. The ideal combination of parameters being a high pitting and repassivation potential each with a low degree of variation. This combination of parameters is only achieved by the wrought part. Despite treatment 1 producing a sample with the highest pitting potential with comparatively low variation to the other AM samples, the variance in pitting potential is larger than that of the wrought part. Collectively the mean standard deviation associated with the treated AM samples (all samples across all conditions excluding wrought and as-built) pitting potentials was 0.135 V compared to 0.284 V for the as-built parts and 0.007 V for the wrought parts. This indicates that the porosity reducing effects of the HIP treatments succeeded in reducing the spread of the pitting potentials by 49.07%. Despite this, samples from treatment 1 failed to

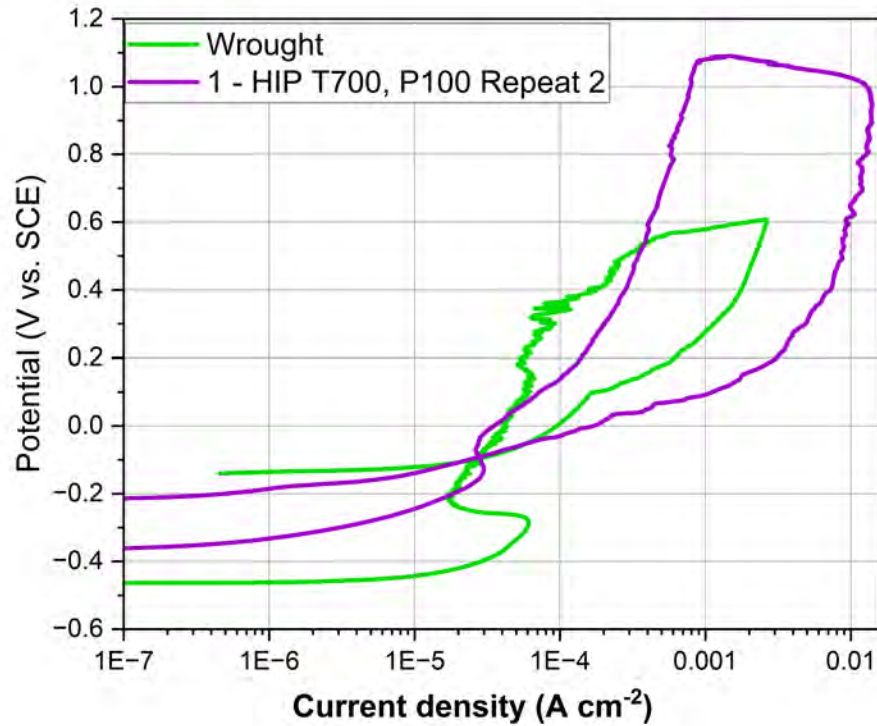


FIGURE 6.16: Cyclic potentiodynamic scans of wrought and 1 - HIP(T_{700} P_{200}) Repeat 2.

Condition	Pitting Potential (V vs. SCE)	Standard Deviation	Repassivation potential (V vs. SCE)	# of repassivations (out of 3)
1 - HIP (T_{700} P_{100})	0.970	0.026	-0.090 *	1
2 - HIP (T_{1125} P_{100})	0.532	0.076	-0.286	1
3 - HIP (T_{1200} P_{100})	0.398	0.213	-0.274	2
4 - HIP (T_{700} P_{137})	0.235	0.119	-0.128	1
5 - HIP (T_{1125} P_{137})	0.277	0.222	0.000	0
6 - HIP (T_{1200} P_{137})	0.569	0.060	-0.278	2
7 - HIP (T_{700} P_{200})	0.615	0.062	0.000	0
8 - HIP (T_{1125} P_{200})	0.543	0.085	-0.261	2
9 - HIP (T_{1200} P_{200})	0.212	0.224	-0.240	2
10 - As-built	0.614	0.284	0.130	2
11 - HIP (T_{1125} P_{200} - long hold)	0.196	0.257	0.000	0
12 - HIP (T_{700} P_{200} - quench)	0.310	0.115	-0.266	3
Wrought	0.576	0.007	-0.103	3

TABLE 6.7: Potentiodynamic values of all 316L samples treated by HIP. *Note the repassivation recorded for condition 1 - HIP (T_{700} P_{100}) was recorded as discussed in section 6.9.

repassivate in two of its tests despite recording the highest mean pitting potential. In the example shown in figure 6.15 sample 1 is shown to reach a potential of 0.94 V vs. SCE. Conversely whilst samples from treatments 12 achieved repassivation in each of its tests, the variation associated with the repassivation potentials was significantly increased compared to wrought. Further to this, the pitting potentials recorded by samples

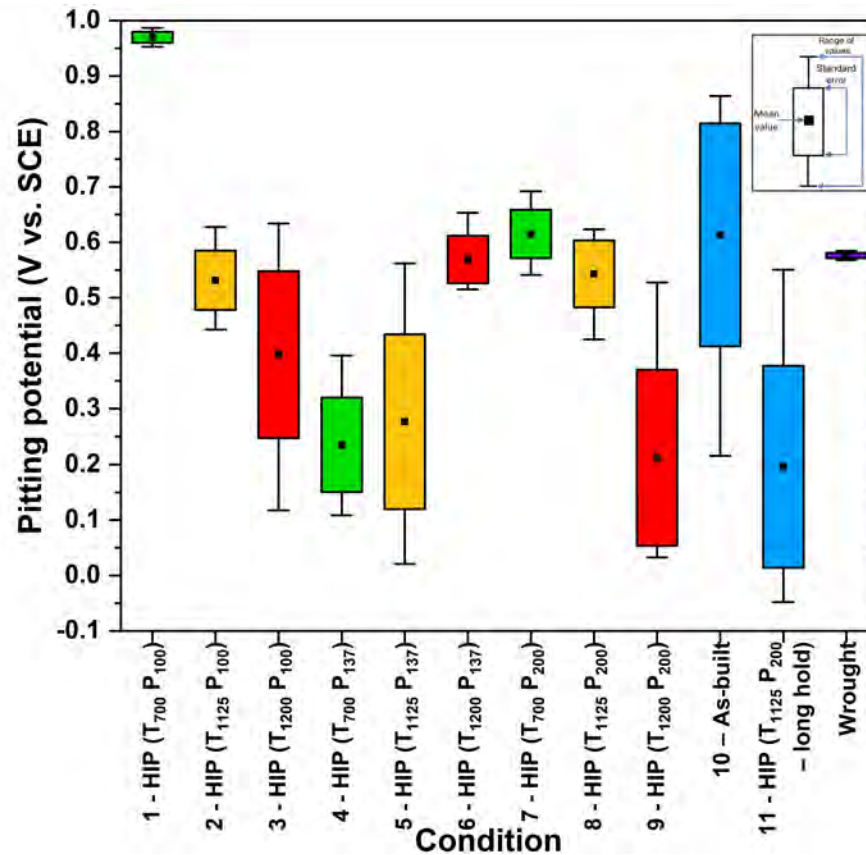


FIGURE 6.17: Mean pitting potential values plotted against treatment number.

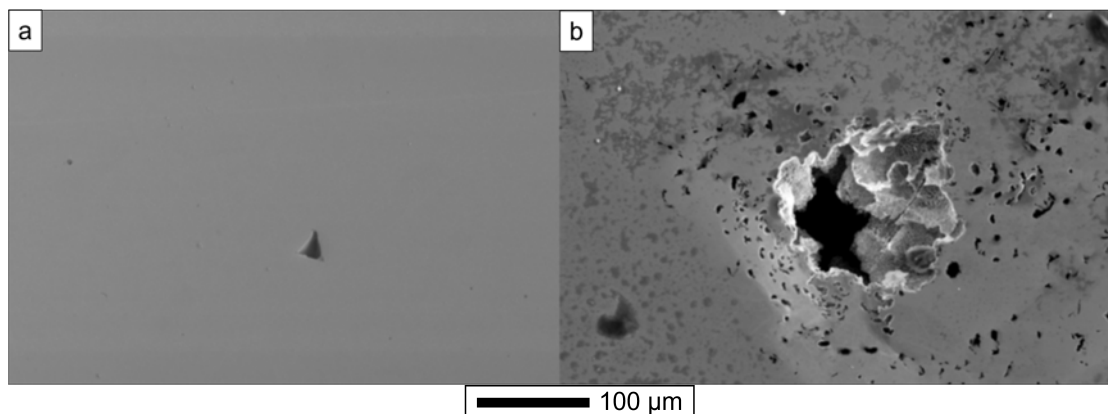


FIGURE 6.18: Micrographs showing a: Porosity feature in the HIP treated part and b: the same porosity feature after localised corrosion attack.

from treatments 12 have large variations. Despite the effect that the microstructure has on the mechanical properties investigated in this work, the pitting corrosion performance of the parts is not significantly affected by the presence of these microstructural features. This is due to the fact that any small irregularity in the surface of the material including small spherical porosity and larger irregularly shaped porosity features can act as initiation sites for localised pitting corrosion [101] [102]. Further to this, porosity with semi-occluded regions are conducive to facilitating localised corrosion through differential

aeration due to the restricted diffusion of oxygen into these regions as per the Fontana Greene mechanism of crevice corrosion [100]. This suggests that the pitting performance of AM parts is heavily dependent on the material's porosity content and whilst HIP treatments, as shown in this work, are able to reduce the presence of porosity, lower levels of porosity are typically necessary to facilitate a pitting performance comparable or superior to wrought 316L. Therefore, whilst the performance of some samples in some aspects of the pitting performance have performed superiorly to wrought 316L, the large variation associated with the corrosion results reduces the confidence in the performance of the AM parts in corrosive environments. Selectively identifying an area to test that is free from any porosity may result in pitting performance comparable or improved compared to the wrought part. However, whilst in-situ it is not always possible to only allow regions with no porosity to be in contact with corrosive environments. Figure 6.18 shows an irregularly shaped porosity feature before and after localised corrosion attack. Whilst microstructural features can determine the corrosion performance of materials, microscopic variations at the surface seem to be the dominant feature. The overarching conclusion from the results are that the microstructural features of the material are highly dependent on the post processing treatment chosen. These microstructural features significantly impact the performance of the material in different situations. Section 5.6 details

6.10 Overall ranking

Comparing the overall mechanical and corrosion properties can be accomplished via numerous methods. Figure 6.19 displays the pitting performance, the ultimate tensile strength and the number of fatigue cycles survived at 375 MPa for every treated and the as-built conditions. Whilst there are relationships between mechanical properties such as higher ultimate tensile strength values for samples with lower tensile fracture elongation section 6.7. Grain size and hardness relationships section 6.6 and hardness-ultimate tensile strength relationships (figure 6.11). There does not seem to be any relationship relating the pitting performance to any mechanical properties aside from the relationship between density and spread of pitting potentials. This is highlighted in figure 6.19 wherein the highest and lowest recorded pitting potentials correspond to amongst the highest ultimate tensile strengths recorded and amongst the lowest and highest number of fatigue cycles survived in the 375 MPa fatigue test.

Taguchi analysis was carried out on each of the tests carried out in this chapter, graphs are displayed in figure 6.20. This analysis allowed for the impact of varying the temperature and pressure to be observed across each experiment for conditions 1 - HIP (T₇₀₀ P₁₀₀)

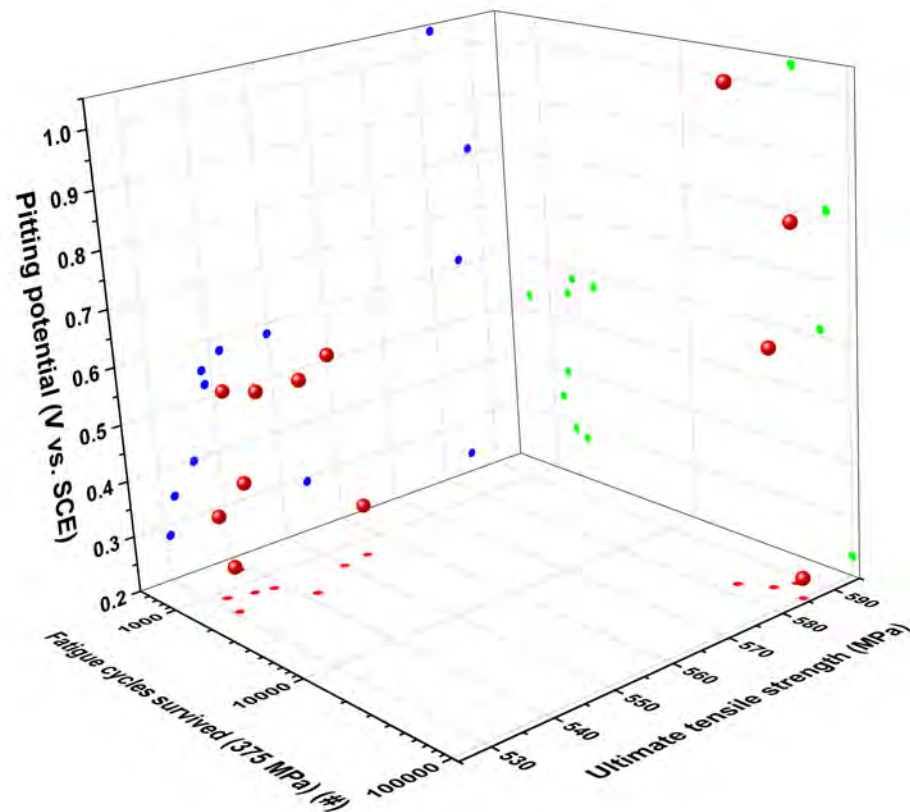


FIGURE 6.19: 3D plot showing the relationship between ultimate tensile strength, fatigue cycles survived and pitting performance.

- 9 - HIP (T_{1200} P_{200}). The results showed that the variation in fatigue performance was heavily related to the treatment pressure with a large drop off in performance across all pressures once temperature was increased beyond the lowest setpoint. For corrosion testing, the pitting potentials were shown to decrease significantly once both temperature and pressure were increased above their lowest setpoints with the lowest pitting potentials recorded at the mid point pressure setpoint. The opposite trend is apparent across elongation recorded in tensile testing wherein the elongation increased with increases in both pressure and temperature setpoints. Expectantly, the hardness and UTS were shown to decrease with the increase of the temperature setpoint. Interestingly however the higher hardness and UTS values were associated with the mid pressure setpoint. The yield strength was shown to not vary significantly with pressure however a large decrease is apparent from low to medium temperature set points.

Understanding and making use of large data sets across a wide range of tests can be a convoluted process. Therefore, a simple process was designed to allow for the straightforward characterisation of the overall performance of parts from each HIP cycle. The process takes the average of the important testing parameters from the aforementioned tests and combines them along with their error into one overall combined performance

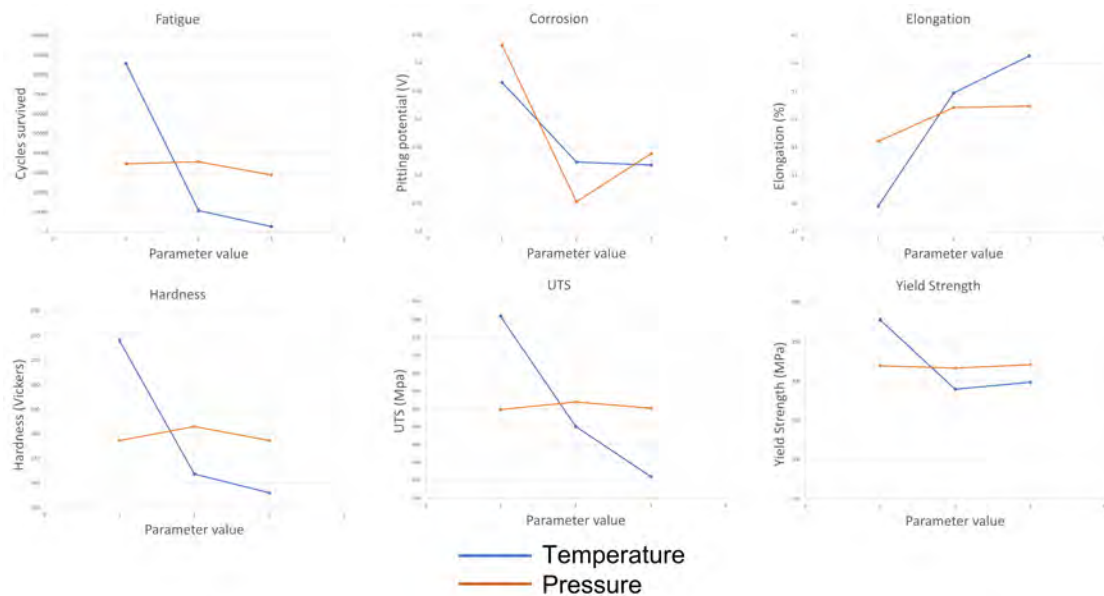


FIGURE 6.20: Graphs depicting the variation of experimental results with low, medium and high setpoints for temperature and pressure.

parameter. This parameter is then compared to the calculated parameter for wrought and as printed parts. The process also contains weighting factors for each of the factors involved which can be adjusted based on the application the parts are designed to be implemented in. For example the fatigue performance of a part which will be used in a role subject to cyclic loading is more important than its overall hardness value. The overall rankings are scored out of a 100 where 100 represents the values produced by the wrought component with literature values accounting for the fatigue and tensile properties. The best performing sample was 4 - HIP (T_{700} P_{137}) with a score of 100.04. (HIP treated at 700° and 137 MPa) as the best performing sample overall due to it being the only sample to reach run out in both fatigue stress tests, whilst producing an ultimate tensile strength value within 3 MPa of the as-built sample. Despite this the pitting corrosion performance of the sample was poor producing amongst the lowest average pitting potentials whilst only repassivating in one of the three tests. The 2nd best performing part was sample 10, the as-built part with a score of 87.13, significantly lower than wrought and 4 - HIP (T_{700} P_{137}). Whilst producing the 2nd best fatigue performance this sample struggled in the pitting corrosion testing, producing a large spread in pitting potentials whilst simultaneously reaching tensile failure at a comparatively low elongation compared to parts treated at medium and high HIP temperature set points. The 3rd placed sample was sample 7 (HIP treated at 700° and 200 MPa) with an overall score of 83.45 placing this samples overall performance close to that of the as-built sample. Ultimately the overall ranking model is inherently subjective to the parameters used but it is still useful as a general guide to compare overall performance across the wide range of post production treatments used.

6.11 Conclusions and further discussion

- Post-processing HIP cycles at mid (1125 °C) and high (1200 °C) temperatures remove the melt pools, melt pool boundaries and sub-grain cellular features that are present in the microstructure from the additive process.
- Such treatments also promoted grain growth which led to a reduction in the tensile strength (UTS 588 MPa 10 – As built to 533MPa treatment 9 - HIP (T₁₂₀₀ P₂₀₀)), hardness (233 HV 10 – As built to 154 HV treatment 9 - HIP (T₁₂₀₀ P₂₀₀)) and fatigue properties of the material, but fracture elongation and ductility were seen to increase.
- HIP treatment 4 - HIP (T₇₀₀ P₁₃₇) was seen to have the highest Nf at higher stress over 10 – As built, whilst being intermediate on ultimate tensile strength and recording the lowest average pitting potential. Samples subject to treatment 4 - HIP (T₇₀₀ P₁₃₇) retain cellular substructures and grain boundaries have not become enlarged, whilst density has been increased by the HIP treatment.
- With fatigue strength in 316L being dominated by microstructure, the results indicate that lower temperature, less aggressive HIP treatments (700-1000°C, 137MPa) are preferable to retain fatigue strength.
- The post-process HIP cycle at the lowest of the temperatures (700 °C) was found to result in an increased yield strength and a reduced elongation to fracture compared to other treatments. Variations in pressure did not induce a significant difference in tensile properties.
- Increasing the hold time of the HIP cycle resulted in no significant improvement in any of the metrics quantified in this work.
- Treatment 1 produced the highest mean pitting potential with a value of 0.970 ± 0.026 V rel. SCE an increase in pitting potential of 68 % relative to wrought.
- HIP treatments succeeded in reducing the spread of the pitting potentials by 52.46 % compared to as-built parts. With the largest reduction in spread achieved in low temperature cycles. However, there is still too large a variation in the corrosion performance of AM parts compared to wrought to instil confidence in their service in corrosive environments over wrought counterparts.
- Considering the pitting and repassivation potentials and their associated errors, none of the AM samples tested performed as well as the wrought sample across all metrics.

7. The corrosion performance of additively manufactured 17-4 PH

7.1 Introduction

17-4PH is a widely used precipitation-hardening stainless steel wherein the name represents the 17% chromium and 4% copper content of the steel. The composition in its entirety is listed in table 7.1 below. Please note that the density of wrought 17-4PH varies with its condition which is dependent on the precipitation hardening treatment the material is subject to, the value itself isn't crucial in this work but the value was taken as is 7.86 g cm^{-3} in this chapter.

Elemental	Weight Percent
Carbon	0.0 - 0.07
Chromium	15.00 - 17.00
Manganese	0.0 - 1.50
Silicon	0.0 - 0.70
Phosphorous	0.0 - 0.04
Sulphur	0.0 - 0.03
Nickel	3.00 - 5.00
Copper	3.00 - 5.00
Molybdenum	0.0 - 0.60
Niobium	0.0 - 0.45
Iron	Balance

TABLE 7.1: Elemental composition of standard 17-4PH in condition A (no heat treatment) [121].

Typically this material is conditioned using a specific heat treatment to modify the properties of the material to suit its use. 17-4PH is considered to be a stainless steel due to its high chromium content allowing a passive chromium oxide layer to form on the surface of the material [121][31]. 17-4PH has a similar elemental composition to 316 wherein the main differences are the increased copper and the reduced molybdenum and nickel content of 17-4PH.

7.2 Building methodology and approach for 17-4PH

The building methodology for this material was to perform a number of builds following an iterative process to identify the build parameters and machine settings that would produce parts of the highest possible density. This was not a trivial task as several of the builds failed. One issue that led to multiple failed builds was allowing for appropriate dosing of the powder per build layer. A potential reason for this include the flowability of the feed powder, however the feed-stock powder was produced by the manufacturer of every powder used in this thesis and the properties of the powder were within their tolerance with the particle sizes wherein 99% of particles are $< 50\mu m$ in diameter. Additionally the rubber wiper which spreads the powder on each successive layer is rotated for each build and changed when it begins to warp. Disassembling the powder doser (labelled B in figure 3.1), cleaning the parts thoroughly and reassembling the doser seemed to solve the issue. This series of events illustrates that although AM can be used to consistently produce parts of densities in the region of 99.8% there are numerous issues that can occur which require dismantling and re assembly of the machine. There are some issues such as malfunctioning Oxygen sensors which cannot be fixed by the user and the machine manufacturer must be contacted to organise suitable repairs.

7.3 Density Measurement Results

Figure 7.1 displays the average density measurements obtained for every 17-4PH part printed against their VED. The error bars represent the standard deviation as a function of repeat measurements at that particular VED. It's worth noting that the data displayed in figure 7.1 are not categorised by build plate location however the parts themselves were spread out across the build plate to minimise any build plate location based density variations. The variation in density as a function of location on the build plate is expanded upon in section 7.3.1. The shape of the graph in figure 7.1 matches those presented for Invar and 316L in figures 4.4 and 5.7. The Red zone represents the region where insufficient energy is being transferred from the laser to melt all of the powder. The Goldilocks zone represents the just right region which is optimal for building in. The measured relative density is at it's highest at this point and in general the variation in density represented by the error bars is lower in this region than in the Red zone and the Keyhole regime. The increased VED built at for 17-4PH however results in the measured relative density of parts to decrease as keyhole welds begin to form in the material once the VED exceeds $90J\text{ mm}^{-3}$ and we enter the region labelled as the keyhole regime [162][163].

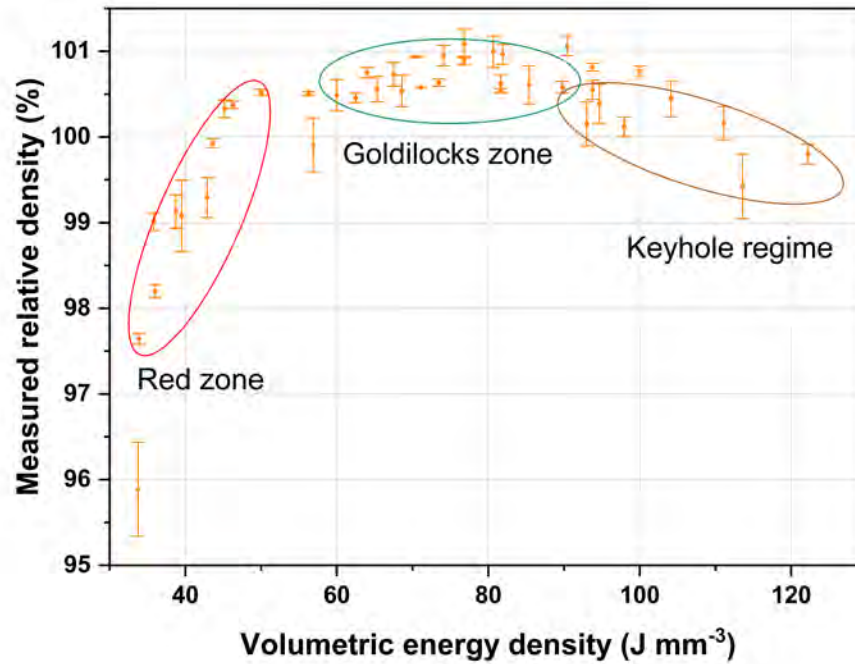


FIGURE 7.1: 17-4PH measured relative density against V.E.D.

7.3.1 Density variation across the build plate

To investigate the variation in density due to the location a build was completed consisting of 9 blocks containing 9 cubes of different VED's. The blocks were positioned as presented in figure 7.2 with each block numbered from one to nine.

The average density recorded across each block is presented in figure 7.3. The colours of the bar represent the location on the build plate with red being the left side, blue the centre and yellow the right side. The results indicate that parts printed in the centre of the build plate (blocks 4, 5, 6) are of highest density, followed by the back of the plate (blocks 1, 2, 3) followed by the lowest measured densities being produced at the front of the build plate (blocks 7, 8, 9). Further to this the standard deviation associated with the density measurements in blocks 7, 8 and 9 are significantly larger than blocks 1 through 6 which have comparative standard deviations.

7.4 CT scanning

CT scanning was carried out following the method outlined in 3.13. Figures 7.5 and 7.4 display the reconstructed images from CT scans carried out on AM 17-4PH. CT scans

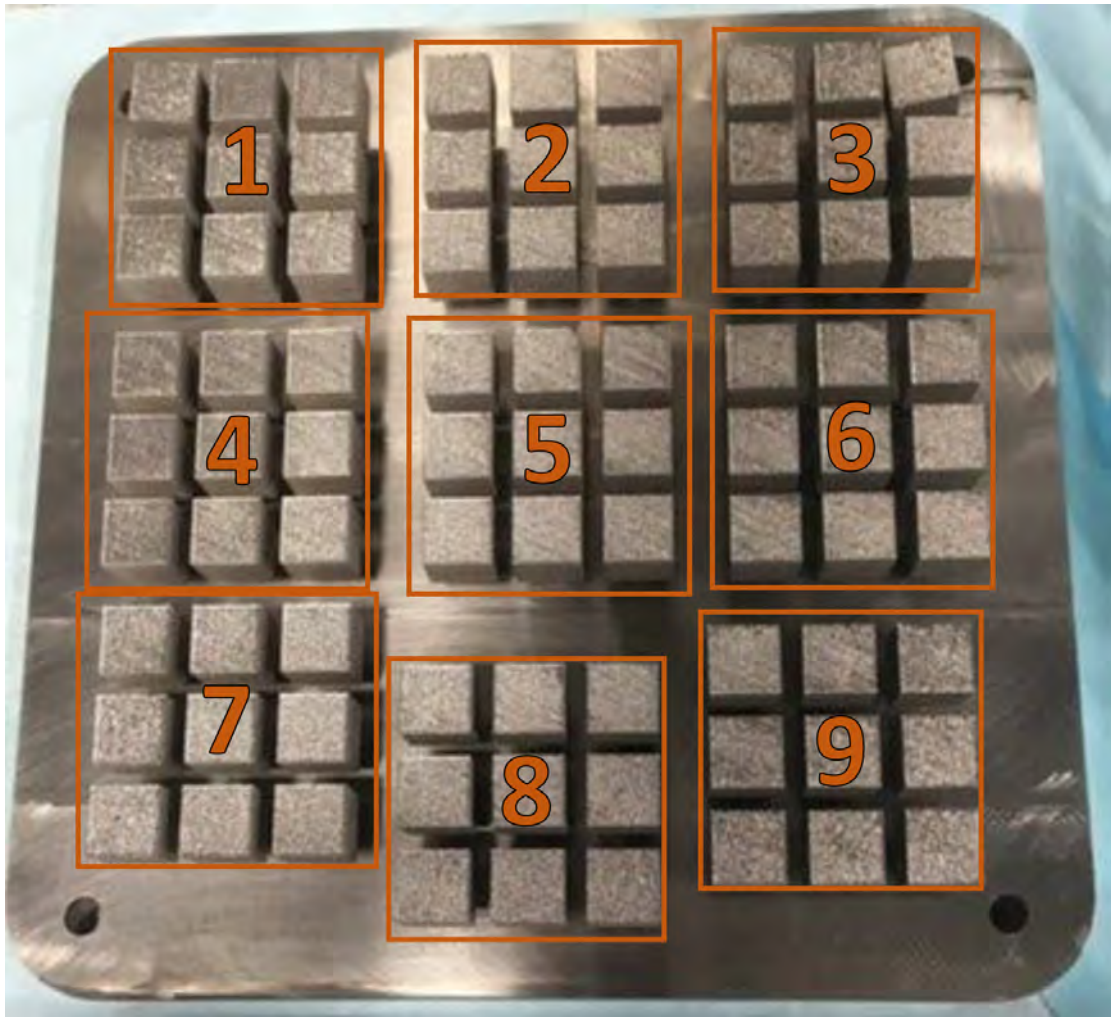


FIGURE 7.2: 17-4PH build showing location of blocks on build plate.

of 17-4PH were taken from a section from sample 4, the left column and middle row cube from block 5. These images show significantly more porosity than displayed in the 316L material in figures 5.10 and 5.11. With porosity being spread throughout the sample and not limited to exterior surfaces. The 3D reconstructed images from the 17-4PH samples suggest that the morphology of the porosity contains the scattered smaller more spheroidal porosity as presented in the 316L samples in section 5.4. To highlight this figure 7.6 displays the largest porosity feature seen across the duration of this work. Supplementary video 4 displays a rotating image of the CT scan which illustrate the spread of uniform and non-uniform porosity spread throughout the scanned samples.

The measured relative density of the sample as well as the largest and average pore size are displayed in table 7.2. The largest pore size displayed is comparable to that presented in 316L in table 5.7. Which on first inspection doesn't seem correct, however the method for producing the value for the largest pore diameter is taken as the largest singular thresholded point across any image slice and is effectively a 2-d measurement. Further

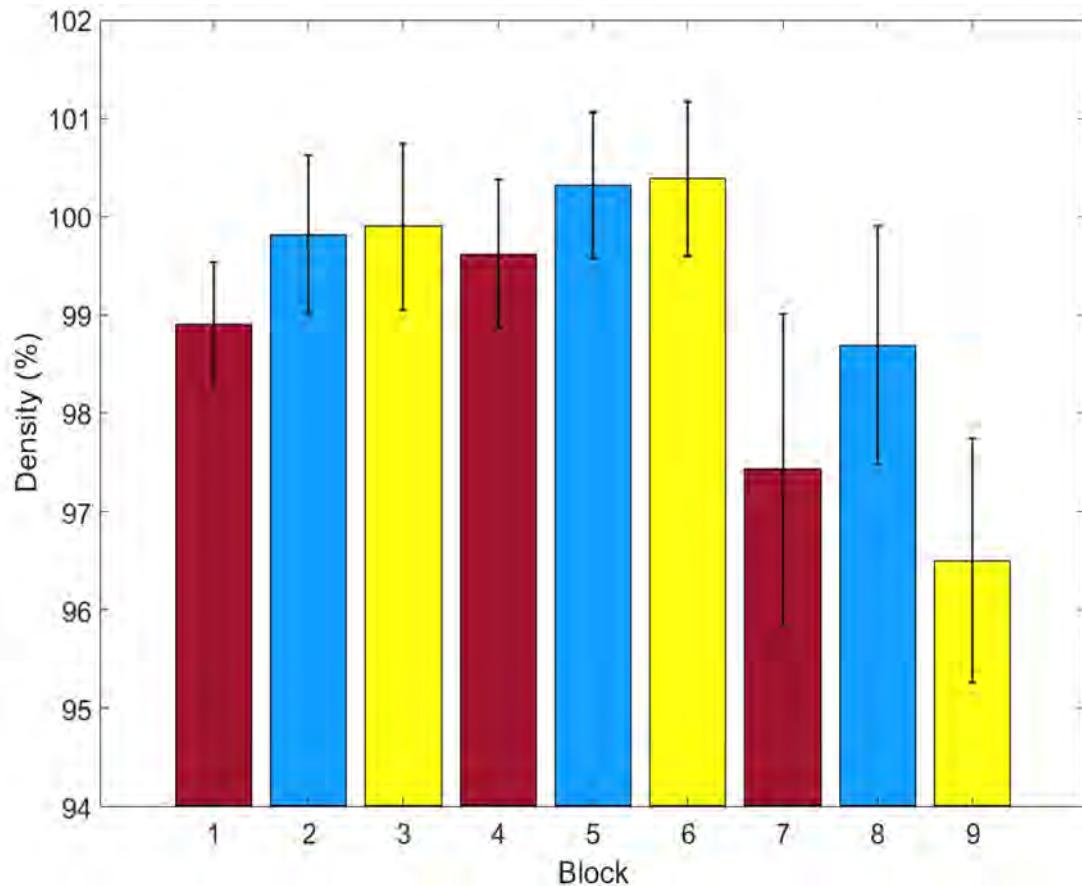


FIGURE 7.3: Mean recorded density with error bars giving the standard deviation per block across repeat measurements.

Material	Test Method	Density (%)	Largest Pore (mm ²)	Average Pore Size (mm ²)
17-4PH	Archimedes measurement	100.14	-	-
17-4PH	CT data	99.72	0.998	0.1350

TABLE 7.2: Table showing the density measured using Archimedes principle and calculated from CT scanning.

to this the value returned at this point is going to be dependent on the axis direction the slices cut across the scanned sample. The average pore size however is significantly larger for the 17-4PH scanned sample, this is likely indicative of the greater presence of lack of fusion porosity seen within this sample which is not present within the scanned 316L sample.

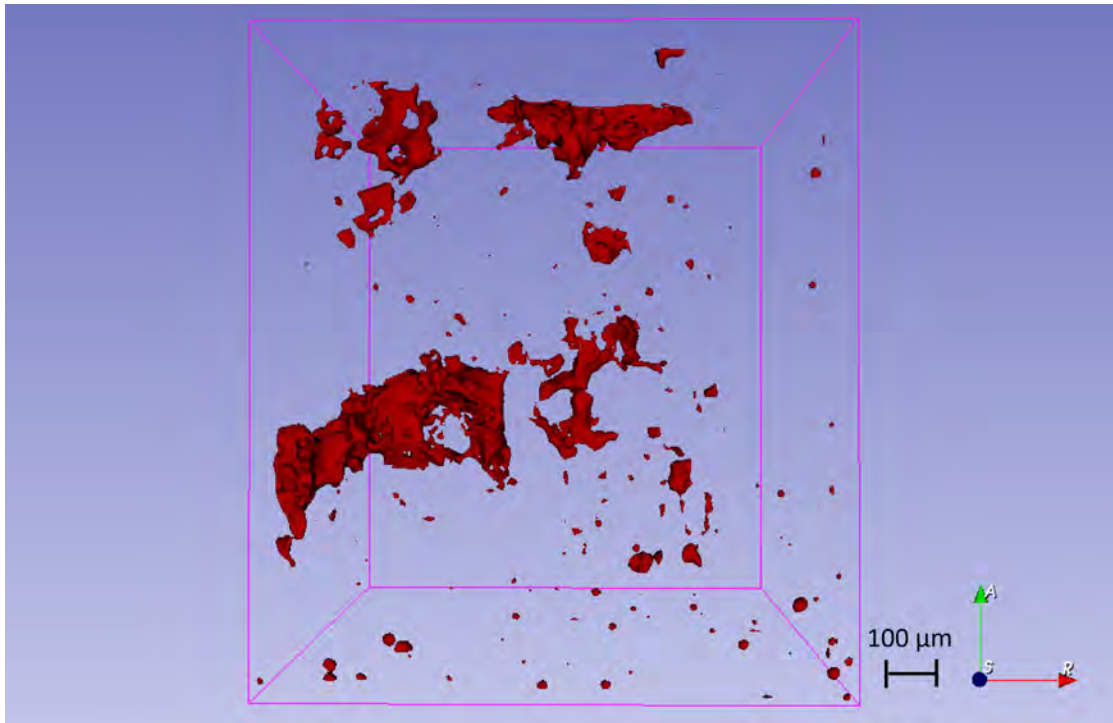


FIGURE 7.4: CT reconstructed image showing the front view of non spherical lack of fusion and spherical porosity within a 17-4PH specimen.

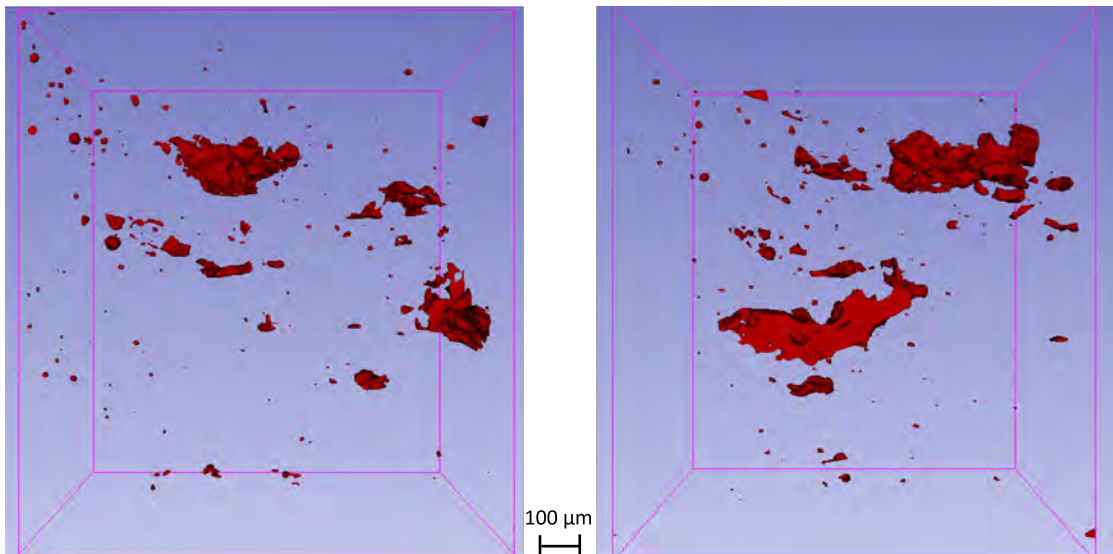


FIGURE 7.5: CT reconstructed image showing Left: Side view and Right: Top down view of non spherical lack of fusion and spherical porosity within a 17-4PH specimen.

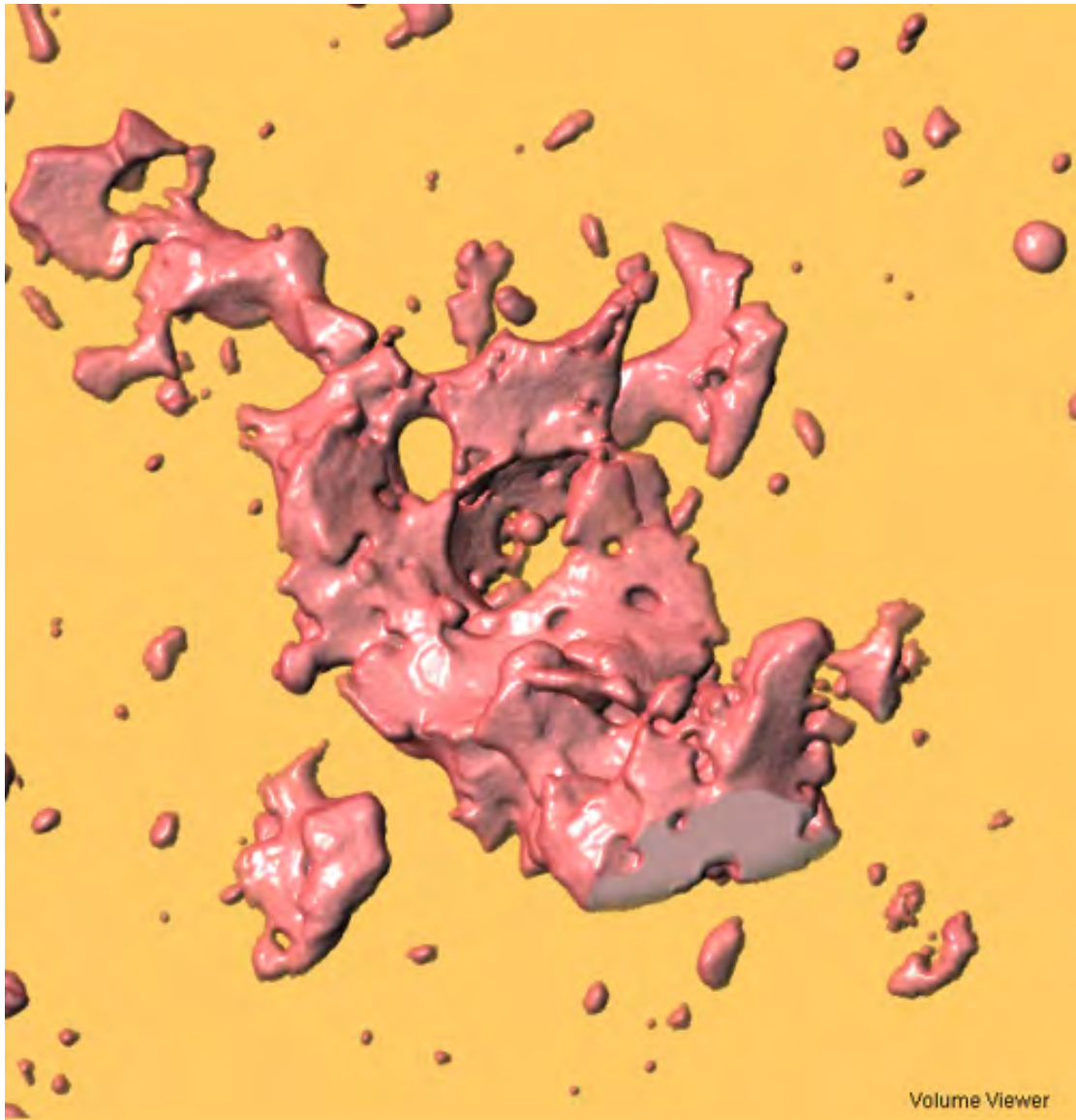


FIGURE 7.6: CT image showing the largest observed porosity observed.

7.5 Corrosion experimentation

7.5.1 Potentiodynamic Scanning

Potentiodynamic scanning was carried out in 3.5% NaCl electrolyte solution using the procedure outlined in section 3.8.2. Figure 7.7 shows the pitting and repassivation potentials on samples printed using the same build parameters but at different locations on the build plate at three different z slices per cube. Slice 1 refers to the top of the sample, with slice 2 being directly below slice 1 as detailed in the left image of figure 3.10.

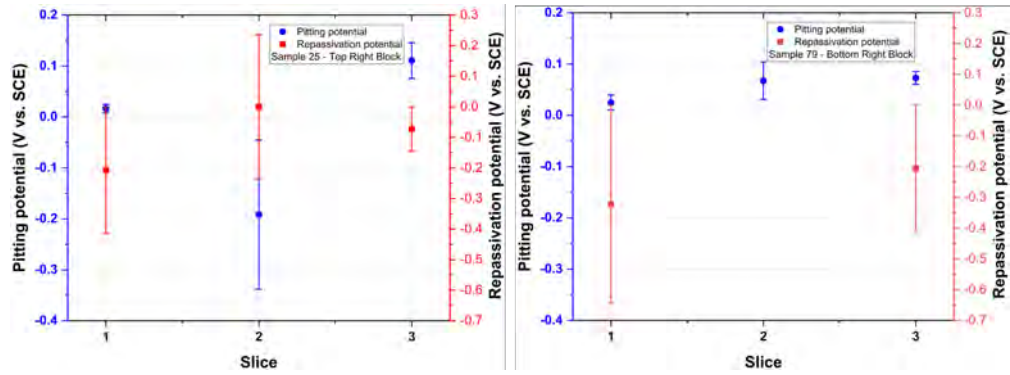


FIGURE 7.7: Pitting and repassivation potentials on samples from cube 25 (left) and 79 (right) printed using the same build parameters but at different locations on the build plate at three different height slices per cube.

The graphs in figure 7.7 show that there is a variation in the pitting and repassivation potentials with respect to the height location of the sample slice that is potentiodynamically scanned. This is not surprising given the large variation in sample porosity across every dimension of the sample as visible in figures 7.4 and 7.5. As discussed previously in section 5.5, 4.4, 6.9 and 1.15.3 any form of porosity defect in the surface of a material can result in reduced localised corrosion performance by facilitating crevice corrosion, pit transition from meta-stable to active or by causing inhomogeneity's in the materials passive layer. A similar experiment was carried out taking slices from the extreme points of a printed cube, one from the top and one from just above the bottom. Similar results were found wherein pitting and repassivation potentials varied from slice to slice. In summary, there is a variation in pitting and repassivation potentials with respect to the slice location on the cube however there is no pattern regarding this variation and the variation is likely due a result of the spread of porosity throughout the sample.

Figure 7.8 shows the pitting and repassivation potentials obtained during potentiodynamic scanning with respect to the measured relative density of the sample. Note for the points with no error bars, repassivation was not recorded on repeat tests for these samples. There is no relationship between the pitting or repassivation potentials recorded on these samples and their measured relative densities. The values at 100 % density represent wrought samples. The wrought sample demonstrated a mean pitting potential of (0.29121 ± 0.015) V vs. SCE. This value is significantly higher than any of the pitting potentials recorded on AM samples. The variation associated with the pitting potential of the wrought sample is smaller than that generally associated with the AM values displayed in figure 7.8. The mean repassivation potential of (-0.184 ± 0.0585) V vs. SCE however is comparable to the values measured on the AM parts. The smallest variation in pitting and repassivation potential was recorded on the AM sample with 101.58 % density. There is no indication given from the data or the build parameters used as to

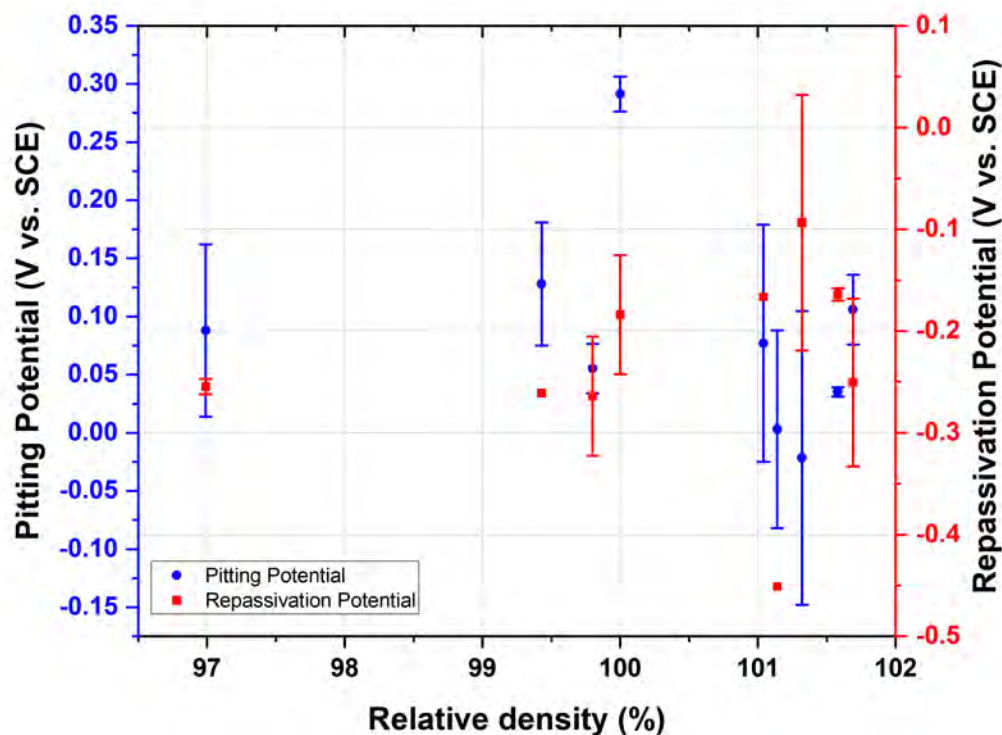


FIGURE 7.8: Pitting and repassivation potentials on AM 17-4PH samples against measured relative density in 1 % NaCl solution.

why this is. Potentially, it could be due to there being a distinct lack of porosity in the regions tested or it could also be due to general coincidence.

7.5.2 Potentiolapse

Potentiolapse testing as outlined in section 3.8.3 was carried out on AM 17-4PH in a 1 % NaCl electrolyte. The 1% NaCl electrolyte was chosen to allow for more still images to be captured than would be possible using a 3.5 % NaCl electrolyte which would result in a more rapid breakdown at a lower applied potential. The video showing a side-by-side view of the sample surface along with the synced potentiodynamic plot are displayed in supplementary video 4, start the slideshow to start both videos simultaneously. Figure 7.9 displays still shots from the video alongside the potentiodynamic curve obtained during the experiment corresponding to the sample surface image at that time step.

Please note that the black object in the lower right portion of the exposed area is a bubble forming underneath the edge of the tape used to expose a certain area. Column B displays the time point when the sample is approaching the breakdown potential, the black irregularly shaped lack of fusion porosity defect at the top right of the image is

the largest porosity defect located on the exposed area. Corresponding to the potentiodynamic scan being in the passive regime where the measured current density remains fairly constant as the applied voltage is increased.

In row B the porosity defect mentioned previously has seemingly is increasing in volume as the applied voltage accelerates the chemical corrosion reaction. This can be seen by the sharp increase in recorded current density with almost no increase to the applied potential difference. This process results in corrosion product being mined from the porosity defect and released into the electrolyte. In row C the material is breaking down rapidly and corrosion product is spreading across the surface of the sample. Breakdown has also occurred at the bottom left of the exposed area where another localised corrosion region is developing. The curved darker lines spreading outward from the bottom left localised corrosion region are of interest. These are believed to be particles of corrosion product that have been ejected from a localised corrosion defect. These metal oxides are then believed to be moving within the solution following the electric field lines produced from the localised corrosion regions. This is visible in supplementary video 4 from both localised corrosion defects between 17 and 22 seconds.

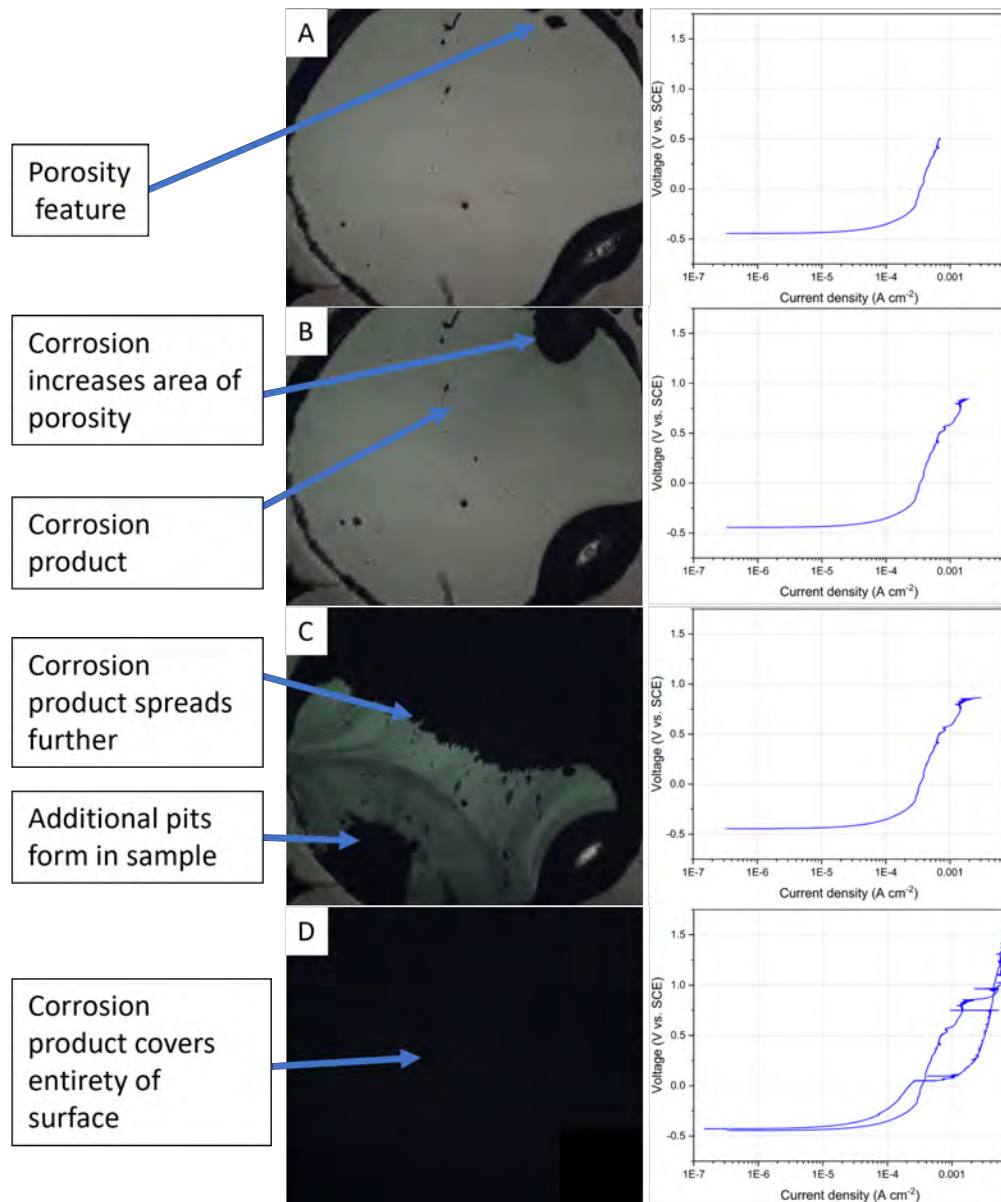


FIGURE 7.9: Potentiolapse technique with samples surface in left column and corresponding potentiodynamic plot in right column.

Once the corrosion product had spread to cover the surface of the sample (between the time intervals shown in rows C and D) it remained for the remainder of the experiment. In row D taken from the end point of the scan after repassivation the entirety of the surface is covered in corrosion product.

In summary from the potentiolapse technique we can establish that localised corrosion initiated at a lack of fusion porosity defect, the largest porosity defect on it's sample surface. This phenomena was similarly observed in numerous time lapse experiments on the material Invar as outlined in section [4.3.2](#) and is likely to occur in any material containing porosity defects on their surfaces. Once breakdown had occurred the material broke down rapidly and another region of the exposed surface suffered from localised corrosion attack resulting in corrosion product quickly covering the surface of the sample. It is possible had there been a flow of electrolyte across the surface of the sample rather than a stagnant surface that this corrosion product could've been swept away and more features would've become visible and observable.

7.6 17-4PH summary and conclusions

In summary the density variation of 17-4PH across the build plate was significantly larger than that of 316L. With the regions best suited to building being the centre of the build plate with a drop off in density when building at the front of the build plate, furthest away from the powder hopper. In general the highest densities were achieved on the right hand side of the build plate, the region where the argon gas flow originates from. This region of the build plate is subjected to the least amount of spatter as the gas flow blows the ejected molten liquid towards the left of the build plate. This could be result in fewer defects and higher density parts being produced on the right side of the build plate. The 3D reconstructed CT images show large amounts of irregularly shaped porosity present throughout the material as well as the spread out smaller regions of prolate spheroid shaped porosity as seen in the 316L images. The corrosion findings indicate that randomly distributed porosity at the surface results in inconsistent corrosion metrics wherein the locality of passive layer breakdown and pitting initiation is highly dependent on local surface features. This is due to pitting initiation mechanics which indicate that the largest available pore is statistically the most likely to facilitate mature pit growth [99] [48]. Porosity with occluded regions facilitates the Fontana Greene mechanism which creates a driving force for crevice corrosion [100]. This aligns with the findings presented in sections 4.5, 5.6 and 6.11.

8. Final Conclusions and Future Work

8.1 Final conclusions

In this work the corrosion properties of LPBF manufactured Invar, 17-4PH and 316L have been investigated. Whilst there are some nuances throughout the work such as the number of factors that lead to differential corrosion performance between wrought and AM 316L there are some key points which cover each material tested.

- Any porosity defects present on the materials surface acts as an initiation site for localised corrosion attack. This attack is more likely to occur at irregularly shaped lack of fusion porosity and was shown to preferentially occur at porosity situated at melt pool boundaries.
- Whilst there can be elemental segregation or differences in microstructure between wrought and LPBF parts ultimately these effects are not dominant at the density level of parts produced and examined in this work.
- In order to eliminate all porosity within a LPBF using the equipment in this work post-production treatments are required.
- The pitting/localised corrosion performance parameters have large variability on LPBF parts.

The vast majority of literature on the corrosion of AM or LPBF parts is focused on the behaviour of 316L, the material often used for applications requiring good mechanical properties in corrosive salt water environments. There is significant literature on this topic, some which is misleading and conveys very situation dependent results without considerations for the variability in results or error bars. This was particularly evident in the first 2 years of carrying out this doctorate. As time has progressed the validity and sincerity of presented literature has improved and a more valid and balanced approach to the corrosion performance of AM 316L in literature is available. The corrosion and

a range of mechanical properties of LPBF 316L treated by HIP was investigated with the goal of improving these properties. Some of the HIP treatments were successful in improving the mechanical properties of the material whilst reducing the scatter of pitting potentials and others reduced the mechanical properties.

- Post-processing HIP cycles at mid (1125 °C) and high (1200 °C) temperatures remove the melt pools, melt pool boundaries and sub-grain cellular features that are present in the microstructure from the additive process. Such treatments also promoted grain growth which led to a reduction in the tensile strength (UTS 588 MPa 10 – As built to 533MPa treatment 9 - HIP (T1200 P200)), hardness (233 HV 10 – As built to 154 HV treatment 9 - HIP (T1200 P200)) and fatigue properties of the material, but fracture elongation and ductility were seen to increase.
- HIP treatment 4 - HIP (T700 P137) was seen to have the best fatigue performance being the only condition to reach runout in both the lower and higher stress fatigue testing. Whilst being intermediate on ultimate tensile strength and recording the lowest average pitting potential. Samples subject to treatment 4 - HIP (T700 P137) retain cellular substructures and grain boundaries have not become enlarged, whilst density has been increased by the HIP treatment.
- The post-process HIP cycle at the lowest of the temperatures (700 °C) was found to result in an increased yield strength and a reduced elongation to fracture compared to other treatments. Variations in pressure did not induce a significant difference in tensile properties. With fatigue strength in 316L being dominated by microstructure, the results indicate that lower temperature, less aggressive HIP treatments (700-1000°C, 137MPa) are preferable to retain fatigue strength.
- Increasing the hold time of the HIP cycle resulted in no significant improvement in any of the metrics quantified in this work.
- HIP treatments succeeded in reducing the spread of the pitting potentials by 52.46 % compared to as-built parts. With the largest reduction in spread achieved in low temperature cycles. Treatment 1 produced the highest mean pitting potential with a value of 0.97 ± 0.026 V rel. SCE an increase in pitting potential of 68 % relative to wrought. However, there is still too large a variation in the corrosion performance of AM parts compared to wrought to instil confidence in their service in corrosive environments over wrought counterparts.

In summary, the mechanical performance of as-built LPBF 316L performs very well compared to wrought 316L. However the inherent porosity present in these parts resulted in large variations in corrosion performance. Increasing the density of the parts via HIP

treatments reduced this variation. Producing porosity free parts or testing only regions with no porosity present results in excellent corrosion behaviour.

8.2 Further Work

There is a large amount of further work to be carried out to allow for the confidence in the performance of AM/LPBF parts in corrosive environments to be comparable to their wrought counterparts. Further to this there is also a large body of work the author would have liked to carry out but this was not possible. These include

- Investigating the composition and different arrangements within the passive layer on austenitic stainless steel powder, AM and wrought parts using XPS.
- Carry out alloying editions to 17-4PH and 316L powder to manipulate the passive layer composition and for increased corrosion performance. i.e. increasing molybdenum and nickel content.
- Produce 100 % dense LPBF parts and test their corrosion properties.
- Measure the surface porosity of an AM sample using white light interferometry than use a nano-indenter to indent porosity into a wrought stainless steel part and compare the corrosion performance of both samples.
- CT scan a large size wrought, LPBF and LPBF HIP sample before, during and after potentiodynamic scanning in steps to view and compare pit growth.
- Carry out sensitisation testing (double loop EPR) on as-built, HIP and heat treated 316L to compare the degree of sensitisation (if any) across these methods.
- Comparing the mechanical and corrosion properties of austenitic stainless steel powder treated via nitriding, varying the build atmosphere, heat treatment gas and HIP gas between argon and nitrogen atmospheres.

Bibliography

- [1] ASTM International. Additive Manufacturing Overview, 2018. URL <https://www.astm.org/industry/additive-manufacturing-overview.html>.
- [2] 3DPrint.com. Robotic Dentist Implants 3D Printed Teeth in Woman’s Mouth in Autonomous Surgery | 3DPrint.com | The Voice of 3D Printing / Additive Manufacturing, 2017. URL <https://3dprint.com/188789/robotic-dentist-3d-printed-teeth/>.
- [3] 3DPrint.com. Chinese Doctors 3D Print a Titanium Pelvic Prosthesis for Cancer Survivor Afflicted with Bone Metastases | 3DPrint.com | The Voice of 3D Printing / Additive Manufacturing, 2014. URL <https://3dprint.com/23760/3d-printed-titanium-pelvis/>.
- [4] Simon Ford and M Elanie Despeisse. Additive manufacturing and sustainability: an exploratory study of the advantages and challenges. *Cleaner Production*, 2016. doi: 10.1016/j.jclepro.2016.04.150. URL <https://bit.ly/2ry4UIG>.
- [5] Renishaw plc. RenAM 500Q, 2018. URL <https://www.renishaw.com/en/renam-500q--42781>.
- [6] W. J. Sames, F. A. List, S. Pannala, R. R. Dehoff, and S. S. Babu. The metallurgy and processing science of metal additive manufacturing. *International Materials Reviews*, 61(5):315–360, 2016. doi: 10.1080/09506608.2015.1116649. URL <https://doi.org/10.1080/09506608.2015.1116649>.
- [7] G. Tapia, A.H. Elwany, and H. Sang. Prediction of porosity in metal-based additive manufacturing using spatial Gaussian process models. *Additive Manufacturing*, 12:282–290, 2016. ISSN 2214-8604. doi: 10.1016/J.ADDMA.2016.05.009. URL <https://www.sciencedirect.com/science/article/pii/S2214860416300938>.
- [8] Ming Tang, P. Chris Pistorius, and Jack L. Beuth. Prediction of lack-of-fusion porosity for powder bed fusion. *Additive Manufacturing*, 14:39–48, 2017. ISSN 2214-8604. doi: 10.1016/J.ADDMA.2016.12.001. URL <https://www.sciencedirect.com/science/article/pii/S2214860416300471>.

- [9] G. Vastola, Q.X. Pei, and Y.-W. Zhang. Predictive model for porosity in powder-bed fusion additive manufacturing at high beam energy regime. *Additive Manufacturing*, 22:817–822, 2018. ISSN 2214-8604. doi: 10.1016/J.ADDMA.2018.05.042. URL <https://www.sciencedirect.com/science/article/pii/S221486041830174X>.
- [10] Adam Hehr, Mark Norfolk, Dan Kominsky, Andrew Boulanger, Matthew Davis, and Paul Boulware. Smart build-plate for metal additive manufacturing processes. *Sensors*, 20(2), 2020. ISSN 1424-8220. doi: 10.3390/s20020360. URL <https://www.mdpi.com/1424-8220/20/2/360>.
- [11] J. Boes, A. Röttger, L. Becker, and W. Theisen. Processing of gas-nitrided aisi 316l steel powder by laser powder bed fusion – microstructure and properties. *Additive Manufacturing*, 30:100836, 2019. ISSN 2214-8604. doi: 10.1016/j.addma.2019.100836. URL <https://www.sciencedirect.com/science/article/pii/S2214860419304762>.
- [12] Jitka Metelkova, Yannis Kinds, Karolien Kempen, Charlotte de Formanoir, Ann Witvrouw, and Brecht Van Hooreweder. On the influence of laser defocusing in selective laser melting of 316l. *Additive Manufacturing*, 23:161–169, 2018. ISSN 2214-8604. doi: 10.1016/j.addma.2018.08.006. URL <https://www.sciencedirect.com/science/article/pii/S2214860418302343>.
- [13] Saad Waqar, Qidong Sun, Jiangwei Liu, Kai Guo, and Jie Sun. Numerical investigation of thermal behavior and melt pool morphology in multi-track multi-layer selective laser melting of the 316l steel. *The International Journal of Advanced Manufacturing Technology*, 112(3-4):879–895, 2020. doi: 10.1007/s00170-020-06360-0.
- [14] Zachary A. Young, Qilin Guo, Niranjana D. Parab, Cang Zhao, Minglei Qu, Luis I. Escano, Kamel Fezzaa, Wes Everhart, Tao Sun, and Lianyi Chen. Types of spatter and their features and formation mechanisms in laser powder bed fusion additive manufacturing process. *Additive Manufacturing*, 36:101438, 2020. ISSN 2214-8604. doi: 10.1016/j.addma.2020.101438. URL <https://www.sciencedirect.com/science/article/pii/S2214860420308101>.
- [15] W.G. Fano, A. Razzitte, and P. Larocca. *Electromagnetic Field Radiation in Matter*. IntechOpen, 2020. ISBN 9781789845181. doi: 10.5772/intechopen.83257. URL <https://books.google.co.uk/books?id=QJYtEAAAQBAJ>.
- [16] Toshi-Taka Ikeshoji, Makiko Yonehara, Chika Kato, Yuma Yanaga, Koki Takeshita, and Hideki Kyogoku. Spattering mechanism of laser powder bed fusion additive manufacturing on heterogeneous surfaces. *Nature Scientific Reports*, 12

- (1), 2022. doi: 10.1038/s41598-022-24828-9. URL <https://doi.org/10.1038/s41598-022-24828-9>.
- [17] Mostafa Yakout, Ian Phillips, M.A. Elbestawi, and Qiyin Fang. In-situ monitoring and detection of spatter agglomeration and delamination during laser-based powder bed fusion of invar 36. *Optics & Laser Technology*, 136:106741, 2021. ISSN 0030-3992. doi: 10.1016/j.optlastec.2020.106741. URL <https://www.sciencedirect.com/science/article/pii/S0030399220313748>.
- [18] Di Wang, Shibiao Wu, Fan Fu, Shuzhen Mai, Yongqiang Yang, Yang Liu, and Changhui Song. Mechanisms and characteristics of spatter generation in slm processing and its effect on the properties. *Materials & Design*, 117:121–130, 2017. ISSN 0264-1275. doi: 10.1016/j.matdes.2016.12.060. URL <https://www.sciencedirect.com/science/article/pii/S0264127516315866>.
- [19] R. R. Dehoff, M. M. Kirka, W. J. Sames, H. Bilheux, A. S. Tremsin, L. E. Lowe, and S. S. Babu. Site specific control of crystallographic grain orientation through electron beam additive manufacturing. *Materials Science and Technology*, 31(8): 931–938, 2015. doi: 10.1179/1743284714Y.0000000734. URL <https://doi.org/10.1179/1743284714Y.0000000734>.
- [20] Lawrence E. Murr, Sara M. Gaytan, Diana A. Ramirez, Edwin Martinez, Jennifer Hernandez, Krista N. Amato, Patrick W. Shindo, Francisco R. Medina, and Ryan B. Wicker. Metal fabrication by additive manufacturing using laser and electron beam melting technologies. *Journal of Materials Science & Technology*, 28(1):1 – 14, 2012. ISSN 1005-0302. doi: 10.1016/S1005-0302(12)60016-4. URL <http://www.sciencedirect.com/science/article/pii/S1005030212600164>.
- [21] H.G. Gong Haijun, J.J.S. Kai Zeng, D. Deepankar Pal, and B. Stucker. Melt pool characterization for selective laser melting of ti-6al-4 v pre-alloyed powder. *Solid Freeform Fabrication Symposium*, pages 256–267, 2014.
- [22] Maria L. Montero-Sistiaga, Miguel Godino-Martinez, Kurt Boschmans, Jean-Pierre Kruth, Jan Van Humbeeck, and Kim Vanmeensel. Microstructure evolution of 316l produced by hp-slm (high power selective laser melting). *Additive Manufacturing*, 23:402 – 410, 2018. ISSN 2214-8604. doi: 10.1016/j.addma.2018.08.028. URL <http://www.sciencedirect.com/science/article/pii/S221486041830280X>.
- [23] Mostafa Yakout, M.A. Elbestawi, and Stephen C. Veldhuis. A study of thermal expansion coefficients and microstructure during selective laser melting of invar 36 and stainless steel 316l. *Additive Manufacturing*, 24:405 – 418, 2018. ISSN 2214-8604. doi: 10.1016/j.addma.2018.09.035. URL <http://www.sciencedirect.com/science/article/pii/S2214860418305827>.

- [24] John J Lewandowski and Mohsen Seifi. Metal Additive Manufacturing: A Review of Mechanical Properties. *Annual Review of Advance Materials Research*, 2016. doi: 10.1146/annurev-matsci-070115-032024. URL www.annualreviews.org.
- [25] C.A. Bronkhorst, J.R. Mayeur, V. Livescu, R. Pokharel, D.W. Brown, and G.T. Gray. Structural representation of additively manufactured 316l austenitic stainless steel. *International Journal of Plasticity*, 2019. ISSN 0749-6419. doi: 10.1016/j.ijplas.2019.01.012. URL <http://www.sciencedirect.com/science/article/pii/S0749641918307654>.
- [26] R. Dörfert, J. Zhang, B. Clausen, H. Freife, J. Schumacher, and F. Vollertsen. Comparison of the fatigue strength between additively and conventionally fabricated tool steel 1.2344. *Additive Manufacturing*, 2019. ISSN 2214-8604. doi: 10.1016/j.addma.2019.01.010. URL <http://www.sciencedirect.com/science/article/pii/S2214860418306912>.
- [27] Neng Li, Shuai Huang, Guodong Zhang, Renyao Qin, Wei Liu, Huaping Xiong, Gongqi Shi, and Jon Blackburn. Progress in additive manufacturing on new materials: A review. *Journal of Materials Science & Technology*, 35(2):242 – 269, 2019. ISSN 1005-0302. doi: 10.1016/j.jmst.2018.09.002. URL <http://www.sciencedirect.com/science/article/pii/S1005030218301786>.
- [28] Sean R Agnew, James M Fitz-Gerald, William R Moore, and Tabitha A Newman. High Strength and Ductility of Additively Manufactured 316L Stainless Steel Explained. *Metallurgical and Materials Transactions A*, 49(36), 2018. doi: 10.1007/s11661-018-4607-2. URL <https://doi.org/10.1007/s11661-018-4607-2>.
- [29] Todd M. Mower and Michael J. Long. Mechanical behavior of additive manufactured, powder-bed laser-fused materials. *Materials Science and Engineering: A*, 651:198 – 213, 2016. ISSN 0921-5093. doi: 10.1016/j.msea.2015.10.068. URL <http://www.sciencedirect.com/science/article/pii/S092150931530530X>.
- [30] NACE International. NACE study estimates global corrosion cost at \$2.5 trillion annually, 2016. URL <https://inspectioneering.com/news/2016-03-08/5202/nace-study-estimates-global-cost-of-corrosion-at-25-trillion-ann>.
- [31] G.S. Frankel. Pitting corrosion of metals a review of the critical factors. *Journal of the Electrochemical Society*, Vol. 145, No. 6, pp. 2186-2198., 1998. doi: 10.1149/1.1838615.
- [32] E. McCafferty. *Introduction to Corrosion Science*. Springer New York, 2010. ISBN 9781441904546. URL <https://books.google.co.uk/books?id=g9oXcE-gQKUC>.

- [33] Corrosionpedia Staff. An Introduction to the Galvanic Series: Galvanic Compatibility and Corrosion, 2017. URL <https://www.corrosionpedia.com/an-introduction-to-the-galvanic-series-galvanic-compatibility-and-corrosion/2/1403>.
- [34] Professor Linn W. Hobbs. LABORATORY 3: Electrochemical Corrosion Gibbs Free Energy, Anodic Corrosion & the EMF Series. Technical report, Massachusetts Institute of Technology, 2006. URL https://ocw.mit.edu/courses/materials-science-and-engineering/3-014-materials-laboratory-fall-2006/labs/w3{}_b2.pdf.
- [35] Marcel Pourbaix. *Atlas of Electrochemical Equilibria in Aqueous solutions*. Pergamon Press, New York, 1966.
- [36] Chemistry LibreTexts. 4.5: Pourbaix diagrams - Chemistry LibreTexts, 2018. URL https://chem.libretexts.org/Bookshelves/Inorganic_Chemistry/.
- [37] Dmitri Kopeliovich. Pourbaix diagrams. *Substances & Technologies*, 2012. URL http://www.substech.com/dokuwiki/doku.php?id=pourbaix_diagrams.
- [38] G. S. Frankel, Tianshu Li, and J. R. Scully. Perspective—Localized Corrosion: Passive Film Breakdown vs Pit Growth Stability. *Journal of The Electrochemical Society*, 164(4):C180–C181, 2017. ISSN 0013-4651. doi: 10.1149/2.1381704jes. URL <http://jes.ecsdl.org/lookup/doi/10.1149/2.1381704jes>.
- [39] Jose R. Galvele. Transport Processes and the Mechanism of Pitting of Metals. *Journal of The Electrochemical Society*, 123(4):464, 1976. ISSN 00134651. doi: 10.1149/1.2132857. URL <http://jes.ecsdl.org/cgi/doi/10.1149/1.2132857>.
- [40] L. F. Lin. A Point Defect Model for Anodic Passive Films. *Journal of The Electrochemical Society*, 128(6):1194, 1981. ISSN 00134651. doi: 10.1149/1.2127592. URL <http://jes.ecsdl.org/cgi/doi/10.1149/1.2127592>.
- [41] D. E. Williams, R. C. Newman, Q. Song, and R. G. Kelly. Passivity breakdown and pitting corrosion of binary alloys. *Nature*, 350(6315):216–219, 1991. doi: 10.1038/350216a0.
- [42] N. J. Laycock and S. P. White. Computer simulation of single pit propagation in stainless steel under potentiostatic control. *Journal of The Electrochemical Society*, 148(7):B264, 2001. doi: 10.1149/1.1376119. URL <https://dx.doi.org/10.1149/1.1376119>.
- [43] Majid Ghahari, Donal Krouse, Nicholas Laycock, Trevor Rayment, Cristiano Padovani, Marco Stampanoni, Federica Marone, Rajmund Mokso, and Alison J.

- Davenport. Synchrotron x-ray radiography studies of pitting corrosion of stainless steel: Extraction of pit propagation parameters. *Corrosion Science*, 100: 23–35, 2015. ISSN 0010-938X. doi: 10.1016/j.corsci.2015.06.023. URL <https://www.sciencedirect.com/science/article/pii/S0010938X15002954>.
- [44] N Cabrera, N F Mott, and H H Wills. Theory of the Oxidation of Metals. Technical report, H.H. Wills Physical Laboratory, University of Bristol, 1949. URL <http://iopscience.iop.org/article/10.1088/0034-4885/12/1/308/pdf>.
- [45] T.P. Hoar, D.C. Mears, and G.P. Rothwell. The relationships between anodic passivity, brightening and pitting. *Corrosion Science*, 5(4):279 – 289, 1965. ISSN 0010-938X. doi: 10.1016/S0010-938X(65)90614-1. URL <http://www.sciencedirect.com/science/article/pii/S0010938X65906141>.
- [46] N. F Mott. The theory of the formation of protective oxide films on metals.—iii. *Transactions of the Faraday Society*, 43:429–434, 1946. doi: 10.1039/TF9474300429.
- [47] P Marcus and J Herbelin. The entry of chloride ions into passive films on nickel studied by spectroscopic (ESCA) and nuclear (^{36}Cl radiotracer) methods. *Corrosion Science*, Vol 34, 34(7):1123–1145, 1993. doi: 10.1016/0010-938X(93)90293-P.
- [48] P. Marcus and J. Oudar. *Corrosion Mechanisms in Theory and Practice*. Corrosion Technology - Marcel Dekker. M. Dekker, 1995. ISBN 9780824795924. URL <https://books.google.co.uk/books?id=d7xRAAAAMAAJ>.
- [49] Jennifer A. Bardwell, B. MacDougall, and G. I. Sproule. Use of SIMS to Investigate the Induction Stage in the Pitting of Iron. *Journal of The Electrochemical Society*, 136(5):1331, 1989. ISSN 19457111. doi: 10.1149/1.2096916. URL <http://jes.ecsdl.org/cgi/doi/10.1149/1.2096916>.
- [50] D. D. Chao, C. Y., Lin, L. F., & Macdonald. A Point Defect Model for Anodic Passive Films. *Journal of The Electrochemical Society*, 128(6):1187–1194, 1981. ISSN 00134651. doi: 10.1149/1.2127591.
- [51] Mirna Urquidi and Digby D. Macdonald. Solute-Vacancy Interaction Model and the Effect of Minor Alloying Elements on the Initiation of Pitting Corrosion. *Journal of The Electrochemical Society*, 132(3):555, 1985. ISSN 00134651. doi: 10.1149/1.2113886. URL <http://jes.ecsdl.org/cgi/doi/10.1149/1.2113886>.
- [52] C. M. Wang, D. R. Baer, L. E. Thomas, J. E. Amonette, Jiji Antony, You Qiang, and G. Duscher. Void formation during early stages of passivation: Initial oxidation of iron nanoparticles at room temperature. *Journal of Applied*

- Physics*, 98(9):094308, 2005. ISSN 0021-8979. doi: 10.1063/1.2130890. URL <http://aip.scitation.org/doi/10.1063/1.2130890>.
- [53] S. Y. Yu, W. E. O'Grady, D. E. Ramaker, and P. M. Natishan. Chloride Ingress into Aluminum Prior to Pitting Corrosion An Investigation by XANES and XPS. *Journal of The Electrochemical Society*, 147(8):2952, 2000. ISSN 00134651. doi: 10.1149/1.1393630. URL <http://jes.ecsdl.org/cgi/doi/10.1149/1.1393630>.
- [54] N. Sato. A theory for breakdown of anodic oxide films on metals. *Electrochimica Acta*, 16(10):1683 – 1692, 1971. ISSN 0013-4686. doi: 10.1016/0013-4686(71)85079-X. URL <http://www.sciencedirect.com/science/article/pii/001346867185079X>.
- [55] Roger Newman. Pitting Corrosion of Metals. Technical report, University of Toronto, 1976.
- [56] Theodore R. Beck. Occurrence of Salt Films during Initiation and Growth of Corrosion Pits. *Journal of The Electrochemical Society*, 126(10):1662, 1979. ISSN 00134651. doi: 10.1149/1.2128772. URL <http://jes.ecsdl.org/cgi/doi/10.1149/1.2128772>.
- [57] S.P Mattin G.T Burstein. Critical factors in localized corrosion ii. *The Electrochemical Society Proceedings Series, Pennington, NJ, PV 95-15*, 1995.
- [58] Peter H . Balkwil Davis E. Williams, John Stewart. The nucleation, growth and stability of micropits in stainless steel. *Corrosion Science*, 36(7):1213–1235, 1994. doi: 10.1016/0010-938X(94)90145-7.
- [59] A. Valor, F. Caleyó, L. Alfonso, J. C. Velázquez, and J. M. Hallen. Markov chain models for the stochastic modeling of pitting corrosion. *Mathematical Problems in Engineering*, 2013, 2013. ISSN 1024123X. doi: 10.1155/2013/108386.
- [60] J. Goldstein. *Practical Scanning Electron Microscopy: Electron and Ion Microprobe Analysis*. Springer US, 2012. ISBN 9781461344223.
- [61] G Pantazopoulos and A Vazdirvanidis. Identification of corrosion and damage mechanisms by using scanning electron microscopy and energy-dispersive x-ray microanalysis: contribution to failure analysis case histories. *IOP Conference Series: Materials Science and Engineering*, 55(1):012015, 2014. URL <http://stacks.iop.org/1757-899X/55/i=1/a=012015>.
- [62] James Sullivan, Nathan Cooze, Callum Gallagher, Tom Lewis, Tomas Prosek, and Dominique Thierry. In-situ monitoring of corrosion mechanisms and phosphate inhibitor surface deposition during corrosion of Zinc Magnesium Aluminium (ZMA)

- alloys using novel time-lapse microscopy. *Faraday Discussions*, 2015. doi: 10.1039/c4fd00251b. URL <http://rsc.li/fd-upcoming-meetings>.
- [63] David G Enos. The potentiodynamic polarization scan. Technical report, University of Virginia, 1997.
- [64] G.S. Frankel and J.A. Beavers. Cpp protocol and interpretation. Technical report, Ohio State University, DNV Columbus, 2016.
- [65] Francesca Borgioli. From austenitic stainless steel to expanded austenite-s phase: Formation, characteristics and properties of an elusive metastable phase. *Metals*, 10(2), 2020. ISSN 2075-4701. doi: 10.3390/met10020187. URL <https://www.mdpi.com/2075-4701/10/2/187>.
- [66] Francois Liot and Christopher A. Hooley. A simple theory of the invar effect in iron-nickel alloys. *Cornell University Publications*, 2008. doi: 10.48550/ARXIV.0811.3673.
- [67] Hamed Asgari, Mehrnaz Salarian, Henry Ma, Adeola Olubamiji, and Mihaela Vlasea. On thermal expansion behavior of invar alloy fabricated by modulated laser powder bed fusion. *Materials & Design*, 160:895–905, 2018. ISSN 0264-1275. doi: 10.1016/j.matdes.2018.10.025. URL <https://www.sciencedirect.com/science/article/pii/S0264127518307810>.
- [68] T. Wegener, F. Brenne, A. Fischer, T. Möller, C. Hauck, S. Auernhammer, and T. Niendorf. On the structural integrity of fe-36ni invar alloy processed by selective laser melting. *Additive Manufacturing*, 37:101603, 2021. ISSN 2214-8604. doi: 10.1016/j.addma.2020.101603. URL <https://www.sciencedirect.com/science/article/pii/S2214860420309751>.
- [69] Chao Wei, Heng Gu, Qian Li, Zhe Sun, Yuan hui Chueh, Zhu Liu, and Lin Li. Understanding of process and material behaviours in additive manufacturing of invar36/cu10sn multiple material components via laser-based powder bed fusion. *Additive Manufacturing*, 37:101683, 2021. ISSN 2214-8604. doi: 10.1016/j.addma.2020.101683. URL <https://www.sciencedirect.com/science/article/pii/S2214860420310551>.
- [70] B Gehrman, H Hattendorf, A Kilb-Telieps, W Kramer, and W Mottgen. Corrosion behaviour of softmagnetic iron-nickel alloys. *Materials and Corrosion*, 48:535–541, 1997.

- [71] Dale O. Condit. Potentiodynamic polarization studies of fe-ni binary alloys in sulfuric acid solution at 25°C. *Corrosion Science*, 12(5):451–462, 1972. ISSN 0010-938X. doi: 10.1016/S0010-938X(72)80091-X. URL <https://www.sciencedirect.com/science/article/pii/S0010938X7280091X>.
- [72] W.D. Callister and D.G. Rethwisch. *Materials Science and Engineering: An Introduction, 8th Edition*. Wiley, 2009. ISBN 9780470941669.
- [73] D.O Condit. Report 69-0044. *Aerospace Research Laboratories*, Wright-Patterson AFB Ohio, 1969.
- [74] Simon C. Potter, Nabeel Alharthi, El-Sayed M. Sherif, and S. Abdo, Hany S. and Zein El Abedin. Effect of nickel content on the corrosion resistance of iron-nickel alloys in concentrated hydrochloric acid pickling solutions. *Advances in Materials Science and Engineering*, 2017, 2017.
- [75] M.F. McGuire. *Stainless Steels for Design Engineers*. EngineeringPro collection. ASM International, 2008. ISBN 9781615030590. URL <https://books.google.co.uk/books?id=QzJDRxLLxNIC>.
- [76] Zuocheng Wang, Eirini-Maria Paschalidou, Antoine Seyeux, Sandrine Zanna, Vincent Maurice, and Philippe Marcus. Mechanisms of cr and mo enrichments in the passive oxide film on 316l austenitic stainless steel. *Frontiers in Materials*, 6:232, 2019. ISSN 2296-8016. doi: 10.3389/fmats.2019.00232. URL <https://www.frontiersin.org/article/10.3389/fmats.2019.00232>.
- [77] S. Mischler, A. Vogel, H.J. Mathieu, and D. Landolt. The chemical composition of the passive film on fe24cr and fe24cr11mo studied by aes, xps and sims. *Corrosion Science*, 32(9):925–944, 1991. ISSN 0010-938X. doi: 10.1016/0010-938X(91)90013-F. URL <https://www.sciencedirect.com/science/article/pii/0010938X9190013F>.
- [78] V. Maurice, W. P. Yang, and P. Marcus. X-ray photoelectron spectroscopy and scanning tunneling microscopy study of passive films formed on (100) fe-18cr-13ni single-crystal surfaces. *Journal of The Electrochemical Society*, 145(3):909–920, 1998. doi: 10.1149/1.1838366. URL <https://doi.org/10.1149/1.1838366>.
- [79] C.O.A. Olsson and Dieter Landolt. Passive films on stainless steels - chemistry, structure and growth. *Electrochimica Acta*, 48:1093–1104, 2003. doi: 10.1016/S0013-4686(02)00841-1.

- [80] Sebastien Dryepondt, Peeyush Nandwana, Patxi Fernandez-Zelaia, and Fred List III. Microstructure and high temperature tensile properties of 316l fabricated by laser powder-bed fusion. *Additive Manufacturing*, 37:101723, 2021. doi: 10.1016/j.addma.2020.101723.
- [81] P. Dong, F. Vecchiato, Z. Yang, P.A. Hooper, and M.R. Wenman. The effect of build direction and heat treatment on atmospheric stress corrosion cracking of laser powder bed fusion 316l austenitic stainless steel. *Additive Manufacturing*, 40:101902, 2021. ISSN 2214-8604. doi: 10.1016/j.addma.2021.101902. URL <https://www.sciencedirect.com/science/article/pii/S2214860421000671>.
- [82] Nahid Sultan Al-Mamun, Kashif Mairaj Deen, Waseem Haider, Edouard Asselin, and Ishraq Shabib. Corrosion behavior and biocompatibility of additively manufactured 316l stainless steel in a physiological environment: the effect of citrate ions. *Additive Manufacturing*, 34:101237, 2020. ISSN 2214-8604. doi: 10.1016/j.addma.2020.101237. URL <https://www.sciencedirect.com/science/article/pii/S2214860420306096>.
- [83] Ashley M. Roach, Benjamin C. White, Anthony Garland, Bradley H. Jared, Jay D. Carroll, and Brad L. Boyce. Size-dependent stochastic tensile properties in additively manufactured 316l stainless steel. *Additive Manufacturing*, 32:101090, 2020. ISSN 2214-8604. doi: 10.1016/j.addma.2020.101090. URL <https://www.sciencedirect.com/science/article/pii/S2214860419315738>.
- [84] Camille Pauzon, Eduard Hryha, Pierre Forêt, and Lars Nyborg. Effect of argon and nitrogen atmospheres on the properties of stainless steel 316l parts produced by laser-powder bed fusion. *Materials & Design*, 179:107873, 2019. ISSN 0264-1275. doi: 10.1016/j.matdes.2019.107873. URL <https://www.sciencedirect.com/science/article/pii/S0264127519303119>.
- [85] Alberta Aversa, Abdollah Saboori, Erica Librera, Michele de Chirico, Sara Biamino, Mariangela Lombardi, and Paolo Fino. The role of directed energy deposition atmosphere mode on the microstructure and mechanical properties of 316l samples. *Additive Manufacturing*, 34:101274, 2020. ISSN 2214-8604. doi: 10.1016/j.addma.2020.101274. URL <https://www.sciencedirect.com/science/article/pii/S2214860420306461>.
- [86] E.H Valente, V.K Andersen, D.B Pedersen, T.L Christiansen, and M.A.J Somers. Influence of atmosphere on microstructure and nitrogen content in aisi 316l fabricated by laserbased powder bed fusion. *Proceedings of the 19th International Conference and Exhibition (EUSPEN 2019)*, pages 244–247, 2019.

- [87] Zhiwei Duan, Cheng Man, Chaofang Dong, Zhongyu Cui, Decheng Kong, Li wang, and Xin Wang. Pitting behavior of slm 316l stainless steel exposed to chloride environments with different aggressiveness: Pitting mechanism induced by gas pores. *Corrosion Science*, 167:108520, 2020. ISSN 0010-938X. doi: 10.1016/j.corsci.2020.108520. URL <https://www.sciencedirect.com/science/article/pii/S0010938X19319365>.
- [88] David J. Sprouster, W. Streit Cunningham, Gary P. Halada, Hanfei Yan, Ajith Pattammattel, Xiaojing Huang, Daniel Olds, Maryam Tilton, Yong S. Chu, Eric Dooryhee, Guha P. Manogharan, and Jason R. Trelewicz. Dislocation microstructure and its influence on corrosion behavior in laser additively manufactured 316l stainless steel. *Additive Manufacturing*, 47:102263, 2021. ISSN 2214-8604. doi: 10.1016/j.addma.2021.102263. URL <https://www.sciencedirect.com/science/article/pii/S2214860421004231>.
- [89] Lan Chen, Brodan Richter, Xinzhou Zhang, Xudong Ren, and Frank E. Pfefferkorn. Modification of surface characteristics and electrochemical corrosion behavior of laser powder bed fused stainless-steel 316l after laser polishing. *Additive Manufacturing*, 32:101013, 2020. ISSN 2214-8604. doi: 10.1016/j.addma.2019.101013. URL <https://www.sciencedirect.com/science/article/pii/S2214860419310334>.
- [90] Xianglong Hou, Quanyou Ren, Youkun Yang, Xianlong Cao, Jie Hu, Cheng Zhang, Hongda Deng, Daliang Yu, Kejian Li, and Wei Lan. Effect of temperature on the electrochemical pitting corrosion behavior of 316l stainless steel in chloride-containing mdea solution. *Journal of Natural Gas Science and Engineering*, 86:103718, 2021. ISSN 1875-5100. doi: 10.1016/j.jngse.2020.103718. URL <https://www.sciencedirect.com/science/article/pii/S1875510020305722>.
- [91] Yang Zhao, Hang Xiong, Xuanpeng Li, Wenlong Qi, Jidong Wang, Yong Hua, Tao Zhang, and Fuhui Wang. Improved corrosion performance of selective laser melted stainless steel 316l in the deep-sea environment. *Corrosion Communications*, 2:55–62, 2021. ISSN 2667-2669. doi: 10.1016/j.corcom.2021.09.002. URL <https://www.sciencedirect.com/science/article/pii/S2667266921000177>.
- [92] M.J.K. Lodhi, K.M. Deen, and Waseem Haider. Corrosion behavior of additively manufactured 316l stainless steel in acidic media. *Materialia*, 2:111–121, 2018. ISSN 2589-1529. doi: 10.1016/j.mtla.2018.06.015. URL <https://www.sciencedirect.com/science/article/pii/S2589152918300401>.

- [93] Majid Laleh, Anthony E. Hughes, Wei Xu, Ian Gibson, and Mike Y. Tan. A critical review of corrosion characteristics of additively manufactured stainless steels. *International Materials Reviews*, 66(8):563–599, 2021. doi: 10.1080/09506608.2020.1855381. URL <https://doi.org/10.1080/09506608.2020.1855381>.
- [94] Jason R Trelewicz, Gary P Halada, Olivia K Donaldson, and Guha Manogharan. Microstructure and Corrosion Resistance of Laser Additively Manufactured 316L Stainless Steel. *The Journal of The Minerals, Metals & Materials Society*, 68, 2016. doi: 10.1007/s11837-016-1822-4. URL <https://www.sunysb.edu/commcms/ampac/research/JOMTrelewiczetal2016.pdf>.
- [95] K. Saeidi, X. Gao, Y. Zhong, and Z.J. Shen. Hardened austenite steel with columnar sub-grain structure formed by laser melting. *Materials Science and Engineering: A*, 625:221–229, 2015. ISSN 0921-5093. doi: 10.1016/J.MSEA.2014.12.018. URL <https://www.sciencedirect.com/science/article/pii/S0921509314015056>.
- [96] Jingjing Nie, Liang Wei, Ying Jiang, Qian Li, and Hongjie Luo. Corrosion mechanism of additively manufactured 316l stainless steel in 3.5 wt. *Materials Today Communications*, 26:101648, 2021. ISSN 2352-4928. doi: 10.1016/j.mtcomm.2020.101648. URL <https://www.sciencedirect.com/science/article/pii/S2352492820326593>.
- [97] Qi Chao, Victor Cruz, Sebastian Thomas, Nick Birbilis, Paul Collins, Adam Taylor, Peter D. Hodgson, and Daniel Fabijanic. On the enhanced corrosion resistance of a selective laser melted austenitic stainless steel. *Scripta Materialia*, 141:94–98, 2017. ISSN 1359-6462. doi: 10.1016/j.scriptamat.2017.07.037. URL <https://www.sciencedirect.com/science/article/pii/S1359646217304542>.
- [98] G. Sander, S. Thomas, V. Cruz, M. Jurg, N. Birbilis, X. Gao, M. Brameld, and C. R. Hutchinson. On the corrosion and metastable pitting characteristics of 316l stainless steel produced by selective laser melting. *Journal of The Electrochemical Society*, 164(6):C250–C257, 2017. doi: 10.1149/2.0551706jes. URL <https://doi.org/10.1149/2.0551706jes>.
- [99] G. S. Frankel, L. Stockert, F. Hunkeler, and H. Boehni. Metastable Pitting of Stainless Steel. *Corrosion*, 43(7):429–436, 1987. ISSN 0010-9312. doi: 10.5006/1.3583880. URL <https://doi.org/10.5006/1.3583880>.
- [100] Mars Guy Fontana and Norbert D. Greene. *Corrosion Engineering*. McGraw-Hill, 1967.

- [101] Iwan S Grech, Natalie Wint, Nicholas P Lavery, James Sullivan, and Shahin Mehraban. *Solid freeform fabrication proceedings (9th) held in Austin, Texas*. Texas Univ. at Austin, 2019.
- [102] G. Sander, J. Tan, P. Balan, O. Gharbi, D.R. Feenstra, L. Singer, S. Thomas, R.G. Kelly, J.R. Scully, N. Birbilis, and et al. Corrosion of additively manufactured alloys: A review. *CORROSION*, 74(12):1318–1350, 2018. doi: 10.5006/2926.
- [103] Nicholas Lavery, J Cherry, Shahid Mehmood, HM Davies, B Girling, E Sacket, S.G.R. Brown, and J. Sienz. Effects of hot isostatic pressing on the elastic modulus and tensile properties of 316l parts made by powder bed laser fusion. *Materials Science and Engineering A*, 693:186–293, 2017. doi: 10.1016/j.msea.2017.03.100.
- [104] I.S. Grech, J.H. Sullivan, R.J. Lancaster, J. Plummer, and N.P. Lavery. The optimisation of hot isostatic pressing treatments for enhanced mechanical and corrosion performance of stainless steel 316l produced by laser powder bed fusion. *Additive Manufacturing*, 58:103072, 2022. ISSN 2214-8604. doi: 10.1016/j.addma.2022.103072. URL <https://www.sciencedirect.com/science/article/pii/S221486042200464X>.
- [105] H. V. Atkinson and S. Davies. Fundamental aspects of hot isostatic pressing: An overview. *Metallurgical and Materials Transactions A*, 31(12):2981–3000, 2000. doi: 10.1007/s11661-000-0078-2.
- [106] A. du Plessis and E. Macdonald. Hot isostatic pressing in metal additive manufacturing: X-ray tomography reveals details of pore closure. *Additive Manufacturing*, 34:101191, 2020. doi: 10.1016/j.addma.2020.101191.
- [107] Anne-Helene Puichaud, Camille Flament, Aziz Chniouel, Fernando Lomello, Elodie Rouesne, Pierre-François Giroux, Hicham Maskrot, Frederic Schuster, and Jean-Luc Béchade. Microstructure and mechanical properties relationship of additively manufactured 316l stainless steel by selective laser melting. *EPJ Nuclear Sciences and Technologies*, 5:23, 2019. doi: 10.1051/epjn/2019051.
- [108] Tomas Cegan, Marek Pagac, Jan Jurica, Katerina Skotnicova, Jiri Hajnys, Lukas Horsak, Kamil Soucek, and Pavel Krpec. Effect of hot isostatic pressing on porosity and mechanical properties of 316 l stainless steel prepared by the selective laser melting method. *Materials*, 13(19):4377, 2020. doi: 10.3390/ma13194377.
- [109] Erica Liverani, Adrian H. Lutey, Alessandro Ascari, and Alessandro Fortunato. The effects of hot isostatic pressing (hip) and solubilization heat treatment on the density, mechanical properties, and microstructure of austenitic stainless steel parts produced by selective laser melting (slm). *The International*

- Journal of Advanced Manufacturing Technology*, 107(1-2):109–122, 2020. doi: 10.1007/s00170-020-05072-9.
- [110] George Krauss. *STEELS Processing, Structure, and Performance*. ASM International, 2015. ISBN 978-1-62708-083-5.
- [111] Pethuel Atanda, A. Fatudimu, and Leke Oluwole. Sensitisation study of normalized 316l stainless steel. *Journal of Minerals and Materials Characterization and Engineering*, 09, 2010. doi: 10.4236/jmmce.2010.91002.
- [112] Majid Laleh, Anthony E. Hughes, Wei Xu, Pavel Cizek, and Mike Yongjun Tan. Unanticipated drastic decline in pitting corrosion resistance of additively manufactured 316l stainless steel after high-temperature post-processing. *Corrosion Science*, 165:108412, 2020. doi: 10.1016/j.corsci.2019.108412.
- [113] Janusz Kluczyński, Lucjan Śnieżek, Krzysztof Grzelak, Janusz Torzewski, Ireneusz Szachogłuchowicz, Artur Oziębło, Krzysztof Perkowski, Marcin Wachowski, and Marcin Małek. The influence of heat treatment on low cycle fatigue properties of selectively laser melted 316l steel. *Materials*, 13(24), 2020. ISSN 1996-1944. doi: 10.3390/ma13245737. URL <https://www.mdpi.com/1996-1944/13/24/5737>.
- [114] Xiaoyu Liang. high cycle fatigue behaviour of additively manufactured stainless steel 316l: free surface effect and microstructural heterogeneity. *Materials. HESAM University*, 2020.
- [115] Pavel Krakhmalev, Gunnel Fredriksson, Krister Svensson, Igor Yadroitsev, Ina Yadroitsava, Mattias Thuvander, and Ru Peng. Microstructure, solidification texture, and thermal stability of 316 l stainless steel manufactured by laser powder bed fusion. *Metals*, 8(8), 2018. ISSN 2075-4701. URL <https://www.mdpi.com/2075-4701/8/8/643>.
- [116] Chola Elangeswaran, Antonio Cutolo, Gokula Krishna Muralidharan, Kim Vanmeensel, and Brecht Van Hooreweder. Microstructural analysis and fatigue crack initiation modelling of additively manufactured 316l after different heat treatments. *Materials & Design*, 194:108962, 2020. doi: 10.1016/j.matdes.2020.108962.
- [117] Punit Kumar, R. Jayaraj, J. Suryawanshi, U.R. Satwik, J. McKinnell, and U. Ramamurthy. Fatigue strength of additively manufactured 316l austenitic stainless steel. *Acta Materialia*, 199:225–239, 2020. ISSN 1359-6454. doi: 10.1016/j.actamat.2020.08.033. URL <https://www.sciencedirect.com/science/article/pii/S1359645420306303>.
- [118] Luqing Cui, Dunyong Deng, Fuqing Jiang, Ru Lin Peng, Tongzheng Xin, Reza Taherzadeh Mousavian, Zhiqing Yang, and Johan Moverare. Superior low

- cycle fatigue property from cell structures in additively manufactured 316l stainless steel. *Journal of Materials Science & Technology*, 111:268–278, 2022. ISSN 1005-0302. doi: 10.1016/j.jmst.2021.10.006. URL <https://www.sciencedirect.com/science/article/pii/S1005030221008665>.
- [119] Meng Zhang, Chen-Nan Sun, Xiang Zhang, Jun Wei, David Hardacre, and Hua Li. High cycle fatigue and ratcheting interaction of laser powder bed fusion stainless steel 316l: Fracture behaviour and stress-based modelling. *International Journal of Fatigue*, 121:252–264, 2019. ISSN 0142-1123. doi: 10.1016/j.ijfatigue.2018.12.016. URL <https://www.sciencedirect.com/science/article/pii/S0142112318307357>.
- [120] Wei-Jen Lai, Avinesh Ojha, Ziang Li, Carlos Engler-Pinto, and Xuming Su. Effect of residual stress on fatigue strength of 316l stainless steel produced by laser powder bed fusion process. *Progress in Additive Manufacturing*, 6:375–383, 2021. doi: 10.1007/s40964-021-00164-8. URL <https://link.springer.com/article/10.1007/s40964-021-00164-8#citeas>.
- [121] Columbia Metals. 17-4ph columbia metals, 2020. accessed 2020-10-06.
- [122] Alan J. Ardell. Precipitation hardening. *Metallurgical and Materials Transactions A*, 1985.
- [123] Rowolt Christian, Milkereit Benjamin, Springer Armin, Kreyenschulte Carsten, and Kessler Olaf. Precipitation-induced changes in microstrain and its relation with hardness and tempering parameter in 17-4 ph stainless steel. *Journal of Materials Science*, 2020.
- [124] Aref Yadollahi, Mohamad Mahmoudi, Alaa Elwany, Haley Doude, Linkan Bian, and James C. Newman. Effects of crack orientation and heat treatment on fatigue-crack-growth behavior of am 17-4 ph stainless steel. *Engineering Fracture Mechanics*, 226:106874, 2020. ISSN 0013-7944. doi: 10.1016/j.engfracmech.2020.106874. URL <https://www.sciencedirect.com/science/article/pii/S0013794419312330>.
- [125] Eric J. Schindelholz, Michael A. Melia, and Jeffrey M. Rodelas. Corrosion of Additively Manufactured Stainless Steels—Process, Structure, Performance: A Review. *Corrosion*, 77(5):484–503, 2021. ISSN 0010-9312. doi: 10.5006/3741. URL <https://doi.org/10.5006/3741>.

- [126] Rebecca F. Schaller, Jason M. Taylor, Jeffrey Rodelas, and Eric J. Schindelholz. Corrosion Properties of Powder Bed Fusion Additively Manufactured 17-4 PH Stainless Steel. *Corrosion*, 73(7):796–807, 2017. ISSN 0010-9312. doi: 10.5006/2365. URL <https://doi.org/10.5006/2365>.
- [127] M.R. Stoudt, C.E. Campbell, and R.E. Ricker. Examining the relationship between post-build microstructure and the corrosion resistance of additively manufactured 17-4ph stainless steel. *Materialia*, 22:101435, 2022. ISSN 2589-1529. doi: 10.1016/j.mtla.2022.101435. URL <https://www.sciencedirect.com/science/article/pii/S2589152922001181>.
- [128] Adrien Barroux, Nadège Ducommun, Eric Nivet, Lydia Laffont, and Christine Blanc. Pitting corrosion of 17-4ph stainless steel manufactured by laser beam melting. *Corrosion Science*, 169:108594, 2020. ISSN 0010-938X. doi: 10.1016/j.corsci.2020.108594. URL <https://www.sciencedirect.com/science/article/pii/S0010938X19325004>.
- [129] Michella Alnajjar, Frédéric Christien, Vincent Barnier, Cédric Bosch, Krzysztof Wolski, A. Dominic Fortes, and Mark Telling. Influence of microstructure and manganese sulfides on corrosion resistance of selective laser melted 17-4 ph stainless steel in acidic chloride medium. *Corrosion Science*, 168:108585, 2020. ISSN 0010-938X. doi: 10.1016/j.corsci.2020.108585. URL <https://www.sciencedirect.com/science/article/pii/S0010938X19320219>.
- [130] Michella Alnajjar, Frédéric Christien, Krzysztof Wolski, and Cedric Bosch. Evidence of austenite by-passing in a stainless steel obtained from laser melting additive manufacturing. *Additive Manufacturing*, 25:187–195, 2019. ISSN 2214-8604. doi: 10.1016/j.addma.2018.11.004. URL <https://www.sciencedirect.com/science/article/pii/S2214860418304664>.
- [131] Hongyu Ma, Rui Liu, Peiling Ke, Yu Cui, Li Liu, and Fuhui Wang. Effect of hydrostatic pressure on the pitting corrosion of 17-4ph martensitic stainless steel. *Engineering Failure Analysis*, 138:106367, 2022. ISSN 1350-6307. doi: 10.1016/j.engfailanal.2022.106367. URL <https://www.sciencedirect.com/science/article/pii/S1350630722003417>.
- [132] Cem Örneç. Additive manufacturing—a general corrosion perspective. *Corrosion Engineering Science and Technology*, 53(7):531–535, 2018. ISSN 17432782. doi: 10.1080/1478422X.2018.1511327. URL <https://doi.org/10.1080/1478422X.2018.1511327>.

- [133] R.N. Kacker, E.S. Lagergren, and J.J. Filliben. Taguchi's orthogonal arrays are classical designs of experiments. *Journal of Research of the National Institute of Standards and Technology*, 96(5):577, 1991. doi: 10.6028/jres.096.034.
- [134] A. Atkinson, A. Donev, and R. Tobias. *Optimum Experimental Designs, With SAS*. Oxford Statistical Science Series. OUP Oxford, 2007. ISBN 9780199296590. URL <https://books.google.co.uk/books?id=oIHsrw6NBmoC>.
- [135] J.L. Rosa, A. Robin, M.B. Silva, C.A. Baldan, and M.P. Peres. Electrodeposition of copper on titanium wires: Taguchi experimental design approach. *Journal of Materials Processing Technology*, 209(3):1181–1188, 2009. ISSN 0924-0136. doi: 10.1016/j.jmatprotec.2008.03.021. URL <https://www.sciencedirect.com/science/article/pii/S0924013608002446>.
- [136] James Sullivan, Shahin Mehraban, and Jon Elvins. In situ monitoring of the microstructural corrosion mechanisms of zinc–magnesium–aluminium alloys using time lapse microscopy. *Corrosion Science*, 53(6):2208 – 2215, 2011. ISSN 0010-938X. doi: 10.1016/j.corsci.2011.02.043. URL <http://www.sciencedirect.com/science/article/pii/S0010938X11001417>.
- [137] Nathan E. Cooze. *The use of a novel time-lapse microscopy technique to study the corrosion effects of zinc magnesium aluminium alloys in aqueous salt solutions*. Phd, Swansea University, 2015.
- [138] H.N. McMurray and D.A. Worsley. *Scanning Electrochemical Techniques for the Study of Localised Metallic Corrosion*, volume 4. Corrosion Advances in Chemical Kinetics J. Electrochem. Soc. ed R.G. Compton and G. Hancock (Oxford, England: Blackwell Science), 1997.
- [139] A. C. Bastos, M. C. Quevedo, O. V. Karavai, and M. G. S. Ferreira. Review—On the Application of the Scanning Vibrating Electrode Technique (SVET) to Corrosion Research. *Journal of The Electrochemical Society*, 164(14):C973–C990, 2017. ISSN 0013-4651. doi: 10.1149/2.0431714jes. URL <http://jes.ecsdl.org/lookup/doi/10.1149/2.0431714jes>.
- [140] C. F. Kannan, B. and Glover, H. N. McMurray, G. Williams, and J. R. Scully. Performance of a Magnesium-Rich Primer on Pretreated AA2024-T351 in Full Immersion: a Galvanic Throwing Power Investigation Using a Scanning Vibrating Electrode Technique. *Journal of The Electrochemical Society*, 165(2):C27–C41, 2018. ISSN 0013-4651. doi: 10.1149/2.0711802jes. URL <http://jes.ecsdl.org/lookup/doi/10.1149/2.0711802jes>.

- [141] ASTM Standard. Astm b962-17 standard test methods for density of compacted or sintered powder metallurgy (pm) products using archimedes principle, 2009.
- [142] ASTM Standard. Astm e8/e8m standard test methods for tension testing of metallic materials, 2013.
- [143] A. Röttger, J. Boes, W. Theisen, M. Thiele, C. Esen, A. Edelmann, and R. Hellmann. Microstructure and mechanical properties of 316l austenitic stainless steel processed by different slm devices. *The International Journal of Advanced Manufacturing Technology*, 108(3):769–783, 2020. doi: 10.1007/s00170-020-05371-1.
- [144] Antonella Sola and Alireza Nouri. Microstructural porosity in additive manufacturing: The formation and detection of pores in metal parts fabricated by powder bed fusion. *Journal of Advanced Manufacturing and Processing*, 1(3):e10021, 2019. doi: 10.1002/amp2.10021. URL <https://aiche.onlinelibrary.wiley.com/doi/abs/10.1002/amp2.10021>.
- [145] Viktor Bläsjö. The isoperimetric problem. *The American Mathematical Monthly*, 112(6):526–566, 2005.
- [146] Claudia Prieto, Marc Singer, Timothy Cyders, and David Young. Investigation of Pitting Corrosion Initiation and Propagation of a Type 316L Stainless Steel Manufactured by the Direct Metal Laser Sintering Process. *Corrosion*, 75(2):140–143, 2018. ISSN 0010-9312. doi: 10.5006/3075. URL <https://doi.org/10.5006/3075>.
- [147] Shashanka Rajendrachari. Non-lubricated dry sliding wear behavior of spark plasma sintered nano-structured stainless steel. *Journal of Materials and Environmental Science*, 10:767–777, 2019. doi: 10(8)(2019)767-777.
- [148] Sergey Astafurov and Elena Astafurova. Phase composition of austenitic stainless steels in additive manufacturing: A review. *Metals*, 11(7), 2021. ISSN 2075-4701. doi: 10.3390/met11071052. URL <https://www.mdpi.com/2075-4701/11/7/1052>.
- [149] Francesca Borgioli. From austenitic stainless steel to expanded austenite-s phase: Formation, characteristics and properties of an elusive metastable phase. *Metals*, 10(2), 2020. ISSN 2075-4701. doi: 10.3390/met10020187. URL <https://www.mdpi.com/2075-4701/10/2/187>.
- [150] Material web material property data. Aisi 316l asutenitic stainless steel annealed bar, 2021. URL <http://www.matweb.com/search/DataSheet.aspx?MatGUID=a2d0107bf958442e9f8db6dc9933fe31>.

- [151] ASM aerospace specification metals inc. Aisi type 316l, annealed plate, 2021. URL <http://asm.matweb.com/search/SpecificMaterial.asp?bassnum=MQ316P>.
- [152] J.S. Zuback and T. DebRoy. The hardness of additively manufactured alloys. *Materials*, 11(11):2070, 2018. doi: 10.3390/ma11112070.
- [153] P.D. Harvey. Engineering properties of aisi type 316l stainless steel, annealed sheet. *Metals Park Ohio: American Society for Metals*, 1982.
- [154] Luqing Cui, Shuang Jiang, Jinghao Xu, Ru Lin Peng, Reza Taherzadeh Mousavian, and Johan Moverare. Revealing relationships between microstructure and hardening nature of additively manufactured 316l stainless steel. *Materials & Design*, 198:109385, 2021. ISSN 0264-1275. doi: 10.1016/j.matdes.2020.109385. URL <https://www.sciencedirect.com/science/article/pii/S0264127520309217>.
- [155] F.R.N Nabarro. Dislocations in a simple cubic lattice. *Proceedings of the physical society*, 2(256):59, 1947.
- [156] F.R.N. Nabarro. Fifty-year study of the peierls-nabarro stress. *Materials Science and Engineering: A*, 234-236:67–76, 1997. ISSN 0921-5093. doi: 10.1016/S0921-5093(97)00184-6. URL <https://www.sciencedirect.com/science/article/pii/S0921509397001846>.
- [157] A.J Foreman, M.A Jaswom, and J.K Wood. Factors controlling dislocation widths. *Proceedings of the physical society, Section A*, 64(2):156–163, 1951.
- [158] Y Wang. Hall-petch relationship in selective laser melting additively manufactured metals: using grain or cell size? *Journal of Central South University*, 28(4):1043–1057, 2021. doi: 10.1007/s11771-021-4678-x.
- [159] M.S. Pham, B. Dovggy, and P.A. Hooper. Twinning induced plasticity in austenitic stainless steel 316l made by additive manufacturing. *Materials Science and Engineering: A*, 704:102–111, 2017. doi: 10.1016/j.msea.2017.07.082.
- [160] Arthur Griebel. Technical brief: Fatigue dimples. *Journal of Failure Analysis and Prevention*, 9:193–196, 2009. doi: 10.1007/s11668-009-9228-z.
- [161] Raul Davalos Monteiro, Jan van de Wetering, Benjamin Krawczyk, and Dirk L. Engelber. Corrosion Behaviour of Type 316L Stainless Steel in Hot Caustic Aqueous Environments. *Materials and Materials International*, 26:630–640, 2020.
- [162] Mohamad Bayat, Aditi Thanki, Sankhya Mohanty, Ann Witvrouw, Shoufeng Yang, Jesper Thorborg, Niels Skat Tiedje, and Jesper Henri Hattel. Keyhole-induced porosities in laser-based powder bed fusion (l-pbf) of ti6al4v: High-fidelity modelling and experimental validation. *Additive Manufacturing*, 30:100835,

2019. ISSN 2214-8604. doi: 10.1016/j.addma.2019.100835. URL <https://www.sciencedirect.com/science/article/pii/S2214860419303914>.
- [163] Wayne E. King, Holly D. Barth, Victor M. Castillo, Gilbert F. Gallegos, John W. Gibbs, Douglas E. Hahn, Chandrika Kamath, and Alexander M. Rubenchik. Observation of keyhole-mode laser melting in laser powder-bed fusion additive manufacturing. *Journal of Materials Processing Technology*, 214(12):2915–2925, 2014. ISSN 0924-0136. doi: 10.1016/j.jmatprotec.2014.06.005. URL <https://www.sciencedirect.com/science/article/pii/S0924013614002283>.